ANARE RESEARCH NOTES 92

Australian auroral and space physics research in Antarctica, 1993

Edited by R.J. Morris

Australian
National
Antarctic
Research
Expeditions

ANARE RESEARCH NOTES (ISSN 0729-6533)

This series allows rapid publication in a wide range of disciplines. Copies of this and other *ANARE Research Notes* are available from the Antarctic Division. Any person who has participated in Australian National Antarctic Research Expeditions is invited to publish through this series. Before submitting manuscripts authors should obtain advice from:

The Publications Office
Antarctic Division
Channel Highway
Kingston 7050
Australia

Published July 1994
ISBN: 0 642 21245 7

CONTENTS

AUSTRALIAN AURORAL AND SPACE PHYSICS RESEARCH IN ANTARCTICA, 1993

Edited by R.J. Morris

Antarctic Division

Department of the Environment, Sport and Territories

Kingston, Tasmania, Australia

PREFACE

The papers in this collection were presented at the Second South Pacific Solar-Terrestrial Energy Program (STEP) Workshop held at the University of Newcastle, New South Wales between 5 and 9 July 1993. This anthology consists of papers considered relevant to Australian Antarctic research which were either presented or introduced at the Workshop.

The majority of the papers are preliminary and are intended as an indication of the current activity of Australian auroral and space physics research in Antarctica. It is anticipated that final results will appear in appropriate journals. The editor thanks the respective authors for their contributions, Judy Whelan for the preparation of the manuscripts and Sandra Potter for organising the final publication.

1. THE GEOELECTRIC FIELD AT DAVIS STATION, ANTARCTICA - REVISITED

G.B. Burns[1], S.K. Parcell[1], M.H. Hesse[1] and S. Malachowski[2]

[1] Auroral and Space Physics
Antarctic Division
Kingston Tasmania 7050
Australia

[2] Physics Department
LaTrobe University
Bundoora Victoria 3083
Australia

ABSTRACT

Approximately a years vertical electric field data (9th July 1989 to 10th July 1990) measured at Davis station, Antarctica (geog: 68.6°S, 78.0°E; PGM – 1988 [Baker and Wing 1989]: 74.6°S, 102.3°E) have been reanalysed using stricter selection criteria to reduce local influences, to determine seasonal-diurnal curves for this site. The initial analysis was reported by Hesse et al. (1992). A paucity of intervals not locally influenced precludes determination of a summer diurnal curve.

The seasonal-diurnal curves each show a peak between 19 and 22 UT that is similar in temporal location and relative magnitude to the global, fair-weather, seasonal-diurnal curves (see Reiter 1992, p 130). A local influence persists in the Davis diurnal curves during the 03 to 10 UT interval and precludes determination of a magnetospheric influence on the ground level geoelectric field at this high magnetic latitude site.

1.1 INTRODUCTION

Hesse et al. (1992) have reported on an initial analysis of approximately a year of vertical electric field measurements recorded at Davis station, Antarctica. To provide a background to this research, a brief overview of the geoelectric field and the Davis site geoelectric field data collection and analysis is reproduced from that paper.

An electric field of the order of 300 kV is maintained, principally by world-wide thunderstorm activity, between the lowest reaches of the ionosphere and the ground. At ground level this electric field is of the order of 100 V m^{-1}. In regions of 'fair weather', a current density of the order of 3 pA m^{-2} (Burke and Few 1978) flows from the ionosphere to the Earth

In the polar regions, the interaction of the solar wind and the Earth's magnetic field leads to the establishment of a variable electric potential of 20 to 150 kV between the dawn and dusk sectors of the polar cap. This electric potential drives the plasma flow in the polar

ionosphere, and by collisional interaction also controls the motion of the neutral atmosphere in the polar thermosphere.

The interaction of these electric fields provides a mechanism by which a so-called 'sun-weather' process (i.e. a linkage between solar activity and tropospheric weather systems) may operate. The possibility of distinguishing the various influences on the measurement of the vertical electric field at any site relies on expected differences due to the control mechanisms.

1. The thunderstorm generated electric potential should be globally synchronised and may be expected to vary diurnally and seasonally in a manner related to globally integrated thunderstorm activity. To determine the component that is globally synchronised, a comparison can be made with the 'Carnegie', seasonal-diurnal, fair-weather curves as presented in Reiter (1992, p 130).

2. Any magnetospheric influences should maximise where the diurnal variation of the ionospheric potential generated by the interaction of the solar wind and the Earth's magnetic field maximises (i.e. at auroral latitudes). The magnitude of the modification to the diurnal variation should be dependent on the magnitude of the polar cap potential.

3. Local meteorological and anthropological influences will be related to local parameters.

The instrumentation for this experiment is located at Davis because, of the Australian Antarctic stations, it has the most consistently fine weather. In addition, its magnetic invariant latitude is 74.6°S, a sensible latitude for seeking a magnetospheric influence.

Reported attempts to measure the geoelectric field in polar regions are few. Park (1976) found a solar sector influence on the geoelectric field measured at the polar plateau site of Vostok. Recently, Byrne et al. (1993) reported on the instrumentation and some initial days data of geoelectric field measurements at South Pole.

The Hesse et al. (1992) paper delineated the dominant local meteorological influences on the measurement of the geoelectric field at the Davis site, suggested possible investigations to determine more subtle influences and presented seasonal-diurnal curves based on a preliminary selection of possible 'fair weather' times from approximately a year of data. This paper reports on a refinement of procedures for reducing local influences in the selected data and a reanalysis of the initially selected Davis data set. Seasonal-diurnal 'average' curves are constructed and discussed in terms of possible 'global' influences and possible remnant 'local' influences. A data splitting technique is used to search for possible magnetospheric influences on the Davis geoelectric field data.

1.2 INSTRUMENTATION AND DATA COLLECTION

A rotating dipole sensor of the 'field mill' type, similar to that used by Park (1976), is used to monitor the vertical electric field at the Davis site.

The values for the electric field (in V m^{-1}, positive for a downward directed field) used in this paper refer to the potential applied across parallel plates of a calibration box used with the mill. They are not intended as an absolute representation of the electric field at the site.

From the calibration measurements, the mill output is linear to the order of 0.1%. This amounts to less than 1 V m^{-1} for 'fair weather' values of the electric field. A variation in offset of 7 V m^{-1} between in-field calibrations was recorded over the period of the measurements reported here. A fixed, average offset value has been used for reduction of the data presented.

The electric field mill is located approximately 200 metres to the east of the main physics laboratory and is generally upwind of possible Davis station atmospheric pollution sources (see Hesse et al. 1992, Figure 1). Measurements of the wind speed, wind direction, temperature, relative humidity and atmospheric pressure are also made at this remote site. Data from all sensors are recorded once every 10 seconds, are collected in UT-daily files and are transmitted back to Antarctic Division (Hobart, Australia) via a satellite data link.

Observations of visibility and cloud cover made daily at 00, 03, 06, 09, 12 and 15 UT by Bureau of Meteorology Observers at Davis are also used in this analysis.

1.3 DATA SELECTION TO MINIMISE LOCAL INFLUENCES

As noted by Hesse et al. (1992), recognising the more dramatic examples of local influences on the electric field measurements is relatively easy, but defining an objective method of data selection to exclude such events is very difficult. To ignore all electric field data with associated wind speeds above the lowest wind speed for which a strong positive association with electric field has been observed (Hesse et al. 1992, Section 3.1), and to ignore all data with an associated wind speed less than the highest wind speed for which a negative correlation with wind speed has been observed (Hesse et al. 1992, Section 3.3), is to exclude all data!

The following subjective judgements were reported by Hesse et al. (1992). Readers are referred to Hesse et al. (1992) for a general discussion and specific examples of the local influences found on the geoelectric field at Davis.

Local effects are *very likely* to influence the measurement of the electric field at the Davis site if:

1. The wind speed is above 25 knots. The probability of the electric field being affected at a particular wind speed is dependent on the relative humidity, but for wind speeds above 25 knots the electric field measurement is *very likely* to be affected, independent of the relative humidity level.

2. The relative humidity is above 85% (snow a possibility). Any falling snow or reduced visibility will effect the electric field measurement.

3. The wind is coming from the direction range between 240°E and 320°E (Davis station emissions may drift over the data collection site).

Local effects *might* influence the measurement of the electric field at the Davis site if:

1. The wind speed is above 20 knots.

2. The wind speed is above 8 knots and the relative humidity is above 45%. The probability of the wind speed affecting the electric field is dependent on the relative humidity level at the time.

3. The wind speed is below 10 knots. Note the overlap with the item above, but remember that we are talking *might.*

Local effects are *unlikely* to influence the measurement of the electric field at the Davis site if:

1. The wind speed is above 10 knots *and* the wind speed is below 20 knots *and* the relative humidity is less than 45% *and* the wind is not coming from the direction range 240°E to 320°E.

Approximately one year of Davis electric field and associated meteorological data was visually examined and, focusing on the possibilities outlined above, data periods when local influences were apparently influencing the measurements were excluded. The data considered were from the period 9th of July 1989 to the 10th of July 1990.

The following additional influences and exclusions were made to the data selected for the Hesse et al. (1992) analysis.

Using the visibility observations undertaken by the Meteorological Observers at Davis, only periods encompassed by two consecutive visibility observations of at least 30 km were retained. This excludes all periods when fog or falling or blowing snow may be influencing the electric field measurements.

In laboratory temperature tests, the electric field mill has proved unreliable around temperatures of 0°C yielding inconsistent, higher than correct, values. This effect is likely related to the condensation of water vapour. A scatter plot of 20-minute averaged electric field data recorded at Davis against similarly averaged temperature data indicated abnominally high values around 0°C. Data collected when the 20-minute average temperature was in the range -3°C to +3°C were excluded.

Figure 1(a) shows a plot of the finally selected 20-minute averages of electric field against similarly averaged relative humidity values. In Figure 1(a) a general trend is apparent, higher electric field values are broadly correlated with low relative humidity values. A linear fit to the data presented yields:

$$E[\text{electric field (V m}^{-1})] = -1.3 \times [\text{relative humidity (\%)}] + 215$$

Because of this relationship, only periods of data over which the relative humidity value remained constant within of the order of 10% were retained.

Figure 1(b) shows a plot of the finally selected 20-minute averages of electric field against similarly averaged wind speed values. A positive relationship between wind speed and electric field data persists. A linear fit to 1(b) yields:

$$E[\text{electric field (V m}^{-1})] = 2.3 \times [\text{wind speed (knots)}] + 140$$

Without more careful analysis, it is impossible to determine if the wind speed influencing the electric field measurements or if there is an average coincident diurnal variation in the electric field and local wind speed. At this stage the relationship is simply noted.

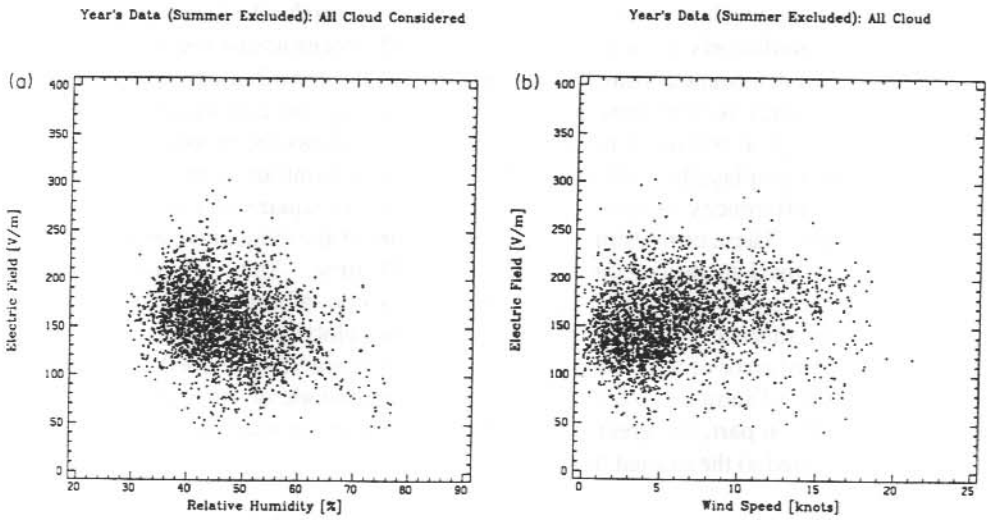

Figure 1. Plots of 20-minute averages for all the data selected for analysis (winter, spring and autumn).

(a) Electric field against relative humidity. Linear best fit:
$E[\text{electric field (V m}^{-1})] = -1.3 \times [\text{relative humidity (\%)}] + 215$

(b) Electric field against wind speed. Linear best fit:
$E[\text{electric field (V m}^{-1})] = 2.3 \times [\text{wind speed (knots)}] + 140$

1.4 SEASONAL, DIURNAL VARIATIONS

All the restrictions applied in an effort to remove local influences from the electric field measurements meant only a small amount of data remain. Because of the paucity of data, segments as small as 2 hours duration were retained. Each of the chosen data segments was averaged with a bin size of 20 minutes and the data collated into periods covering the four seasons: summer – 1st November to 31st January; autumn – 1st February to 30th April; winter – 1st May to 31st July; and spring – 1st August to 31st October. The restrictions on temperature and on the variation in relative humidity meant that only 154 hours (6.4 days) of summer data remained and this season was removed from further consideration. Data remaining for the other seasons amount to: autumn – 315 hours (13.1 days); winter – 332 hours (13.8 days) and spring – 460 hours (19.2 days).

A simple average of the data in each time bin was used to derive the diurnal curves for the meteorological parameters. The electric field requires a more complex form of averaging to

reduce the significant variability in the offsets of the data segments. The association of the measured electric field values with relative humidity is of particular relevance in this regard. For each data sequence, the differences between each consecutive 20-minute average were calculated. The averages of these differences were calculated. The average consecutive differences calculated from all selected data are plotted in the top curve of Figure 2(a). From this curve it can be seen that positive differences dominate the interval 15 – 20 UT and negative differences the interval 20 – 02 UT. The differences are evenly spread between positive and negative values over the remaining time interval. A diurnal curve can be constructed by cumulatively adding the consecutive differences across the 24 hour period. An initial offset is determined from an averaged sum of the contributing data points, with allowance being made for the time of the sample by using the constructed 'cumulative differences' curve. The second of the plots in Figure 2(a) shows the reconstructed diurnal curve. Error bars displayed on all except the initial data point are ± twice the standard deviation of the 'differences' in each time bin, divided by the square-root of the number of samples in that bin. These error estimates take no account of the cumulative error due to the addition process used to derive the value at each UT time. They are thus an under-estimation of the error, but are included to allow some relative comparison of the significance of the diurnal curves presented. The error bar plotted on the initial data point is ± twice the standard error of the electric field values in this time bin, divided by the square-root of the number of samples in that bin. The larger magnitude of the error on the initial data point reflects, in part, the greater variability in the average magnitude of the electric field signal compared to the diurnal trend.

The method of construction of the diurnal curves allows the possibility that uncertainties in the mean of the 'consecutive differences' will accumulate in a random walk manner across the diurnal curve and the 0010 UT and 2350 UT derived values may be significantly different. If there is a generally consistent diurnal trend in the electric field, and if sufficient data are averaged, then the discrepancy of the 0010 UT and 2350 UT values will be small. The difference of these values can be compared with the general displacement of consecutive values to determine if this random walk accumulation of uncertainties has significantly affected the derivation of the diurnal curves.

The reconstructed diurnal curve for the combined winter, autumn and spring data (1107 hours, 46.1 days; see Figure 2a) shows a peak value of 178 V m^{-1} at 2050 UT and a diurnal range of 39 V m^{-1}. A minor rise between 03 UT and 10 UT appears correlated with a small rise in the wind speed diurnal curve and to a lesser extent with the weak diurnal dip in the relative humidity curve. Local geographic noon at Davis occurs around 0650 UT, and the broad low rise in the electric field around this time may be a local effect that we have been unable to remove. Further evidence that this is a local phenomena will be provided by the seasonal data splits.

Figure 2(b) shows the diurnal trend derived by including only data encompassed by consecutive total cloud observations at Davis in the range 0/8-2/8. The cloud cover restriction limits the data to 386 hours (16.1 days). The diurnal curves of average 'consecutive differences', the 'constructed' curve, and of the wind speed and relative humidity are presented in Figure 2(b) in a manner analogous to Figure 2(a). The general features of the two curves are similar. These are the broad peak between 19 and 24 UT and the minor rise between 03 and 09 UT. Specifically, the constructed diurnal curve

derived using the cloud cover restrictions shows a peak value of 184 V m^{-1} but at later time of 2210 UT, and diurnal range of 48 V m^{-1}. Because the general trends of the yearly data, excluding summer, remain the same using data inclusive of all cloud conditions, and because of the overall paucity of data, we include data in the following data splits irrespective of the local cloud cover.

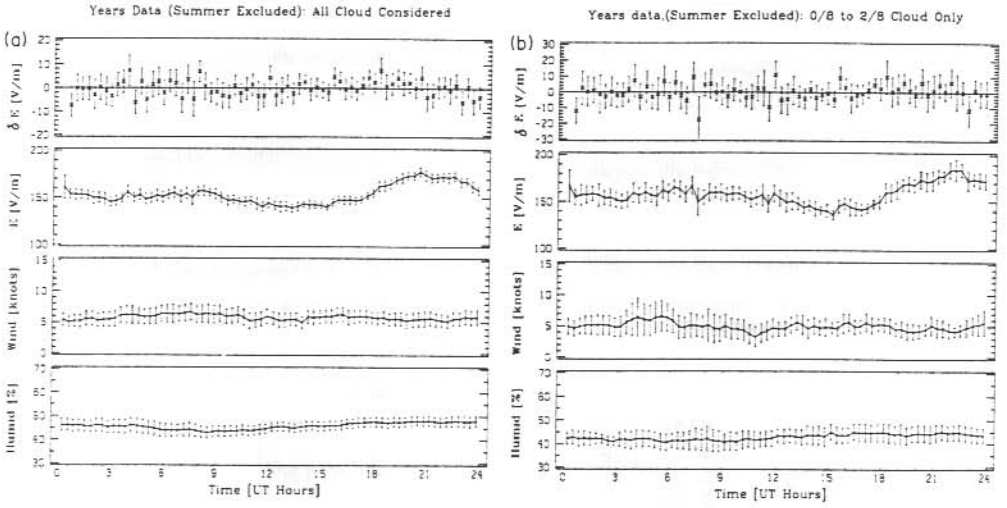

Figure 2. Top panel: average 20-minute consecutive differences.
2nd panel: the diurnal curve in electric field.
3rd panel: the associated average wind speed curve.
Bottom panel: the associated average relative humidity curve.
(a) All data selected for analysis (winter, spring and autumn).
(b) All data for which consecutive meteorological cloud observations were in the range, 0/8 – 2/8.

Figure 3(a) shows the electric field diurnal curve for the winter season and the associated diurnal curves of the meteorological parameters. The winter curve has a peak value of 184 V m^{-1} which occurs at 2030 UT, and a diurnal range of the order of 49 V m^{-1} amounting to some 31% of the diurnal mean value. The generally flat nature of the diurnal curves of wind speed and relative humidity gives confidence that there is no significant local control of the winter diurnal electric field curve. The 'fair weather' Carnegie diurnal curve for the northern hemisphere summer (Reiter 1992, p 130) gives a peak near 21 UT and a diurnal range which amounts to 31% of the mean. If global thunderstorm activity controls the 'fair weather' geoelectric field, then the northern hemisphere summer curve is appropriate for comparison with a southern hemisphere winter curve. The peak of the global 'fair weather' curve is thus discernible in the Davis winter data. The minimum of the Carnegie 'fair weather' northern hemisphere summer curve occurs around 0330 UT,

significantly different from the Davis winter minimum near 13 UT. The Davis winter curve is very flat away from the peak compared to the Carnegie summer curve.

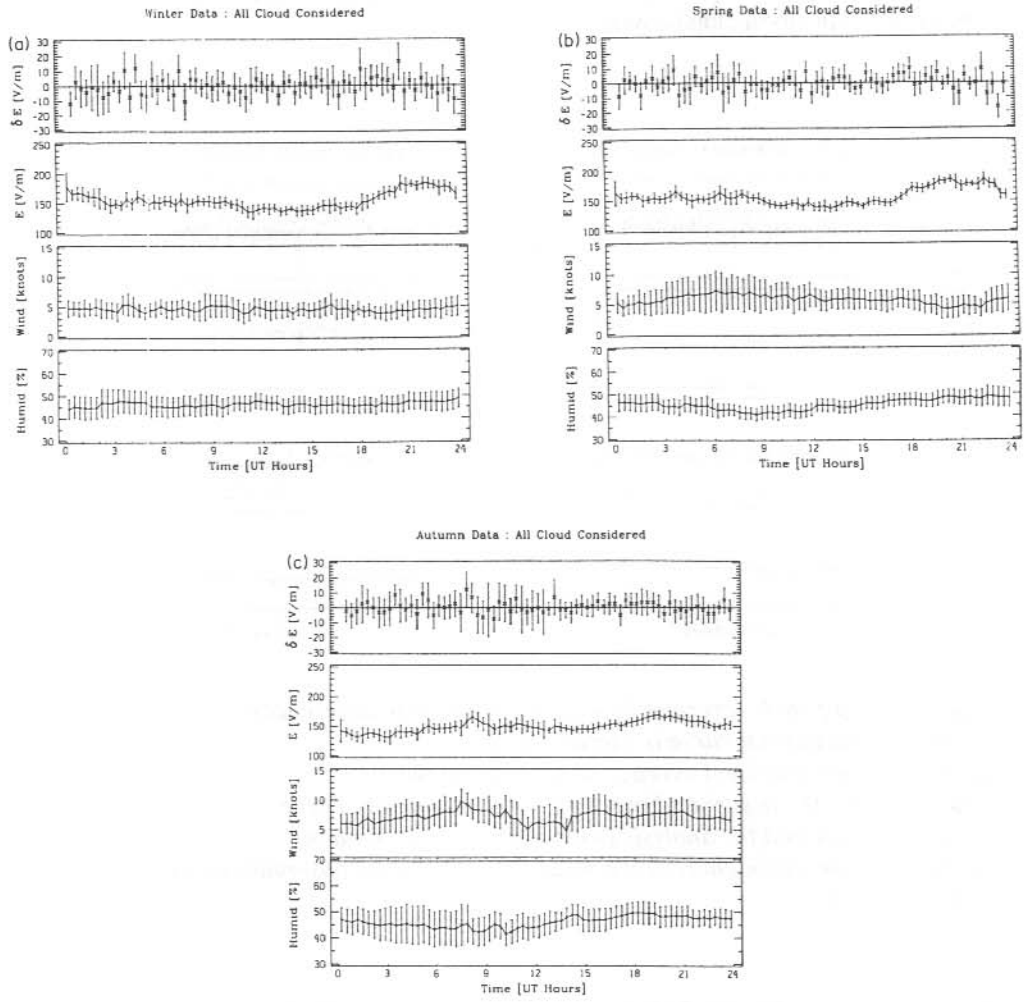

Figure 3. Format as per Figure 2.
(a) Winter: 1st May to 31st July.
(b) Spring: 1st August to 31st October.
(c) Autumn: 1st February to 30th April.

The spring and autumn diurnal curves are shown in Figures 3(b) and (c). The spring curve has a peak value of 186 V m^{-1} occurring at 2250 UT and a diurnal range of the order of 49 V m^{-1}, amounting to some 31% of the diurnal mean value. The spring and winter curves are very similar. The diurnal variations of the meteorological parameters are, however, more substantive. The wind speed peaks around 06 UT and the relative

humidity minimises at 0830 UT. The autumn curve has a peak value of 169 V m^{-1} occurring at 1930 UT and a diurnal range of the order of 37 V m^{-1}, amounting to some 25% of the diurnal mean value. The autumn diurnal curve has a secondary maxima of 165 V m^{-1} near 08 UT. The value of the secondary maxima is almost of the magnitude of the major peak. The local maxima around 08 UT is correlated with a rise in wind speed and a dip in relative humidity. The Carnegie 'fair weather' equinoctial curve (Reiter 1992, p 130) peaks at 19 UT and has a diurnal range of 31% of the average value. The Davis autumn curve shows the Carnegie seasonal trend of an earlier peak. The Davis spring curve has a fairly broad peak that maximises at a later time.

The Carnegie 'fair weather' curves do not show the secondary rise in the diurnal curve between 03 and 10 UT that is a feature of varying significance in all the Davis seasonal curves (see Figures 3a, b and c). For the Davis autumn curve, where this secondary peak is most obvious, there is a strong positive correlation with a diurnal wind speed variation and a negative correlation with a diurnal relative humidity variation. Both these variations would enhance the measured electric field at this time (see the correlations in Figure 1). When the Davis data were previously analysed without the restriction on the relative humidity variation and without the temperature restriction around 0°C (Hesse et al. 1992), the summer diurnal curve showed a broad, dominant peak between 05 and 13 UT and a minor peak around 19 UT. The autumn diurnal curve for these less restrictive conditions had a dominant peak around 08 UT with a secondary peak centred around 20 UT. Stronger local rejection criteria have thus reduced the significance of the autumn 08 UT peak and precluded a summer diurnal curve determination. This behaviour is strongly suggestive of a degree of local control on the 03 to 10 UT secondary peaks in the determined Davis seasonal diurnal curves.

While we believe that the 03 to 10 UT peak is of local origin, the peak between 19 and 22 UT appears to be a global signal with its magnitude and some seasonal behaviour (the autumn peak shift) consistent with the Carnegie 'fair weather' curves. That the Davis curves do not have a minimum around 04 UT like the Carnegie curves may be due to remnant local influences. Magnetospheric effects may also have an influence in this time period.

1.5 LOOKING FOR A MAGNETOSPHERIC INFLUENCE

The Davis winter and spring diurnal electric field curves are similar in shape and magnitude. The autumn curve is apparently dominated by local influences around 08 UT. We combined the spring and winter data and then split this combined data set on the basis of the level of global magnetic activity as measured by the 3-hourly Kp index. Global magnetic activity is broadly dependent on the strength of the interaction between the solar wind and the Earth's magnetic field and thus on the magnitude of the dawn-to-dusk electric field imposed across the polar cap. Figure 4 shows the diurnal curves derived for the winter-spring data, split for various levels of Kp. The amount of data in each split are as follows: Kp <= 2+, 433 hours (18.1 days); Kp >= 3-, 358 hours (14.9 days); Kp >= 4-, 145 hours (6.1 days) and Kp >= 5-, 79 hours (3.3 days). The signature that could be expected from an imposed magnetospheric field is an increase in the geoelectric field in the magnetic dawn sector and a decrease in the magnetic dusk sector. Magnetic noon at Davis occurs near 10 UT. The curves in Figure 4 show a trend towards an increased separation of pre-noon

and post-noon electric field values and also increased variability as the Kp level increases and as the amount of data decreases. An increase in the magnitude of the major peak between 19 and 23 UT is also apparent, particularly for the high Kp data splits, but the separation of the electric field values at 0010 UT and 2350 UT by 44 V m^{-1} for the Kp >= 4 - split shows the inconsistency of this small data set.

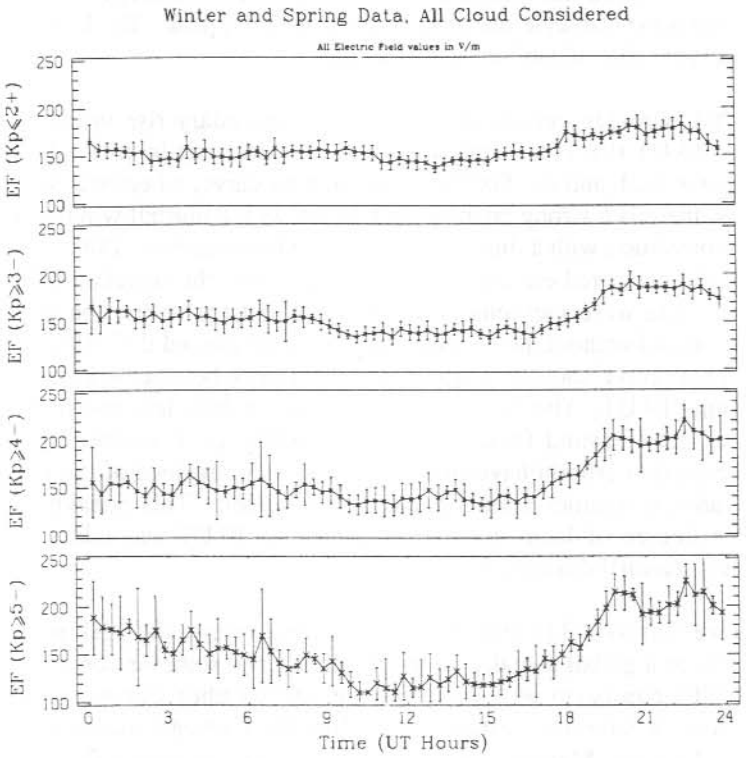

Figure 4. Diurnal curves determined by the 'cumulation of consecutive differences' method for data split by Kp.
Top panel: Kp <= 2+ (18.1 days data). 2nd panel:Kp >= 3- (14.9 days data).
3rd panel: Kp >= 4- (6.1 days data). Bottom panel:Kp >= 5- (3.3 days data).

There are only sufficient data for a meaningful comparison of the Kp >= 3- and Kp <= 2+ diurnal curves. When introducing the method of deriving the diurnal curves by the cumulative addition of the average 20-minute differences, we noted that the derived 0010 and 2350 UT values may be significantly different as uncertainties associated with each step accumulate in a random walk manner. The fact that generally the discrepancy between the 0010 and 2350 UT derived values has been sufficiently small to be ignored, is an indication that the process adopted is appropriate for deriving the diurnal curves for the amount of data available. In comparing the Kp >= 3- and Kp <= 2+ curves however, the discrepancy between the 0010 and 2350 UT values of the two curves becomes significant.

For the Kp <= 2+ curve the discrepancy (see Figure 4) is +8.1 V m^{-1} and for the Kp >= 3- curve the discrepancy is -6.5 V m^{-1}. Before comparing the curves, we forced them to be self-consistent at 0010 and 2350 UT by dividing the discrepancy of each curve by 72 (the number of 20-minute steps in a day) and subtracted that amount from each of the 20-minute difference averages. This removes the discrepancy by assuming that it was due to a linear trend imposed on the diurnal curve. This is the best approximation possible to the accumulated random walk discrepancy in the diurnal curves as initially derived.

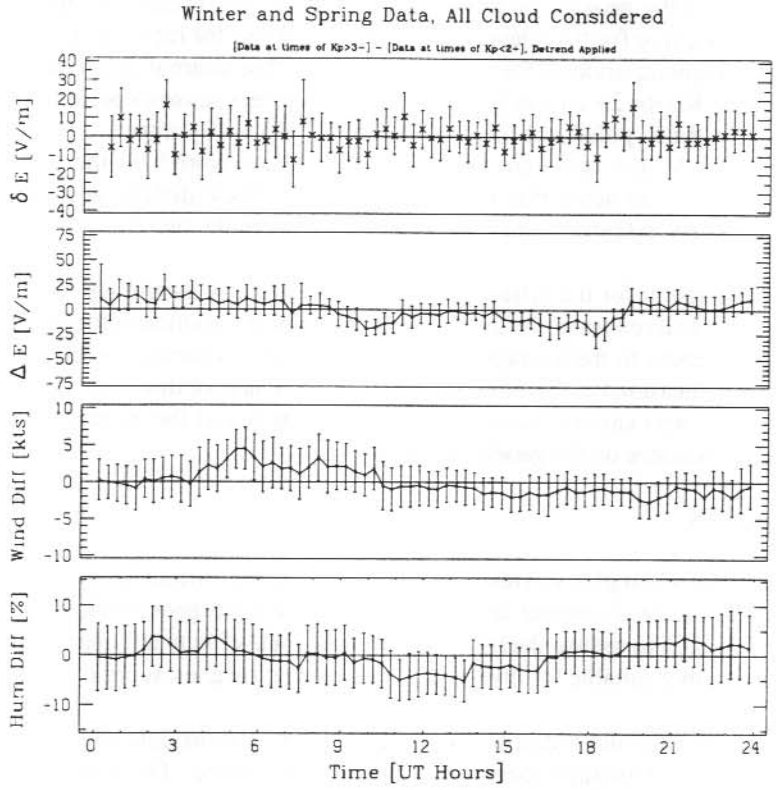

Figure 5. The difference between the [Kp <= 3-] and [Kp <= 2+] curves after removal of linear trends as per text.
Top panel: differences in average 20-minute consecutive differences between the two data sets.
2nd panel: the diurnal difference between the two curves.
3rd panel: the diurnal difference in average wind speed between the two data sets.
Bottom panel: the diurnal difference in average relative humidity between the two data sets.

Figure 5 shows the difference [(Kp >= 3-) - (Kp <= 2+)] between the modified diurnal curves. The top panel shows the differences in the average 20-minute differences. The error estimates are plotted as the square-root of the sum of the squares of the errors plotted in the individual curves. A diurnal curve is derived by the cumulative addition of these differences in the manner previously described. Diurnal difference curves are also derived for the wind speed and relative humidity curves. The error estimates for the diurnal curves of the differences in the meteorological parameters are also evaluated as the square-root of the sum of the squares of the error estimates in the diurnal meteorological curves from which the 'difference' curve is derived.

Figure 5 shows that the geoelectric field values of the Kp >= 3- diurnal curve are greater than the Kp <= 2+ curve for the interval 23 to 07 UT and less for most of the interval from 09 to 19 UT. Magnetic noon at Davis is near 10 UT. The diurnal discrepancy between the Kp >= 3- and Kp <= 2+ curves generally has the correct sense expected of a stronger applied dawn-to-dusk polar cap potential for the Kp >= 3- curve. Estimating the discrepancy at 15 V m^{-1} between dawn and dusk as measured by the Davis ground instrumentation, we can scale this to an approximate 30 kV difference in the average applied dawn-to-dusk potential across the polar cap, between the two data sets.

A different explanation for the differences between the Kp >= 3- and Kp <= 2+ curves is possible from the differences in the average meteorological parameters for the two curves. The diurnal differences in the average wind speed for the two curves has the correct sense to account for the measured electric field differences. Because of this local influence on the split Kp data sets, we cannot conclude that we have measured the ground signature of a magnetospheric influence on the geoelectric field.

1.6 DISCUSSION

The discussion and examples in Hesse et al. (1992) and the further analysis presented in this paper demonstrate a number of local influences on the geoelectric field at Davis. Careful data selection to reduce the influence of these local effects left approximately 13% of the data as possibly suitable for investigating global and magnetospheric influences.

It is possible to reconstruct a diurnal curve from a set of short data segments using the 'cumulative addition of average consecutive differences' method. Davis winter, spring and autumn curves constructed in this manner show a peak between 19 and 22 UT that is similar in magnitude and some seasonal behaviour with the Carnegie curves. The Carnegie curves are generally taken as representative of the global 'fair-weather' geoelectric field.

Local factors preclude the determination of a summer curve. Local factors also influence a minor peak between 03 and 10 UT seen to some extent in all other seasons. Of the remaining seasons, this 'locally influenced' feature is most significant in autumn. Autumn is excluded from a search for a magnetospheric influence on the geoelectric field at Davis.

When the combined winter and spring data sets are split on the basis of Kp, there is a trend in the diurnal curves that is consistent with an expected magnetospheric influence. Differences in average meteorological parameters between the data sets split on the basis of

Kp can also account for the differences in the geoelectric field measurements. At high Kp, when the possible magnetospheric signal is largest, the data are too sparse.

With a larger data set it should be possible to resolve the ambiguity between local meteorological and magnetospheric control of the geoelectric field at Davis. The paucity of data led us to combine the winter and spring data sets. Geomagnetic activity is greater during the equinoxes than the solstices. This, combined with seasonal meteorological variations may have generated the weak variation observed with the Kp data splitting. A larger data set would allow separating the winter and spring data prior to selection on the basis of a parameter related to the polar cap dawn-to-dusk electric potential. If, on the other hand, the magnitude of the magnetospheric influence is of the order of the minor variation seen, then four years of geoelectric field data from the Davis site should be adequate to confirm the signal.

There is another possibility for progress. Tightening the determination of local contamination may yield a data set for which we can be certain that local influences are absent. It may then be possible to examine individual extreme magnetospheric events for their effect on the Davis geoelectric field. Such events would include high Kp events, cosmic ray Ground Level Enhancements, polar cap absorption and relativistic electron precipitation events.

1.7 ACKNOWLEDGMENTS

The collection of the Davis electric field data for 1989 was the responsibility of Dr Russell McLoughlin. Meteorological information which was not recorded directly in association with the electric field data was supplied by the Australian Bureau of Meteorology. Dr Damian Murphy and Mr David Rasch provided valuable discussions on the interpretation of these data. The manufacture of research instrumentation and the maintenance of a remote observatory facility requires concerted effort from many people. To those who assisted in ensuring the collection of these data, our thanks.

REFERENCES

Burke, H.K. *and* Few, A.A. (1978). Direct measurements of the atmospheric conduction current. *Journal of Geophysical Research 83*:3093 – 3098.

Baker, K.B. *and* Wing, S. (1989). A new magnetic coordinate system for conjugate studies at high latitudes. *Journal of Geophysical Research 94*:9139 – 9143.

Byrne, G.J., Benbrook, J.R., Bering, E.A., Few, A.A., Morris, G.A., Trabucco, W.J. *and* Paschal, E.W. (1993). Ground-based instrumentation for measurements of atmospheric conduction current and electric field at the South Pole. *Journal of Geophysical Research 98*:2611 – 2618.

Hesse, M.H., Burns, G.B. *and* Malachowski, S. (1992). Ground based electric field measurements at Davis station, Antarctica. In: G. Burns *and* M. Duldig (Eds). *Australian upper atmospheric and space physics research in Antarctica, 1992, ANARE Research Notes 88*. Pp. 165 – 179.

Park, C.G. (1976). Solar magnetic effects on the vertical atmospheric electric field at Vostok, Antarctica. *Geophysical Research Letters 3*:475–479.

Reiter, R. (1992). *Phenomena in atmospheric and environmental electricity*. Elsevier.

2. DAVIS AND CASEY MAGNETIC FIELD DATA

G.B. Burns and A.R. Klekociuk

Auroral and Space Physics
Antarctic Division
Kingston Tasmania 7050
Australia

ABSTRACT

Ten second resolution digital magnetometer data have been collected from Davis (geog. 68.58°S, 78.0°E; mag.[PGM–1988] 74.61° S, 102.3°E, L~14.2) since 16 February 1988 and from Casey (geog. 66.28°S, 110.5°E; mag.[PGM–1988] 80.39°S, 156.1°E, L~35.9) since 17 January 1989. Data from these sites have been processed to the end of 1992. Neither site is of 'observatory status' as the variations in the baselines are not sufficiently defined over this period and the records are not continuous. Information on the format, quality and availability of the data is given. Unprocessed, 10 second resolution, data are available from Macquarie Island (geog. 54.50°S, 159.0°E; mag.[PGM–1988] 64.34°S, 246.9°E, L~5.3) since 7 September 1987 and from Mawson (geog. 67.60°S, 62.9°E; mag.[PGM–1988] 70.52°S, 92.1°E, L~9.0) since 8 January 1991. The high-time resolution Macquarie Island and Mawson magnetometer data are collected, by arrangement, from the Australian Geological Survey Organisation 'observatory status' variometers at these sites.

2.1 DAVIS AND CASEY INSTRUMENTATION AND 'RAW' DATA FORMAT

Modified EDA FM100C fluxgate magnetometers are used to record large scale variations in the X, Y and Z (geographic north, east and vertically downward) components of the Earth's magnetic field at both Davis and Casey. The modifications include provision of temperature stabilisation of the fluxgate sensors and daily calibration of the instruments at 1630 UT by means of a predetermined current fed to a coil mounted in the sensor unit. A further modification increased the sensitivity of the EDA FM100C from 10000 nT/V to 200 nT/V. Absolute calibration of the instruments is obtained by reduction of magnetic absolute measurements made on QHM (giving H–field strength, magnetic north direction, horizontal plane – and D – difference of horizontal field direction from geographic north) and PPM (giving F– total field strength) instruments provided by, and operated on behalf of, the Geomagnetism Section of the Australian Geological Survey Organisation (AGSO). The magnetic absolute readings used to calibrate the Davis and Casey magnetometers are classified as 'preliminary' by AGSO, as they are derived prior to final adoption of instrument corrections based on international recalibration of the QHM and PPM instruments.

A Doric AD2060 temperature sensor is co-located with the magnetic sensors at both sites. A heating system is used to maintain the temperature in the sensor enclosure to within 1°C of a selected value, generally 20°C at Davis and 15°C at Casey (the Casey unit was reset to 20°C from late December 1992). Although the digital output of the Doric temperature

sensor has a resolution of 0.1°C, and it is this that is used to control the sensor enclosure heating circuit, the analog output has only a 1°C resolution. The manufacturer specifies the EDA-100C temperature sensitivity as 1 nT/°C.

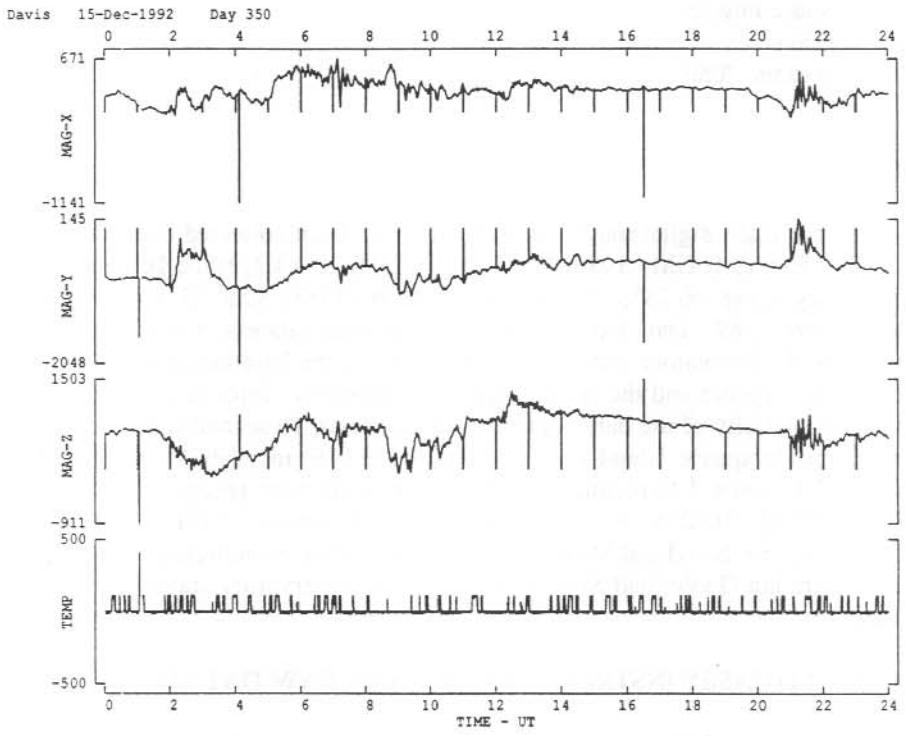

Figure 1. Raw data file, Davis 15 December 1992. Shows hour marks, automatic calibration sequence at 1630 UT, manually activated calibration sequence around 0407 UT and interference spikes on the Y and Z channel around 0104 UT associated with a logging system failure.

The analog output of each magnetometer channel (X, Y and Z) and the temperature sensor (T) are input to an Antarctic Division amplifier/conditioner containing a low-pass filter with a corner frequency of approximately 15 Hz. The output of the amplifier/conditioners are input via an Analog-to-Digital (A-to-D) card to a PDP LSI-11/02 computer system. Data are stored in UT-daily files written in PDP Fortran unformatted binary. The time is recorded with each X, Y, Z, and T sequence. Timing accuracy is maintained to within 50 ms by an Austron 8120 chronometer. The raw digital data are transferred by satellite data links from the stations to the Antarctic Division Head Office in Kingston, Tasmania, within 6–8 weeks of data collection. The raw data are not processed until calibration values for a complete year of data are selected, generally 3–4 months into the following year. Magnetometer data are also recorded on chart at 10 cm/hr at a sensitivity of approximately 10 nT/mm.

The alteration made to increase the sensitivity of the magnetometers to 200 nT/V resulted in the baseline offset potentiometers on the front of the magnetometers being made very sensitive. Early calibrations of the Casey data revealed two separate occasions when there was a significant baseline change in only one channel, indicative of a minor movement in that channels baseline potentiometer. By the end of 1992, the EDA FM100C magnetometers at both stations had either fixed value baseline resistors or significantly reduced sensitivity potentiometers installed.

For the first minute of each hour, the magnetometer output of each channel is shorted to provide a baseline value. For the minute following 1630 UT, a current is passed through a coil co-located with the magnetometer sensors and each component is deflected by a calibrated amount. Raw data files may also have additional manually activated calibration marks (routinely instigated in association with chart changes), noise spikes associated with local electrical interference coupling to the data collection (rare except for particular long term interferences discussed in association with the specific sites), known data corruption due to activity near the sensor site (the events we know about are rare) and data gaps due to disk changeover and system calibration. An example of a raw data file, Davis–15 December 1992, is plotted in Figure 1. The hour marks and 1630 UT calibration are readily apparent. Also shown are a manually activated calibration around 0407 UT and interference spikes on the Y and Z channels around 0104 UT that are associated with a logging system failure.

System calibration is performed in two steps. Each channel of the magnetometer is calibrated to convert volts output into a nT value. Each channel of the computer interface system is calibrated to convert digital counts to volts into the amplifier/conditioner. We make a distinction between these components of the total system because calibrations and alterations to the amplifier/conditioners have generally been independent of magnetometer baseline variations. In practise, magnetometer baseline uncertainties have been of much greater magnitude than any uncertainties in the computer interface component of the system. A similar two step calibration process is applied to the temperature channel. The general calibration terminology used is indicated below.

Equations describing the Magnetometer Instrument

$$B_X\ [nT] = S_X\ [nT/volt] \times V_X\ [volts] + BL_X\ [nT]$$
$$B_Y\ [nT] = S_Y\ [nT/volt] \times V_Y\ [volts] + BL_Y\ [nT]$$
$$B_Z\ [nT] = S_Z\ [nT/volt] \times V_Z\ [volts] + BL_Z\ [nT]$$

Equation describing the Doric Thermometer

$$T\ [°C] = S_T\ [°C/volt] \times V_T\ [volts] + BL_T\ [°C]$$

Equations describing the Logging System

$$V_X\ [volts] = (D_X\ [dig] - Offset_X\ [dig]\ ) / (+204.8 \times Gain_X\ [dig/volt])$$
$$V_Y\ [volts] = (D_Y\ [dig] - Offset_Y\ [dig]\ ) / (+204.8 \times Gain_Y\ [dig/volt])$$
$$V_Z\ [volts] = (D_Z\ [dig] - Offset_Z\ [dig]\ ) / (+204.8 \times Gain_Z\ [dig/volt])$$
$$V_T\ [volts] = (D_T\ [dig] - Offset_T\ [dig]\ ) / (+204.8 \times Gain_T\ [dig/volt])$$

where

B_X, B_Y and B_Z are the components of the magnetic field in [nT].

S_X, S_Y and S_Z are the sensitivities of the magnetometer channels in [nT/volt].
V_X, V_Y and V_Z are the voltage outputs of the magnetometer channels (and thus the voltage inputs to the signal conditioner channels) measured in [volts].
BL_X, BL_Y and BL_Z are the baselines for the magnetometer. That is the value of each field component needed to produce zero volts out of the appropriate channel of the magnetometer. Measured in [nT].
T is the temperature in degrees [°C] at the magnetometer fluxgate sensor.
S_T is the sensitivity of the temperature channel in [°C/volt].
V_T is the voltage output of the DORIC thermometer (and thus the voltage input to the signal conditioner channels) measured in [volts].
BL_T is the temperature baseline. That is the temperature at the magnetometer fluxgate sensors that produces zero volts out of the DORIC thermometer. Measured in [°C].
D_X, D_Y and D_Z are the logged digital values representing the three components of the magnetic field. Measured in [digital units].
$Offset_X$, $Offset_Y$ and $Offset_Z$ are the digital values corresponding to zero volts out of the magnetometer (ie. the digital values corresponding to field components being equal to the baselines). Measured in [digital units]
$Gain_X$, $Gain_Y$ and $Gain_Z$ are the amplification factors of the analogue signal conditioner channels in [digital units/volt].
D_T is the logged digital value representing the temperature at the magnetometer fluxgate sensors. Measured in [digital units].
$Offset_T$ is the digital value of the temperature channel corresponding to zero volts out of the DORIC thermometer. Measured in [digital units].
$Gain_T$ is the amplification factor of the signal conditioner unit for the temperature channel in [digital units/volt].
204.8 is the [digital units/volt] value obtained from 4096 digital units over a 20 volt range.

2.2 THE 'FULLY PROCESSED' DATA

The raw data from each station are separately processed to calibrated nT values and stored in VAX ASCII, UT-day, files. No time information is included with the fully processed data, rather missing data are blank filled with a 999999 record. Hour marks, the 1630 UT calibration data, any manually activated calibration sequences and any known or apparent interference are also replaced with a 99999 record. Figure 2 is a plot of the processed data from Davis -- 15 December 1992.

There are 8640 (24*60*6) lines of data in each UT-day file with the time of the record inferred from its location in the data sequence. The data are recorded to an accuracy of a tenth of a nT (one digital unit corresponds to approximately 0.5 nT) in a compressed form discussed below.

There are three lines of information in the processed data files prior to the listing of the data, and a variable number of lines following the data sequence that give further information. An example of a processed file, with most of the data lines removed, is contained in Appendix 1. The initial line of the processed data indicates the file name. This is of the form PSSIIYY.DDD, where P indicates a 'processed' data file, SS is a two letter station code (DA for Davis, CA for Casey), II is an instrument code (MG for magnetometer data), YY is a two number year indicator and DDD is the day number of the year. This

information is included in case of file renaming. A second line of code lists the date/time that the file was created. The third line of information, immediately preceding the data, consists of three numbers which indicate an offset applied to the X, Y and Z channels to give a limited form of data compression. To reconstruct the data, the channel offset is multiplied by 1000 and added to the 'compressed' channel value. This gives the value for that channel, at the appropriate time, expressed in tenths of nT.

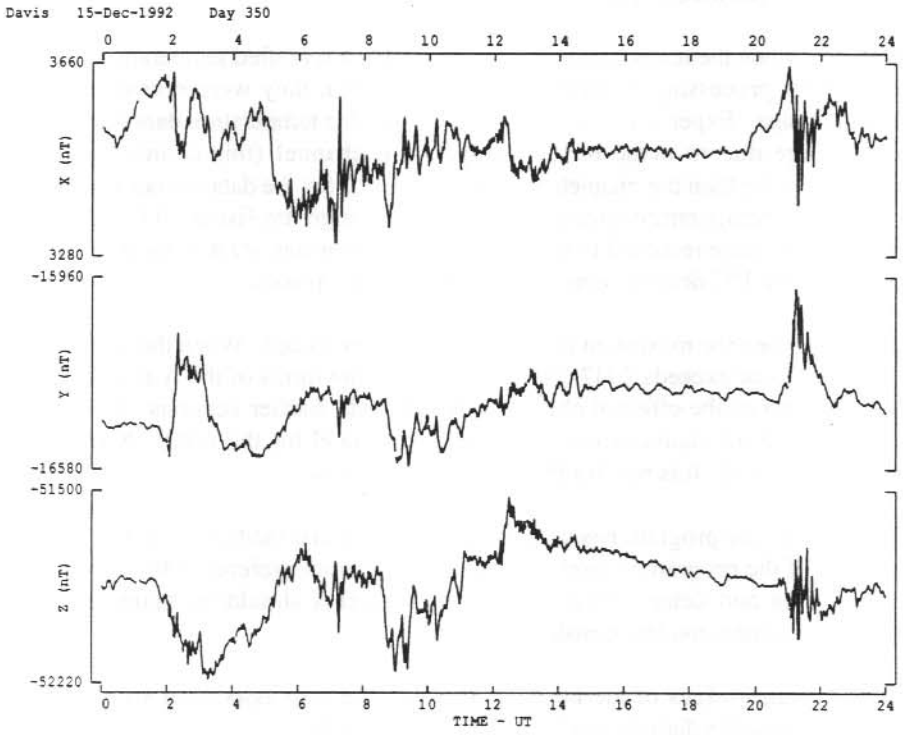

Figure 2. Processed data file, Davis 15 December 1992.

Following the data are eleven information sections, each separated by a # symbol (see Appendix 1).

#1 The station location (in geographic coordinates) and the coordinate system for the magnetic components (X: geographic north, Y: geographic east and Z: vertically down).

#2 An explanation of how to restore the compressed data to the correct nT value.

#3 The calibration equations used in reducing the raw data for this UT day.

#4 The zero short locations blanked from the raw data (the hourly baseline calibration marks). The format shows the start time, end time and width of each pulse. The times are given in hrs:min:sec and in line numbers (1 – 8640).

#5 The time location of the calibration pulse, specified as above.

#6 The time of any user specified data rejections (used to remove apparent or known data contamination), specified as per above.

#7 Indicates when the temperature channel is outside a specified temperature range. Early versions of the processing program rejected data when they were outside the specified temperature range. Experience showed that generally the temperature data were outside the specified range due to noise on the temperature channel (this channel proved more susceptible to noise than the magnetometer channels). Now the data are not rejected, but the times when the temperature exceeds the specified range are listed. The maximum and minimum temperature recorded in the sensor heads for the day are also listed. These have a resolution of only 1°C despite being listed to two decimal places.

#8 Indicates when the maximum range of the data is exceeded. When the magnitude of the raw value equals or exceeds 2047 (this indicates that the limits of the A-to-D converter are reached) the data of the effected channels are blanked. Earlier versions of the processing program blanked all channels even if only one channel hit the limit. Now, individual channels are blanked. It is rare for the data to 'hit the rails'.

#9 Times when the program has determined that a manual calibration has been activated. This portion of the program is rarely activated, the general preference being for looking at the plotted data and determining if and how segments should be blanked rather than allowing an automatic routine to make a selection.

#10 The average values of the hourly shorts and the step associated with the 1630 UT calibration are listed in digital units for each of the channels.

#11 Finally there is a comments section which contains at least a general synopsis of the years data quality. Any number of specific comments on the data can be made, each are separated by a $ and are selected from a prepared text file which contains a code as to which UT-days data they are to be appended to. Apart from the general comment on the data quality, there may be information as to why there are specific data gaps in the days data.

The digital Davis and Casey magnetometer data have also been processed into minute average data and provided in the appropriate form to World Data Centre-A, Boulder, Colorado, USA.

2.3 THE DAVIS SITE

A number of internal Antarctic Division publications give information on the calibration of the Davis data and the difficulties with it. These are:

'Davis Magnetometer Calibration 1990' by M. Hesse.

'Davis Magnetometer Calibration September 1991' by M. Hesse and L. Symons.

'Davis Magnetometer Calibration January 1992' by M. Hesse and L. Symons

'Davis Magnetometer Calibration March 1992' by M. Hesse, L. Symons and G. Burns.

'1992 Davis Fluxgate Magnetometer Report' by D. Neudegg.

The initial calibration of the Davis digital magnetometer data uncovered an unexpected seasonal variation that is most apparent in a plot of H baseline (H is magnetic intensity in the horizontal plane and equals $\sqrt{X^2 + Y^2}$) against day number, with 1 January 1990 being day 1 (see Figure 3). There is a large scatter on the data, far greater than expected from the absolute instrument accuracy of the order of one nT, but a seasonal variation is still readily apparent. Features of the seasonal variation are that there is a gradual change between more stable winter (day 80 to day 300) and summer (day -30 to day 20 and day 350 to day 550) values and, although the initial summer data (day -30 to day 20) are highly variable, the baseline does not return to the same level in successive summers.

Initially we believed site contamination was responsible for this seasonal variation. At the approximate times of the variations shown in Figure 3, station vehicles were 'winterised' and stored within 60 meters of the magnetic absolutes pier and subsequently removed prior to the next summer. There were other site contaminations around and subsequent to this period. These included operations of helicopters from a helipad over summer (within 80 m of the magnetic absolutes pier), the construction of a new Auroral and Space Physics laboratory (which, at closest, is 85 m from the pier), and the removal of the old laboratory (75 m from the pier). All these forms of contamination have been removed or stabilised and the seasonal variation is still apparent, although the reduced regularity of magnetic absolutes readings (reduced from 2 sets a week to one set a month from 1991) means the variation is not as well defined as for this early data. We now suspect that the freezing and thawing of the 'gravel' on which the concrete pad for the magnetometer sensors is located is causing a seasonal tilt in the sensors. This may be responsible for the baseline variation observed. An attempt will be made in the second half of 1993 to take magnetic absolute readings regularly enough (two per week) to accurately follow the seasonal variation and to hopefully confirm its origin.

Magnetic absolute readings have not been regular enough over the period of digital data collection to accurately follow the seasonal change. Calibrations of the Davis magnetometer have essentially revolved around a significant number of readings taken at particular times. We initially thought that this could be done annually, as we believed the baselines would not vary significantly. Due to changing conditions in the vicinity of the Davis site (building of new laboratory, removal of old laboratory, clearing of possible contaminating material from the site), more regular calibrations of the magnetometer data have been made and are incorporated in variations in the equations used to process the raw data. These result in abrupt, 'unphysical' changes in the calibrated nT values that are the final processed output. We do not believe that the changes measured at these particular times accurately reflect the site changes they were instigated to measure. We suspect the variations due to the site changes would be of a considerably smaller magnitude than the variations measured. We suspect the seasonal variation is the dominant influence in the variation between successive calibrations.

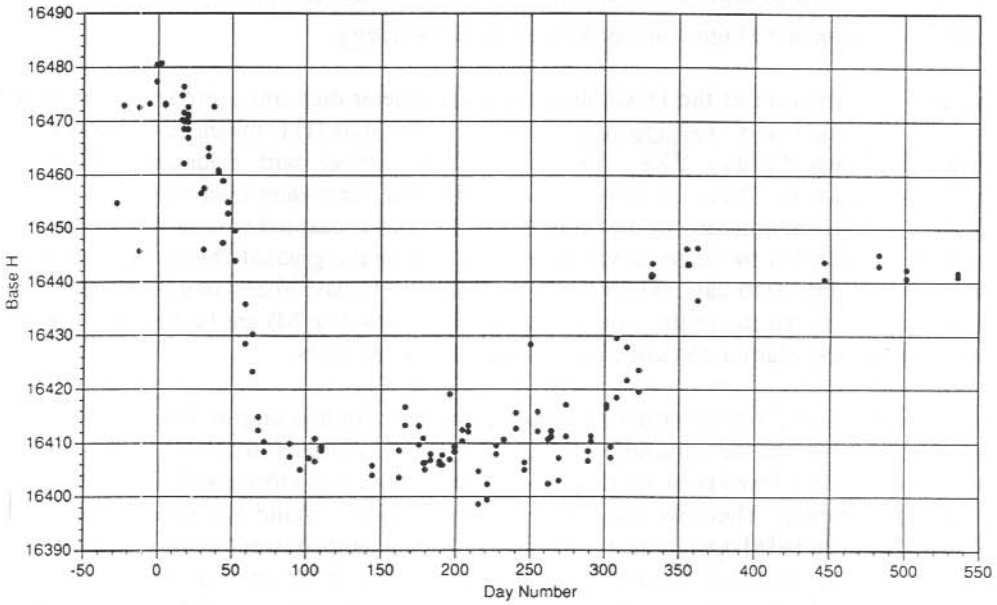

Figure 3. H baseline (nT) at Davis against Day Number. Day Number 1 corresponds to 1 January 1990. A seasonal variation in the baseline is readily apparent.

Calibrations of the 'logging system' have been regularly undertaken. These result in small, 'unphysical' steps in the processed data when changing from one set of logging system calibration equations to another. The steps are insignificant in comparison to the variations that exist in the baseline values.

The 'logging system' and 'baseline' calibration equations used for the Davis data are listed in Appendix 2. The magnitude of the abrupt variations in the baselines for each channel give a fair indication of the uncertainty existing in this data set. Over the four years that digital data have been collected at Davis, the range of the baselines amounts to 76 nT for the X-channel, 77 nT for the Y-channel and 37 nT for the Z-channel.

An uncertainty over the instrument corrections for magnetic absolute instrument QHM 494 (measures H – horizontal magnetic field strength, and declination, D – the angle between the direction of the horizontal magnetic field and geographic north) further complicates the Davis digital data set at present. An in-field comparison calibration of this instrument resulted in the instrument corrections of QHM 494 being changed by an amount that resulted in approximate variation in baselines of -96 nT for the X-channel, -15 nT for the Y-channel and +7 nT for the Z-channel. On 21 January 1993 a comparison was made

between QHM 494 and a DIM (measures Inclination, I – the angle the magnetic field vector makes to the horizontal plane, and Declination, D – the angle between the direction of the horizontal magnetic field and geographic north). When combined with associated PPM (measures F – total field strength) readings and corrected for the variation in the field between the times of the readings (using the variometer data) significant differences remained amounting to approximately +109 nT for the X-channel, +28 nT for the Y-channel and -1 nT for the Z-channel. These differences are yet to be resolved.

Table 1. The monthly data coverage for the Davis site. The 1992 column is split into (X, Z) and (Y) channel percentages as intermittent interference on the Y-channel resulted in considerable data loss between 1 August and 6 October 1992.

MONTH	1988	1989	1990	1991	1992 (X,Z)	1992 (Y)
January	-	31.8%	97.3%	87.0%	95.0%	95.0%
February	44.0%	72.5%	93.4%	11.7%	64.1%	95.1%
March	86.1%	89.4%	87.1%	60.1%	99.2%	99.2%
April	91.9%	99.9%	56.9%	87.5%	99.3%	99.3%
May	96.8%	95.7%	24.6%	96.5%	98.3%	98.3%
June	97.3%	66.6%	99.8%	95.8%	92.9%	92.9%
July	92.6%	80.0%	96.1%	96.1%	99.9%	99.9%
August	96.8%	88.4%	91.5%	95.2%	99.9%	42.4%
September	90.4%	89.8%	94.6%	93.2%	99.5%	60.8%
October	95.0%	94.1%	99.8%	98.6%	99.9%	89.3%
November	98.1%	85.4%	94.9%	98.9%	99.1%	99.1%
December	86.7%	96.6%	77.5%	98.2%	98.7%	98.7%

There have been some substantial gaps in the continuity of the data collection at Davis. The most significant are:

29 December 1988 to 31 December 1989; 3 to 13 January 1989; 26 January to 2 February 1989: System upgrades and operator inexperience.

22 April to 20 May 1990: Relocation of laboratory computer systems.

5 February to 8 March 1991: System failure.

18 to 23 February 1993: Changeover to new laboratory.

Table 1 lists the data coverage in monthly percentages. The 1992 data is listed in two separate columns for the Y channel and the combined X and Z channels. The Y channel data was intermittently noise contaminated (a bad connector) between 1 August and 6 October 1992.

We have not completely delineated the baseline variations appropriate to the Davis data collected to the end of 1992. We do not anticipate further reviewing these data. The information does not exist to enable them to be of more use than as 'variometer' data, which is how we promote them.

2.4 THE CASEY SITE

The magnetometer data from the Casey site are fairly well defined for the interval from 17 January 1989 to 26 May 1990 (except for some particular intervals for individual channels). For the period from 26 May 1990 to the end of 1992 the data are less well defined. A number of internal Antarctic Division publications give information on the calibration of the Casey data and the difficulties with it. These are:

'Casey Magnetometer Calibration, 20/7/90' by R. McLoughlin.

'Casey Magnetometer Calibration Oct/Nov 1991' by M. Hesse and P. Roberts.

'Casey Magnetometer Calibration Feb 1993' by L. Symons.

One interesting feature found with the initial analysis of the Casey magnetometer data was that on two separate occasions there was a substantial baseline shift in one channel. An example of this is shown in Figure 4. These are due to a minor shifts in the front-panel calibration potentiometers. The front-panel calibration potentiometers were made particularly sensitive when the overall sensitivity of the EDA FM100C magnetometers was increased. The front panel potentiometers of the Casey magnetometer were replaced by fixed resistors during a site relocation in December 1992 and the Davis instrument front panel potentiometers were replaced by fixed resistors and less sensitive potentiometers on 16 November 1992. This problem should now not recur.

The principal baseline uncertainty with the data from the period 17 January 1989 to 26 May 1990 results from the interval between absolute readings when the baseline shifts occurred on individual channels. The determined shifts were ultimately estimated to be 35 nT for the Y-channel jump shown in Figure 4 and 32 nT for a separate Z-channel jump. It is worth noting that the X-channel at Casey is particularly difficult to define because the horizontal component of the magnetic field is close to 90° west, making the calibration particularly sensitive to the measurement of the magnetic declination (D – the angle between the horizontal component of the magnetic field and geographic north). The baseline values for

this early period are known to within 5 nT for the Y and Z channels (except for the period of uncertainty associated with the occurrence of the baseline jumps) while the X-channel baseline has a 20 nT change associated with a recording system change, but is otherwise known to within 10 nT over this period. The greatest uncertainty with the data for this period is associated with the scale values of the channels. These have not been defined for the Casey instrument to better than 0.02 nT/[digital unit].

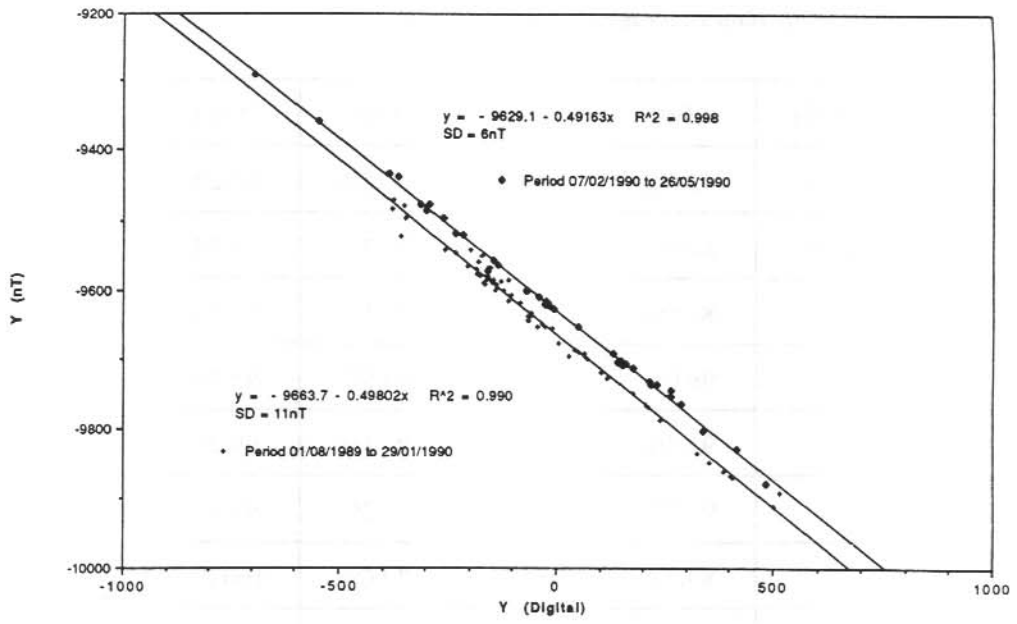

Figure 4. Casey Y value in nT calculated from magnetic absolute readings plotted against the Y channel digital value. The data are divided into two sets to indicate the baseline shift that occurred sometime between the magnetic absolute readings on 29 January and 7 February, 1990. The minor differences between the best fit equations shown and the magnetometer calibrations used (see Appendix 3) are due to ultimately fixing a scale value (nT per digital unit) for the entire Casey data set and then best-fitting to obtain the baseline intercept and corrections to be applied to allow for the Casey logging system calibration.

The channel scale-values of the Davis unit are defined by a deflection generated by passing a known current through a calibrating coil co-located with the magnetic sensors. This coil was calibrated by the Geomagnetism Section of the Australian Geological Survey Organisation (AGSO) in Canberra prior to the instrument being deployed at Davis. Subsequent checks of the channel scale-values determined from the calibration coil deflections have been consistent with the magnetic absolute readings taken. The Casey unit was not calibrated in this manner. The scale-values, and in fact the magnitude of the

calibration coil deflections, have been determined from the magnetic absolute readings in the interval 17 January 1989 to 26 May 1990.

There is no evidence to suggest that the Casey site suffers from a seasonal variation as occurs at Davis. On the contrary, the consistency of the baselines for in excess of a years data is strong evidence that any such effect must be minor.

Table 2. The monthly data coverage for the Casey site.

MONTH	1989	1990	1991	1992
January	43.0%	99.5%	94.5%	96.2%
February	80.9%	94.7%	72.7%	98.3%
March	86.9%	47.6%	92.5%	98.2%
April	96.0%	93.4%	93.9%	95.4%
May	92.3%	92.3%	91.1%	99.2%
June	93.2%	94.3%	88.2%	96.1%
July	89.3%	96.4%	79.0%	100.0%
August	88.1%	97.2%	75.1%	100.0%
September	80.1%	95.7%	90.3%	100.0%
October	99.4%	96.7%	99.5%	90.3%
November	91.0%	91.1%	96.4%	98.9%
December	97.9%	74.5%	81.4%	30.9%

The data are less well defined after 26 May 1990 as they have been re-calibrated only on specific occasions when a significant number of absolute readings have been taken for the express purpose of defining the baselines. The processed data are uncertain at least to the level of the differences noted in these recalibrations which amount to 14 nT in the X-channel, 42 nT in the Y-channel and 7 nT in the Z-channel. From 1991, magnetic absolute readings at Casey have only been taken once a month, in the belief that this would adequately define the magnetometer baselines. It would be difficult to determine channel

baseline shifts due to variations in the baseline potentiometers, as found in the initial analysis, with the limited number of absolute measurements taken in this later period. Appendix 3 lists the magnetometer, temperature sensor and collection system calibration equations used to process the Casey site data through to the end of 1992.

The large changes in the magnetic baselines apparent in the calibrations applied from 25 December 1992 are associated with the relocation of the EDA FM100C sensors from the 'old Casey' site closer to the new station location. As the data are referenced to the same magnetic absolutes pier, this change should have no effect on the continuity of the data set.

There is some cause for concern about the magnetic integrity of the Casey magnetic absolutes pier. For a number of years the magnetic readings of the QHM and PPM were taken on different piers. These piers are only some 10 m apart but differ by some 423 nT in total field value as measured by the PPM. This indicates a sharp gradient in the local magnetic field in the vicinity of the piers. When a DIM absolute instrument was introduced to Casey to replace the QHM, a measurement was made of the difference in magnetic field associated with the approximately 20 cm height difference of the instruments on the primary pier. This amounts to 46 nT, indicating a strong gradient in the vicinity of the pier. The source of these local gradients is yet to be determined.

There have been two substantial gaps in the continuity of the data collection at Casey. These are:

6 to 20 March 1990: Computer system failure.

5 to 24 December 1992: Relocation of magnetometer sensors and laboratory.

Table 2 lists the data coverage in monthly percentages.

2.5 MACQUARIE ISLAND AND MAWSON 10-SECOND DATA

The Geomagnetism Section of the Australian Geological Survey Organisation (AGSO) operate 'observatory standard' magnetometers at Macquarie Island and Mawson. AGSO routinely record magnetic field data at these sites with a 1 minute resolution. By arrangement, the Auroral and Space Physics group of the Australian Antarctic Division samples the output of the AGSO magnetometers at both sites every 10 seconds and records the data in UT-daily files written in PDP Fortran unformatted binary, consistent with the raw data files from Casey and Davis. No further processing of these data has been undertaken. The data sequences are not continuous, but span the periods from 7 September 1987 at Macquarie Island and from 8 January 1991 for Mawson. Any inquiries for Macquarie Island and Mawson magnetometer data should be made to the Geomagnetism Section, AGSO [GPO Box 378, Canberra, ACT 2061].

2.6 ACKNOWLEDGMENTS

The data collection program was written by Howard Burton. The initial processing program was written by Dr Barry Giles and was upgraded by Dr Steven Newbery. The initial calibration of the Casey digital magnetometer data was undertaken by Dr Russell McLoughlin and the Davis data by Michael Hesse. The Geomagnetism Section of the Australian Geological Survey Organisation have provided advice, assistance with the

magnetometer installation, absolute calibration instruments and training in their use. Particular thanks to Stewart Dennis and Wendy Prohasky of AGSO. The following ANARE expeditioners had responsibility for the collection of the Davis and Casey magnetometer digital data: Mike Craven (D88), Russell McLoughlin (D89), Michael Hesse (D90), Lloyd Symons (D91), David Neudegg (D92), Mark Underwood (D92), Owen Holmwood (C89), Helen Beggs (C90), Perry Roberts (C91) and Devindar Singh (C92). Andrew McEwin (AGSO) has provided helpful comments on the draft text. The maintenance of a remote observatory facility requires the concerted effort of many people, not only those directly involved. To those who assisted with the collection of these data, our thanks.

APPENDIX 1.

SAMPLE OUTPUT OF A PROCESSED FILE

PDAMG92.350

CREATED ON 28-APR-93 AT 14:04:23
33 -166 -523
999999999999999
999999999999999
999999999999999
999999999999999
999999999999999
999999999999999
2317 1755 4429
2321 1750 4410
2321 1745 4391
2321 1735 4372
2307 1730 4353

2170 2053 4110
2174 2048 4096
2170 2043 4100
2165 2043 4096
2160 2038 4096
2155 2033 4086
2151 2028 4086
2141 2023 4072
2132 2019 4072
2122 2014 4062
999999999999999

#

1) BASIC INFORMATION:-

Station	DAVIS
Latitude	-68:35 S
Longitude	77:58 E

The magnetometer data are presented in a geographic right handed co-ordinate system

X component	– positive geographic North	(horizontal)
Y component	– positive geographic East	(horizontal)
Z component	– positive downwards	(vertical)

#

2) FILE FORMAT AND COMPRESSION RESTORATION:-

The data values are in the order X, Y, Z.
The first values are an offset base line.

TO UN-COMPRESS:-

value (nT) = (offset * 1000 + value) / 10.0
blank (99999) values should be set to 99999.9

#

3) CALIBRATION EQUATIONS:-

X AXIS (nT)

VOLTS =	0.002436 (±)	0.000010	*	DIG VAL	+	-0.004223 (±)	0.000100
VALUE =	-194.80 (±)	5.00	*	VOLTS	+	3622.00 (±)	50.00

Y AXIS (nT)

VOLTS =	0.002436 (±)	0.000010	*	DIG VAL	+	0.001650 (±)	0.000100
VALUE =	200.70 (±)	5.00	*	VOLTS	+	-16069.00 (±)	50.00

Z AXIS (nT)

VOLTS =	0.002436 (±)	0.000010	*	DIG VAL	+	0.002030 (±)	0.000100
VALUE =	195.60 (±)	5.00	*	VOLTS	+	-52142.00 (±)	50.00

T SCALE (Deg.C)

VOLTS =	0.001011 (±)	0.000010	*	DIG VAL	+	2.002730 (±)	0.000100
VALUE =	10.19 (±)	0.10	*	VOLTS	+	-0.41 (±)	0.10

#

4) USER SPECIFIED ZERO SHORT POSITIONS:- Total = 167

0:	0:10	(1)	To	0:	1:	0	(6)	Width =	6
1:	0: 0	(360)	To	1:	1:	0	(366)	Width =	7
2:	0: 0	(720)	To	2:	1:	0	(726)	Width =	7
3:	0: 0	(1080)	To	3:	1:	0	(1086)	Width =	7
4:	0: 0	(1440)	To	4:	1:	0	(1446)	Width =	7
5:	0: 0	(1800)	To	5:	1:	0	(1806)	Width =	7
6:	0: 0	(2160)	To	6:	1:	0	(2166)	Width =	7
7:	0: 0	(2520)	To	7:	1:	0	(2526)	Width =	7
8:	0: 0	(2880)	To	8:	1:	0	(2886)	Width =	7
9:	0: 0	(3240)	To	9:	1:	0	(3246)	Width =	7
10:	0: 0	(3600)	To	10:	1:	0	(3606)	Width =	7
11:	0: 0	(3960)	To	11:	1:	0	(3966)	Width =	7
12:	0: 0	(4320)	To	12:	1:	0	(4326)	Width =	7
13:	0: 0	(4680)	To	13:	1:	0	(4868)	Width =	7
14:	0: 0	(5400)	To	14:	1:	0	(5046)	Width =	7
15:	0: 0	(5440)	To	15:	1:	0	(5406)	Width =	7
16:	0: 0	(5760)	To	16:	1:	0	(5766)	Width =	7

```
17:  0: 0   (6120)    To   17:  1:  0   (6126)   Width =  7
18:  0: 0   (6480)    To   18:  1:  0   (6486)   Width =  7
19:  0: 0   (6840)    To   19:  1:  0   (6846)   Width =  7
20:  0: 0   (7200)    To   20:  1:  0   (7206)   Width =  7
21:  0: 0   (7560)    To   21:  1:  0   (7566)   Width =  7
22:  0: 0   (7920)    To   22:  1:  0   (7926)   Width =  7
23:  0: 0   (8280)    To   23:  1:  0   (8286)   Width =  7

#
5)   USER SPECIFIED CAL PULSE POSITION:-        Total = 6

     16 : 30 : 10  (5941)    To    16 : 31 : 0  (5946)   Width =  6

#
6)   USER SPECIFIED REJECTED WINDOWS:-          Total = 9

1: 3: 40   ( 382)         To    1:  3: 50    ( 383)    Width =  2
4: 7:  0   (1482)         To    4:  8:  0    (1488)    Width =  7

#
7)   PROGRAM TEMPERATURE CHECKS:-               Total = 0

     Outside window   15.00  TO  25.00  Deg. C
     Range (min – max) 19.80  TO  24.22  Deg. C

#
8)   RAW VALUES OVER LIMIT POSITIONS:-          Total = 0

#
9)   LOCATED MANUAL CALIBRATIONS:-             Total = 0

#
10)  ZERO + CAL. PULSE STATISTICS:-

   Calibration data
     Zeros      #1      0.1      #2      0.0      #3     -1.0
     Cal.       #1   -1390.5     #2   -12120      #3    710.5

#
11)  RELEVANT COMMENT MESSAGES:-               Total = 2

$
++++++++++++++++++++++++++   COMMENT   ++++++++++++++++++++++++++
COMMENT  FILE   DAMG92.COM                 FILE COMMENT NO.    1
DATA     FILE   DAMG92.350                 DAY  COMMENT NO.    1
START    DATE     1/ 1/92    TIME  0: 0: 0  LINE NO.        0
END      DATE    31/12/92    TIME 23:59:50  LINE NO.     8639
-------------------------------------------------------------------------------------------------
```

Calibration via magnetic absolute readings during 1991 and 1992 indicate that considerable inaccuracy, or at least uncertainty, in the base-lines for 1992 exist. As an indication of these variation, the base-lines used in the reduction of the data values are as follows:

1 Nov	90 – 31 Dec	90	Bx = +3644 nT,	By = -16014 nT,	Bz = -52151 nT
1 Jan	91 – 7 Jan	92	Bx = +3557 nT,	By = -16042 nT,	Bz = -52142 nT
8 Jan	92 – 29 Feb	92	Bx = +3632 nT,	By = -16074 nT,	Bz = -52121 nT
1 Mar	92 – 31 Mar	92	Bx = +3611 nT,	By = -16051 nT,	Bz = -52128 nT
1 Apr	92 – 16 Nov	92	Bx = +3597 nT,	By = -16077 nT,	Bz = -52142 nT
16 Nov	92 – 31 Dec	92	Bx = +3622 nT,	By = -16069 nT,	Bz = -52142 nT

THESE INDICATE THE EXTENT OF THE POSSIBLE VARIATION IN THE ABSOLUTE VALUE OF THIS DATA. BEWARE!

It is presently believed that there is a seasonal variation in the Davis baselines due to tilting of the EDA magnetometer by freezing and thawing of the soil beneath the magnetometer pad. The following publications give an indication of the development of this idea.
'Davis Magnetometer Calibration 1990' by M. Hesse.
'Davis Magnetometer Calibration September 1991' by M. Hesse and L. Symons.
'Davis Magnetometer Calibration January 1992' by M. Hesse and L. Symons.
'Davis Magnetometer Calibration March 1992' by M. Hesse and L. Symons.
'1992 Davis Fluxgate Magnetometer Calibration Report' by D. Neudegg.

Magnetic absolute data (QHM and PPM) are collected monthly. Information on the magnetic absolutes readings obtained are included with each days processed data, on which the readings were taken.

The absolute measurements taken for the calibration of this variometer data are not considered to be accurate or regular enough to follow the seasonal variation believed to exist in the data. The data are considered usefull for ionospheric and auroral physics purposes but unsuitable for secular variation studies. Only the broad changes in the baselines are reflected in the changes incorporated in calibration equations.

Further uncertainty on the baseline values for the Davis data is due to doubt over the correction constants of QHM 494 (see '1992 Davis Fluxgate Magnetometer Calibration Report' by D. Neudegg). This uncertainty amounts to approximately 100 nT in the X-baseline, 20 nT in the Y-baseline and less than 10 nT in the Z-baseline. Even when this discrepancy is resolved, these data will not be corrected as no useful purpose would be served, the data would still not be useful for secular variation studies.

Relative magnitude calibrations are conducted daily by the application of a known current to the sensor heads at 16:30 UT, for a duration of 1 minute. This current is measured to be of magnitude 3.201 ±0.001 mA and the respective channels have the following sensitivities:

X channel	+206.0 nT/mA	or	-659.4 nT deflection
Y channel	-185.2 nT/mA	or	-592.8 nT deflection
Z channel	+106.2 nT/mA	or	+339.9 nT deflection

$

++++++++++++++++++++++++++ COMMENT ++++++++++++++++++++++++++

COMMENT	FILE	DAMG92.COM			FILE COMMENT NO.		75
DATA	FILE	DAMG92.350			DAY COMMENT NO.		2
START	DATE	15/12/92	TIME	0: 0: 0	LINE NO.	0	
END	DATE	15/12/92	TIME	23:59:50	LINE NO.	8639	

Disk change around 0104 UT lead to spikes on Y, Z and T channels, interfered data blanked.

Extra manual calibration around 0407 – 0408 UT, note saturation at this time on Y-channel.

APPENDIX 2.

DAVIS MAGNETOMETER SYSTEM CALIBRATION EQUATIONS

A2.1 Equations describing the Davis Magnetometer Calibrations

From 1000 UT 16 February 1988 to 0000 UT 1 December 1989

B_X [nT] = -194.8 [nT/volt] x V_X [volts] + 3,600 [nT]
B_Y [nT] = +200.7 [nT/volt] x V_Y [volts] -16,000 [nT]
B_Z [nT] = +195.6 [nT/volt] x V_Z [volts] -52,150 [nT]

From 0000 UT 1 December 1989 to 0000 UT 1 March 1990

B_X [nT] = -194.8 [nT/volt] x V_X [volts] + 3,653 [nT]
B_Y [nT] = +200.7 [nT/volt] x V_Y [volts] -16,042 [nT]
B_Z [nT] = +195.6 [nT/volt] x V_Z [volts] -52,141 [nT]

From 0000 UT 1 March 1990 to 0000 UT 1 November 1990

B_X [nT] = -194.8 [nT/volt] x V_X [volts] + 3,596 [nT]
B_Y [nT] = +200.7 [nT/volt] x V_Y [volts] -16,000 [nT]
B_Z [nT] = +195.6 [nT/volt] x V_Z [volts] -52,158 [nT]

From 0000 UT 1 November 1990 to 0000 UT 1 January 1991

B_X [nT] = -194.8 [nT/volt] x V_X [volts] + 3,644 [nT]
B_Y [nT] = +200.7 [nT/volt] x V_Y [volts] -16,014 [nT]
B_Z [nT] = +195.6 [nT/volt] x V_Z [volts] -52,151 [nT]

From 0000 UT 1 January 1991 to 0000 UT 8 January 1992

B_X [nT] = -194.8 [nT/volt] x V_X [volts] + 3,577[nT]
B_Y [nT] = +200.7 [nT/volt] x V_Y [volts] -16,042[nT]
B_Z [nT] = +195.6 [nT/volt] x V_Z [volts] -52,142 [nT]

From 0000 UT 8 January 1992 to 0000 UT 1 March 1992

B_X [nT] = -194.8 [nT/volt] x V_X [volts] + 3,632 [nT]
B_Y [nT] = +200.7 [nT/volt] x V_Y [volts] -16,074 [nT]
B_Z [nT] = +195.6 [nT/volt] x V_Z [volts] -52,121 [nT]

From 0000 UT 1 March 1992 to 0000 UT 1 April 1992

B_X [nT] = -194.8 [nT/volt] x V_X [volts] + 3,611 [nT]
B_Y [nT] = +200.7 [nT/volt] x V_Y [volts] -16,051 [nT]
B_Z nT] = +195.6 [nT/volt] x V_Z [volts] -52,128 [nT]

From 0000 UT 1 April 1992 to 0800 UT 16 November 1992

B_X [nT] = -194.8 [nT/volt] x V_X [volts] + 3,597 [nT]
B_Y [nT] = +200.7 [nT/volt] x V_Y [volts] -16,077 [nT]
B_Z [nT] = +195.6 [nT/volt] x V_Z [volts] -52,142 [nT]

From 0800 UT 16 November 1992 to 0000 UT 1 January 1993

B_X [nT] = -194.8 [nT/volt] x V_X [volts] + 3,622 [nT]

B_y [nT] = +200.7 [nT/volt] x V_y [volts] -16,069 [nT]
B_z [nT] = +195.6 [nT/volt] x V_z [volts] -52,142 [nT]

A2.2 Equation describing the Davis DORIC Thermometer

From 1000 UT 16 February 1988 to the present
T [C] = +10.19 [C/volt] x V_T [volts] - 0.409

A2.3 Equations describing the Davis Logging System, Temperature Channel

From 1000 UT 16 February 1988 to 0000 UT 17 September 1990
V_T [volts] = (D_T [dig] + 2030.4) / (205 x 5)
V_T [volts] = 0.000976 x D_T [dig] + 1.98165

From 0000 UT 17 September 1990 to 0000 UT 17 March 1991
V_T [volts] = (D_T [dig] + 2018.0) / (204.8 x 4.972)
V_T [volts] = 0.000982 x D_T [dig] + 1.98164

From 0000 UT 17 March 1991 to 0000 UT 1 January 1993
V_T [volts] = (D_T [dig] + 1980.9) / (204.8 x 4.830)
V_T [volts] = 0.001011 x D_T [dig] + 2.00273

A2.4 Equations describing the Davis Logging System, X, Y and Z channels.

From 1000 UT 16 February 1988 to 0745 UT 16 March 1988
V_X [volts] = (D_X [dig] - 1) / (205 x 5)
V_X [volts] = 0.0009756 x D_X [dig] - 0.000976

V_Y [volts] = (D_Y [dig] - 3) / (205 x 5)
V_Y [volts] = 0.0009756 x D_Y [dig] - 0.00293

V_Z [volts] = (D_Z [dig] - 3) / (205 x 5)
V_Z [volts] = 0.0009756 x D_Z [dig] - 0.00293

From 0745 UT 16 March 1988 to 0000 UT 1 January 1989
V_X [volts] = (D_X [dig] - 1) / (205 x 2)
V_X [volts] = 0.002439 x D_X [dig] - 0.002439

V_Y [volts] = (D_Y [dig] - 4) / (205 x 2)
V_Y [volts] = 0.002439 x D_Y [dig] - 0.00976

V_Z [volts] = (D_Z [dig]) / (205 x 2)
V_Z [volts] = 0.002439 x D_Z [dig]

From 0000 UT 1 January 1989 to 0000 UT 1 December 1989
V_X [volts] = (D_X [dig] - 2) / (204.8 x 1.986)
V_X [volts] = 0.002459 x D_X [dig] - 0.004917

V_y [volts] = (D_y [dig] - 6) / (204.8 x 2.004)
V_y [volts] = 0.002437 x D_y [dig] - 0.01462

V_z [volts] = (D_z [dig] - 1) / (204.8 x 1.982)
V_z [volts] = 0.002464 x D_z [dig] - 0.00246

From 0000 UT 1 December 1989 to 0000 UT 24 March 1991
V_x [volts] = (D_x [dig] - 2) / (204.8 x 1.986)
V_x [volts] = 0.002459 x D_x [dig] - 0.004917

V_y [volts] = (D_y [dig] - 8) / (204.8 x 2.004)
V_y [volts] = 0.002437 x D_y [dig] - 0.01949

V_z [volts] = (D_z [dig] - 2) / (204.8 x 1.982)
V_z [volts] = 0.002464 x D_z [dig] - 0.00493

From 0000 UT 24 March 1991 to 0715 UT 5 March 1992
V_x [volts] = (D_x [dig] - 0.3) / (204.8 x 2.003)
V_x [volts] = 0.002438 x D_x [dig] - 0.000732

V_y [volts] = (D_y [dig] + 0.5) / (204.8 x 2.002)
V_y [volts] = 0.002439 x D_y [dig] + 0.00122

V_z [volts] = (D_z [dig] - 0.2) / (204.8 x 2.002)
V_z [volts] = 0.0002439 x D_z [dig] - 0.000488

From 0715 UT 5 March 1992 to 0715 UT 11 December 1992
V_x [volts] = (D_x [dig] - 1.4) / (204.8 x 2.005)
V_x [volts] = 0.002435 x D_x [dig] - 0.00341

V_y [volts] = (D_y [dig] + 0.3) / (204.8 x 2.006)
V_y [volts] = 0.002434 x D_y [dig] + 0.00073

V_z [volts] = (D_z [dig] + 0.5) / (204.8 x 2.005)
V_z [volts] = 0.0002435 x D_z [dig] + 0.00122

From 0715 UT 11 December 1992 to 0000 UT 1 January 1993
V_x [volts] = (D_x [dig] - 1.734) / (204.8 x 2.0045)
V_x [volts] = 0.002436 x D_x [dig] - 0.004223

V_y [volts] = (D_y [dig] + 0.678) / (204.8 x 2.0056)
V_y [volts] = 0.002436 x D_y [dig] + 0.00165

V_z [volts] = (D_z [dig] + 0.833) / (204.8 x 2.0046)
V_z [volts] = 0.0002436 x D_z [dig] + 0.00203

APPENDIX 3.

CASEY MAGNETOMETER SYSTEM CALIBRATION EQUATIONS

A3.1 Equations describing the Casey Magnetometer Calibrations

From 0000 UT 17 January 1989 to 0000 UT 4 March 1989

B_X [nT] = -185.0 [nT/volt] x V_X [volts] - 210 [nT]
B_Y [nT] = -204.0 [nT/volt] x V_Y [volts] - 9,667 [nT]
B_Z [nT] = -200.0 [nT/volt] x V_Z [volts] - 64,118 [nT]

From 0000 UT 4 March 1989 to 0400 UT 1 August 1989 (Z-channel change only)

B_X [nT] = -187.0 [nT/volt] x V_X [volts] - 210 [nT]
B_Y [nT] = -204.0 [nT/volt] x V_Y [volts] - 9,667 [nT]
B_Z [nT] = -200.0 [nT/volt] x V_Z [volts] - 64,086 [nT]

From 0400 UT 1 August 1989 to 0000 UT 30 January 1990 (X-channel change only)

B_X [nT] = -187.0 [nT/volt] x V_X [volts] - 190 [nT]
B_Y [nT] = -201.0 [nT/volt] x V_Y [volts] - 9,667 [nT]
B_Z [nT] = -200.0 [nT/volt] x V_Z [volts] - 64,086 [nT]

From 0000 UT 30 January 1990 to 0000 UT 5 December 1990 (Y-channel change only)

B_X [nT] = -187.0 [nT/volt] x V_X [volts] - 190 [nT]
B_Y [nT] = -201.0 [nT/volt] x V_Y [volts] - 9,632 [nT]
B_Z [nT] = -200.0 [nT/volt] x V_Z [volts] - 64,086 [nT]

From 0000 UT 5 December 1990 to 0000 UT 25 December 1992

B_X [nT] = -187.0 [nT/volt] x V_X [volts] - 204 [nT]
B_Y [nT] = -201.0 [nT/volt] x V_Y [volts] - 9,590 [nT]
B_Z [nT] = -200.0 [nT/volt] x V_Z [volts] - 64,079 [nT]

From 0000 UT 25 December 1992 to the present

B_X [nT] = -187.0 [nT/volt] x V_X [volts] - 698 [nT]
B_Y [nT] = -201.0 [nT/volt] x V_Y [volts] - 9,918 [nT]
B_Z [nT] = -200.0 [nT/volt] x V_Z [volts] - 64,109 [nT]

A3.2 Equation describing the Casey DORIC Thermometer

From 0000 UT 17 January 1989 to 0000 UT 25 December 1992

T [C] = +13.21 [C/volt] x V_T [volts] - 5.645[C]

From 0000 UT 25 December 1992 to the present

T [C] = +10.00 [C/volt] x V_T [volts] - 0.38[C]

A3.3 Equations describing the Casey Logging System, Temperature Channel

From 0000 UT 17 January 1989 to 0000 UT 25 December 1992

V_T [volts] = D_T [dig] / (204.8 x 1)

V_T [volts] = 0.004883 x D_T [dig]

From 0000 UT 25 December 1992 to the present

V_T [volts] = (D_T [dig] + 201.473) / (204.8 x 0.492)

V_T [volts] = 0.000991 x D_T [dig] + 1.9995

A3.4 Equations describing the Casey Logging System, X, Y and Z channels.

From 0000 UT 17 January 1989 to 0400 UT 1 August 1989

V_X [volts] = D_X [dig] / (204.8 x 1)

V_X [volts] = 0.004883 x D_X [dig]

V_y [volts] = D_y [dig] / (204.8 x 1)

V_y [volts] = 0.004883 x D_y [dig]

V_Z [volts] = D_Z [dig] / (204.8 x 1)

V_Z [volts] = 0.004883 x D_Z [dig]

From 0400 UT 1 August 1989 to 0000 UT 30 January 1990

V_X [volts] = (D_X [dig] -3) / (204.8 x 2)

V_X [volts] = 0.002441 x D_X [dig] - 0.00732

V_y [volts] = (D_y [dig] -2) / (204.8 x 2)

V_y [volts] = 0.002441 x D_y [dig] - 0.00488

V_Z [volts] = (D_Z [dig] -3) / (204.8 x 2)

V_Z [volts] = 0.002441 x D_Z [dig] - 0.00732

From 0400 UT 30 January 1990 to 0800 UT 19 November 1990

V_X [volts] = (D_X [dig] -3) / (204.8 x 2.003)

V_X [volts] = 0.002438 x D_X [dig] - 0.00731

V_y [volts] = (D_y [dig] -2) / (204.8 x 2)

V_y [volts] = 0.002441 x D_y [dig] - 0.00488

V_Z [volts] = (D_Z [dig] -3) / (204.8 x 2)

V_Z [volts] = 0.002441 x D_Z [dig] - 0.00732

From 0800 UT 19 November 1990 to 2000 UT 3 May 1991

V_X [volts] = (D_X [dig] -3) / (204.8 x 2.003)

V_X [volts] = 0.002438 x D_X [dig] - 0.00731

V_y [volts] = D_y [dig] / (204.8 x 1.993)

V_y [volts] = 0.002449 x D_y [dig]

V_Z [volts] = (D_Z [dig] -4) / (204.8 x 2.001)
V_Z [volts] = 0.002440 x D_Z [dig] - 0.00976

From 2000 UT 3 May 1991 to 0000 UT 25 December 1992

V_X [volts] = D_X [dig] / (204.8 x 1.977)
V_X [volts] = 0.002469 x D_X [dig]

V_Y [volts] = D_Y [dig] / (204.8 x 1.977)
V_Y [volts] = 0.002469 x D_Y [dig]

V_Z [volts] = D_Z [dig] / (204.8 x 1.984)
V_Z [volts] = 0.002461 x D_Z [dig]

From 0000 UT 25 December 1992 to the present

V_X [volts] = (D_X [dig] +0.7) / (204.8 x 1.981)
V_X [volts] = 0.002465 x D_X [dig] + 0.001725

V_Y [volts] = (D_Y [dig] +0.8) / (204.8 x 1.981)
V_Y [volts] = 0.002465 x D_Y [dig] + 0.001972

V_Z [volts] = (D_Z [dig] +0.3) / (204.8 x 1.986)
V_Z [volts] = 0.002458 x D_Z [dig] + 0.000737

3. A LIDAR FOR THE STUDY OF THE ATMOSPHERE ABOVE DAVIS, ANTARCTICA

A.R. Klekociuk[1], P.S. Argall[2,3], R.J. Morris[1], P. Yates[1], A. Fleming[1], R.A. Vincent[2], I.M. Reid[2], P.A. Greet[1,4] and D.J. Murphy[1]

(1) Auroral and Space Physics
Antarctic Division
Kingston Tasmania 7050
Australia

(2) Department of Physics and Mathematical Physics
University of Adelaide
Adelaide SA 5005
Australia

(3) Department of Physics
University of Western Ontario
London Ontario N6A 3K7
Canada

(4) Institute for Antarctic and Southern Ocean Studies
University of Tasmania
Hobart Tasmania 7001
Australia

ABSTRACT

An atmospheric lidar developed by the University of Adelaide is currently being upgraded, tested and prepared for Antarctic operation by the Australian Antarctic Division. From early 1996 this instrument will routinely monitor the structure and dynamics of the stratosphere and mesosphere above Davis, Antarctica. Importantly, this instrument will provide new data in a sparsely sampled region that is important in the context of understanding global atmospheric dynamics.

This paper reviews the current status of the project, and describes the scientific objectives and operational capabilities of the lidar.

3.1 INTRODUCTION

Lidar (LIght Detection And Ranging) systems have been utilised in the remote sensing of the atmosphere for more than three decades (for reviews, see for example, Kent and Wright 1970; Carswell 1983). The lidar technique relies on the interaction (via various scattering and absorption processes) of a high intensity laser beam with gases and aerosols. By measuring the characteristics of the radiation back-scattered from the interaction volume, basic parameters (such as density, temperature and wind velocity) of the bulk atmosphere or its constituent species as a function of range may be inferred.

The versatility of the lidar technique is currently being applied by several groups to address concerns and uncertainties relating to global atmospheric change. Recent predictive modelling of middle atmosphere (10 – 100 km) chemistry and dynamics (by, for example, Rind et al. 1990, Roble and Dickinson 1989) suggests that the first and largest changes in atmospheric temperature associated with increased anthropogenic 'greenhouse' gas concentrations will be manifest as a cooling of the stratosphere and mesosphere. There is general consensus that recent observations lend support to these predictions. For example, satellite and lidar data reported by Aiken et al. (1991) have shown a cooling trend of approximately 0.3 K/yr in stratospheric temperatures while sodium lidar observations reported by Clemesha et al. (1992) are consistent with decreasing temperatures and densities in the mesopause region. It is clear that further long term monitoring of middle atmosphere temperatures are required not only to assess these trends, but to more fully understand the complex influence of natural and anthropogenic sources on the climate of this region.

A region that may be particularly sensitive in the context of global atmospheric change is the polar mesopause (near 90 km altitude; see, for example, Lübken and von Zahn 1991). The recent apparent dramatic increase in the frequency, extent and intensity of noctilucent clouds (NLCs) in the polar regions during summer is believed to be associated with decreasing mesopause temperatures and possibly to increased oxidisation of the 'greenhouse' gas methane (Gadsden 1990; Thomas et al. 1989). Lidar and radar techniques are currently being applied in the study of NLCs and related phenomena and to quantify parameters in the mesopause region. To date, most of this effort has been concentrated in the northern hemisphere.

It is clear that accompanying 'greenhouse'-induced temperature changes in the middle atmosphere will be the redistribution of constituent species and alteration of atmospheric densities and scale heights. This will influence the propagation and dissipation of the various naturally occurring wave processes in the region, specifically gravity waves, planetary waves and tides. These waves are at best only crudely parameterised in existing global circulation models. However, they are known to exert a substantial influence on thermal and constituent structure and general circulation throughout the atmosphere. Lidars are currently playing an important role in probing wave processes over a large range of spatial and temporal scales.

With the aim of contributing to the debate relating to atmospheric change, the Auroral and Space Physics (ASP) group of the Antarctic Division, and the Department of Physics and Mathematical Physics of the University of Adelaide, are collaborating in an innovative and exciting project involving the operation of a lidar with unique capabilities at Davis, Antarctica (68.6°S, 78.0°E) beginning early 1996. This paper provides information on the project with the hope of engendering interest in the national and international scientific communities.

3.2 ATMOSPHERIC SCIENCE AT DAVIS

The ASP group is currently establishing a suite of research instruments at Davis which will probe various overlapping regions of the atmosphere, from the ground to the thermosphere, using a diverse range of techniques. Davis is an important site in the context of

investigating atmospheric dynamics, because it lies in a sparsely sampled region of Antarctica at the northern edge of the stratospheric polar vortex and passes under the dayside projection of the auroral oval, in a region known as the magnetospheric cusp.

The atmospheric science instruments at Davis include a single etalon scanning Fabry-Perot spectrometer (FPS) for measuring winds and temperatures in regions associated with the mesospheric hydroxyl (OH) and sodium (Na) emissions, and thermospheric O(^{1}D) airglow (in collaboration with LaTrobe University), a spectrophotometer and six-channel photometer for measuring OH rotational temperatures, a medium frequency radar for measuring winds in the mesosphere and lower thermosphere, between altitudes of 60 and 100 km (in collaboration with the University of Adelaide), and an airglow imager for gravity wave studies. The incorporation of a three-field photometer for moving-pattern analysis of airglow structures (in collaboration with LaTrobe University) is planned. An 'observatory' program involving a three-component fluxgate magnetometer, a two component induction magnetometer, a dual-channel auroral photometer and a riometer provide additional data on prevailing geophysical conditions. In addition, the Australian Bureau of Meteorology conducts a routine program of surface and upper-air (to altitudes of about 30 km) observations.

The work at Davis forms the core of the strategic science program being developed by the ASP group to address the atmospheric research priorities recommended by the Antarctic Science Advisory Committee of the Australian Academy of Science. The lidar is an integral part of this program.

3.3 ORIGINS OF THE LIDAR PROJECT

The lidar was designed by the late Dr. Fred Jacka of the University of Adelaide in the early 1980's. Dr. Jacka recognised that the operation of a lidar capable of directly measuring winds and temperatures in the middle atmosphere would be important for the understanding of atmospheric dynamics, particularly in the Antarctic region. To achieve this capability, it was proposed to use a dual scanning FPS to measure the Doppler shift and temperature broadening imposed on the spectral profile of the laser line in the backscattering process (Jacka and Argall 1987).

The development of the lidar has built on the considerable experience acquired in the construction and operation of optical tools for remotely sensing the middle and upper atmosphere by the University of Adelaide, most notably in the 'stand-alone' FPS systems that are currently operating at the Australian Antarctic stations of Mawson and Davis. Construction of the lidar began in 1985, largely through the efforts of Dr. Jacka, electronics engineer Don Crieghton, and Ph.D. student Stephen Argall. The first stage of the project culminated in the measurement of atmospheric density, inferred temperature and aerosol loading for altitudes between 18 and 60 km at Buckland Park near Adelaide during 1992 and 1993. This work lead to the submission of a Ph.D. dissertation by Stephen Argall (Argall 1993).

The untimely passing of Dr. Jacka in 1992 meant the loss of a considerable reservoir of knowledge and experience in atmospheric research which was of great importance to the scientific drive behind the project. During 1993, the Antarctic Division secured funds for

the completion of the instrument, with the intention of carrying out Dr. Jacka's original vision of operating the instrument in Antarctica.

3.4 CONFIGURATION

The design of the lidar has been described by Jacka and Argall (1987) and Argall (1993). Originally, the system utilised the 510 nm emission from a copper vapour (CuV) laser. The effective upper range of the lidar was limited to about 60 km by the average power level of the laser (~ 6W maximum) and its 2 kHz pulse repetition frequency. In order to extend the range of the instrument to the more scientifically interesting mesopause region, a higher power commercial Nd:YAG laser is currently being integrated into the system by the Antarctic Division. This laser produces an average power of 30 W at 532 nm (the second harmonic of the principal Nd:YAG emission) with a PRF of 50 Hz.

Initially, the new laser will operate in 'low-power' mode (by virtue of a beam attenuator) with the existing optics. Some design modifications are necessary to avoid gas breakdown and optical damage when operating at the highest pulse energies.

The 'power-aperture' product of a backscatter lidar (that is, the average laser power times the area of the collector) provides a measurement of its effectiveness. The new Nd:YAG laser will increase the 'power-aperture' product of our lidar to about 24 Wm^2, placing it amongst the most powerful of atmospheric systems in operation.

The present optical configuration is shown in Figure 1. Laser pulses are transmitted to the sky by a series of optical elements culminating in a Cassegrain telescope with a 1 metre aperture. Both the primary and secondary mirrors of the telescope are manufactured from aluminium. The telescope can be rotated in azimuth and tilted to a maximum zenith angle of 45°.

The use of common optics for transmitting and receiving components of the system ensures that the volume under study is identical to that being illuminated. Light received by the telescope is optically relayed to the detection system which is operated in one of four modes by virtue of a 'switching mirror' arrangement. In 'total power' detection mode, the received light is passed through a 0.3 nm bandwidth interference filter and detected by a cooled photomultiplier. Pulses from the photomultiplier are integrated as a function of range; that is, as a function of time after the start of each transmitted laser pulse. This type of operation will be used almost exclusively for high time resolution density measurements at night when the contamination from background ('non-laser') light is sufficiently low to permit detectable returns from altitudes up to the mesopause.

The other detection modes make use of the FPS to measure spectra of the received light as a function of range with three different spectral resolutions. The basic design of the FPS is similar to that described by Wilksch (1975) and Jacka (1984). The upper and lower etalons of the FPS provide 'narrow' (2 pm) and 'wide' (25 pm) spectral passbands respectively, and both or either of the etalons may be introduced prior to the interference filter by the 'switching mirror' system. The Nd:YAG laser is frequency stabilised by the 'injection seeding' process, and has a bandwidth of ~ 0.85 pm. Drift in the central wavelength of the laser will be less than ± 0.1 pm rms over periods of hours for the expected temperature

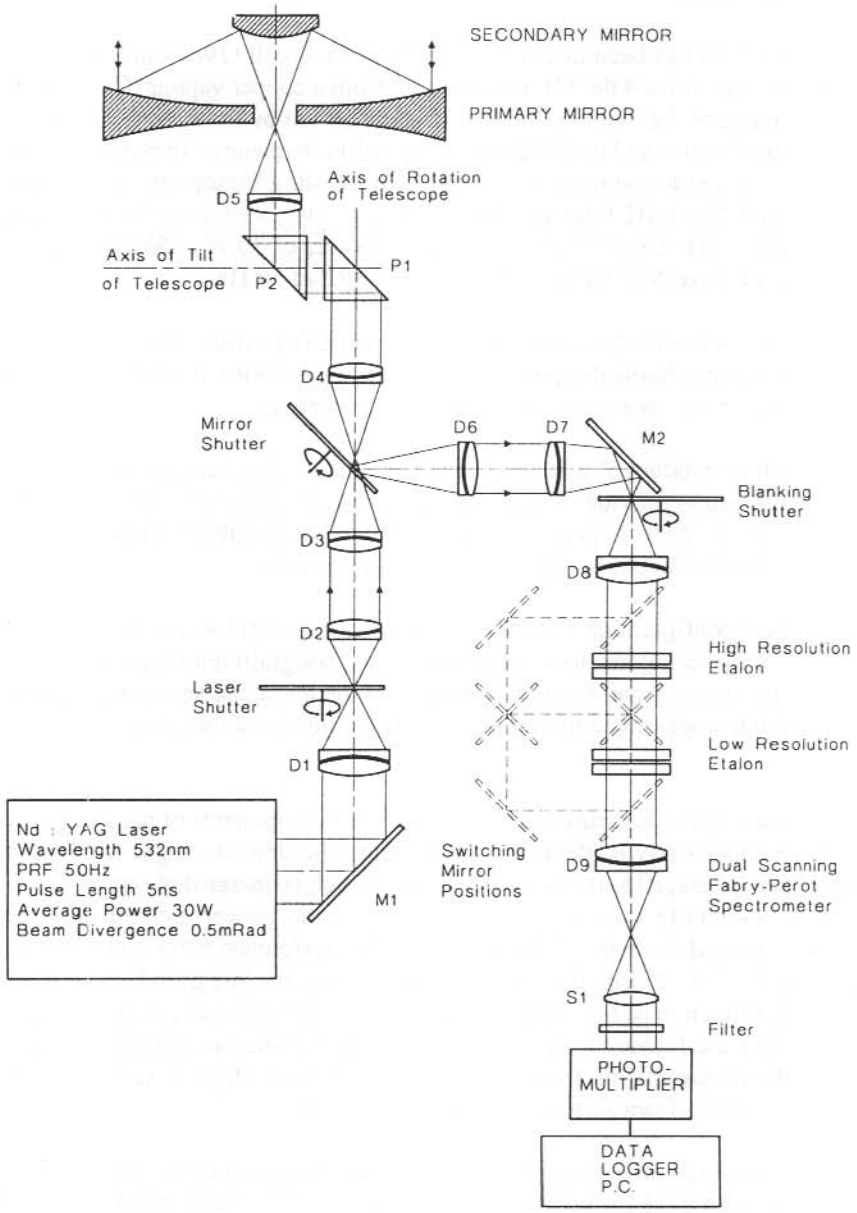

Figure 1. Schematic diagram of the lidar. The FPS is shown with the switching mirror arrangement configured for dual etalon mode.

variation of the operating environment. Light from the laser will be used to accumulate the 'instrument profile' spectrum in tandem with the atmospheric measurements.

Performance simulations for the lidar operating with the CuV laser have previously been reported by Jacka and Argall (1987). New simulations are currently being run for the upgraded system and these will be reported in a forthcoming paper in the ANARE Research Notes series. As an indication of the anticipated performance, 'total power' measurements during the night at the mesopause will yield density and temperature estimates with 5% and 10 K rms errors, respectively, for an altitude resolution of 0.3 km and a dwell time of 10 minutes. To achieve similar accuracy during the day, a dwell time of 30 minutes using the FPS in 'wide' bandwidth mode is required. It should be noted that considerably better performance is achieved at lower altitudes.

Three high speed (24,000 rpm) shutters that are electrically synchronised with the firing of the laser form an integral part of the lidar. The 'blanking shutter' blocks the photomultiplier while the laser is firing to protect it from stray photons. The 'laser shutter' prevents any photons that may be emitted by the laser after each pulse from scattering along the optical path to the detection system. The provision of this shutter was essential for the operation of the lidar with the CuV laser, as the cavity of the laser produced a significant amount of thermal radiation after each pulse. It is likely that the Nd:YAG laser will produce sufficiently low 'off-pulse' emission to allow the removal of this shutter and simplification of the optical train prior to the 'mirror shutter'. The mirror shutter switches the system between transmit and receive modes. It consists of an aluminium disk with a highly reflective upper surface from which five identically shaped regions ('cut-outs') have been symmetrically removed. The rotation of this shutter is synchronised so that each laser pulse passes through one of the cut-outs while the return signal is reflected by the upper surface to the detection system. The cut-outs are profiled so that backscattered light returned from ranges below 5 km passes back towards the laser (and is hence not analysed), while light corresponding to ranges between 5 and 18 km is attenuated in a progressively decreasing manner in order to protect the photomultiplier from saturation.

The optical elements D2 to D5 and the beam steering prisms P1 and P2 are manufactured from a type of fused silica known as Dynasil. All other elements are BK7/LF7 achromatic doublets. Dynasil was chosen to avoid fluorescence in common elements of the transmitter and receiver illuminated by the CuV laser. Initially, it was found that more commonly used optical glasses (e.g. BK7) fluoresce with a decay time constant of a few hundred microseconds, which is on the order of the return time from ranges of a few tens of kilometres. In the presence of fluorescence, the detectability of the backscattered signal, particularly for the longest ranges, is significantly degraded. The fluorescence performance of the current optical materials when illuminated by the highest energy pulses from the Nd:YAG laser is still to be determined.

3.5 OPERATION

At Davis, the lidar facility will be housed in two prefabricated modules adjacent to the existing ASP Building (see Figure 2). The 'Instrument Module' will house the lidar itself, providing a temperature-stabilised environment for the laser and the FPS, and an enclosure to protect the telescope. The design of the covering for the telescope is still to be finalised.

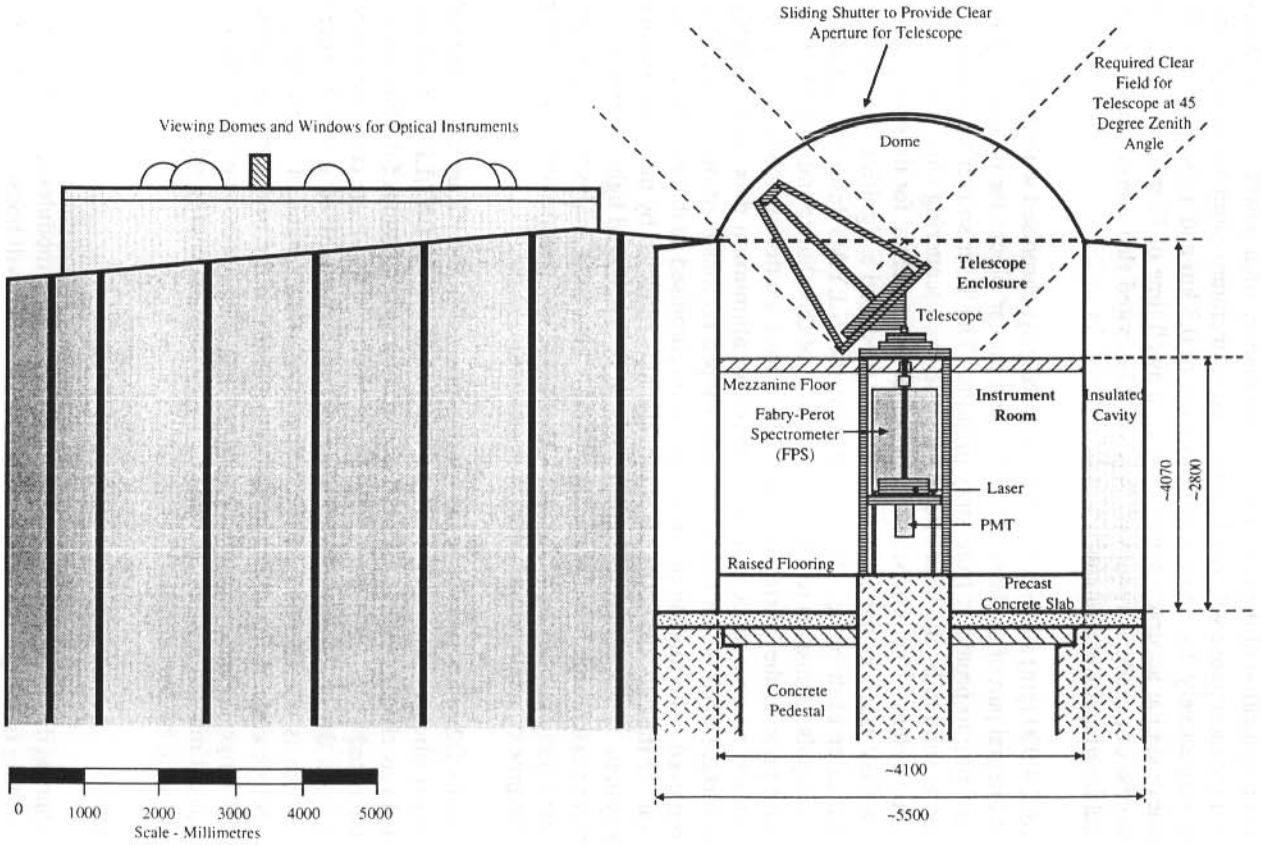

Figure 2. 'Cut-away' side view of the proposed configuration of the lidar modules at the north-eastern end of the Davis ASP Building.

A rotatable 'observatory' type dome with an unobstructed aperture movable in zenith angle is a possible option. The 'Laboratory Module' will provide a working environment from which the instrument will be run. Initially, the lidar modules will be established at Antarctic Division Head Office (Tasmania) to allow integration and testing of the entire system.

Routine operation of the lidar at Davis will be conducted during day and night fair-weather conditions. Initially, high spatial and temporal resolution measurements of atmospheric density, temperature, wind velocity and aerosol loading as a function of altitude will be obtained from near the tropopause (about 18 km altitude) through to the mesopause region.

The methods for recovering atmospheric parameters are discussed in Jacka and Argall (1987). In 'total power' mode, the signal strength as a function of range is combined with in-situ radiosonde measurements or an assumed density value at a particular height (usually where the contribution to scattering due to aerosols is minimal) to recover the density-height profile. Account is made of the background scattered light and instrument noise by 'off-pulse' measurements or by fitting a background term to the signal versus range profile. By assuming that the atmosphere obeys the perfect gas law and is in hydrostatic equilibrium, the density measurements may be used to recover a temperature profile by an iterative method which works down in altitude from a level of known or assumed atmospheric pressure (see, for example, Hauchecorne and Chanin 1980). In addition, the variation of backscattered signal as a function of height, when combined with a model of the molecular atmosphere yields information on the importance of aerosols in the scattering process (Fiocco 1984). Sequential measurements at particular azimuth angles with a fixed zenith angle can be used in a 'moving pattern' analysis to infer wind velocity (Jacka and Argall 1987).

The analysis of spectral observations requires the deconvolution of the 'instrument' profile. The line-of-sight Doppler wind speed and mean molecular temperature as a function of height may then be recovered. The wind vector profile is obtained from measurements over a range of lines-of-sight (Jacka 1984). As noted by Jacka and Argall (1987), temperature estimates for the molecular atmosphere inferred from FPS spectra will underestimated in regions where the mixing ratio of aerosols is significant (usually below ~ 30 km). In these regions, it may be possible to obtain additional temperature estimates if the pure rotational Raman spectra of N_2 and O_2 can be resolved. By integrating individual spectra over the wavelength domain, estimates of 'total power' backscatter intensity may be obtained and then inverted to obtain density-height profiles.

3.6 SCIENTIFIC AIMS

The scientific aims of the lidar project are:

(a) To establish the current state of basic atmospheric parameters from the troposphere to the upper mesosphere above Davis, Antarctica, and commence the acquisition of a high-quality data base extending over at least one solar activity cycle, focussing on the temperature and dynamics of the mesopause region and the dynamics of stratospheric ozone to assess variations that may be related to global atmospheric change.

(b) The synthesis of these data together with routine and campaign-based data obtained at Davis from radar, optical and balloon-borne programs in the study of coupling processes

throughout the atmosphere at high spatial and temporal resolution, especially the effects of planetary waves, tides, gravity waves and turbulence and their influence on constituent transport and mean flow interactions.

It is anticipated that at least two physicists and one electronics engineer will 'winter-over' at Davis in support of the total atmospheric science program. On-site analysis of lidar data will be performed, and near real-time data transfer to Australia will allow on-going productive research. Workshop-style intensive studies of selected special intervals will be undertaken utilising data from other Davis-based and international programs (such as STEP, CEDAR and TIMED). Other Antarctic lidars are in operation at South Pole, McMurdo, Syowa and Dumont D'urville (see for example Collins et al. 1993 and references therein) and it is hoped that collaborative work will take place with the groups operating these instruments.

The main thrust of the initial research will be the development of an understanding of the dynamics and climatology of the atmosphere above Davis. In addition to the study of noctilucent clouds (NLCs), the lidar will also provide valuable data for regions associated with Polar Stratospheric Clouds (PSCs), and possibly, Polar Mesospheric Summer Echoes (PMSEs). The formation of PSCs is temperature dependent, and linked to surface chemistry on aerosols resulting from anthropogenic activity and natural sources. Studies of PSCs have so far been limited to summer periods when they are evident in reflected sunlight. The lidar will allow studies of these clouds during winter, when they are expected to be far more prevalent due to lower stratospheric temperatures. PMSEs appear to be associated with sub-visual ice particles and as such are linked to the water vapour concentration and temperature of the middle atmosphere (Cho and Kelly 1993). To date, the published literature does not contain any reports of PMSE detections in the southern hemisphere (see, for example, Balsley 1993). The possible future installation of a VHF radar at Davis, combined with lidar observations, has the potential to provide important new data on this phenomenon.

The transport of aerosols to stratospheric altitudes, particularly from volcanic events, is regarded as playing an important role in the cooling of the lower atmosphere. Although single-wavelength lidar provides only limited information on the optical properties of high altitude aerosols, the measurement of vertical aerosol distribution and transport will provide further insights into large-scale circulation.

A future upgrade of the laser system (possibly towards the end of the decade) will allow the investigation of stratospheric ozone dynamics which is relevant to the study of the annual depletion mechanism and its impact on the climatology of the lower atmosphere and biological systems. This work will link with planned ozone spectrophotometer and balloon-borne 'ozone-sonde' measurements. In addition, the capability for fluorescence measurements of the sodium layer (between altitudes of about 85 and 95 km) is proposed to allow comparison with observations by the 'stand-alone' FPS at the site. These measurements could potentially provide temperature estimates near the mesopause with higher precision than those obtained by the backscatter observations.

3.7 CONCLUSIONS

The establishment of the lidar facility at Davis will be an important aspect of future Australian Antarctic research into atmospheric change. The wealth of new information from this project coupled with the coordinated approach to atmospheric science being developed at Davis has the potential to focus international attention on this site. The work is directly relevant to a number of 'high-investment' international programs, such as components of NASA's 'Mission to Planet Earth'.

It is likely that increased greenhouse gas concentrations in the lower atmosphere is influencing the climate at higher altitudes. The rarefied polar atmosphere is a litmus site' for predictive models of climate change. Lidar measurements will be vital for testing and tuning these models and assisting in the identification of natural and anthropogenic sources of climate forcing. Studies relating to PSCs, NLCs and aerosol loading will also be vital aspects of this work. There is potential to extend the lidar investigations into the troposphere, examining additional climate-related aspects such as cloud thicknesses and ceilings. The future ability to study stratospheric ozone dynamics is essential for fully addressing key issues of current climate change research.

The development of models that accurately treat the atmosphere as a coupled system are vital to developing strategies for coping with anticipated levels of climate change in the lower atmosphere. By studying the dynamics of the atmosphere above Davis on an intensive basis with a range of techniques, we will not only develop a detailed local appreciation of coupling processes, but hopefully add to theoretical understanding of global atmospheric processes.

3.8 ACKNOWLEDGMENTS

The pioneering work of the late Fred Jacka is respectfully acknowledged. Don Creighton, Daryl White and Wayne Hocking have made numerous invaluable contributions in aspects of the design and construction of the lidar. Funding for the development of the lidar has been provided by the Australian Research Council (grant number A69231890), the University of Adelaide, and the Antarctic Division.

REFERENCES

Argall, P.S. (1993). Lidar studies of the middle atmosphere. Ph.D. Thesis, University of Adelaide.

Aikin, A.C., Chanin, M.L., Nash, N. *and* Kendig, D.J. (1991). Temperature trends in the lower mesosphere. *Geophysical Research Letters 18:*416–419.

Balsley, B.B, Woodman, R.F., Sarango, M., Urbina, J., Rodriguez, R., Ragaini, E. *and* Carey, J. (1993). Southern-hemisphere PMSE: where are they? *Geophysical Research Letters 20:*1983–1985.

Carswell, A.I. (1983). Lidar measurements of the atmosphere. *Canadian Journal of Physics 61*:378–395.

Cho, J.Y.N. *and* Kelley, M.C. (1993). Polar mesosphere summer radar echoes: observations and current theories. *Reviews of Geophysics 31:*243 – 265.

Clemesha, B.R., Simonich, D.M. *and* Batista, P.P. (1992). The annual variation of the height of the sodium layer at 23°S. *Geophysical Research Letters 19:*457 – 460.

Collins, R.L., Bowman, K.P. *and* Gardner, C.S. (1993). Polar stratospheric clouds at the South Pole in 1990: lidar observations and analysis. *Journal of Geophysical Research 98D:*1001 – 1010.

Fiocco, G. (1984). Lidar systems for aerosol studies: an outline. *Middle Atmosphere Program – Handbook 13:*56 – 68.

Gadsen, M. (1990). A secular change in noctilucent cloud occurrence. *Journal of Atmospheric and Terrestrial Physics 52:*247 – 251.

Hauchecorne, A. *and* Chanin, M-L. (1980). Density and temperature profiles obtained by lidar between 35 and 70 km. *Geophysical Research Letters 7*: 565 – 568.

Jacka, F. (1984). Application of Fabry-Perot spectrometers for measurement of upper atmosphere temperature and winds. *Middle Atmosphere Program – Handbook 13:*19 – 40.

Jacka, F. *and* Argall, P.S. (1987). A lidar system for stratosphere studies – performance simulation. In: Burns, G.B. *and* Craven, M. (Eds). *ANARE Research Notes Number 48*, Australian Antarctic Division. Pp. 226 – 235.

Kent, G.S. *and* Wright, R.W.H. (1970). A review of laser radar measurements of atmospheric properties. *Journal of Atmospheric and Terrestrial Physics 32*:917 – 943.

Lübken, F.-J. *and* von Zahn, U. (1991). Thermal structure of the mesopause region at polar latitudes. *Journal of Geophysical Research 96D:*20841 – 20857.

Rind, D., Suozzo, R., Balachandran, N.K. *and* Prather, M.J. (1990). Climate change and the middle atmosphere: the doubled CO_2 climate. *Journal of Atmospheric Science 47:*475 – 494.

Roble, R.G. *and* Dickinson, R.E. (1989). How will changes in carbon dioxide and methane modify the mean structure of the mesosphere and thermosphere? *Geophysical Research Letters 16:*1441 – 1444.

Thomas, G.E., Olivero, J.J., Jensen, E.J., Schroeder, W. *and* Toon, O.B. (1989). Relation between increasing methane and the presence of ice clouds at the mesopause. *Nature 338:*490 – 492.

Wilksch, P.A. (1975). Measurements of thermospheric temperatures and winds using a Fabry-Perot spectrometer. Ph. D. Thesis, University of Adelaide.

4. ABSOLUTE ORDER DETERMINATION OF MAWSON FABRY-PEROT SPECTROMETER

P.A. Greet [1, 2]

[1] Auroral and Space Physics
Antarctic Division
Kingston Tasmania 7050
Australia

[2] IASOS
University of Tasmania
Hobart Tasmania 7001
Australia

ABSTRACT

For analysis of high-resolution Fabry-Perot spectrometer (FPS) observations a number of calibrations are necessary. The order of interference, or separation of the etalon plates, must be known. This is usually done by recording a number of lines whose relative positions uniquely determine the order within a wide range of plate spacings. In February 1993 observations of the OH (6–2) $P_1(3)$ and $Q_1(2)$ lines commenced. These lines are in the near-infra-red. When trying to determine the order using lines in both the visible and near-infra-red allowance for the phase change on reflection was required to make all measurements give consistent results.

4.1 INTRODUCTION

For a Fabry-Perot etalon the order of interference at wavelength λ, plate separation t, angle of incidence θ, is given by

$$m = \frac{2t\cos\theta}{\lambda} + \frac{\phi}{\pi}$$

where ϕ is the phase change on reflection at each plate surface. For two wavelengths λ_1 and λ_2 at separation t'.

$$m_1\lambda_1 = 2t'\cos\theta + \lambda_1\frac{\phi_1}{\pi}$$

$$m_2\lambda_2 = 2t'\cos\theta + \lambda_2\frac{\phi_2}{\pi}$$

Thus providing the plate separation remains constant

$$m_1\lambda_1 - m_2\lambda_2 = \lambda_1\frac{\phi_1}{\pi} - \lambda_2\frac{\phi_2}{\pi}\ .$$

In the method of exact fractions, usually used to calculate the order, it is assumed that

$$m_1\lambda_1 - m_2\lambda_2 = 0$$

This is true if and only if

$$\lambda_1 \frac{\phi_1}{\pi} = \lambda_2 \frac{\phi_2}{\pi}$$

i.e. the phase change is inversely proportional to wavelength. Price (1983) notes 'An air gap can be thought of as introducing a phase change obeying such a relationship to a beam passing through it. Consequently, a phase change which is proportional to the wavenumber is indistinguishable from a change in the thickness of the air gap.'

The Mawson Fabry-Perot spectrometer has been used for observations in the visible region, λ 630 nm, λ 558 nm, and λ 589 nm. Modifications were made to the instrument to enable observations of the mesospheric OH (6–2) $P_1(3)$ and $Q_1(2)$ lines at near-infra-red (NIR)wavelengths, λ 843.01 nm. The instrument and calibrations required for data analysis are described in detail in Jacka (1984). To make a precise order determination for calculations of the Λ-doubling of the OH (6–2) lines (Greet et al. 1994) Fabry-Perot spectrometer (FPS) profiles at eleven different wavelengths were recorded. Scans of 256 channels covering at least one order were obtained and where the scan included two complete peaks calculations of the channels per order were made. All measurements were made when the instrument was stable and etalon drift was monitored by recording ^{198}Hg λ 546.0753 nm profiles after each filter change or at fifteen minute intervals. From the ^{198}Hg lamp λ 579.0660 and 576.960 nm lines were also recorded. These two lines are passed through the same filter and the correct assignation of wavelength was determined by the channels per order calculation on the line for which two peaks were covered in the scan range. A frequency stabilised HeNe laser at λ 632.8165 nm, a Neon line λ 630.4789 nm, and an Argon line at λ 842.4648 nm were also recorded. The following sky lines were recorded: oxygen λ 630.0311 and λ 557.7341 and hydroxyl, OH (6–2) $P_1(3)$ doublet λ 843.003/843.020 nm and $Q_1(2)$ doublet 834.460 (separation unknown thought to be a few picometers). Figure 1 shows most of the profiles required for order measurements on day of year (DOY) 051. Some of the profiles have been edited to remove incomplete peaks to enable analysis of peak position with routine programs. Measurements were made on several days but results are presented for DOY 051 as this is the only day to date on which calculations have been completed.

Using just the visible wavelengths, the program ABO developed by Mark Conde (personal communication) gave a value of 5.5781006 mm for the separation of the etalon plates (with a residual of 0.02 orders). This program uses the method of exact fractions and wavelengths are corrected for non-standard temperature and pressure. When the NIR wavelengths were incorporated the result was inconclusive. When the visible wavelengths were used to predict the position of the NIR lines the values obtained were far from those measured.

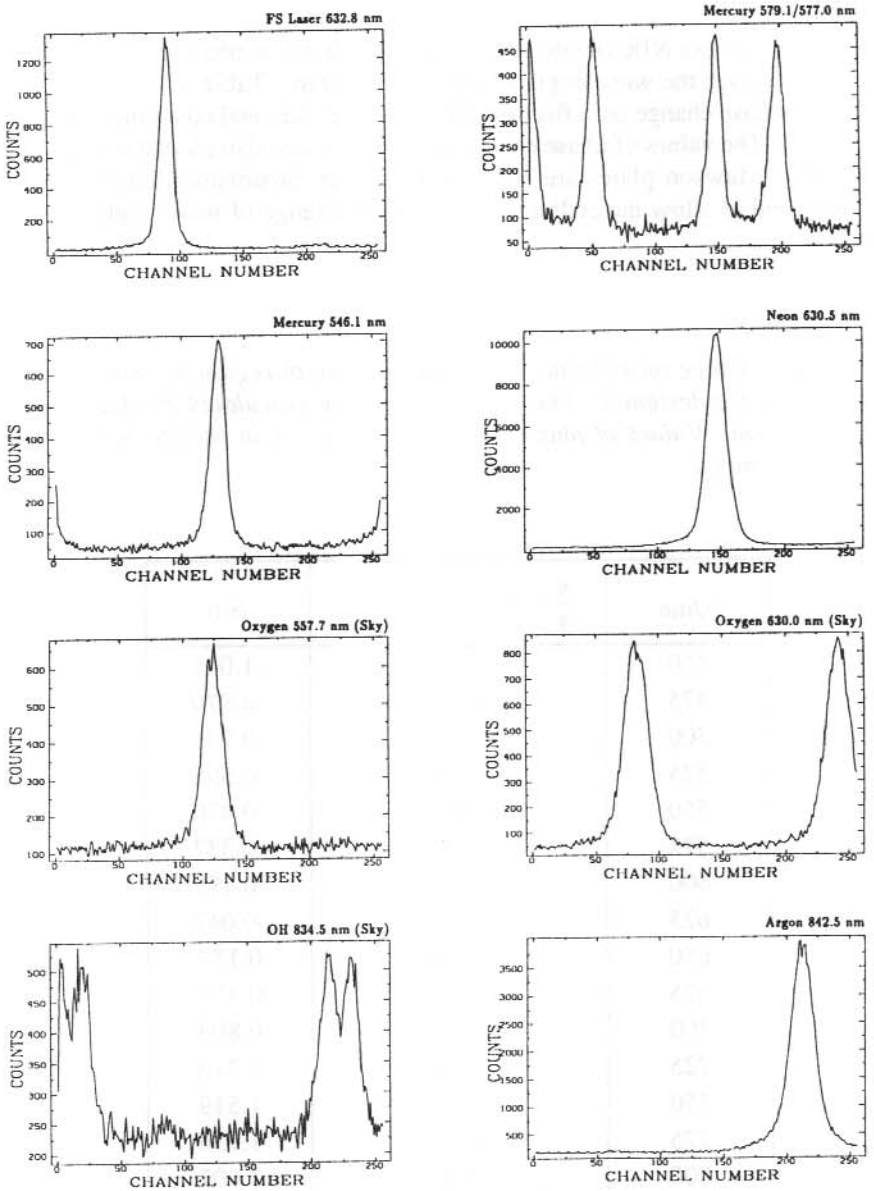

Figure 1. Eight of the profiles acquired for the order determination on DOY 051. The etalon was stable with time and the separation kept at the same value. Some profiles have been edited to remove partial peaks so that either the single profile or channels per order analysis program, which splits the profile and analyses two peaks, could be used to accurately determine the peak positions. The Mercury 579.1/577.0 profile was edited into two profiles one with two peaks and one with a single peak (the partially complete peak on the left was edited out). The scan range covers a whole order even at the longest wavelengths used.

4.2 PHASE CHANGE ON REFLECTION

It was thought that these NIR/visible discrepancies were due to phase change on reflection being non-linear over the wavelength range 630 – 830 nm. Table 1 lists the theoretical calculations of phase change on reflection, (R. Schaeffer, personal communication), for the Mawson plates. The values of phase change on reflection are also plotted in Figure 2. The coatings on the Mawson plates are soft, thirteen-layer, broadband dielectric reflective coatings designed to allow the etalon to be used over a range of wavelengths from 450 – 850 nm.

Table 1. Phase change on reflection over the wavelength region for which the Fabry-Perot coatings were designed. The values of Δm are calculated for later reference, using λ_1 = 631 nm. Values of phase change on reflection at specific wave lengths of interest are also noted.

λ/nm	$\frac{\phi}{\pi}$ radians per surface	Δm
450	0.976	-1.041
475	1.041	-0.870
500	1.079	-0.736
525	1.134	-0.595
550	1.180	-0.470
575	1.241	-0.337
600	1.314	-0.199
625	1.410	-0.042
650	1.550	0.154
675	1.771	0.427
700	2.105	0.809
725	2.465	1.213
750	2.729	1.519
775	2.907	1.736
800	3.042	1.907
825	3.164	2.064
850	3.299	2.231
557	1.1955	
558	1.1978	
630	1.433	
631	1.4382	
730	2.5504	
733	2.5619	

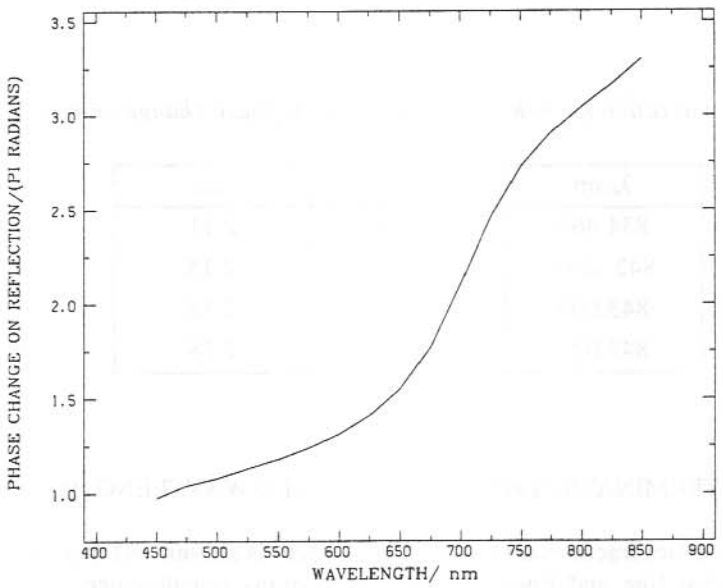

Figure 2. Manufacturer's theoretical calculations of phase change on reflection over the wavelength range of interest.

Thus when using one reference wavelength, λ_1, the order at a second wavelength is determined from the reference wavelength using:

$$m_2 = \frac{\phi_2}{\pi} - \frac{\lambda_1}{\lambda_2}\frac{\phi_1}{\pi} + \frac{\lambda_1}{\lambda_2} m_1$$

$$= \Delta m + \frac{\lambda_1}{\lambda_2} m_1$$

where $\Delta m = \frac{\phi_2}{\pi} - \frac{\lambda_1}{\lambda_2}\frac{\phi_1}{\pi}$

The term Δm can be thought of as the order correction due to phase change on reflection not being inversely proportional to wavelength. Over the wavelength range covered by the visible lines of interest, λ 546–632 nm the order correction is less than half an order. Over the wavelength range from 630–830 nm the order correction is greater than two. Table 2 gives the order correction, for the order as determined on DOY 051, using the theoretical

values of phase change on reflection, with 630/632 nm as the reference wavelength. These NIR wavelengths are predicted to be at least two whole orders different from that at λ 631 nm. So the method of exact fractions would not give adequate predictions of the position of the NIR peaks. The order correction does not vary significantly over this range of wavelengths.

Table 2. Order correction for NIR wavelengths due to phase change on reflection.

λ/nm	m	Δm
834.460	13369	2.11
842.4648	13242	2.18
843.003	13233	2.18
843.020	13235	2.18

4.3 ORDER DETERMINATION AT NEAR-INFRA-RED WAVELENGTHS

In the method of exact fractions a reference wavelength is chosen and then the fractional order between that line and lines at other wavelengths is calculated. This gives a measurement of the order. Knowing that phase change on reflection accounts for a small number of orders, say two, three, or four whole orders plus a fraction a measurement of the fractional order can be made assuming the order is that determined by the method of exact fractions ± 1...5. The measured fraction is determined from the channels per order and the position of the peak channel. The difference between the measured fraction and the calculated fraction is then a measure of the phase change on reflection. Plotting this as a function of (wavenumber)$^{-1}$ gives a straight line, as illustrated in Figure 3. The number of lines indicates the phase change on reflection for several orders either side of the order calculated from the visible lines by the method of exact fractions. This figure also plots the theoretical phase change on reflection, which indicates that the real order is 17626. Thus by allowing for the whole order changes due to phase change on reflection the correct order can be determined.

Using the method of exact fractions Figure 3 indicates that the order should be 17629. Allowing for the theoretical phase change on reflection the order should be 17626, i.e. three orders are due to phase change on reflection. This is equivalent to a change in plate separation of 1 x 10^{-6} m.

The calculations presented here are similar to those by Price (1983) who assessed the plates then in the Mt Torrens FPS. These plates had silver reflective coatings with two dielectric booster layers. Price (op. cit.) summarised 'The metal dielectric plates of the Mt Torrens interferometer introduce a phase change on reflection which departs only slightly from a linear relationship with wavenumber. Within the wavelength range λ 550 nm and λ 650 nm (i.e. wavenumber range 97000 cm^{-1} to 114000 cm^{-1} used when making airglow observations, this relationship is well maintained.' In our case the relationship is less linear

over the same wavelength range, λ 550 nm – λ 650 nm, and is definitely quite non-linear over the complete range of interest λ 550 nm – λ 850 nm.

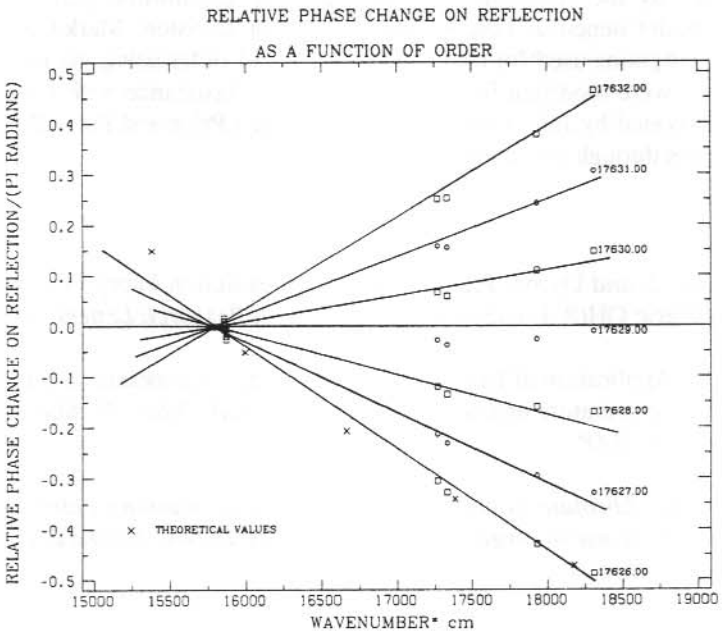

Figure 3. Relative phase change on reflection (pcor) as a function of (wavenumber)$^{-1}$. The values grouped around the horizontal line through zero indicate the pcor using the method of exact fractions to calculate the order. Assuming the order is some whole number of orders different to this, further calculations of phase change on reflection are indicated by the circles and squares. The crosses are the manufacturers specifications of pcor. This plot indicates that the order, at λ 632.816 nm is 17629 with three orders due to phase change on reflection.

4.4 CONCLUSIONS

Over the wavelength range of interest, λ 630 nm – λ 840 nm, phase change on reflection is not inversely proportional to wavelength. Thus when calculating the order the method of exact fractions cannot be used. Allowance must be made for phase change on reflection. Similarly, when predicting the position of lines in the NIR from positions of lines in the visible, phase change on reflection must be considered.

If a larger number of lines were available in the wavelength range λ 830 nm – λ 850 nm then the method of exact fractions could be used. The four lines we have are insufficient and not well spaced for an order calculation.

4.5 ACKNOWLEDGMENTS

This work was carried out as part of the Australian National Antarctic Research Expeditions and was funded by the Antarctic Science Advisory Committee grants Scheme, the Australian Research Council, and the Australian Antarctic Division. Mark Conde developed the computing programs used for routine calculations of order using the method of exact fractions. These were modified for the current work. Assistance with measurements at Mawson was provided by John Innis. Mark Conde, Gina Price and Peter Dyson provided comments at times through the development of ideas.

REFERENCES

Greet, P.A., Innis, J. *and* Dyson, P.L. (1994). High-resolution Fabry-Perot observations of mesospheric OH(8-3) emissions. *Geophysical Research Letters* (in press).

Jacka, F. (1984). Application of Fabry-Perot spectrometers for measurement of upper atmosphere temperature and winds. In: Vincent, R.A. (Ed.). *Middle Atmosphere Handbook for MAP*.

Price, G.D. (1983). *Absolute wavelength calibration of a scanning Fabry-Perot spectrometer for use in airglow studies*. Honours Thesis. University of Adelaide, Australia.

5. HIGH-RESOLUTION FABRY-PEROT OBSERVATIONS OF MESOSPHERIC OH (6–2) EMISSIONS

P.A. Greet [1, 2], J. Innis [1] and P.L. Dyson [3]

[1] Auroral and Space Physics
Antarctic Division
Kingston Tasmania 7050
Australia

[2] IASOS
University of Tasmania
Hobart Tasmania 7001
Australia

[3] La Trobe University
Bundoora Victoria 3083
Australia

ABSTRACT

Over the 1992/93 summer the Fabry-Perot spectrometer at Mawson, Antarctica was modified to permit observations of two lines in the OH (6–2) band near λ 840 nm. Preliminary observations were obtained on five nights in early February. Analysis of these lines, permiting estimates of mesospheric winds and temperatures, will be presented. Λ-doubling of OH (6–2) $Q_1(2)$ and $P_1(3)$ lines was measured to be 5.50 ±0.01 pm and 19.17 ±0.06 pm respectively. Future routine observing for study of mesospheric winds and temperatures is planned.

5.1 INTRODUCTION

The Mawson high-resolution Fabry-Perot spectrometer, FPS, has been used to study a number of airglow and auroral emissions, λ 630 nm oxygen emission from the thermosphere, λ 558 nm oxygen emission from the lower thermosphere, and λ 589 nm sodium emission from the mesopause region. In recent years interest in the mesosphere has increased as its coupling with the lower atmosphere has become better understood. Changes in mesospheric dynamics and thermodynamics will reflect changes in the troposphere. Techniques for ground-based measurements of mesospheric temperatures have only recently been developed.

This report presents preliminary measurements of the OH (6 – 2) $P_1(3)$ and $Q_1(2)$ doublets. The emission originates from a layer near 87 km with mean thickness of 12 km (Baker and Stair 1988). Several techniques have been used to study the emission. Imaging cameras integrate several bands to study gravity waves (e.g. Taylor et al. 1993). By measuring the relative intensity of at least two lines of a branch within a band the rotational temperature can be measured (reviewed by Sivjee 1992). Winds and temperatures are determined from

FPS measurements of the Doppler shift and width of single emission lines within an OH band (Rees et al. 1990, Hernandez et al. 1992).

The preliminary measurements reported here were made to determine if the Mawson and proposed Davis FPS's could be used in routine monitoring of mesospheric winds and temperatures.

5.2 INSTRUMENTATION

The Mawson high-resolution FPS has been described at length elsewhere (Jacka 1984). Some minor modifications were required for observations at the OH (6–2) wavelength, 830 – 850 nm. The region used for parallelism control was moved to slightly higher wavelengths. The S20 photocathode used for observations in the visible was replaced with a GaAs photocathode operating at -20°C with an average dark count of about 70 counts/sec. For the measurements described here the plate separation was 5.577148 mm. For the P doublet this gave an order of 13235, and for the Q doublet 13369.

Reflective finesse values, at λ 834 nm, $N_A = 38 \pm 2$ and at λ 843 nm, $N_A = 28 \pm 1$, were determined from transmission measurements. These gave results consistent with the manufacturers design (Schaeffer, personal communication). Ideally the reflective finesse at OH wavelengths should be measured and this will be done for future observations.

A frequency stabilized laser was used to determine the instrument function. Assuming the laser has an effective temperature of zero Kelvin, the Airy function at the laser wavelength is deconvolved from the recorded laser profile. This profile is then convolved with the Airy function at the observing wavelength. To determine the respective Airy functions the reflective finesse, order, and channels per order must be known. This technique is described by Jacka (1984) however using the λ 546.1 nm line of ^{198}Hg lamp described there led to misleading temperatures. It would appear that the effective operating temperature of the Hg lamp is somewhat higher than originally thought. This led to anomalously low temperatures from sky observations and negative widths for the frequency stabilized laser. Although the Hg lamp gives a useful wavelength reference further studies are required to determine the source function. Lamp profiles may be broadened by the Stark effect leading to apparent temperatures near 1400 K.

5.3 DATA AND ANALYSIS

Forty-two useful Q profiles and nine P profiles were obtained over five nights, 12–20 February 1993. The lines are not simple lines but doublets. Lambda, Λ, doubling of the emission lines, due to the nuclear spin of the molecule, must be considered. Figure 1 shows profiles obtained on DOY 051. The P branch profile was from a zenith angle of 80°. The Q branch profile was obtained looking in the zenith. Both profiles were from 200 scans of 128 channels with a dwell time of 50 ms per channel. Van Rijn correction factor to normalize the P branch intensities to the zenith is approximately four.

A similar procedure was used to analyse both P and Q doublet profiles. The profiles were fitted with the convolution of the sum of two Gaussians and the empirical instrument profile. Five parameters are fitted, one temperature, two peak positions, and two

intensities. The fitting is done in the Fourier transform domain and only those parts of the spectrum where the signal greatly exceeds the noise are used. Temperature and wind information are obtained from the fitted Gaussian curves. First estimates of the peak position are varied for P and Q doublet profiles. Figure 1 shows raw data and fitted profiles in the upper panel and residuals in the lower panel for both the P and Q doublets.

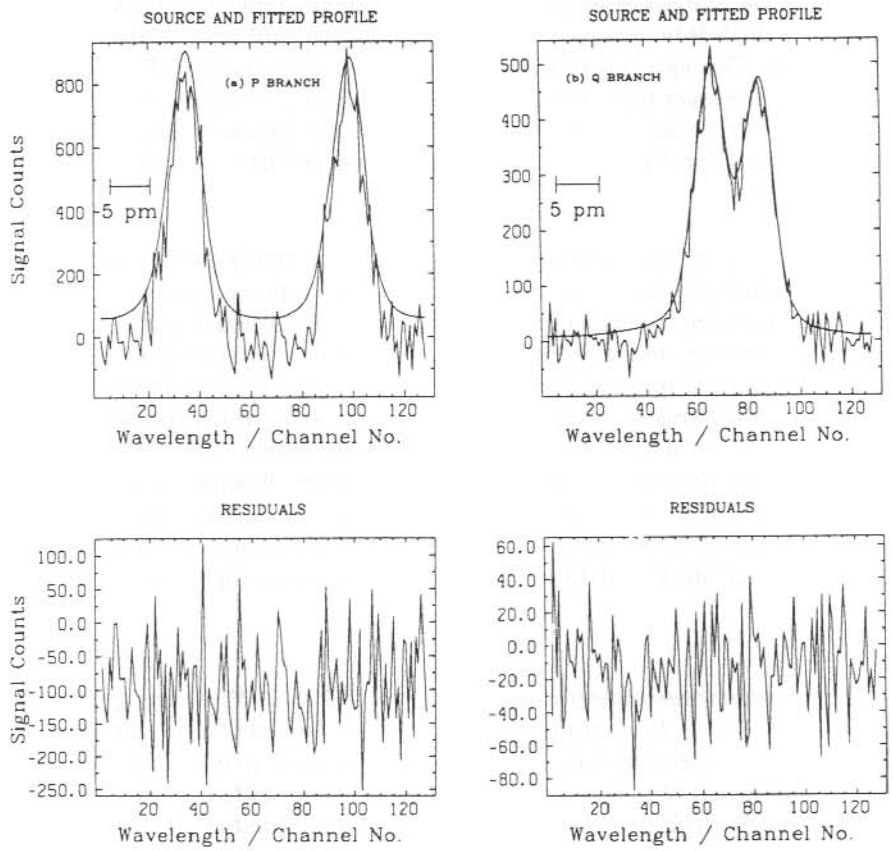

Figure 1. Raw data, fitted profiles, and residuals for (a) OH (6–2) $P_1(3)$ doublet and (b) OH (6–2) $Q_1(2)$ doublet. The fitting is done in the Fourier transform domain. These profiles, obtained at 1800 UT (P) and 1925 UT (Q), had the same temperature 124 K. The Q profile was obtained in the zenith and the P profile at a zenith angle of 80°, azimuth 0°.

To compare instrument throughput at the two wavelengths (λ 834.46 nm and λ 843.01 nm) a white light spectrum was scanned. This assumes the filter profiles are identical and the light output is the same at the two wavelengths. To a first approximation these assumptions are valid. The white light throughput for the λ 834 nm filter is 0.87 times the throughput for the λ 843 nm filter. Thus for emission lines of similar intensity a profile of approximately 1.1 times the duration would be required for the λ 834 nm filter to obtain similar signal-to-noise ratios. That, on average, acquire times for the P doublet were

three times longer than for the Q doublet, for similar observing zenith angles, shows that the P doublet is significantly less intense than the Q doublet. The time required to collect P doublet profiles with this instrument makes them of only marginal use for determining mesospheric winds and temperatures.

As the Λ-doubling for the $Q_1(2)$ line was not known it was necessary to fit two peak positions. From the analysis of the profiles obtained a measurement of the Λ-doubling can be made. From the 9 P branch profiles the mean and standard error of the separation is 19.17 ± 0.06 pm. This agrees well with the value from calculations by Coxon and Foster (1982), 19.2 pm; however their observed value was slightly different, 17.2 pm. For the Q doublet Coxon and Foster (1982) do not provide calculations or observations of the Λ-doubling. From 41 profiles we obtain a measurement of OH (6 – 2) $Q_1(2)$ Λ-doubling of 5.50 ± 0.01 pm.

There are two difficulties in comparing temperatures from P and Q doublet profiles. As the P doublet is considerably less intense the signal-to-noise ratio is lower and two or more profiles must be averaged to obtain reliable temperatures. The P and Q profiles are obtained consecutively rather than simultaneously thus temporal variation in temperature, due to for example gravity waves, must be considered. The values of mesospheric temperature obtained from the observations are summarised in Table 1 which lists the number of profiles and the mean of the temperatures, $\overline{T}$, and the mean uncertainty, $\overline{err}$ in the temperature from the fit, determined from the set of profiles obtained each night. For the P branch, the values in the T column were obtained by adding all P profiles for each night, shifting each profile to allow for instrument drift, and analysing the combined profile. Agreement between the P and Q temperatures on any one night can be considered reasonable.

Table 1. Daily mean temperatures determined from OH (6–2) $P_1(3)$ and $Q_1(2)$ profiles. $\overline{T}$ is the mean of the n individual temperatures obtained on each day. $\overline{err}$ is the mean of the error in the temperature fit for each profile. As the P profile had low signal-to-noise ratios, and hence very high errors, the profiles were added, shifting each one to allow for instrument drift, and then analysed to give the T and error in columns three and four.

DOY	P doublet						Q doublet			
	n	T	err	$\overline{T}$	s.d.	$\overline{err}$	n	$\overline{T}$	s.d.	$\overline{err}$
044							9	156	19	23
045	3	178	36	174	14	63				
046	2	190	39	295	40	62	8	203	26	19
050	3	258	16	270	12	30	6	215	22	16
051	1	124	42				17	163	24	18

Only on the night of 20 February was the data appropriate for wind determinations. On that night three hours of cardinal point observations of the Q doublet were obtained at a zenith angle of 60°. Useful profiles were obtained in 12 minutes. Zonal and meridional winds were determined by assuming that the average vertical velocity was zero. Velocities between 0 and 50 ms^{-1} were obtained which are typical values for mesospheric winds. Routine observations using the Q branch should allow useful wind data to be obtained and in the future comparisons with the spaced antenna medium frequency radar at Davis will be made.

5.4 CONCLUSIONS

Preliminary FPS observations of the OH (6–2) $Q_1(2)$ and $P_1(3)$ have been made at Mawson. From observations on five short nights nine P branch and 41 Q branch profiles were obtained. The results show that mesospheric temperatures can be derived from both the $P_1(3)$ and $Q_1(2)$ profiles even though the $Q_1(2)$ doublet is not completely resolved. The $Q_1(2)$ profile, not previously studied, is considerably more intense than the $P_1(3)$ profile and therefore will provide more useful data in the routine observing campaign proposed for Davis station (68.6° S, 78.0° E) in 1994. An instrument similar to that at Mawson will be used.

Measurements of the Λ-doubling gave values in agreement with those published for the $P_1(3)$ line, 19.17 ± 0.06 pm. The $Q_1(2)$ Λ-doubling was measured to be 5.50 ± 0.01 pm.

5.5 ACKNOWLEDGMENTS

This work was carried out as part of the Australian National Antarctic Research Expeditions and was partly funded by the Antarctic Science Advisory Committee grants scheme and the Australian Research Council. Support by the Australian Antarctic Division and in particular the Auroral and Space Physics engineer at Mawson, was appreciated.

REFERENCES

Baker, D.J. *and* Stair, A.T. (1988). Rocket measurements of the altitude distributions of the hydroxyl airglow. *Physica Scripta 37*:611–622.

Coxon, J.A. *and* Foster, S.C. (1982). Rotational analysis of hydroxyl vibration-rotation emission bands: Molecular constants for OH $X^2\Pi$, $6 \leq v \leq 10$. *Canadian Journal of Physics 60*:41–48.

Hernandez, G., Smith, R.W. *and* Conner, J.F. (1992). Neutral wind and temperature in the upper mesosphere above South Pole, Antarctica. *Geophysics Research Letters 19*:53–56.

Jacka, F. (1984). Application of Fabry-Perot spectrometers for measurement of upper atmosphere temperature and winds. In: Vincent, R.A. (Ed.). *Middle Atmosphere Handbook for MAP*.

Rees, D., Aruliah, A., Fuller-Rowell, T.J., Wickwar, V.B. *and* Sica, R.J. (1990). Winds in the upper mesosphere at mid-latitude: First results using an imaging Fabry-Perot Interferometer. *Geophysics Research Letters 17*:1259 – 1261.

Sivjee, G.G. (1992). Airglow hydroxyl emissions. *Planetary and Space Science 40*: 235 – 242.

Taylor, M.J., Ryan, E.H., Tuan, T.F. *and* Edwards, R. (1993). Evidence of preferential directions for gravity wave propagation due to wind filtering in the middle atmosphere. *Journal of Geophysics Research 98*:6047 – 6057.

6. INVESTIGATION OF THE O(^{1}S) EXCITATION PROCESS IN PULSATING AURORA USING A GROUND-BASED PHOTOMETER

A.R. Klekociuk and G.B. Burns

Auroral and Space Physics
Antarctic Division
Kingston Tasmania 7050
Australia

ABSTRACT

The O(^{1}S) excitation process is investigated using maximum-entropy impulse response analysis applied to 0.05 s time resolution photometric measurements of λ 427.8 nm N_2^+ (1NG) (0, 1) and λ 557.7 nm O(^{1}S – ^{1}D) emissions during pulsating aurora. Previous workers have used similar analysis techniques to infer the effective lifetime of the O(^{1}S) state and the existence of, and percentage contribution from, an indirect excitation process. However, the parameters returned by impulse response analysis may be biased by two effects. Firstly, random 'noise' associated with the measurement process may lead to over-estimation of both the fraction of the O(^{1}S) population inferred as being indirectly excited, and the effective lifetime attributed to the intermediary species of the indirect process. Secondly, the inherent non-linearity between the O(^{1}S – ^{1}D) and N_2^+ (1NG) intensities of pulsating aurora may lead to the over-estimation of the O(^{1}S) effective lifetime.

We have developed a method of data selection to minimise the biases introduced by noise and non-linearity in the study of the indirect excitation model. By using synthetic time-series based on observed data, we demonstrate that non-linearity is not a significant source of bias in our analysis. Importantly, after accounting for the influence of noise, we infer that indirect excitation accounts for between 30% and 50% of O(^{1}S) production, compared with values of between 50% to 100% obtained by previous workers.

Using calibrated measurements not influenced by scattered light from clouds or the moon, we show that the O(^{1}S) effective lifetime is correlated with the mean O(^{1}S – ^{1}D) to N_2^+ (1NG) (0, 1) emission intensity ratio of pulsating aurora. From this relationship, we infer that at least ~25%, and perhaps more typically ~55%, of the variation in the mean O(^{1}S – ^{1}D) to N_2^+ (1NG) (0, 1) emission intensity ratio during auroral pulsations is dependent on increased collisional quenching associated with the higher energy of the incident electrons.

6.1 INTRODUCTION

Excitation of the O(^{1}S) state in the auroral atmosphere takes place predominantly in the lower thermosphere, at altitudes near 100 km. The excitation process is primarily driven by the precipitation of magnetospheric electrons. However, the details of the mechanism are still to be conclusively defined, despite more than three decades of effort. Clarification of this problem would assist in efforts to remotely measure the energy spectrum of precipitating auroral electrons, and the concentration of constituent species in the upper atmosphere.

Several workers have examined the $O(^1S)$ excitation process using data from ground-based multi-channel photometers. The aim of these studies has been to infer the $O(^1S)$ 'impulse response function'; that is, the response in $O(^1S)$ production to an 'instantaneous' change in the flux of precipitating auroral electrons. The fundamental relation used in this approach is;

$$I_O(T) = I_N(T) * h(t) \qquad (1)$$

Here the $O(^1S)$ impulse response function, h(t), is a causal (i.e. $t \geq 0$) linear filter which relates $I_O(T)$, the intensity of λ 557.7 nm $O(^1S - {}^1D)$ 'green line' emission (measured as a function of time T), to $I_N(T)$, the intensity of the N_2^+ (1NG) band emission system. The convolution operator is denoted by '*'. This relation makes use of the widely held premise that the intensity of the N_2^+ (1NG) band system is directly related to the total energy deposited in the atmosphere by auroral electrons.

Impulse response analysis has provided evidence that the $O(^1S)$ state is created by direct and indirect excitation processes (see, for example; Brekke and Pettersen 1972, Brekke 1973, Burns and Reid 1984, Paulson et al. 1990, Shepherd et al. 1991, Klekociuk and Burns 1994). Indirect excitation has been attributed to the production of between 50% and 100% of the $O(^1S)$ population (Burns and Reid 1984, Paulson et al. 1990). The impact of directly excited $N_2(A^3\Sigma_u^+)$ (Shepherd et al. 1991) and O_2^* (Solheim and Llewellyn 1979) on atomic oxygen, and the dissociative recombination of O_2^+ (Bates and Zipf 1980) are currently considered as viable indirect excitation processes, although their relative significance is yet to be conclusively demonstrated. Direct excitation is attributed to electron impact on atomic oxygen (Rees et al. 1967, 1969, Donahue et al. 1968, Zipf and McLaughlin 1978).

If the rate of indirect excitation is proportional to the concentration of an intermediary species, and the rate of production of the intermediary species and $O(^1S)$ direct excitation are proportional to the intensity of the N_2^+ (1NG) band system, then

$$h(t) = A\, e^{-t/\tau} - B\, e^{-t/\tau'} \qquad (2)$$

where A and B are constants, τ is the 'effective lifetime' of the $O(^1S)$ state, and τ' is the 'effective lifetime' of the intermediary species (Parkinson 1971, Henriksen 1973, 1974, Burns and Reid 1984, Burns and Reid 1985). The observable or 'effective' lifetime of an excited state in the atmosphere is expected to be shorter than its theoretical free-space value due to collisional deactivation.

The two terms in equation (2) describe the direct and indirect excitation processes, respectively. If the $O(^1S)$ state is solely directly excited, then $B = 0$. The percentage contribution of the indirect processes to $O(^1S)$ excitation is given by

$$P = \frac{B(\tau - \tau')}{A\tau - B\tau'} \cdot 100\% \qquad (3)$$

(Burns and Reid 1984).

The theoretical free-space radiative lifetime of the $O(^1S)$ state is approximately 0.8 s (Nicolaides et al. 1971). The range of observed $O(^1S)$ effective lifetimes are consistent with an upper limit near the theoretical free-space value (Burns and Reid 1984, Paulson et al. 1990). The average effective lifetime of the metastable species taking part in the indirect excitation process is approximately 0.1 s (Burns and Reid 1984, Burns and Reid 1985, Paulson et al. 1990).

Methods for deconvolving h(t) from observational data have been provided for the time domain (Burns and Reid 1984) and the frequency domain (Shepherd and Paulson 1965, Brekke and Pettersen 1972, Paulson et al. 1990). These methods are best suited to time series for which variations in amplitude on time-scales less than the effective lifetimes to be estimated are significantly larger than the corresponding measurement errors. Observations of pulsating aurora best meet this requirement.

The central assumption in equation (1) is that h(t) is invariant over the measurement interval T; that is, the associated time series are linearly related. Two processes associated with electron energy variation during auroral pulsations are known to produce a non-linearity in the relationship between the $O(^1S - {}^1D)$ and N_2^+ (1NG) intensities. Firstly, the characteristic energy of the precipitating electrons increases between the 'off' and 'on' states of auroral pulsations (McEwen et al. 1981). Secondly, velocity dispersion along the path from the equatorial location of the electron modulation region causes the highest energy electrons associated with a pulsation to arrive at the atmosphere first (Johnstone 1983). These effects result in the general decrease of the $O(^1S - {}^1D)$ to N_2^+ (1NG) column integrated intensity ratio that is seen to accompany an increase in energy of the precipitating electrons (Gerdjikova and Shepherd 1987, Steele and McEwen 1990), at least for mean electron energies near 1 keV.

Burns and Reid (1984) have examined the influence of non-linearity and random measurement 'noise' on $O(^1S)$ impulse response analysis in the time domain. Using synthetic $O(^1S - {}^1D)$ and N_2^+ (1NG) time series based on observed data, they have shown that non-linearity may result in the under-estimation of the $O(^1S)$ effective lifetime, and that noise may produce a signature in the recovered impulse response function that mimics the response expected from an indirect excitation process. Burns and Reid (1984) went on to develop a method of data selection to order to minimise the influence of non-linearity and noise on their estimates of the $O(^1S)$ excitation model parameters.

In this paper, we extend the work of Burns and Reid (1984) in the investigation of the $O(^1S)$ excitation mechanism. Firstly, we describe a method of data selection, developed in the spirit of the approach adopted by Burns and Reid (1984), that minimises the biases introduced by noise and non-linearity in the study of the indirect excitation model. We find that the distribution of $O(^1S)$ effective lifetime obtained from the selected data is consistent with findings of Burns and Reid (1984). Using absolutely calibrated data that are not influenced by scattered light from clouds or the moon, we provide a method to conveniently estimate the mean $O(^1S - {}^1D)$ to N_2^+ (1NG) (0, 1) intensity ratio during auroral pulsations. We show that the intensity ratio is correlated with the $O(^1S)$ effective lifetime. We use this relationship to infer that part of the variation in the intensity ratio during pulsating aurora is dependent on increased collisional quenching associated with the higher energy of the incident electrons.

By using synthetic time-series based on observed data, we demonstrate that non-linearity is not a significant source of bias in our analysis. Importantly, we further confirm the existence of an indirect excitation process, but show that its true contribution may be significantly over-estimated if the influence of measurement noise is not taken into consideration.

6.2 ANALYSIS

6.2.1 *Data collection and calibration*

The instrumentation and data reduction methods have previously been reported by Klekociuk and Burns (1992A, 1992B, 1994). Briefly, a dual-channel beam-splitting photometer viewing a 1° diameter field centred on the magnetic zenith was operated at Macquarie Island (geographic coordinates 54.5°S, 159.0°E; magnetic latitude 64.3°S) between May 1988, and February 1989. The photometer was operated in 'pulse counting' mode, and obtained simultaneous digital intensity time-series of the λ 5 57.7 nm O(^{1}S–^{1}D) line and the λ 427.8 nm N_2^+ (1NG) (0, 1) band with a sampling resolution of 0.05 s during periods of rapidly fluctuating auroral intensities. Data obtained during each five minute interval were stored by a computer in separate files for each channel. The data were collected and analysed in five minute segments as this time-scale allowed impulse responses of suitable 'signal-to-noise' ratio to be recovered, while at the same time providing an adequately short time resolution to investigate the stability of the inferred parameters of the excitation process.

Individual data samples were corrected for 'pulse pile-up' and 'dark count', and then converted to an inferred incident column emission intensity in Rayleighs (R). The latter step used measurements of the combined transmission of the beam-splitter and filter of each channel as a function of wavelength, and intensity calibrations using a standard lamp. The fraction of the N_2^+ (1NG) (0, 1) band detected by the photometer was evaluated by convolving a 300 K synthetic emission spectrum (supplied by Dr. Dick Gattinger of the National Research Council, Ottawa) with the measured channel transmission profile. The calibration calculations also made allowance for the transmission of the window above the photometer. The inferred absolute intensities have not been corrected for atmospheric scattering and extinction (except where noted), or the van Rhijn effect. The latter is negligible as the zenith angle of the photometer was only 12°.

6.2.2 *Data reduction and selection*

A total of 1389 pairs of five minute duration data sequences, for which the maximum corrected pulse frequency in each channel was less than 10 MHz (the upper limit of the 'pulse pile-up' correction), were retained for analysis. The estimator of the O(^{1}S) impulse response function, h(t) in equation (1), was calculated with 0.05 s resolution over the interval $-2 \text{ s} \leq t < 8$ s for each data sequence, using the method described by Burns and Reid (1984).

The choice of 'window' for h(t) provided adequate acausal (i.e. $t < 0$) and causal intervals for the examination of the influence of 'noise', and the estimation of the time-constants in equation (2), respectively. As shown by Burns and Reid (1984), independent random

noise in the $I_O(T)$ and $I_N(T)$ time-series causes a 'rounding' in the recovered the impulse function near $t = 0$ (i.e. some of the area under the impulse function is redistributed from the causal to the acausal domain). Non-linearity between the time-series influences primarily the estimation of the $O(^1S)$ effective lifetime and increases the magnitude of the first and last bins of the impulse function.

Each impulse function was scaled to have unit area between (but not including) the first and last bins. This normalisation allowed the comparison of parameters that were subsequently used to measure the influence of noise and non-linearity on the impulse responses. A double exponential function of the form given by equation (2) was fitted with uniform weighting to each scaled impulse response by a generalised non-linear least-squares technique (Bevington 1969) over the interval $0.05 \text{ s} \leq t \leq 2 \text{ s}$. The rational behind the choice of fitting interval is provided by Klekociuk and Burns (1994). The $t = 0$ point was not included in the fits as its amplitude is modified from the double-exponential model by the discrete nature of the sampling (Burns 1983). A model fit was deemed to have converged if the χ^2 parameter from successive iterations differed by less than an arbitrary value ε, chosen as the smallest value of the decadal increments between 10^{-6} and 10^{-10} inclusive. All of the 117 impulse functions that failed the fitting convergence test exhibited a very low 'signal-to-noise' ratio, and significant rounding near $t = 0$ (i.e. the lack of convergence did not result from the attempt to fit a model with two exponential terms where fitting only one term may have sufficed).

6.2.3 *Data selection*

A set of parameters were obtained to characterise each recovered impulse function and its model fit. A series of correlation analyses were performed on the entire parameter set, irrespective of the influence of cloud or moonlight on the measurements. This enabled a set of parameters to be chosen that, when suitably restricted, selected impulse functions minimally influenced by noise and non-linearity. The parameter restriction were performed until there was no significant change in the distribution of the $O(^1S)$ effective lifetime τ. A stable distribution of τ was achieved using the following restrictions;

- $\delta\tau \leq 0.025$ s — the one-sigma standard error in τ
- $\Sigma_n \leq 0.4 \text{ s}^{-1}$ — the magnitude of the sum of the five impulse response amplitudes immediately prior to $t = 0$
- $\Sigma_{n-1} \leq 0.65 \text{ s}^{-1}$ — the summed magnitudes of the first and last impulse response amplitudes corrected for noise

The parameters $\delta\tau$ and Σ_n protect against the effects of noise, while Σ_{n-1} protects against non-linearity. The method used in the calculation of Σ_{n-1} is provided by Klekociuk and Burns (1994).

We retained 71 of the 127 impulse responses selected by this approach that were recovered from clear-sky and moon-free observing conditions. The distribution of the $O(^1S)$ effective lifetime obtained from these 'τ-set' impulse responses is shown in Figure 1. The distribution has a sharp upper cut-off near the theoretical free-space radiative lifetime (0.8 s), consistent with the findings of Burns and Reid (1984, 1985). It should be noted

that the τ distribution is 'smeared' somewhat by the statistical uncertainty of the individual estimates. The distribution has a mean of 0.71 s, and a standard deviation of 0.05 s. As explained by Klekociuk and Burns (1994), the choice of limit on Σ_{n-1} ensured that the distribution in Figure 1 is not significantly biased to lower values of τ by non-linear effects associated primarily with electron energy variation during auroral pulsations.

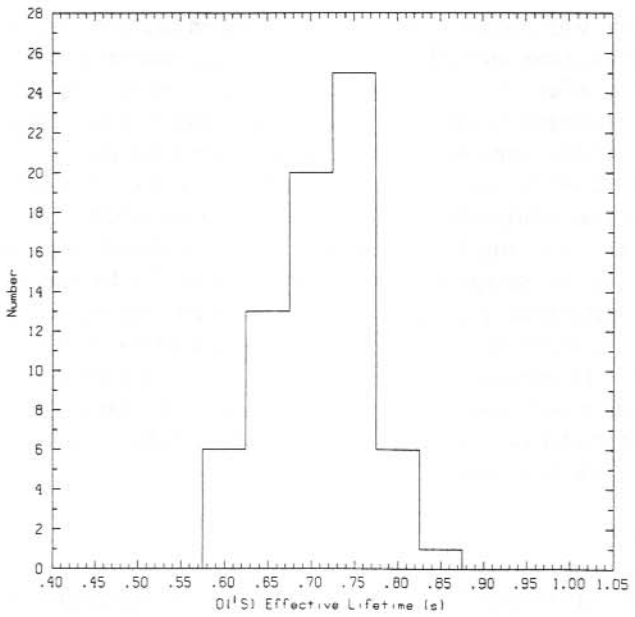

Figure 1. Distribution of the inferred $O(^1S)$ effective lifetime for 71 selected 5-minute intervals of pulsating aurora. The 2σ standard error on the estimates is typically ± 0.04. The bin width is 0.05 s.

The estimates of the indirect effective lifetime (τ') obtained from the τ-set impulse responses exhibited a weak correlation with h(-0.05), the amplitude of the t = -0.05 s point, and δh(0), the magnitude of the difference between the t = 0 point and the fitted value of the t = 0 point corrected for sampling. This behaviour indicated the need to restrict these parameters in order to select those impulse functions with a low level of 'rounding' due to noise, thereby obtaining adequately unbiased estimates of τ'. The following additional restrictions removed any significant parameter correlations with τ', and resulted in the selection of 22 events (which we refer to as the 'τ'-set');

- $\delta\tau' \leq 0.015$ s the one-sigma standard error in τ'
- h(-0.05) ≤ 0.17 s^{-1}
- δh(0) ≤ 0.5 s^{-1}

Here the parameter $\delta\tau'$ also protects against the effects of noise. We examined the impulse responses rejected on the basis of the δh(0) limit to ensure that none failed selection because of the inability to fit sensible parameters to the indirect excitation term of the model; that is,

we ensured that impulse responses were not rejected because they resulted from purely direct excitation.

The τ' distribution, as shown in Figure 2, is significantly broader relative to the mean value than is the τ distribution, even when consideration is made of the 'smearing' due to statistical uncertainty. The distribution has a mean of 0.10 s and a standard deviation of 0.03 s.

The distribution of the percentage contribution of the inferred indirect process, P, calculated using equation (3), for τ'-set is presented in Figure 3. One impulse response yielded a P of 115%. This value was arbitrarily set to 100%, and included in the bin centred on 95% in the distribution. The mean of the distribution is 75% with a 2σ standard error of 40%.

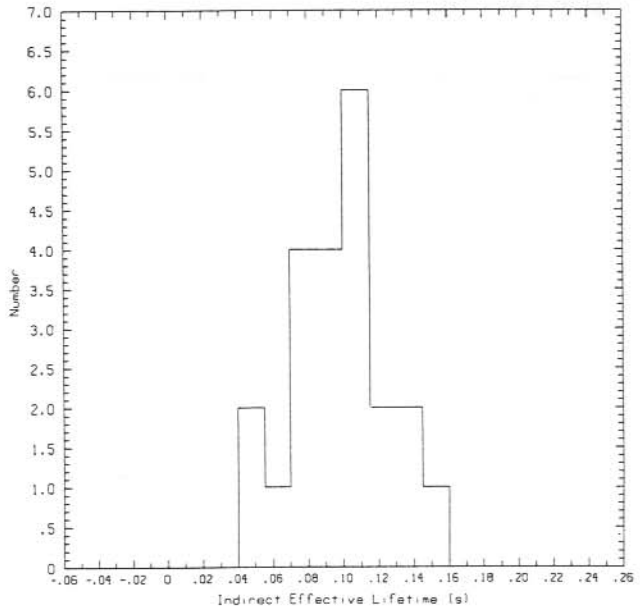

Figure 2. Distribution of the effective lifetime of the inferred indirect O(^{1}S) excitation process for 22 selected 5-minute intervals of pulsating aurora. The 2σ standard error on the estimates is typically ±0.02 s. The bin width is 0.015 s.

6.3 THE VARIATION OF O(^{1}S) EFFECTIVE LIFETIME WITH 557.7 NM TO 427.8 NM INTENSITY RATIO

We were motivated to compare the O(^{1}S) effective lifetime with the 557.7 nm to 427.8 nm intensity ratio, because the latter exhibits a weak negative correlation with mean electron energy during auroral pulsations (see, for example, McEwen et al. 1981). A suitable definition of the 557.7 nm to 427.8 nm intensity ratio is

$$R(T) = \text{'I(557.7)/I(427.8)'} = \frac{I_O(T+\delta T) - I_{OA}}{I_N(T) - I_{NB}} \qquad (4)$$

where I_{OA} and I_{NB} are the inferred 557.7 nm 'airglow plus background' and 427.8 nm 'background' intensities, respectively, and δT is a time lag which accounts for the delay introduced by the $O(^1S)$ effective lifetime. Here, δT may be conveniently represented as the lag of the maximum cross-correlation of the 557.7 nm time-series relative to the 427.8 nm time-series.

Figure 4 shows the negative correlation between R(T) and the 427.8 nm intensity that is typical of auroral pulsations. In order to calculate R(T), values of I_{OA} and I_{NB} were evaluated from clear sky observations when auroral activity was absent. The value of I_{NB} adopted was 60 R-equivalent. This corresponds to a continuum spectral radiant intensity of ~120 Rnm^{-1}, considerably higher than the ~ 10 Rnm^{-1} expected for the night sky based on data in Allen (1963). The discrepancy is attributed to the contribution from local light sources. Estimates of I_{OA} varied from day-to-day, and ranged between 84 R and 210 R. The value used for Figure 4 was 210 R.

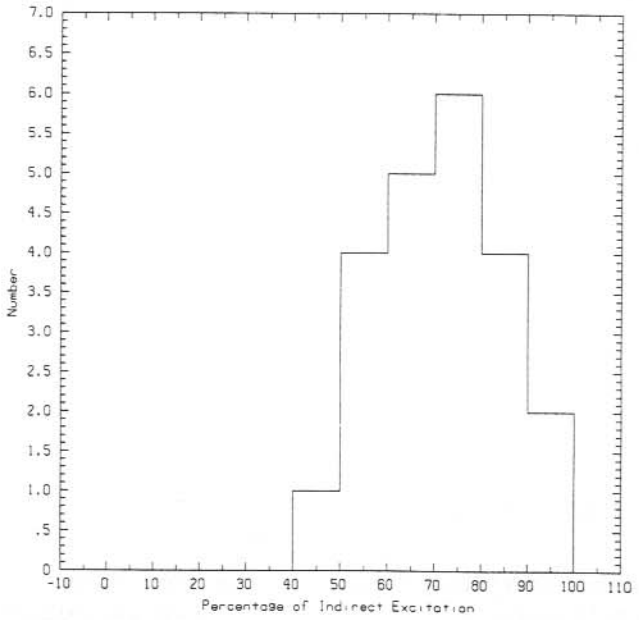

Figure 3. Distribution of the percentage of $O(^1S - ^1D)$ emission due to the inferred indirect excitation process for 22 selected 5-minute intervals of pulsating aurora. The 2σ standard error on the estimates is typically ±40%. The bin centred on 95% has been augmented by one event for which the percentage of indirect excitation was originally estimated as 116%. The bin width is 10%.

As can be seen from Figure 4, the value of the intensity ratio ascribable to the 'fluctuating' component of the auroral activity is difficult to quantify, particularly given the arbitrary nature of equation (4). A more suitable estimator of the mean intensity ratio associated with the fluctuations in the 557.7 nm and 427.8 nm time-series is R_I, the area under the

associated impulse response function. The evaluation of this estimator does not require knowledge of the background intensities, nor the relative phase difference between the time-series.

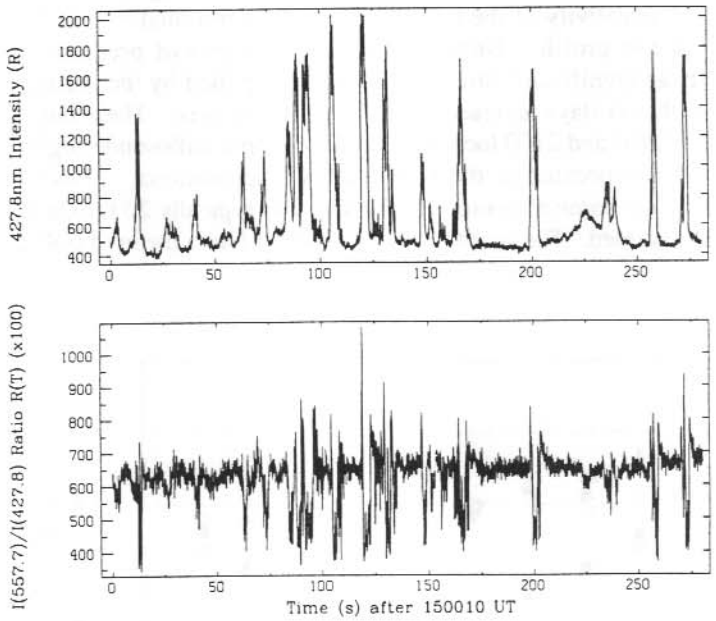

Figure 4. The intensity time-series of 427.8 nm emission (without the background contribution removed) and the corresponding I(557.7 nm)/I(427.8 nm) intensity ratio R(T) (calculated using equation (4)) for 12 July 1988, 1500-1505 UT. No correction has been made for the effects of atmospheric scattering.

Twenty of the intervals represented in the τ'-set consisted of well-defined pulsations on a relatively constant background. For each of these, we calculated R_I, the mean and mode of R(T), and estimated 'by eye' (where possible) the mean value of R(T) at the pulse 'on' and 'off' phases. These values are plotted as a function of the mean 427.8 nm intensity (corrected for background) in Figure 5. It can be seen that R_I provides a reasonable measure of the mean intensity ratio of the pulsating auroral emissions across a broad range of mean 427.8 nm intensity, particularly above ~400 R. At low emission intensities, errors associated with the choice of appropriate background and airglow intensities are regard as producing the relatively large scatter in the estimators based on R(T).

The processes of absorption and scattering in the atmosphere are wavelength-dependent, and effectively remove more blue auroral photons than green from the field-of-view of the photometer. An estimator for R_I which corrects for the presence of the intervening atmosphere may be defined as

$$R_I^* = f_t R_I$$

where f_t is the ratio of the atmospheric transmission at 428 nm to that at 558 nm between the photometer and the altitude of the auroral emission. Using the LOWTRAN7 atmospheric transmission model (Kneizys et al. 1988) for maritime conditions with background stratospheric aerosol content and a 12° zenith angle, we obtained $f_t \cong 0.83$. We examined the sensitivity of the transmission values returned by LOWTRAN7 on the assumed atmospheric profile. Unpublished measurements of pressure, dew-point and relative humidity at 'significant' altitude levels were supplied by the Australian Bureau of Meteorology for the six days represented in the τ'-set intervals. These data were obtained from twice-daily (0900 and 2100 local time) balloon-borne radiosonde flights at Macquarie Island and were incorporated in the LOWTRAN7 calculations. Above the maximum altitude of the balloon-borne measurements (which was typically 20 km), a maritime model atmosphere was assumed. The set of f_t values obtained had a mean of 0.83 and a standard deviation of 0.02.

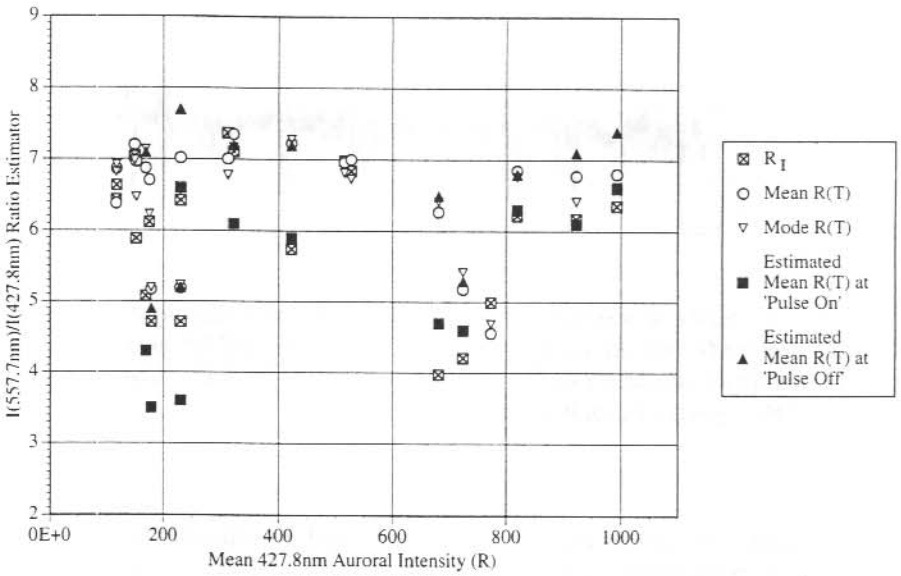

Figure 5. Comparison of estimators of the I(557.7 nm)/I(427.8 nm) intensity ratio as a function of mean auroral 427.8 nm intensity for 20 selected 5-minute measurement intervals. No correction has been made for the effects of atmospheric scattering.

A limitation in using LOWTRAN7 to estimate f_t is that the influence of scattering into the field-of-view of the photometer from the surrounding sky is not calculated. This problem was examined by Dr. Denis O'Brien of the CSIRO Division of Atmospheric Research (Melbourne) who evaluated f_t using a Monte Carlo simulation of multiple scattering (O'Brien 1992) in the case where the photometer observes an isotropic emitting layer through a standard atmosphere. For a ground albedo of zero, $f_t \cong 0.94$, indicating that blue photons are preferentially scattered into the field-of-view from the surrounding sky. For real observing conditions, the distribution of auroral emission near the field-of-view will be

inhomogeneous. We conclude that f_t obtained from the LOWTRAN7 calculations is likely to be a reasonable lower limit.

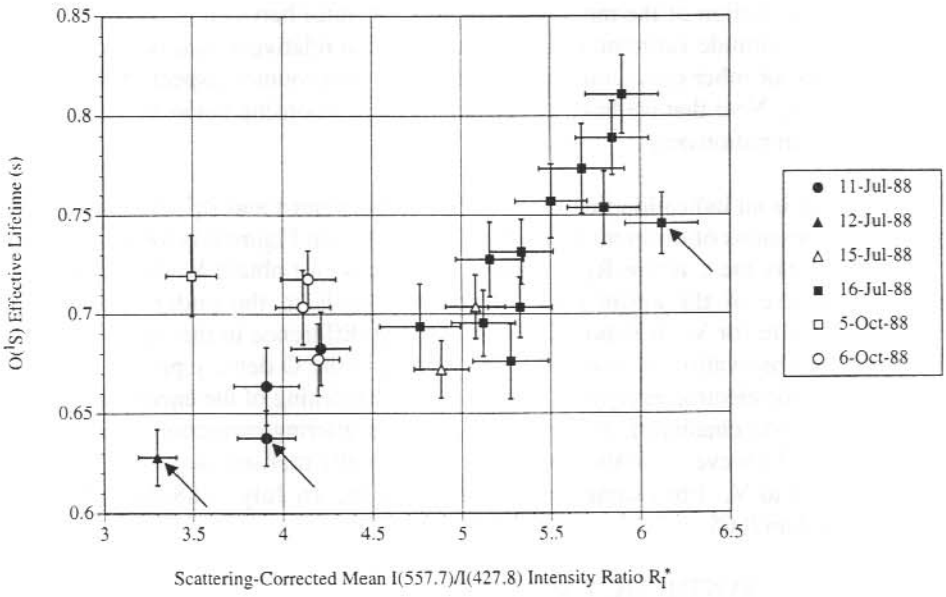

Figure 6. The variation of $O(^1S)$ effective lifetime τ with the mean scattering-corrected I(557.7 nm)/I(427.8 nm) intensity ratio estimator R_I^* (calculated for f_s=0.83) for 22 selected 5-minute intervals. The arrowed estimates are those selected in the τ'-set for which τ is possibly slightly over-estimated owing to the positive non-zero mean of the associated impulse response tail residuals in the interval 2.0 s < t ≤ 4.0 s (see Klekociuk and Burns 1994). The error bars are ±1σ.

In Figure 6, R_I^* is plotted against τ, indicating a significant positive correlation between these parameters. We do not attempt to convert these R_I^* values to estimates of mean electron energy, but instead make inferences directly from the observed relationship between τ and R_I^*. The range of R_I^* values is consistent with those obtained by Steele and McEwen (1990) and Gerdjikova and Shepherd (1987) for average aurorae, and by McEwen et al. (1981) for pulsating aurora. The positive correlation of τ with R_I^* is what we would expect if $O(^1S)$ state is quenched lower in the atmosphere as the energy of the exciting electrons increases. If the concentration of O (which is one of the primary quenchers of $O(^1S)$) was to increase while the electron energy remained constant, we would expect τ to be negatively correlated with R_I^*. From the data in Figure 6 we can estimate the fraction of variation in the I(557.7)/I(427.8) ratio between pulsations that is controlled by a change in energy of the auroral electrons, V, under the assumption that the abundance of atmospheric constituents as a function of altitude was constant during each measurement. We have

$$V \sim \frac{a_T - R_I^*(0)\cdot R_{I\tau}^*}{a_T}$$

where $R_{I\tau}^*$ is the value of R_I^* where τ equals the $O(^1S)$ free-space radiative lifetime, and a_T is the integral of $R_I^*(\tau)$ between $R_I^* = 0$ and $R_{I\tau}^*$. Using a linear expression for $R_I^*(\tau)$ given by a regression analysis of the τ versus R_I^* values, we obtained $V \sim 0.25$. The remainder of the variation of the mean I(557.7)/I(427.8) ratio between pulsations (~75%) must be due to the altitude variation of the O concentration relative to that of N_2, the $O(^1S)$ precursor species, or other quenching species, or some unaccounted aspect of the indirect excitation process. Note that we have assumed a linear relationship between τ and R_I^* for the purposes of estimation only.

In Figure 6, there is an indication that the relationship between τ and R_I^* changes between the observation sessions of different days. Most of the data in Figure 6 is for 16 July 1988. On considering only the τ versus R_I^* estimates of this day, we obtain $V \sim 0.55$. It would appear that the use of the entire data set possibly leads to the under-estimate of a representative figure for V. It is possible that any true difference in the dependence τ on R_I^* between the observation sessions reflects changes in the O density profile and/or the characteristics of the electron energy spectrum (e.g. the hardening of the energy spectrum to be less-Maxwellian in character). It is possible that the scattering correction factor f_t varies from day-to-day. However, variation of f_t over a physically realistic range results in only minor adjustment to V. For example, if $f_t = 0.73$ for the 16 July 1988 data, then V is reduced by less than 0.05.

6.4 ANALYSIS OF SYNTHETIC TIME-SERIES

We now present the results of simulations which tested the hypothesis that the short-timescale term in equation (2) is contributed by the action of measurement noise, non-linearity due to variation of the precipitating energy flux, or a combination of these two effects, on the signature of a purely direct excitation process.

6.4.1 *Simulation of the effects of measurement noise*

A single-exponential model ($B = 0$ in equation (2)) was fitted to each of the impulse functions in the τ'-set over the window $0.5 \text{ s} \leq t \leq 2.0 \text{ s}$. The range of recovered time-constants was ~0.65 s to ~0.80 s. The recovered time constant and amplitude term were then used to create a 'synthetic' impulse function $h'(t)$ (with an amplitude at $t = 0$ that was corrected for the sampling effect) which was convolved with the observed 427.8 nm time-series $I_N(T)$ to create a simulated 558 nm time-series $I'_O(T)$. The equation describing the discrete convolution is

$$I'_O(T) = \sum_{t=0}^{t_l} I_N(T - t)\, h'(t)$$

where t_l is the temporal limit of $h'(t)$. Each time-series value was then scaled to the true pulse rate for the sampling interval, replaced by a value selected from a Gaussian random number distribution with the same mean as the pulse rate and a standard deviation given by a factor N times the square root of the total number of counts in the sampling interval, and then rescaled to units of absolute intensity. The synthetic time-series were then fed into the impulse analysis procedure, and the resulting impulse function was fitted with a double-exponential model. The factor N used was identical for each of the two time-series, and was adjusted in an iterative manner until the standard deviation of the set of residuals

resulting from the fit (excluding the end points and the three bins either side of and including the t = 0 bin) matched that for the impulse function recovered from the original data.

The value of N achieved for this scheme was typically 3; N should be unity for the simulation of noise contributed purely by the statistics of photon counting. Confirmation of the magnitude and similarity of N between the 557.7 nm and 427.8 nm time-series was obtained from calculations of the variance over short segments of data obtained during quiet auroral conditions. It is suspected that the excess noise in the observed time-series was introduced in the counter stage which followed the pulse-height discriminator.

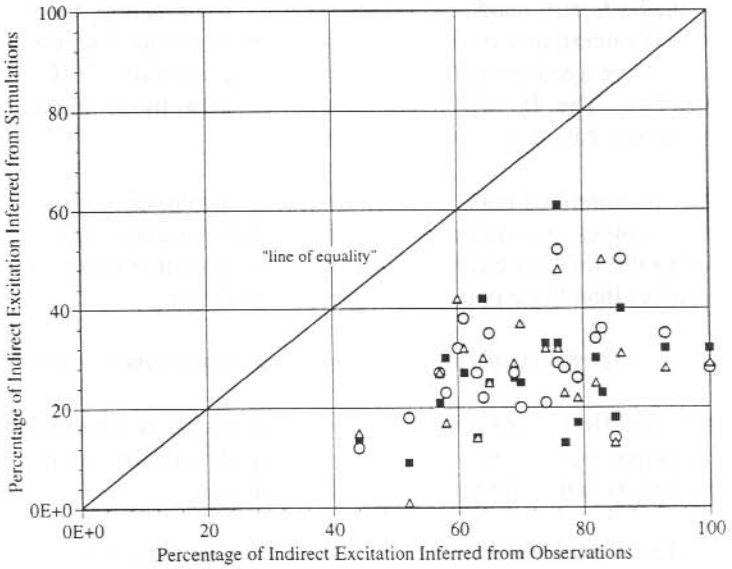

Figure 7. Inferred percentage of indirect excitation from simulations of a direct excitation model influenced by purely measurement noise (filled squares), I(557.7)/I(427.8) ratio variation in combination with measurement noise (triangles) and combined I(557.7)/I(427.8) intensity ratio variation, O(^{1}S) effective lifetime variation and measurement noise (circles) plotted as a function of percentage of indirect excitation inferred from observations for 22 selected 5-minute intervals. For one event, the value of the percentage of indirect excitation obtained from the observations has been reduced from the original value of 116% to 100%.

The final set of synthetic impulse responses was then fitted with the double-exponential model. The τ distribution obtained was essentially the same as that for the single-exponential fits to the observed data, while the τ' distribution peaked about a mean of 0.05 s. The P values were widely scattered over the 0%-100% range, with a maximum frequency near 50%, and 5 values greater than 100%. Only 6 of the simulations passed the τ'-set selection criteria. Importantly, most were rejected on the basis of their h(-0.05)

value. An approximate doubling of the h(-0.05) limit would have passed all of the simulations. As expected, the values of the non-linearity parameter $\Sigma_{n\text{-}1}$ were within the selection limit; the maximum value was 0.13 s^{-1}.

It is apparent that the simulated level of measurement noise mimics an indirect excitation response for which $\tau' \sim 0.05$ s. However estimates of the amplitude term B are likely to be in error due to the level of impulse response noise combined with the similarity of τ' to the sampling resolution. This conclusion is supported by the fact that the values of $\delta h(0)$, the residual at $t = 0$, were generally larger than those for the observed data, and in three cases exceeded the selection limit of 0.5. We performed model fits to the simulations for which τ' was held constant at the value obtained from the corresponding interval of original data, while the other parameters were free-ranging. The result was the reduction of $\delta h(0)$ to values below 0.27 s^{-1}, well inside the selection limit. The resulting τ distribution (after consideration of the uncertainty of the individual estimates) was essentially unchanged, while the P values were symmetrically distributed with a mean of ~30% and a standard deviation of ~15%. The P values are compared with those obtained from the corresponding observed data in Figure 7.

We conclude that measurement noise is likely to be responsible for at least a portion of the shortest inferred τ' values, and more importantly, contributes about half of the signature that is attributed to the indirect excitation process. We note that these simulations give higher h(-0.05) values than those obtained for the observed data.

6.4.2 *Simulation of the effects of ratio variation and measurement noise*

We then simulated the effect on a purely direct excitation process of non-linearity introduced between the measured time-series due to the observed variation of the 557.7 nm to 427.8 nm intensity ratio in the presence of measurement noise.

Under a purely direct excitation model, the amplitude of the corresponding impulse function, A, is given by

$$A = \frac{R_I}{\tau} \qquad s^{-1} \tag{5}$$

We created synthetic 557.7 nm time-series for which R_I varies in the manner of R(T) using the following convolution expression;

$$I'_O(T) = \sum_{t=0}^{t_l} I_N(T - t)\, h_{T\text{-}t}(t) \qquad R \tag{6}$$

where

$$h_{T\text{-}t}(t) = \frac{R(T\text{-}t)}{\tau} e^{-t/\tau}$$

and $h_{T\text{-}t}(0)$ is corrected for sampling. Here the τ values used were those obtained from the single exponential fits to the observed impulse functions. Noise was added to the driven and driving time-series according the factor N used in the previously described simulations. The impulse response functions were then calculated.

Again we allowed only three free-ranging parameters in the double-exponential fits to the impulse functions. Only 2 simulations passed the τ'-set selection criteria. The remainder were rejected by the h(-0.05) limit. However, the h(-0.05) values were generally lower than those for the measurement noise simulation, giving impulse responses that more closely resembled those of the observations (i.e. non-linearity appears to remove some of the acausal response contributed by noise). Of additional note is that the distribution of $\Sigma_{n\text{-}l}$ was somewhat broader than that inferred from the observations, although the selection limit was not exceeded. As noted earlier, the R(T) time-series is likely to be more variable than the true I(557.7)/I(427.8) intensity ratio, and so the simulated level of non-linearity is likely to be higher that in reality. It would appear that the simulated level non-linearity symmetrically broadens the τ distribution to a range of ~ 0.55 s to ~ 0.95 s.

The P values are shown in Figure 7. These have a similar distribution and the same mean as the values from the simulation of measurement noise. We conclude that the influence of the simulated level of non-linearity on our original hypothesis is masked by that of measurement noise.

6.4.3 *Simulation of the effects of ratio variation, lifetime variation and measurement noise*

This simulation was similar to that described in Section 6.4.2, however this time we included an effect that mimicked the expected change in τ due to energy-dependent quenching of the $O(^1S)$ state. We again constructed synthetic 557.7 nm time-series using equation (6) but this time τ in equation (5) was calculated by substituting R(T) for R_I in a linear relationship fitted to the τ dependence on R_I^* shown in Figure 7. We stipulated that τ did not exceed 0.8 s. Noise was added according to the N-factors used previously. The τ' parameter was again fixed during the fitting procedure.

The parameter distributions obtained for the set of synthetic impulse responses were very similar to those discussed in previous section. Only 2 impulse responses were passed by the τ'-set selection criteria; again the rejections were the result of the h(-0.05) limit. The τ distribution was narrower than that obtained for the second simulation method, and similar to that obtained from the observed data. It is likely that the broadening of the τ distribution from the second series of simulations is forced by requiring all of the non-linearity to be absorbed in the amplitude term of $h_{T\text{-}I}(t)$ in equation (6). As we have shown, in reality some of the non-linearity is manifest as the variation of the quenching rate.

As shown in Figure 7, the P values (which have a mean of $\sim 30\%$) are distributed in a similar manner to those of the other simulations. We conclude that measurement noise provides the dominant contribution over our simulated non-linear process in producing a response which may be misinterpreted as the signature of indirect excitation.

6.5 CONCLUSIONS

We have introduced a technique to estimate the influence of measurement noise and non-linear processes due to electron energy variation in the recovery of parameters of an assumed indirect excitation process. We have shown that for our observations, the non-linear processes associated with variation of the I(557.7)/I(427.8) intensity ratio less

significantly influence the inferred parameters of the excitation model than does measurement noise.

Using carefully selected data, we have further confirmed that indirect excitation accounts for a portion of $O(^1S)$ state in pulsating aurora. In the case of our observations, measurement noise leads to the over-estimation of the percentage of indirect excitation of $O(^1S)$ by ~30%. The likely level of indirect excitation for our selected data is in the range 30% to 50%. This is lower than the values of 50% to 100% obtained by previous workers.

A positive correlation exists between the $O(^1S)$ effective lifetime and the ratio of the pulsating part of the $O(^1S - {}^1D)$ and N_2^+ (1NG) (0, 1) emissions. We interpret this as implying that at least ~25%, and perhaps more typically ~55% of the variation of the I(557.7)/I(427.8) intensity ratio during auroral pulsations is dependent on collisional quenching of the $O(^1S)$ state. It is possible that the apparent variation of the dependence of the $O(^1S)$ effective lifetime with I(557.7)/I(427.8) intensity ratio between observation sessions is related to changes in the O density profile and/or variation of the energy characteristics of the precipitating electrons.

We find that the distribution of 71 measurements of the $O(^1S)$ effective lifetime has a sharp cut-off near the theoretical free-space radiative lifetime. The distribution has a mean value of 0.71 s and a standard deviation of 0.10 s, and is not significantly biased by variation of τ within each of the selected 5-minute data spans. While a non-linear contribution to the covariance of the $O(^1S - {}^1D)$ and N_2^+ (1NG) (0, 1) emissions may lead to an artificial broadening of estimates of the $O(^1S)$ effective lifetime obtained using our analysis technique, we have shown that the level of non-linearity present in our selected data results in a broadening which is not significant in comparison with the statistical uncertainty of the individual lifetime estimates. We caution other workers to be aware of the influence of non-linearity and noise when using the impulse analysis technique to investigate the $O(^1S)$ excitation process.

6.6 ACKNOWLEDGMENTS

Logistical support by the Australian Antarctic Division is gratefully acknowledged. The impulse analysis algorithm used in this research was developed by Dr. John Reid. Dr. Dick Gattinger of the National Research Council, Ottawa, Canada, provided a model N_2^+ (1NG) band emission profile. Dr. Denis O'Brien and Dr. Ross Mitchell of the CSIRO Division of Atmospheric Research, Melbourne, assisted with calculations of atmospheric scattering. Bryan Powell of the Australian Broadcasting Corporation provided calibration data for our standard optical sources. The photometer was originally designed by Dr. Andre Phillips and the late Dr. Fred Jacka. Jon Reeve, Stephen McBurnie, and Ricky Besso provided invaluable assistance with the installation of the photometer equipment at Macquarie Island. Jon Reeve provided additional support during the observing program. ARK wishes to thank the 1988 and 1989 Macquarie Island ANARE expeditioners for their comradeship during the experimental phase of this project.

REFERENCES

Allen, C.W. (1963). *Astrophysical Quantities*. Althone Press, London. Pp. 134 – 135.

Bevington, P. (1969). *Data Reduction and Error Analysis for the Physical Sciences.* McGraw-Hill, New York. P. 235.

Brekke, A. (1973). A discussion of the energy transfer from $N_2(A^3\Sigma_u^+)$ to $O(^1S)$ in pulsating aurora. *Planetary and Space Science 21*:698–702.

Brekke, A. *and* Pettersen, K. (1972). A possible method for estimating any indirect process in the production of the $O(^1S)$ atoms in aurora. *Planetary and Space Science 20*:1569–1576.

Burns, G.B. (1983). *Pulsating aurora: Photometer, riometer and microupulsation coil observations*. Ph.D. thesis, LaTrobe University, Australia.

Burns, G.B. *and* Reid, J.S. (1984). Impulse response analysis of 5577Å emissions. *Planetary and Space Science 32*:515–523.

Burns, G.B. *and* Reid, J.S. (1985). A comparison of methods for calculating $O(^1S)$ lifetimes. *Australian Journal of Physics 38*:647–656.

Donahue, T.M., Parkinson, T.D., Zipf, E.C., Doering, J.P., Fastie, W.G. *and* Miller, R.E. (1968). Excitation of the auroral green line by dissociative recombination of the oxygen molecular line: analysis of two rocket experiments. *Planetary and Space Science 16*:737–747.

Gerdjikova, M.G. *and* Shepherd, G.G. (1987). Evaluation of auroral 5577Å excitation processes using Intercosmos Bulgaria 1300 satellite measurements. *Journal of Geophysical Research 92A*:3367–3374.

Henriksen, K. (1973). Photometric investigation of the 4278Å and 5577Å emissions in aurora. *Journal of Atmospheric and Terrestrial Physics 35*:1341–1350.

Henriksen, K. (1974). The reaction of nitric oxide with atomic nitrogen as a possible excitation source of the auroral green line. *Journal of Atmospheric and Terrestrial Physics 36*:1437–1439.

Johnstone, A.D. (1983). The mechanism of pulsating aurora. *Annales Geophysicae 1*:397–410.

Klekociuk, A.R. *and* Burns, G.B. (1992). $O(^1S)$ excitation and effective lifetimes. In: Burns, G.B. *and* Duldig, M.L. (Eds). *ANARE Research Notes Number 88*, Australian Antarctic Division. Pp. 117–129.

Klekociuk, A.R. *and* Burns, G.B. (1994). Parameters of the $O(^1S)$ excitation process deduced from photometer measurements of pulsating aurora. *Journal of Atmospheric and Terrestrial Physics* (in press).

Kneizys, F.X., Shettle, E.P., Abreu, L.W., Chetwynd, J.H., Anderson, G.P., Gallery, W.O., Selby, J.E.A. *and* Clough, A.A. (1988). Users guide to LOWTRAN7,

Technical Report AFGL-TR-88-0177, Air Force Geophysics Laboratory, Massachusetts.

McEwen, D.J., Duncan, C.N. *and* Montalbetti, R. (1981). Auroral electron energies: comparison of *in situ* measurements with spectroscopically inferred energies. *Canadian Journal of Physics 59*:1116 – 1123.

Nicolaides, C., Sinanoglu, O. *and* Westhaus, P. (1971). Theory of atomic structure in electron correlation. IV. Method for forbidden transition probabilities, with results for [OI], [OII], [NI], [NII] and [CI]. *Physical Review A 4*:1400 – 1410.

O'Brien, D.M. (1992). Accelerated quasi Monte Carlo integration of the radiative transfer equation. *Journal of Quantum Spectroscopy and Radiative Transfer 48*:41 – 59.

O'Neil, R.R., Lee, E.T.P. *and* Huppi, E.R. (1979). Auroral O(^{1}S) production and loss processes: ground-based measurements of the artificial aurora experiment Precede. *Journal of Geophysical Research 84A*:823 – 833.

Paulson, K.V., Chang H. *and* Shepherd, G.G. (1990). The evaluation of time-varying parameters pertinent to the excitation of O(^{1}S) in aurora. *Planetary and Space Science 38*:161 – 172.

Paulson, K.V. *and* Shepherd, G.G. (1965). A cross-spectral method for determining the mean lifetime of metastable oxygen atoms for photometric observations of quiet aurorae. *Journal of Atmospheric and Terrestrial Physics 27*:831 – 841.

Parkinson, T.D. (1971). A phase and amplitude study of auroral pulsations. *Planetary and Space Science 19*:251–255.

Rees, M.H., Stewart, A.I. *and* Walker, J.C.G. (1969). Secondary electrons in aurora. *Planetary and Space Science 17*:1997 – 2008.

Rees, M.H., Walker, J.C.G. *and* Dalgarno, A. (1967). Auroral excitation of the forbidden lines of atomic oxygen. *Planetary and Space Science 15*:1097 – 1110.

Shepherd, G.G., Paulson, K.V., Brown, S., Gault, W.A., Moise, A. *and* Solheim, B.H. (1991). Identification of the auroral O(^{1}S) precursor in photometric time sequences of pulsating aurora. *Geophysical Research Letters 18*:1939 – 1942.

Solheim, B.H. *and* Llewellyn, E.J. (1979). An indirect mechanism for the production of O(^{1}S) in the aurora. *Planetary and Space Science 27*:473 – 479.

Steele, D.P. *and* McEwen, D.J. (1990). Electron auroral excitation efficiencies and intensity ratios. *Journal of Geophysical Research 95A*:10321 – 10336.

Zipf, E.C. *and* McLaughlin, R.W. (1978). On the dissociation of nitrogen by electron impact and e.u.v. photo absorption. *Planetary and Space Science 26*:449 – 46.

7. MACQUARIE ISLAND PULSATING AURORA STUDIES

W.J.R. French, A.R. Klekociuk, G.B. Burns and D.J. Rasch

Auroral and Space Physics
Antarctic Division
Kingston Tasmania 7050
Australia

ABSTRACT

This paper reviews the operation and calibration of a set of wide angle photometers for the study of pulsating aurora at Macquarie Island, 1992. Simultaneous 10 Hz samples of the oxygen λ 557.7 and λ 630.0 nm line emissions and the nitrogen λ 427.8 and λ 391.4 nm band emissions were recorded, together with fast response riometer (cosmic noise absorption) and all sky auroral imager data. The study aims to determine the incident energy of pulsating fluxes, ionospheric recombination times (from the fast response cosmic noise measurements) and the location of a source region for pulsation modulation using a set of conjugately located photometers at Kotzebue, Alaska. Absolute calibration of the photometers involved consideration of interference filter parameters, photomultiplier 'pulse pileup' effects and properties of an absolute intensity calibration lamp. The photometer data is calibrated in Rayleighs with an error of the order of 15%. Incident particle energy estimates from emission ratios can only be extracted from pulsating aurora on clear moonless nights. A primary consideration is to account for scattering through cloud (or drifting salt spray at Macquarie Island) and to estimate airglow and background contributions to the respective intensity measurements. The seasonal and temporal variations in airglow and background for these emissions are presented.

7.1 INTRODUCTION

The striking phenomenon of pulsating aurora; a repetitive, sub-visual, on-off switching of auroral intensity has been studied during 1992 at the ANARE station on Macquarie Island (gg: 54.5°S; 159.0°E mag: L = 5.3, 64.3°S; 246.9°E).

This station was chosen as the site for these studies, despite its frequently overcast conditions, because of the suitable location of its magnetically conjugate partner at Kotzebue, Alaska (gg: 66.9°N; 197.4°E mag: 64.7°N; 248.2°E). Due to the extent of the southern hemisphere oceans and the location of the auroral zone, this pair provides one of the few sites available for land based conjugacy studies.

Pulsating aurora are most frequently observed in the morning sector of the auroral oval and during the recovery phase of substorm events. They may extend from a few 10's of km in irregular patches to the order of 1000 km in narrow east-west aligned arcs. Pulse frequency generally decreases as the night progresses, with 1 – 2 s pulses dominating the evening hours and 12 – 20 s pulses dominating the morning hours. Neighbouring patches may pulsate with independent frequency and phase.

Pulses are characterised by rapid rise and decay times, varying in intensity, for the λ 557.7 nm line, by only a few kiloRayleighs (kR), and may be superimposed on discrete background aurora of wide ranging intensity.

The bulk of the pulsation activity is concentrated at the equatorward edge of a discrete auroral display, consistent with pulsating fluxes being contained within closed field lines on the inside boundary of the plasma sheet.

Currently, the most widely accepted mechanism for pulsating aurora is pitch angle diffusion of stably trapped electrons into the loss cone. The loss cone describes the range of electron pitch angles, from field aligned to the loss cone limit, for which the electrons are likely to attain sufficiently low altitude to collide with atmospheric atoms. Outside the loss cone they are likely to be reflected at their mirror points.

Observational evidence from the rocket borne experiments of Whalen et al. (1971) and Yau et al. (1981) show that between pulsations the electron pitch angle distribution for electron energies up to 30 keV is anisotropic, peaking at angles perpendicular to the local field. At pulse maximum, an isotropic distribution is apparent and therefore a process is required that results in the diffusion or scattering of electrons into the loss cone.

Current thinking is that resonant interaction of the electrons with oppositely moving VLF or ELF waves is responsible, and it is the anisotropy in the electron pitch angle distribution itself which causes the VLF wave growth. Intuitively, this is most likely to occur where the magnetic field strength is at a minimum, i.e. at the geomagnetic equator, and high time-accuracy conjugate experiments such as this work and velocity dispersal rocket experiments show that this is so.

A most important role in this model is played by the small percentage (perhaps 10–20%) of backscattered loss cone electrons. Given that there is a minimum threshold in the degree of pitch angle anisotropy required before VLF waves of sufficient amplitude are generated, to in turn cause pitch angle redistribution, those backscattered electrons fill in to some extent the loss cone part of the returning pitch angle distribution, reducing the degree of anisotropy so that VLF wave growth, and redistribution may not occur.

It is possible then that the same group of electrons may propagate several times between the poles before the anisotropy in its pitch angle distribution is sufficient to cause VLF wave growth, pitch angle redistribution and a subsequent pulse on its next encounter with the atmosphere.

Indeed, as a minimum case, there must be at least one pass through the geomagnetic equator which does not generate VLF waves and pitch angle redistribution, for pulsation activity to exist at all.

7.2 EXPERIMENTAL DATA

Pulsating aurora were observed at Macquarie Island between April and November 1992 with four wide angle (60° field-of-view) photometers. The advantage of wide field of view

photometers in pulsating aurora studies is to avoid, to a large extent, intensity fluctuations due to aurora expanding into or drifting through the field of view.

Simultaneous 10 Hz samples of the oxygen λ 557.7 and λ 630.0 nm line emissions and the nitrogen λ 427.8 and λ 391.4 nm band emissions were recorded in fortnightly campaign periods centred on each new moon. Three co-located experiments greatly increase the value of these data. A 30 MHz fast response riometer (relative ionospheric opacity) measured cosmic noise absorption to gain information on ionospheric recombination times, H and D magnetic induction coils measured the magnetic field response to pulsating fluxes (but will not be discussed here) and an image intensified all-sky auroral imaging system collected time lapse video images of the night sky at 6 second intervals.

A total of 198 nights of photometer and/or auroral imager observations were made between 24 April and 7 November. Of these, 135 nights (71%) contained visible aurora at some time over the night, 55 nights (29%) contained some clear-aurora data and 133 nights (70%) contained cloudy-aurora data. Pulsating aurora were observed on 111 nights (58%) with 48 nights (25%) containing clear pulsating aurora and 107 nights (56%) containing cloudy epulsating aurora data. Thirty-four nights (18%) contained some clear-no aurora data and 8 nights were lost due to camera malfunction.

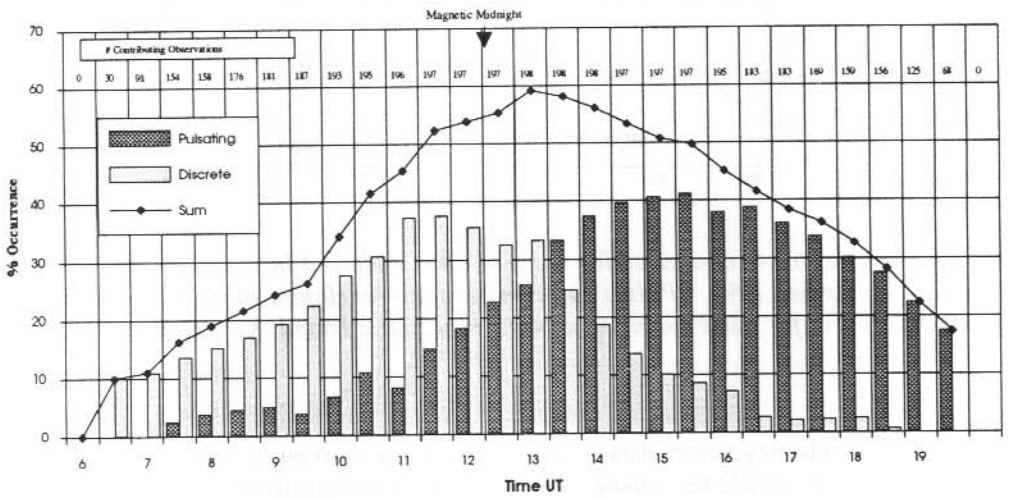

Figure 1. Auroral occurrence frequency for 198 observing nights at Macquarie Island 1992. The distribution shows peak occurrences in discrete aurora (38% of nights) and pulsating aurora (41% of nights) at 1130 and 1530 UT respectively. Auroral activity in general peaked at 13 UT on 59% of nights.

Figure 1 shows the results of a statistical study on the occurrence times of discrete and pulsating aurora extracted from these records. Each half hour interval, on each observing night was classified as pulsating aurora, if any pulsation activity could be detected, discrete

aurora, for any other auroral activity or quiet, for no detectable activity. As we expect, pulsation activity peaks in the morning sector of the auroral oval, at about 1530 UT over Macquarie Island, on 41% of nights during 1992. Discrete auroral activity peaked just prior to magnetic midnight, at 1130 UT, on 38% of nights. If these two distributions are summed, a peak in auroral activity is noted just after magnetic midnight on 59% of nights.

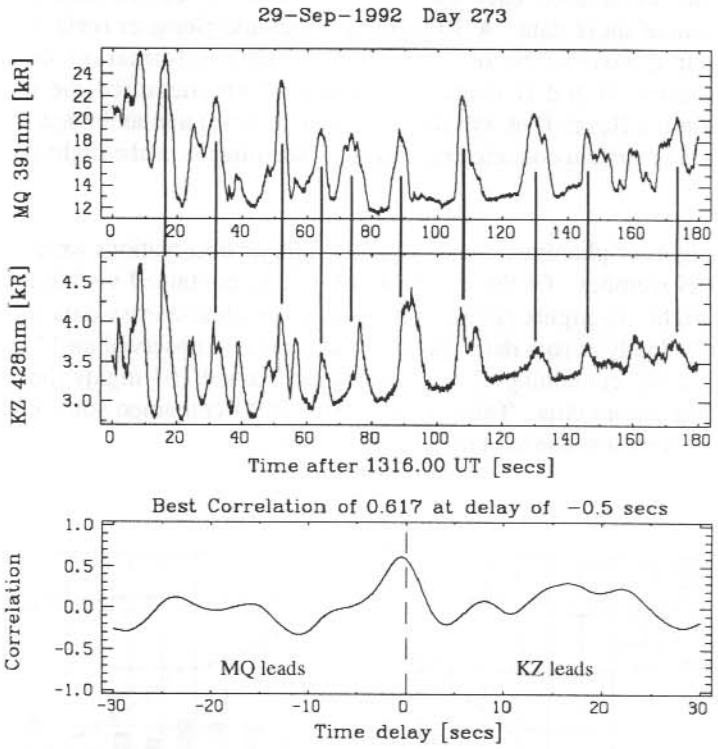

Figure 2. An example of a pulsating auroral event observed in conjucate hemispheres from 29 September 1992. Pulses show maximum correlation at -0.5 s implying an equatorial source for pulse modulation. MQ = Macquarie Island, KZ = Kotzebue.

The clear-sky pulsating aurora data set was reduced to a working set for incident particle energy calculations of 212 ten minute files over 28 days, principally by selecting only those files with no contamination by moonlight .

Timing accuracy for all digital data was maintained to within a few milliseconds from a laboratory chronometer and HF time signals, such accuracy was required to achieve the principle objective of the conjugacy campaign in September/October; to identify a source region for pulsation modulation from the correlation of conjugate fluxes. This period is one of two annual windows in which photometric observations can be made simultaneously in both hemispheres and Figure 2 is an example of a conjugate event observed during this campaign. Given that the bounce period for an electron between conjugate sites is of the

order of 10 seconds (energy dependent) (Thomas and Rothwell 1979), correlation of conjugate fluxes within a few seconds implies an equatorial source.

Absolute intensity ratios between the optical emissions can give a measure of the incident particle energy, but account must be taken of airglow and background contributions and this approach is only valid for clear, moonless nights. In general, it was easy to determine if cloud contaminated the data when it was backlit by some auroral display. The auroral imager proved invaluable, not only in the identification of pulsating patches but also in the assessment of cloud contamination. However, for those dark (moonless and auroraless), apparently clear nights, from which estimates of the subvisual airglow and background contributions were made (see Figures 8 A – B), it was hoped that variations in the nitrogen band 427.8/391.4 ratio would give some indication of the presence of cloud. In practice this proved inconclusive and regular visual observations were necessary.

Importantly, the nitrogen N_2^+ band emissions are instantaneous indicators (lifetime 10^{-7} sec) of incident electron energy flux (Omholt 1975), and can be used directly for the timing of electron injection into the ionosphere. The excited states of the oxygen λ 558 nm (O^1S) and λ 630 nm (O^1D) line emissions are metastable, and consequently these emissions may be delayed with respect to excitation. Collisional deactivation may also occur for these states, a process which is altitude dependent, and thus also dependent on incident auroral electron energy. Typical effective lifetimes for the O^1S and O^1D states are 0.7 s (Burns and Reid 1984) and 40 s (Ono 1992) respectively.

For the 558/428 and 630/428 emission intensity ratios, given that each of the oxygen data are shifted in time by their respective effective lifetimes, the energy E_o of incident particles can be estimated from the empirical relationships of Steele and McEwan (1990).

$$\frac{I_{558}}{I_{428}} \approx 5.4E_o^{-0.3} \qquad (1)$$

$$\frac{I_{630}}{I_{428}} \approx 3.3E_o^{-2.1}$$

It can be seen that the 630/428 intensity ratio is by far the more sensitive of the two to changes in incident electron energy and it has been widely used for energy studies in discrete aurora. However, due to the long effective lifetime of the λ 630 nm emission, this ratio does not respond well to the rapid intensity variations of pulsating aurora and it is necessary to use the 557/428 ratio. Figures 3 and 4 are typical examples of the 557/428 ratio variation during a pulsating event. They indicate a hardening of the electron energy spectrum during the pulse on phase, typically by a few keV (McEwan et al. 1981).

The injection of electrons during a pulsation event increases ionisation. Recovery from such an electron density perturbation via dissociative recombination follows the ionospheric rate equation

$$\frac{dN}{dt} = \frac{q(t, h)}{1+\lambda} - \alpha N^2 \qquad (2)$$

where dN/dt [cm^{-3} s^{-1}] is the rate of change of electron density, λ is the fraction of negative ions to total ions, q [cm^{-3} s^{-1}] is the height dependent ionisation rate which can be considered as directly proportional to the N_2^+ (1NG) band emission intensities, and α [cm^3 s^{-1}] is the effective recombination coefficient. For sufficiently small dN/dt, considered as a small perturbation ΔN on a background at equilibrium N_0 equation (2) reduces to an exponential of the form

$$\Delta N = (\Delta N)_o e^{-\frac{\Delta t}{2\alpha N_o}} \qquad (3)$$

where the ionospheric recovery time constant is defined as

$$\tau = \frac{1}{2\alpha N_o}. \qquad (4)$$

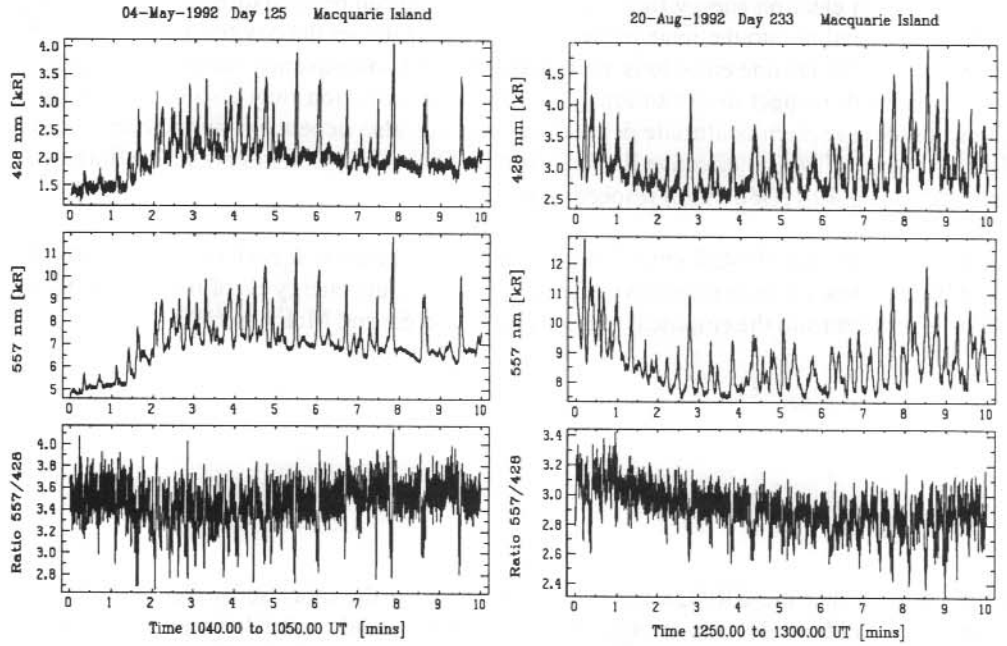

Figures 3 and 4. Examples of the variation in intensity ratio, which is a measure of the energy of incident auroral electrons. A decrease in the intensity ratio indicates a hardening of the electron energy spectrum during the pulse on phase of pulsating aurora.

For a given electron density N(h, t) the amount of cosmic noise absorption A observed at radio wave frequencies above 30 MHz and integrated over the height h of the absorbing layer, is proportional to the product

$$A[dB] \propto N\upsilon h \qquad (5)$$

where $\upsilon(h)$ is the electron collision frequency (Eather and Jacka 1966).

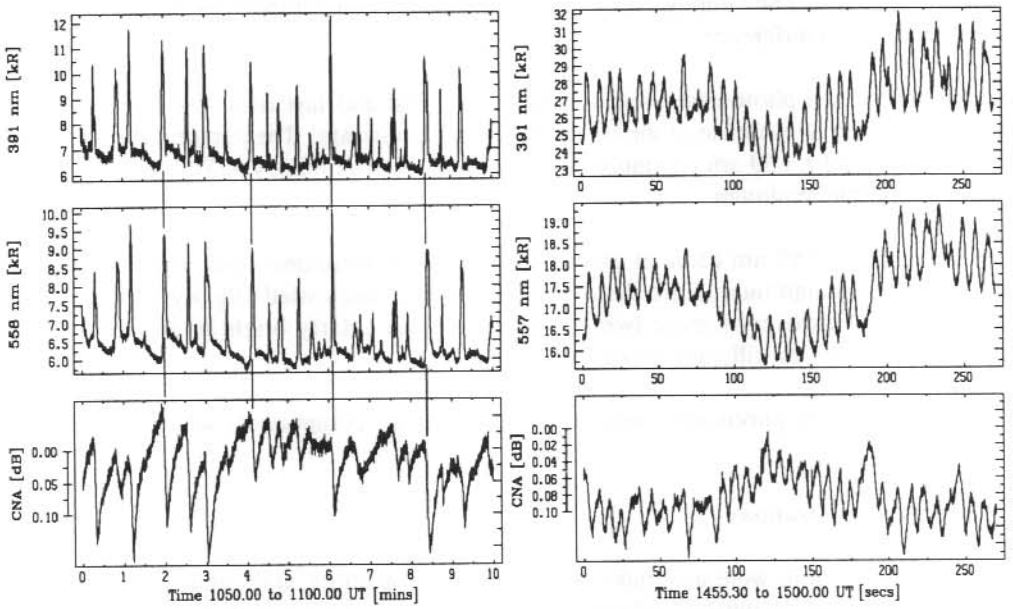

Figure 5. An example of a pulsating aurora event from 4 May 1992 clearly showing an exponential CNA recovery from each pulse: Figure 6. An example from 4 September 1992 of fast pulsating aurora. The CNA pulses here exhibit a much faster recovery rate, indicating that larger electron densities and incident particle energies are involved. Part of the project aims include a determination of the relationship between the ionospheric recombination rate and incident auroral electron energy.

Thus, the rate of recovery observed in the CNA data is a measure of the recombination rate following a perturbation in electron density, and this, itself, is a delayed response to a pulse in ionisation q(t, h).

Furthermore, the magnitude of ionisation is dependent on incident particle energy. With the energy estimates from intensity ratios via equation (1) a relationship may be established between effective recombination rate α and the energy of incident auroral energies, and thus in altitude.

Figure 5 is an excellent example of the ionospheric recovery time observed on 4 May 1992 and has a duration in this case of the order of 30 s. Figure 6 exhibits a much faster recovery rate (the order of 5 s) and indicates that larger electron densities and incident particle energies are involved.

7.3 INSTRUMENT CALIBRATION

Accurate timing and calibration of the digital photometer and riometer data has been of primary concern throughout this project. Digital data were collected at a sampling rate of 10 Hz and stored in 10 minute computer files. Analogue chart records were also kept at a typical rate of 30 cm hr^{-1} during the campaign periods for visual inspection and comment on cloud cover and interference.

A shutter on each photometer was closed for the first and last files in each observing session to obtain an estimate of the background dark count rate. The photomultiplier tubes on the λ 428 and λ 630 nm channels were cooled to approximately -25°C, keeping dark counts to a stable minimum.

The λ 391 and λ 558 nm channel photomultiplier tubes were uncooled, and dark counts were orders of magnitude larger than the cooled tubes, and varied slightly with ambient temperature. However as these two emissions are particularly bright in the aurora, the signal/noise level was still quite acceptable.

Calibrations of the photometer systems involved three components which are briefly discussed here.

7.3.1 *Filter Calibrations*

Full filter calibrations were undertaken in March and November, at the start and end of the observing program. A partial calibration was also made mid-year to check as much of the filter characteristics as possible without disturbing them. The variation in filter characteristics was less than 5% over the year and Table 1 summarises the parameters assumed to apply to all data.

Filter profile calibrations utilised a SIROSPEC grating monochromator, accurately stepped across a narrow range of wavelengths from a white light source, to illuminate the observing filter of interest and so obtain its peak position, bandwidth and transmission profile. The filter was then removed and the scan repeated to acquire a white light profile, from which the percentage transmission of the filter T_f can be determined.

The monochromator wavelength scale itself was calibrated, both prior to, and following each profile scan, against known spectral lines around the wavelength of interest using a Hg/Cd/Zn discharge lamp. Once the monochromator offset was determined in March, it could be accurately set to the observing wavelength and the filter tilt tuned to maximise transmission.

Scanned profiles were recorded digitally at 10 Hz and in 2 minute files. The fractional transmission of the filter at the auroral line or band, is an important factor for absolute intensity calibrations. In the case of the single line oxygen emissions, this is merely the transmissions at λ 557.73 and λ 630.03 nm relative to the peak of the filter profile. However, in the case of the nitrogen band emissions, this parameter is derived from the integration of a discrete synthetic band profile over the same range as the filter profile.

Table 1. A summary of the filter and calibration parameters assumed for all data.

		Wavelength / Channel			Errors (2*sigma)		
Filter Parameter	Symbol	**630.0**	**427.8**	**557.7**	**630.0**	**427.8**	**557.7**
100% Equivalent Bandwidth [Å]	$\lambda_{100\%}$	2.33	3.7975	3.64	± 0.1673	± 0.2682	± 0.1815
Peak Equivalent Bandwidth [Å]	λ_{peak}	4.6575	24.307	9.863	± 0.2605	± 1.1464	± 0.2489
Filter transmission [%]	T_f	49.10%	14.53%	37.83%	± 1.54%	± 1.30%	± 1.30%
Transmission at line/band [%]	T_{obs}	89.87%	76.90%	94.31%	± 7.72%	± 3.03%	± 3.41%
Total transmission at line [%]	T	44.13%	11.18%	35.68%	± 4.03%	± 1.09%	± 1.78%
Transmission multiplier	F	5.1825	31.6098	10.4585	± 0.5310	± 1.9418	± 0.4609
Pile-up corrected counts [Hz]	C_T	1427528	34601	2214672	± 30158	± 1618.1	± 51216
Spectral radiant intensity [R/A]	α	3121	77.4	1002	± 95	± 8.8	± 56
Observing window transmission[%]	T_w	75.18%	80.73%	84.70%	± 3%	± 3%	± 3%
Final Rayleighs/Hz	R	0.015071	0.087587	0.005587	0.00175	0.01247	0.00046
Percentage Error					11.60%	14.24%	8.29%
Typical darks (closed shutter) [Hz]	d	*60 Hz*	*72 Hz*	*6400 Hz*			
		0.90 R	*6.31 R*	*35.75 R*			
Typical background/airglow [Hz]	a	*6000 Hz*	*1000 Hz*	*43200 Hz*			
		90.43 R	*87.59 R*	*241.34 R*			

The filter equivalent bandwidth in Table 1 is defined as the width of a rectangular bandpass with area equivalent to that under the filter transmission profile. The equivalent bandwidth at 100% transmission is related to the equivalent bandwidth at the transmission peak by

$$\lambda_{100\%} = \lambda_{peak} \cdot T_f \qquad (6)$$

Unfortunately, as a result of the white light source, optic fibre transfer or monochromator reflectance characteristics, transmission through the calibration system was severely attenuated below λ 400 nm and a calibration of the λ 391 nm filter was not possible. An absolute intensity calibration factor for this channel was estimated from the theoretical 391/428 intensity ratio of 3.2833.

7.3.2 *Correction for 'pulse pile-up'*

A characteristic of the photometer EMI 9658B (prismatic cathode) and 9558A photomultiplier tubes used in pulsed mode is the space charge saturation or 'pulse pileup' effect. It is necessary to choose this mode of operation in preference to the direct current mode which is recommended only for steady low light level applications.

The pulse pileup effect is a departure from linearity between input light level and pulse output which becomes significant at large input light intensities. For these tubes, it was determined that a pileup correction factor was required for count rates above about 200 kHz.

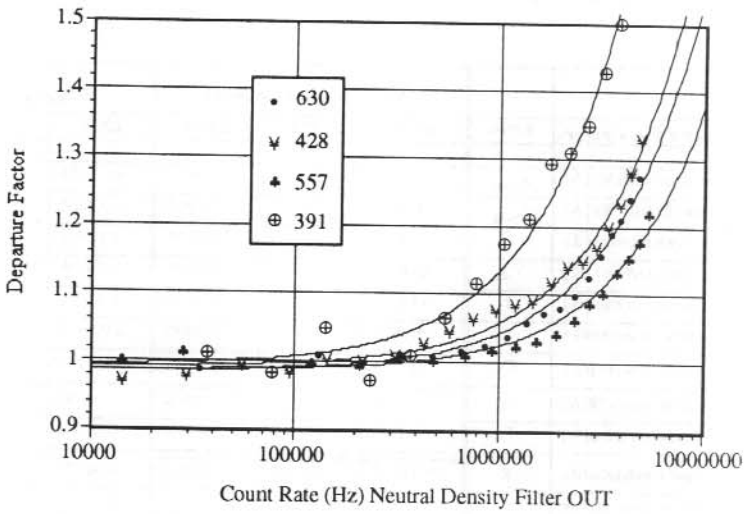

Figure 7. Pulse pileup departure factor curves for each of the photometer channels. All raw data above the asymptotic break point are corrected by multiplying by this factor.

The approach to quantifying this effect was to use a white light input to the monochromator (tuned to the observing wavelength) and then via optic fibre into the photometer. The white light source was incrementally stepped through a range of operating currents (hence light intensity) and the photomultiplier count rate recorded. The procedure was then repeated with a neutral density filter (NDF) in place, reducing the transmission to approximately 7% (wavelength dependent). If the photomultiplier response was linear with increasing intensity, then the ratio between NDF_{in} and NDF_{out} count rates C should be constant at the NDF transmission level T_{NDF}. Thus, if b is the background dark count the quantity

$$D = \frac{C_{NDFin} - b}{(C_{NDFout} - b)T_{NFDF}} \qquad (7)$$

describes the departure of the photomultiplier count rate from linearity, to which a correction curve can be fitted and applied to the raw count rate data before conversion to absolute intensity. Figure 7 illustrates the pulse pileup curves for each channel.

7.3.3 *Absolute intensity calibration*

Calibration of the photometer data for absolute intensity was initially made *in situ* using a portable low brightness source at Macquarie Island. The spectral radiant intensity of this source (in units of Rayleighs/Angstrom) was determined at each of the observing wavelengths from comparative measurements with the low brightness source LBS during October 1992 at the Institute for Space and Atmospheric Studies (ISAS) in Saskatoon,

Canada. The source could be mounted directly on top of each photometer and a corresponding count rate measured.

Three further factors are applied to the clear sky pulsating aurora data before particle energy calculations can be made, namely, an assessment of the transmission through the laboratory observing window T_w at each wavelength (see also Table 1), the van Rhijn correction to zenith intensity and the subtraction of airglow or background contributions as described in the following section. Given then, a raw count rate corrected for pulse pileup and a dark count contribution removed, the conversion factor to absolute intensity can be written as

$$R = \frac{\alpha \lambda_{100\%}}{C_T T_f T_{obs} T_w} \quad \text{by equation (6)}$$

$$= \frac{\alpha \lambda_{peak}}{C_T T_f T_{obs} T_w}$$

$$= \frac{\alpha F}{C_T T_w} \quad \text{in R Hz}^{-1} \qquad (8)$$

where F is the transmission multiplier listed in Table 1.

While much care was taken to ensure accuracy of the absolute calibrations, significant departures (by a factor of at least 2) were found between the intensity ratios previously reported in the literature and the current results.

As some questions arose over the calibration of this low brightness source, in particular its inconsistency with previous results, the photometer system was reconstructed in the Antarctic Division laboratories in Kingston and recalibrated with a second calibration source. This source was calibrated by the ABC's Colour Measurement Laboratory in units of W sr^{-1} nm^{-1} at each observing wavelength. If ϕ is in units of W sr^{-1} nm^{-1} , α the photometer aperture and Ω_{lamp} and Ω_{phot} the calibration lamp and photometer solid angles respectively, then ϕ may be converted to α(in RHz^{-1}) via equation (9).

$$\alpha = \phi \, \Omega_{lamp} \, \frac{\lambda}{hc} \, \frac{4\pi}{\Omega_{phot} a.10^6} \qquad (9)$$

These calibrations provide excellent agreement with intensity ranges for airglow and background with those previously reported and these are discussed in the following section. We are confident that a study of the energetics of pulsating aurora can now proceed, in particular the energy variation between the 'pulse on' and 'pulse off' phases, a comparison of the energetics of pulsating aurora and other types of aurora, and diurnal variation in the average energy of pulsating aurora.

7.4 AIRGLOW AND BACKGROUND

The component of the absolutely calibrated data, which is attributable to airglow or background and not representative of auroral electron energies, were estimated from all

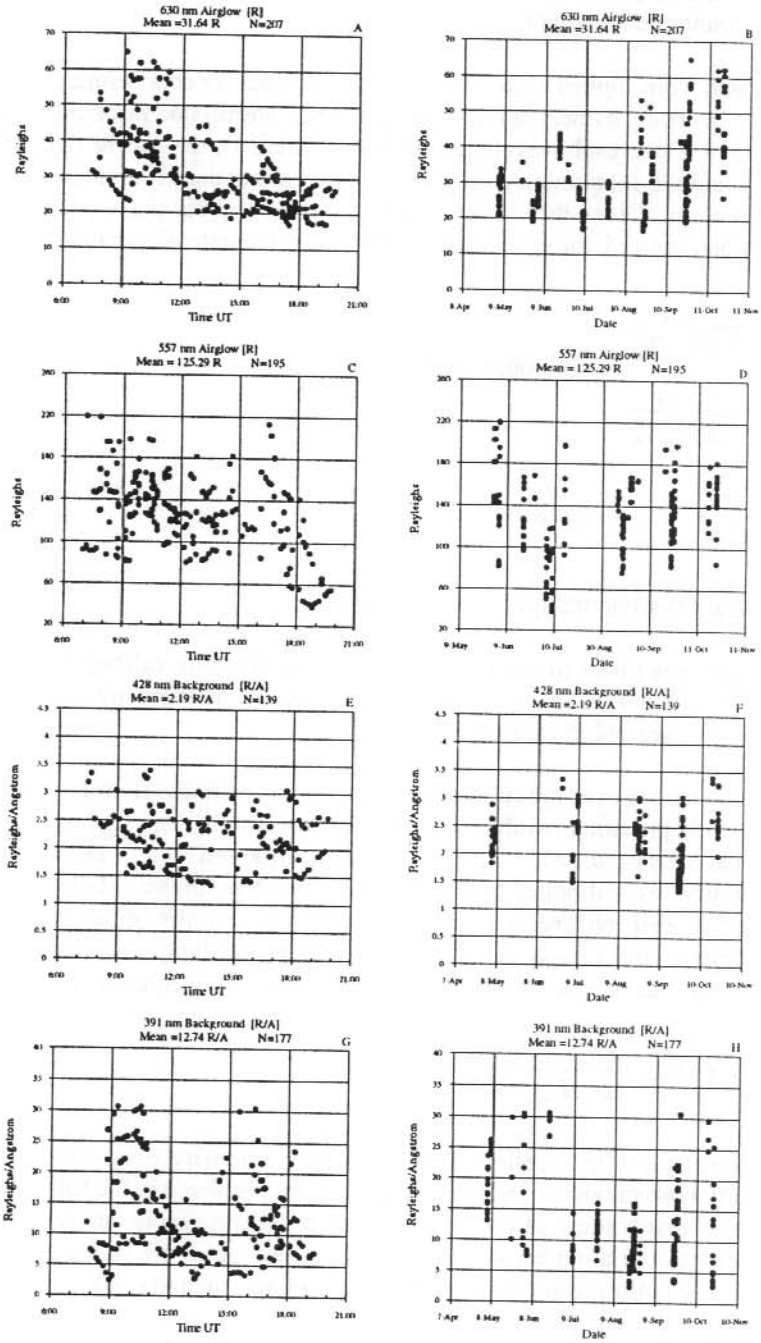

Figure 8 A–H. Estimates of the temporal variations in the λ 630 and λ 557 nm airglow, and the λ 428 and λ 391 nm background emissions at Macquarie Island. Each point represents the mean of a 10 minute file observed during clear, moonless nights when there was no visible aurora.

nights of clear moonless sky and no visible auroral activity during the observing campaigns, and are presented in Figures 8 (A–H) for each channel. The intensity scale applies to the latter calibration factors and provide excellent agreement with previous work (e.g. Chamberlain 1961).

Although the data are sparse over the year, due mainly to the maritime climate of Macquarie Island, the oxygen λ 630 and λ 558 nm airglow plots show significant temporal and seasonal variation. Both are relatively high prior to magnetic midnight and diminish toward the end of the evening, particularly after 15 UT. A winter minimum and summer maximum is also apparent for these data.

Little temporal variation is expected for the background nitrogen emissions and this is evident in the data (plots E and G). The contribution here is principally the stellar background as no natural airglow occurs. In this case the background is an integration over the filter passband and not equivalent to an emission intensity contribution of a discrete nitrogen band system. The large scatter in the λ 391 nm data is mainly due to photomultiplier noise as this tube was operated at ambient temperature.

7.5 CONCLUSIONS

An extensive data set has been collected on pulsating aurora, utilising four optical photometer channels, a fast response riometer and an all sky auroral imager. Pulsating aurora were observed on 111 nights over seven months, including over 35 hours of moonless, clear sky pulsating aurora events and several events from conjugate sites. A statistical study of the percentage occurrence times of pulsating and discrete aurora is presented. The distribution of pulsating aurora occurrence maximised at 1530 UT at Macquarie Island on 41% of nights and discrete aurora at 1130 UT on 38% of nights.

The conjugate events from the September/October campaign confirm pulses in conjugate hemispheres are correlated to within a few seconds, implying an equatorial source for pulsation modulation and supporting the model of VLF wave/auroral electron interaction.

Estimates of the airglow contributions of the λ 630 and λ 558 nm oxygen emissions are extracted from all the clear, quiet, moonless data recorded. Both show evidence of a seasonal variation; maximising in the austral summer and minimising in winter, and a temporal variation; decreasing as the night progresses, particularly after 15 UT. The stellar background contribution to the λ 428 and λ 391 nm emissions show no discernible temporal or seasonal variation.

The ratio data clearly show a decrease during the 'pulse on' phase of pulsating aurora implying a hardening of the electron energy spectrum at this time. Calculation of incident electron characteristic energies from emission intensity ratios was initially hampered by inconsistencies in the absolute intensity calibrations. A second calibration lamp has provided much more consistent results and the energy implications of pulsating aurora can be more thoroughly addressed. In particular, the energy variation between 'pulse on' and 'pulse off' phases, energies relative to discrete aurora, and to the period and width of pulses (with implications on pulsating aurora mechanisms), and finally with the analysis of the

CNA time constant data, to establish a relationship between energy and ionospheric recombination rates.

7.6 ACKNOWLEDGMENTS

This project was carried out with the assistance and logistical support of the Australian National Antarctic Research Expeditions. Special thanks are made to the fellow wintering expeditioners at Macquarie Island 1992 who assisted in this project with much enthusiasm.

REFERENCES

Chamberlain, J.W. (1961). Physics of aurora and airglow. *Academic Press, NY.*

Eather, R.H. *and* Jacka, F. (1966). Auroral absorption of cosmic radio noise. *Australian Journal of Physics 19*:215–239.

McEwan, D.J., Duncan, C.N. *and* Montalbetti, R. (1981). Auroral electron energies: comparisons of in situ measurements with spectroscopically inferred energies. *Canadian Journal of Physics 59*:1116–1123.

Omholt, A. (1971). The optical aurora. Springer-Verlag.

Steele, D.P. *and* McEwen, D.J. (1990). Electron auroral excitation efficiencies and intensity ratios. *Journal of Geophysics Research 95*:10321–10336.

Thomas, R.W. *and* Rothwell, P. (1979). A latitude effect in the periodicity of auroral pulsating patches. *Journal of Atmospheric and Terrestrial Physics 41*:1179–1184.

Whalen, B.A., Miller, J.R. *and* McDiarmid, I.B. (1971). Energetic particle measurements in a pulsating aurora. *Journal of Geophysics Research 76*:978–986.

Yau, A.W., Whalen, B.A. *and* McEwen, D.J. (1981). Rocket-borne measurements of particle pulsation in pulsating aurora. *Journal of Geophysics Research 86*:5673–5681.

8. TEMPORAL CONJUGACY OF PULSATING AURORA BETWEEN MACQUARIE ISLAND AND KOTZEBUE

G.B. Burns[1] A.R. Klekociuk[1], W.J.R. French[1], D.J. Rasch[1] and J.V. Olson[2]

[1] Auroral and Space Physics
Antarctic Division
Kingston Tasmania 7050
Australia

[2] Geophysical Institute
University of Alaska
Fairbanks Alaska 99775
USA

ABSTRACT

Eight nights of simultaneous wide-angle (60° field-of-view) photometric observations of pulsating aurora at Macquarie Island (geog: 54.50°S, 159.0°E; PGM–1988 (Baker and Wing 1989): 64.34°S, 246.9°E) and Kotzebue (geog: 66.9°N, 197.4°E; PGM–1988: 64.74°N, 248.2°E) are used to determine when these regions were conjugate and to investigate the spatial variability of the source region of the pulsating fluxes. From almost 18 hours of pulsating aurora observations, cross-correlation analysis yielded 8 hours 10 minutes of conjugate data. Temporal conjugacy displacements of 1.6 s and 2.2 s are measured to persist for periods of 22 and 12 minutes respectively, making it likely that both the source region and the average energy of the 'on' phase electrons are remaining constant over these periods. For those intervals when a temporal conjugacy displacement was measured, Macquarie Island optical pulsations generally lead the Kotzebue optical pulsations.

8.1 INTRODUCTION

Pulsating aurora in its most traditional form consists of diffuse, irregularly-shaped patches which switch rapidly between 'on' and 'off' states with a quasi-periodicity that covers at least the range from 2 to 20 s. Pulsating patches range in intensity from sub-visual to a maximum of 10 kilo-Rayleighs (kR) in the 428 nm, N_2^+ 1NG (0, 1) band emission. They vary in size from 10 to 100 km across. A number of patches may be simultaneously visible from one site, and each may pulsate independently of the others. East-west aligned pulsating arcs (of width up to 10 km, and length of the order of 1000 km) and randomly oriented arc segments (some 100 km in length) are also observed. Pulsating aurora are most commonly observed equatorward of the auroral oval, after magnetic midnight, and in the recovery phase of an auroral substorm. (Johnstone 1978, Johnstone 1983, Tanskanen 1991).

Experimental evidence strongly supports the mechanism for pulsating aurora being by pitch-angle scattering of stably trapped electrons into the loss-cone in the region of the magnetic equator (Johnstone 1983). Auroral electrons in the equatorial regions can be in resonance

with oppositely propagating, doppler shifted, whistler-mode ELF waves. It is likely that electron pitch-angle diffusion resulting from this wave-particle interaction is the mechanism for generation of pulsating aurora (Johnstone 1983, Tanskanen 1991). If the growth of the ELF waves is controlled by the electron pitch-angle anisotropy generated by the interaction of the electrons and the upper atmosphere, then the quasi-periodicity of the pulsations can be controlled by the electron distributions within individual flux-tubes. For this mechanism to generate pulsations, then, following an equatorial wave-particle interaction leading to an isotropic electron pitch-angle distribution and enhanced precipitation for the next interaction with the ionosphere, atmospheric back-scatter of electrons into the loss-cone must preclude wave growth on the next equatorial passage (Davidson 1986a, b).

Evidence for an equatorial origin for the source mechanism of pulsating aurora comes principally from the velocity dispersal of precipitating pulsating fluxes measured by rockets (Bryant et al. 1975, Smith et al. 1980). This method has yielded rapidly varying distances to the modulation region. Variations from 40,000 km to 90,000 km in under a minute have been reported (Bryant et al. 1975). This implies either a rapid expansion of the magnetosphere or some discrepancy with the assumptions made in inferring the distance (Johnstone 1983).

8.2 SITES, INSTRUMENTATION AND DATA

Macquarie Island (geog: 54.50°S, 159.0°E; PGM – 1988: 64.34°S, 246.9°E) and Kotzebue (geog: 66.9°N, 197.4°E; PGM – 1988: 64.74°N, 248.2°E) are one of few close conjugate pairs at a latitude at which pulsating aurora is commonly observed. We operated wide-angle (60° field-of-view) photometers at Macquarie Island and Kotzebue over the period from 23 September to 2 October 1992. The sites are conjugate in the PGM coordinate system (Baker and Wing 1989) to within 110 km while the photometer fields-of-view amount to 115 km at a 100 km altitude. Using the Tsyganenko (1987) model, Burns et al. (1991) calculate the diurnal range for the Macquarie Island conjugate point during the equinoxes for a Kp level of 3 to be 140 km.

For the period of these observations, simultaneous darkness suitable for photometric auroral observations at both sites extended from 9 to 15 UT. Magnetic midnight for the sites is approximately 1215 UT.

At Kotzebue the $O(^1S - ^1D)$ line emission at 558 nm and the N_2^+ 1NG (0, 1) band emission at 428 nm were monitored using the wide-angle photometers. These emissions, as well as the $O(^1D - ^3P)$ line emission at 630 nm and the N_2^+ 1NG (0, 0) band emission at 391 nm, were monitored at Macquarie Island. All optical channels, with the exception of 391 nm, were calibrated by measurements of a standard lamp. The 391 nm channel was calibrated by comparison with the related 428 nm channel. H and D component induction coils were operated at both sites, but these data are not utilised in this analysis. All channels were recorded digitally at 10 Hz. Timing accuracy was maintained to within 10 milliseconds at Macquarie Island and at Kotzebue by using Austron 8120 chronometers to control the data acquisition.

We intended to use the 558 nm/428 nm ratio as an indicator of the average energy of the incident electrons (Rees and Luckey 1974, Steele and McEwen 1990). At Macquarie

Island, after allowing for airglow and background contributions estimated from measurements of clear, no-moon intervals with no aurora, the 558 nm/428 nm ratios we measured were lower than the accepted values by approximately a factor of two. From 28 hours of pulsating aurora measurements at clear, no-moon times we obtained an average 558 nm/428 nm ratio of 2.5 and from 32 hours of 'non-pulsating' aurora we obtained an average ratio of 2.9. At Kotzebue, from 6 hours of clear, no-moon, pulsating aurora data the average 558 nm/428 nm ratio was even lower at 1.4, and from 10 hours of clear, no-moon, 'non-pulsating' aurora we obtained a ratio of 1.6. At Macquarie Island, from 34 hours of clear, no-moon, airglow observations we obtained an average 558 nm airglow value of 243 R. This value is, if anything, higher than could be reasonably expected. We thus suspect that we have significantly overestimated the 428 nm intensity, perhaps by a factor between two and four. Because the 391 nm intensity is calibrated directly from the 428 nm measurement, it will also be overestimated. In this paper, we persist with using the intensities we have derived from our standard lamp calibration but note the discrepancy in our data.

Additional instrumentation operated at Macquarie Island included an all-sky imager, a ring-core fluxgate magnetometer, a 30 MHz standard riometer and a wide-band, 'fast-response' riometer. The all-sky imager collected 558 nm images integrated over 1 s, with a repetition rate of 6 s. All-sky imager data were recorded on video tape. The ring-core magnetometer and 30 MHz standard riometer data were recorded at one sample every 10 s. The fast-response riometer has a bandwidth of 4 MHz centred around 32 MHz and gives a resolution of 0.02 dB. The fast-response riometer data were recorded at 10 Hz.

8.3 ANALYSIS AND DISCUSSION

The photometric data from the two sites were plotted, examined visually and a cross-correlation analysis was performed on selected segments using the N_2^+ 1NG (0, 0) 391 nm band intensity from Macquarie Island and the N_2^+ 1NG (0, 1) 428 nm band from Kotzebue. The N_2^+ 1NG (0, 0) 391 nm channel is chosen for the Macquarie Island site because of its better 'signal-to-noise' performance compared with the N_2^+ 1NG (0, 1) 428 nm channel. The N_2^+ 1st Negative band emissions are 'allowed transitions' and essentially measure the temporal variation in total electron energy deposited within the field-of-view of the photometers. The N_2^+ 391 nm and 428 nm intensities are related in the ratio 3.28:1. Specific intervals of interest are discussed below.

8.3.1 *1316 – 1319 UT, 29 September 1992*

On 29 September 1992 there was a brief period (1316 to 1319 UT) when the optical pulsations at Macquarie Island and Kotzebue were well correlated. This was a dark moon period and the skies were clear at both sites. The N_2^+ 1NG (0, 0) 391 nm band intensity at Macquarie Island and the N_2^+ 1NG (0, 1) 428 nm band intensity at Kotzebue are presented with the cross-correlation function for this interval in Figure 1. Also shown, as the top panel in Figure 1, is the fast-response riometer time series for this interval. Lines are drawn from selected peaks in the Macquarie Island intensity time series through to the other panels to aid visual interpretation of the alignments.

The cross-correlation function for the selected interval peaks at 0.62 for a lag of -0.5 s. A negative lag indicates that, on average, the Macquarie Island optical pulsations lead the Kotzebue optical pulsations. The similarity of the optical intensity records at the two sites, supported by the cross-correlation function, enables us to conclude that for this interval there is a direct linkage of part of the field-of-view of the wide-angle photometers at the two sites to the same pulsating patch. The width of the cross-correlation function indicates that no significance should be placed on the non-zero time lag. The data are consistent with a modulation region at the geomagnetic equator.

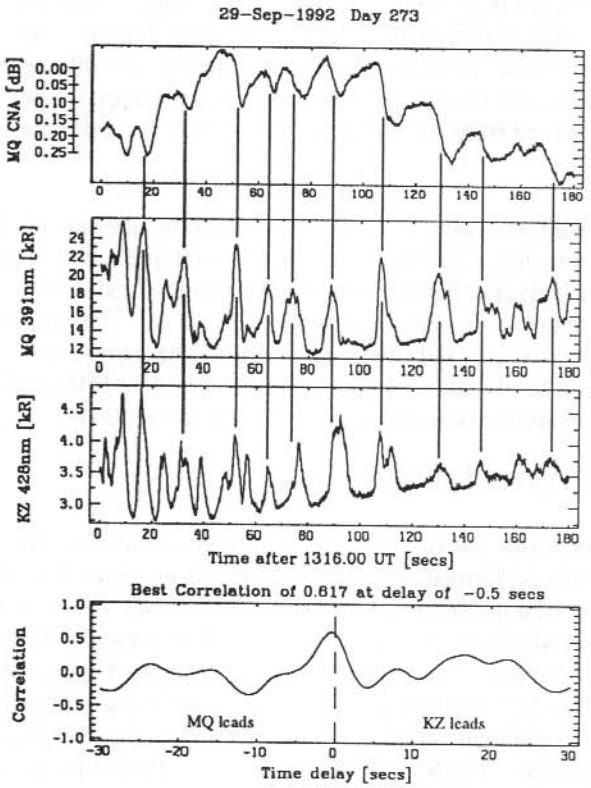

Figure 1. 1316 – 1319 UT, 29 September 1992. Cosmic noise absorption and N_2^+ 1NG (0, 0) 391 nm band intensity at Macquarie Island, and the N_2^+ 1NG (0, 1) 428 nm band intensity at Kotzebue. The cross-correlation function of the optical emissions is shown in the bottom panel. There is correlation of the optical pulsations at the two sites with a near zero lag.

The background cosmic noise absorption (cna) measured at 30 MHz by the standard riometer at Macquarie Island is 4 dB. The pulse-for-pulse association of the optical and cna pulsations and the time delay of the electron recombination process are both apparent in Figure 1. Increased absorption associated with individual optical pulsations ranges from 0.05 to 0.15 dB. These high levels of absorption imply a high energy pulsation event.

The Macquarie Island all-sky images of this event show the dominant optical pulsation patch to be irregular in shape, elongated in a magnetic N – S direction and extending beyond the photometer field-of-view in this direction. Figure 2 shows a one minute sequence of photometric data and associated all-sky images. A complex pattern of auroral activity covers the entire sky at Macquarie Island. There is no indication from the 'sparse' Macquarie Island all-sky images of any horizontal propagation of the intensity variations measured by the photometer beyond the dimensions of the pulsating patch.

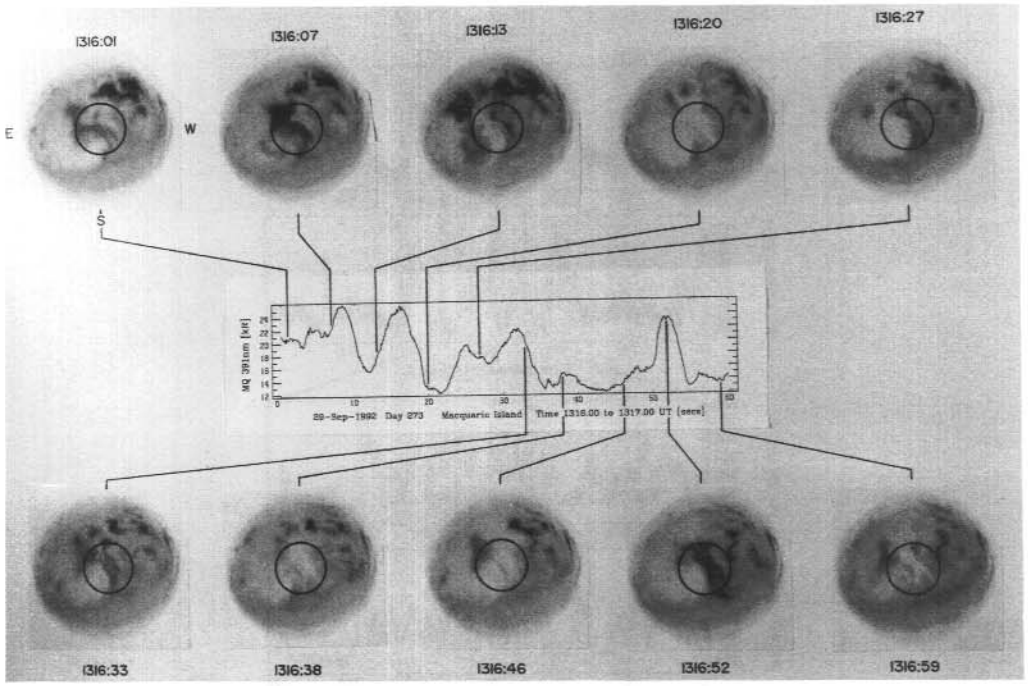

Figure 2. Macquarie Island all-sky images compared with the N_2^+ 1NG (0, 0) 391 nm time series for the interval 1316 – 1317 UT, 29 September 1992. An enhanced intensity appears dark on these images. The field-of-view of the photometers and the geographic orientation of the images (note the lateral inversion) is marked. Magnetic north at Macquarie Island is 29° E of geographic north. The dominant pulsating patch is shown to be of irregular shape, covering an extensive portion of the photometer field-of-view, and elongated in the magnetic N – S direction.

8.3.2 *1400 – 1500 UT, 27 September 1992*

The period from 1400 to 1500 UT on 27 September 1992 contains intervals of strong correlation between the optical pulsations at Macquarie Island and Kotzebue. It is a period of clear sky at Macquarie Island and of patchy cloud at Kotzebue. The optical pulsations are contiguous during the early part of the event but the intervals of pulsations become more widely spaced as the event progresses until individual pulses or brief bursts of pulsations become mosı prevalent. Figures 3, 4 and 5 show segments of the event and selected enhancements and cross-correlations within each segment. The strong correlation of

Macquarie Island and Kotzebue optical pulsations during the event is readily apparent from the ten minute interval intensity time-series plots at the top of these Figures. The rise in the optical intensity at Kotzebue later in the event (see Figure 5) is due to sunrise. The cross-correlation functions for all three intervals support the contention that the Macquarie Island optical pulsations lead the Kotzebue optical pulsations by a significant amount.

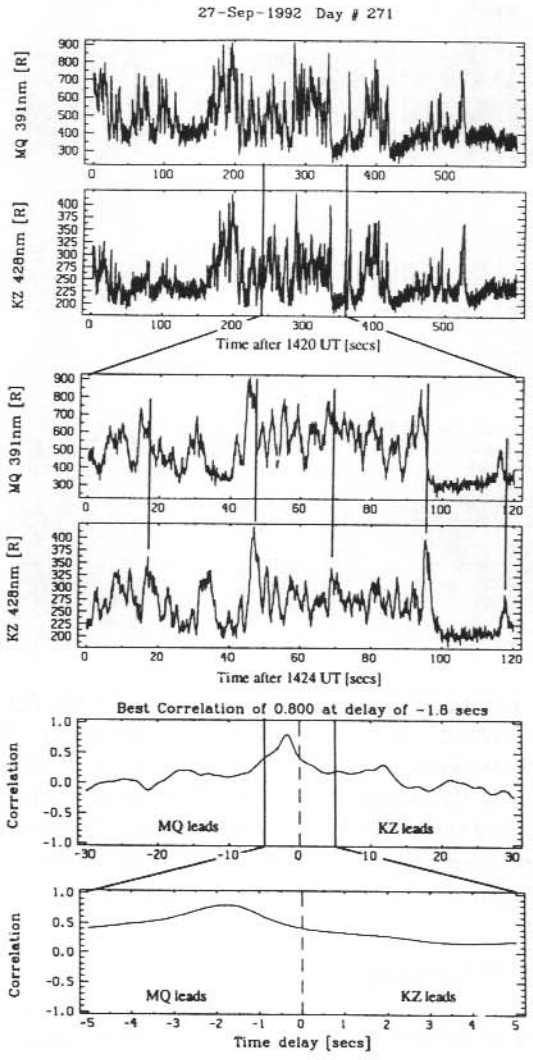

Figure 3. 1420–1430 UT, 27 September 1992. The N_2^+ 1NG (0, 0) 391 nm band time series at Macquarie Island and the N_2^+ 1NG (0, 1) 428 nm band time series at Kotzebue. The interval 1424–1426 UT is shown in expanded format with the associated cross-correlation function. A significant displacement of the modulation region from the mid-point of the field lines linking the sites is apparent.

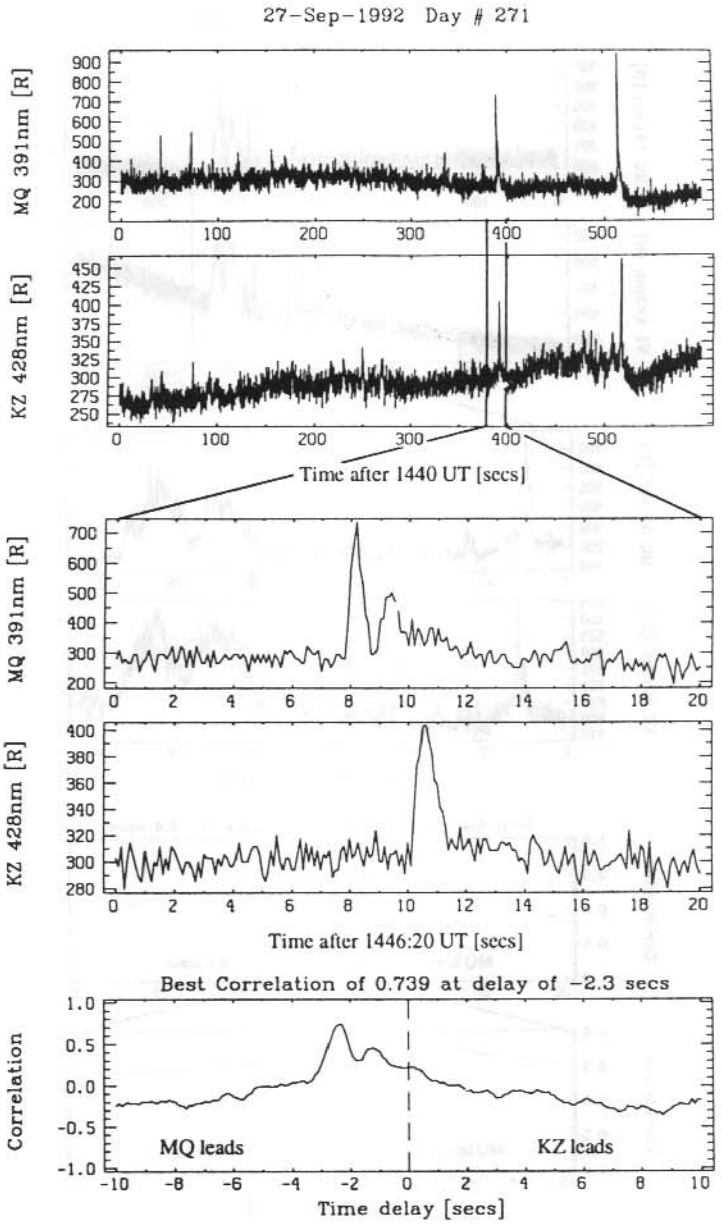

Figure 4. 1440–1450 UT, 27 September 1992. The N_2^+ 1NG (0, 0) 391 nm band time series at Macquarie Island and the N_2^+ 1NG (0, 1) 428 nm band time series at Kotzebue. The interval 1446:20–1446:40 UT is shown in expanded format with the associated cross-correlation function. The isolated pulsation bursts at the two sites are correlated with a significant non-zero lag. Multiple pulses are apparent in the Macquarie Island time series.

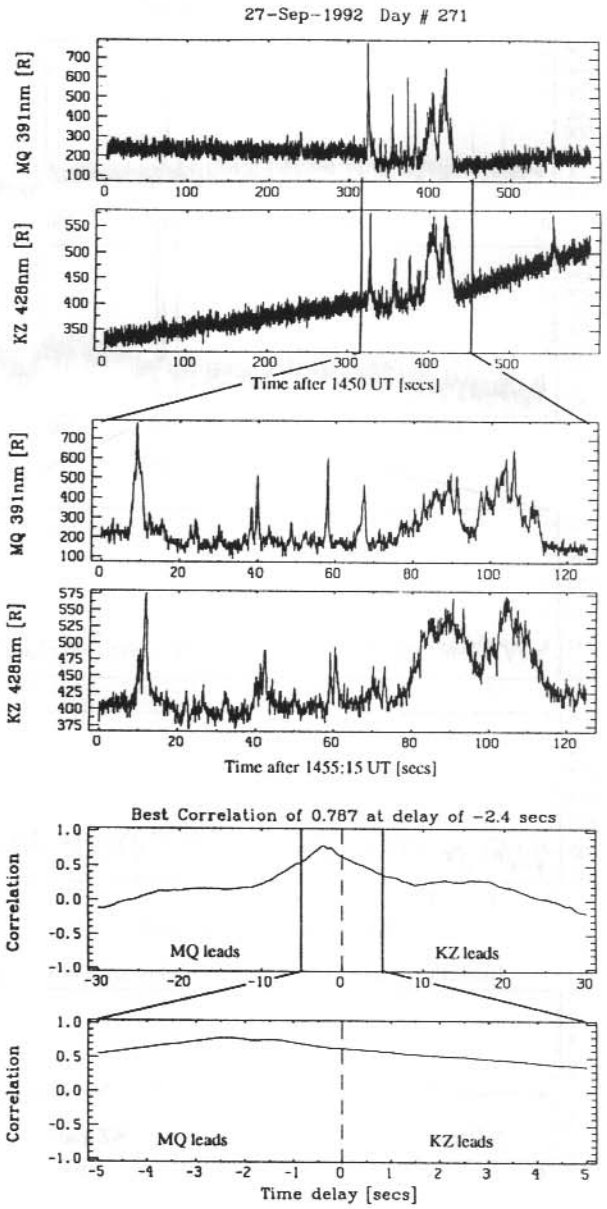

Figure 5. 1450–1500 UT, 27 September 1992. The N_2^+ 1NG (0, 0) 391 nm band time series at Macquarie Island and the N_2^+ 1NG (0, 1) 428 nm band time series at Kotzebue. The interval 1455:15–1457:20 UT is shown in expanded format with the associated cross-correlation function. There is some indication of a double peak in the cross-correlation function.

Table 1 lists some values derived from cross-correlations evaluated for intervals across the event. The interval analysed, the width of the cross-correlation window, the time of the peak correlation and the peak correlation value are shown. A negative lag indicates that the optical pulsations recorded at Macquarie Island preceded the Kotzebue pulsations. For the early part of the event, when the pulsations are contiguous, consecutive two minute cross-correlation intervals are evaluated. During the later stages of the event, particular intervals related to the occurrence of pulsation activity are chosen. There is change from lags of approximately -1.6 s to lags of -2.2 s as the event progresses. The consistency of the measured lags for independent segments within the two intervals, gives confidence in the value of the lags. This consistency also gives credence to a consistent source region

Table 1. Results of the cross-correlation analysis of selected intervals from the September 1992 event. Listed are the interval analysed, the width of the cross-correlation window, the time of the peak correlation and the peak cross-correlation value.

Time Interval	Interval for x-corr	'lag'	X-corr.
1404 – 1406 UT	± 30 s	-2.0 s	0.54
1406 – 1408 UT	± 30 s	-1.8 s	0.43
1408 – 1410 UT	± 30 s	-1.8 s	0.59
1410 – 1412 UT	± 30 s	-1.9 s	0.52
1412 – 1414 UT	± 30 s	-1.7 s	0.56
1414 – 1416 UT	± 30 s	-1.9 s	0.66
1416 – 1418 UT	± 30 s	-1.7 s	0.72
1418 – 1420 UT	± 30 s	-1.6 s	0.72
1420 – 1422 UT	± 30 s	-1.6 s	0.72
1422 – 1424 UT	± 30 s	-1.6 s	0.86
1424 – 1426 UT	± 30 s	-1.6 s	0.80
1426 – 1427 UT	± 30 s	-1.8 s	0.74
1427:30 – 1428:30	± 30 s	-2.1 s	0.58
1446:20 – 1446:40	± 10 s	-2.3 s	0.74
1448:30 – 1448:45	± 5 s	-2.2 s	0.90
1455:15 – 1457:20	± 30 s	-2.4 s	0.79

displaced from the mid-point between the sites or a consistent energy differential between the electrons travelling towards the two hemispheres, for at least the intervals 1404 – 1426 UT and 1446 – 1458 UT.

An interesting feature in Figures 4 and 5 is that there is a reduction in the intensity at both sites following the occurrence of the isolated pulsation bursts. In looking for this effect in the Kotzebue records, some account has to be taken of the general background trend related to sunrise.

There is no absorption apparent on the Macquarie Island 30 MHz riometer for this event. The fast-response riometer indicates that any absorption associated with the pulsation bursts of this event is of the order of the 0.02 dB resolution of the instrument. The incident electrons are thus unlikely to have been very energetic.

8.3.3 *1316 – 1320 UT, 25 September 1992*

Superficially, the optical activity at Macquarie Island and Kotzebue for the period from 1316 – 1320 UT on 25 September 1992, shown in Figure 6, looks to be well correlated. The top two frames show the N_2^+ 1NG (0, 0) 391 nm band intensity at Macquarie Island for the period 1310 – 1320 UT and the N_2^+ 1NG (0, 1) 428 nm band intensity at Kotzebue for the same interval. Optical pulsations that are almost sinusoidal in appearance become more dominant in the later part of the interval at both sites. The sky at Kotzebue was clear at this time but rapidly drifting cloud patches are apparent in the Macquarie Island all-sky video images. The broad scale modulation apparent in the Macquarie Island intensities may thus be a cloud effect. Figure 6 also shows an expansion of the interval 1316 – 1320 UT and the cross-correlation function evaluated for this interval. The cross-correlation function is indicative of two periodic functions drifting in and out of phase. This is readily apparent from an examination of the individual pulse alignments. Lines are drawn from the peaks of the Kotzebue pulses into the Macquarie Island time-series to show how the optical pulses drift in and out of phase at the two sites. In the early part of this interval, up to 1316:40 UT, the optical pulses at the two sites are well correlated but after this time they drift out of phase. These 'almost-sinusoidal' optical pulsations seen at both sites are atypical of pulsating aurora. Pulsating aurora generally has pulses with sharp rise and fall slopes and with variable pulse widths and spacings. The pulse periods at both sites appear to lengthen after 1318:15 UT.

There may be a general expansion of the magnetosphere, and thus a lengthening of the field lines linked to both sites, at this time. This may result in a lengthening of the pulsation period in the manner postulated for the latitude dependent pulsation periods reported by Thomas and Rothwell (1979). There is some indication of an overlap of the dominant Kotzebue pulsations in the Macquarie Island field-of-view. The Kotzebue optical pulsations which occur at 1318:25, 1319 and 1319:40 UT correspond with minor pulsations apparent between the dominant optical pulsations at Macquarie Island. Our conclusion is, however, that the sites are on field lines where similar auroral processes are operating, but because the dominant optical pulsations at each site drift in and out of phase, there is no conclusive evidence that the fields-of-view are linked by the Earth's magnetic field at this time.

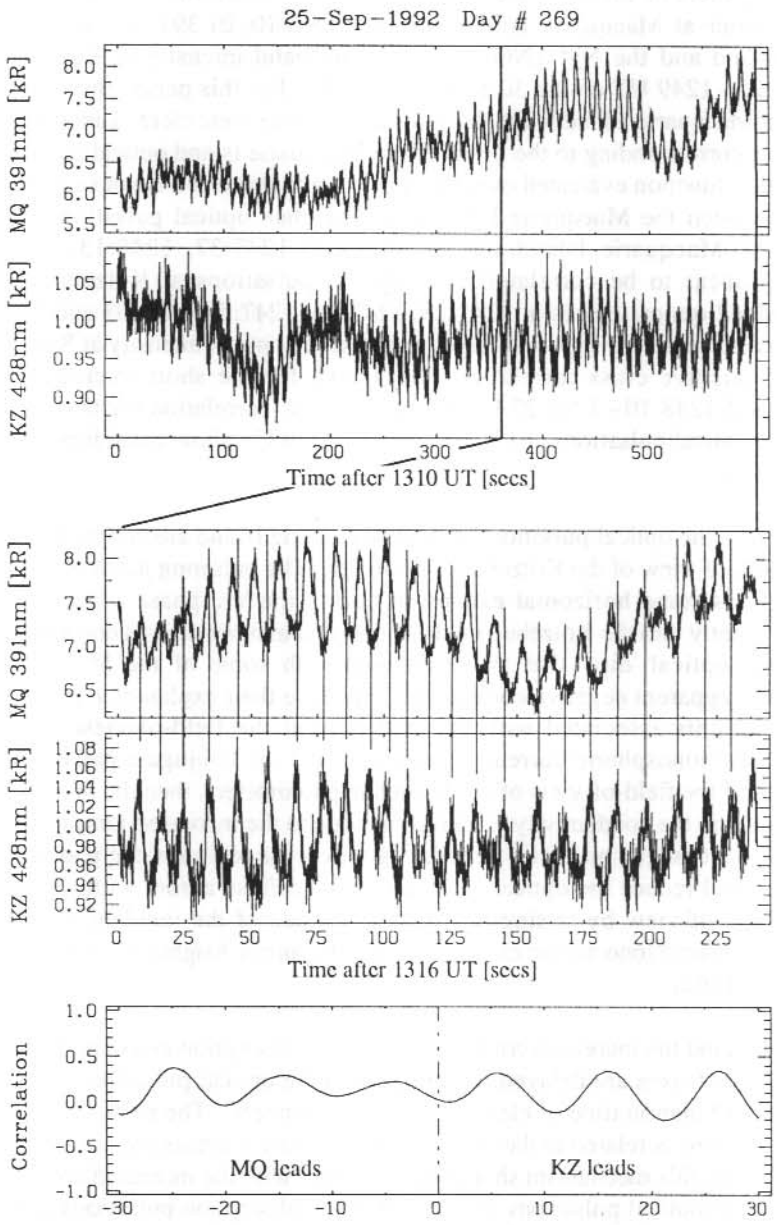

Figure 6. 1310–1320 UT, 25 September 1992. The N_2^+ 1NG (0, 0) 391 nm band time series at Macquarie Island and the N_2^+ 1NG (0, 1) 428 nm band time series at Kotzebue. The interval 1316–1320 UT is shown in expanded format with the associated cross-correlation function. This interval shows pulsations which are superficially similar at the two sites, but the dominant pulsations are uncorrelated.

8.3.4 *1247:25 – 1249 UT, 30 September 1992*

The top three panels of Figure 7 are the cosmic noise absorption measured by the fast-response riometer at Macquarie Island, the N_2^+ 1NG (0, 0) 391 nm band intensity at Macquarie Island and the N_2^+ 1NG (0, 1) 428 nm band intensity at Kotzebue for the interval 1247:25 – 1249 UT on the 30 September 1992. For this period there was variable cloud cover at Macquarie Island while the skies at Kotzebue were clear. Lines link the three panels at times corresponding to the peaks of the Macquarie Island optical pulsations. The cross-correlation function evaluated over the entire period presented is not supportive of any correlation between the Macquarie Island and Kotzebue optical pulsations. On closer inspection, the Macquarie Island optical pulses at 1247:37, 1248:13, 1248:22 and 1248:39 UT appear to be correlated with optical pulsations at Kotzebue, while the Macquarie Island optical pulses at 1247:28, 1247:46, 1247:55 1248:03 and 1248:31 UT appear to be correlated with slightly delayed decreases in optical intensity at Kotzebue. The negative and positive cross-correlations are shown for the short intervals 1247:40 – 1248:10 UT and 1248:10 – 1248:27 UT below the cross-correlation for the entire period. The Kotzebue optical pulsations at 1247:37 and 1248:39 UT show considerable overshoot and slow recovery.

We postulate that the optical pulsations seen at Macquarie Island are conjugate close to the edge of the field-of-view of the Kotzebue photometer. The pulsating patch is likely to be of the form that has some horizontal expansion during the 'on' phase. Occasionally this extends significantly into the Kotzebue field-of-view and at other times a correlated peak can be seen in the optical 'dips' that are associated with some of the Macquarie Island pulsations. The apparent negative correlations may have their explanation in the increased ionospheric currents associated with the 'just beyond the field-of-view' pulsations at Kotzebue. If the ionospheric current is westward and the conjugate patches are on the poleward edge of the field-of-view of the Kotzebue photometers, then the increased current flow resulting from the conductivity enhancement due to the increased ionisation during an 'on' pulse will increase the magnetic field strength over the region of the photometer field-of-view. This will reduce the optical intensity of any diffuse aurora within the Kotzebue photometer field-of-view by raising the 'mirror' altitude of the incident electrons. The possibility of enhanced ionospheric currents raising the mirror height of incident electrons is raised by Cole (1962).

At Macquarie Island the increased conductivity and the absorption associated with incident pulsating electron fluxes are delayed with respect to the optical pulsations because of the significant recombination time of electrons in the ionosphere. The enhanced mirroring of the incident electrons is related to the increased ionospheric currents and the decrease in the optical intensity by this mechanism should be correlated with the increased absorption. The delay between the optical pulsations and cosmic noise absorption pulsations at Macquarie Island over the interval considered is 1.2 s, similar to the 1.3 s delay measured for the negative correlation between the Macquarie Island and Kotzebue optical pulsations for the 1247:40 – 1248:10 UT interval.

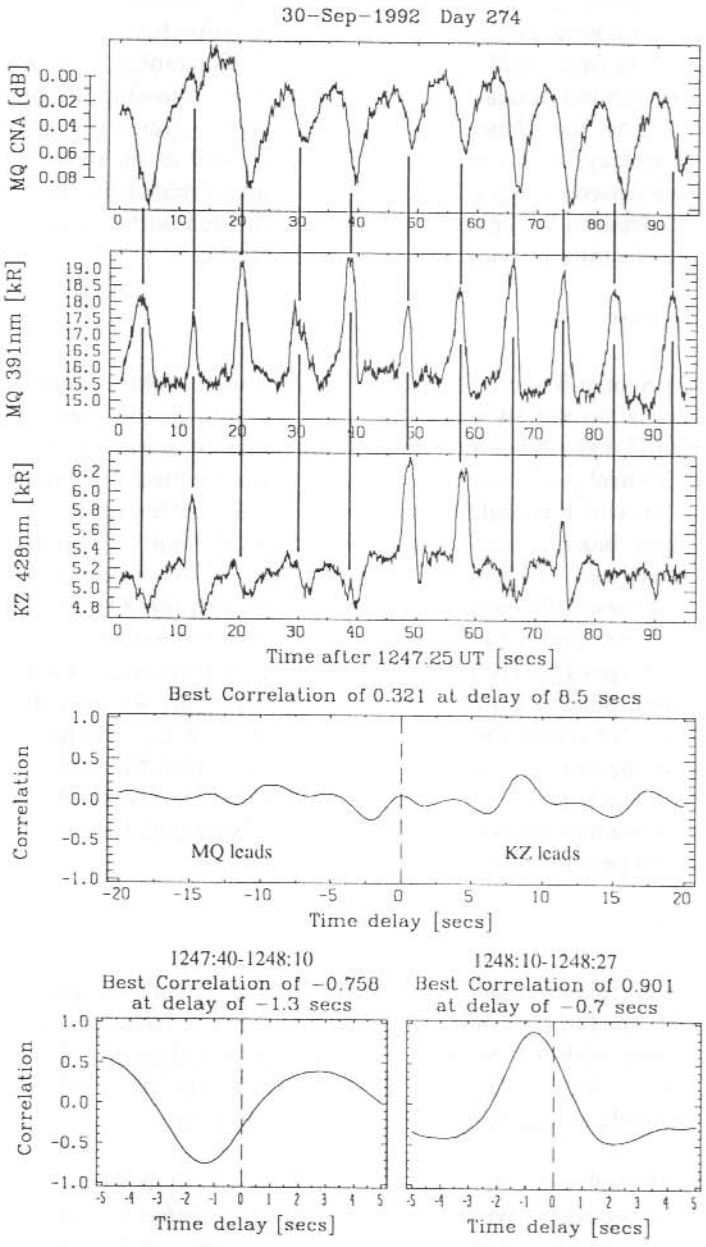

Figure 7. 1247:25 – 1249 UT, 30 September 1992. Cosmic noise absorption and N_2^+ 1NG (0, 0) 391 nm band intensity at Macquarie Island, and the N_2^+ 1NG (0, 1) 428 nm band intensity at Kotzebue. Negative and positive cross-correlations are shown for the short intervals 1247:40 – 1248:10 UT and 1248:10 – 1248:27 UT below the cross-correlation for the entire period.

It is not necessary to postulate a rise in the 'mirror' altitude in order to decrease the optical intensity following an optical pulsation. In some of the individual pulsations seen in the later stages of the event from 1400–1500 UT on the 27 September, there is an apparent decrease in the background optical intensity at both sites following the pulsations (see Figures 3 and 4). The 'on' phase of optical pulsations is generally associated with increased average energy of the incident electrons as well as an isotopic pitch-angle distribution. This increased energy imparted at the equatorial modulation region may result in an interval of decreased background intensity associated with the delay of the less energetic 'off' phase electrons arriving after the optical pulsation.

8.3.5 *Overall Statistics*

From the period 23 September to 2 October 1992, there were eight nights on which some conjugate optical pulsation activity was observed between Macquarie Island and Kotzebue. It was generally found that, within the limitations on the accuracy of the determination of the lag between the optical pulsations at the conjugate sites, the measured lag was consistent for those intervals for which it could be measured over at least ten minutes. Considering the data in ten-minute blocks, there were 107 intervals (17 hours 50 minutes) for which optical pulsation activity was observed at Macquarie Island. No consideration was given to cloud conditions. Of these 107 ten-minute intervals there were 49 (8 hours 10 minutes) for which a cross-correlation analysis of some segment of that ten-minutes convinced us that there was a direct linkage of part of the field-of-view of the wide-angle photometers at the two sites to the same pulsating aurora patch(es). There were 44 ten-minute intervals (7 hours 20 minutes) for which there were no indications of any linkage of the optical pulsation activity at the two sites and 14 (2 hours 20 minutes) for which we could not decide the appropriate allocation. There were 36 ten-minute intervals for which we were prepared to assign an average lag between the Macquarie Island and Kotzebue sites. All but two of the lags ranged between -2.4 s and +0.8 s.

8.4 CONCLUSIONS

We have used cross-correlation analysis to determine the temporal conjugacy of intervals of pulsating aurora recorded at the conjugate sites of Macquarie Island and Kotzebue. The evidence is consistent with a modulation of the pulsating fluxes in the region of the geomagnetic equator. For the data we have examined, the Macquarie Island optical pulsations are more likely to lead the Kotzebue optical pulsations.

Significant temporal displacements of 1.6 s and 2.2 s are found to be stable for periods of 22 and 12 minutes respectively. We cannot distinguish if the differences are due to a source region displaced from the mid-point between the two sites, or to a consistent energy differential between the electrons travelling towards the two hemispheres. The constancy of a significant lag over intervals of 22 and 12 minutes means that it is likely that both the source region and the average energy of the electrons remained constant for these intervals. On at least these occasions, the source region is not varying as dramatically as has been inferred at times from rocket measurements of velocity dispersal (Bryant et al. 1975). It is unlikely that the source region and average electron energy would vary in a consistent manner so as to maintain the measured time differential. Such conclusions cannot be drawn for intervals when the time differential is close to zero, as the average electron energy can

vary, and the distance to the source region can vary by increasing the length of the linking field line, without altering the zero lag.

On the balance of probabilities, it is significant that the largest temporal displacements are measured for the least energetic pulsations. A source region displaced from the mid-point between two conjugate sites has a larger temporal displacement for lower average electron energies.

Evidence has been presented that for the later part of the event on 27 September 1992 we may be seeing the signature of two modulation regions slightly displaced from each other along a linking magnetic field line. Some of the cross-correlation functions for this event show a secondary peak at a lag slightly displaced from the lag of the dominant correlation.

The event between 1316–1320 UT on 25 September 1992 shows an interval of quasi-sinusoidal pulsations at both sites that are not conjugate. These atypical examples of pulsating aurora may be an example of a resonance condition dependent on the inter-hemispheric length of the flux tube in which the pulsations are occurring.

An interesting event of negatively correlated optical time series is explained in terms of a precipitation induced ionospheric current modulation raising the altitude of the 'mirror' point of diffuse aurora.

The sharp temporal gradients of optical intensity in pulsating aurora have proved to be good time markers for an investigation of the source region of the modulated fluxes and the conjugate photometric time series have also proved useful in examining some interesting aspects of pulsating aurora.

8.5 ACKNOWLEDGMENTS

At Kotzebue, the equipment was set up at the Chukchi Community College, which is a branch campus of the University of Alaska. The assistance of personnel from the College, particularly by Mr Lynn Johnson, the Director of the College, was essential to the success of this project. Dr. R. Gattinger of the National Research Council, Ottawa, Canada assisted by providing programs on the band profiles of the N_2^+ 1NG emissions. Helpful discussions with Dr. Don McEwen are gratefully acknowledged. The manufacture of research instrumentation and the maintenance of remote observatory facilities requires the concerted effort of many people. To those who assisted with the collection of these data, our thanks.

REFERENCES

Baker, K.B. *and* Wing, S. (1989). A new magnetic coordinate system for conjugate studies at high latitudes. *Journal of Geophysical Research 94*:9139–9143.

Bryant, D.A., Smith, M.J. *and* Courtier, G.-M. (1975). Distant modulation of electron intensity during the expansion phase of an auroral substorm. *Planetary and Space Science 23*:867–868.

Burns, G.B., McEwen, D.J., Steele, D. *and* Hearn, D. (1991). Optical auroral conjugacy: history and potential. In Australian upper atmospheric and magnetospheric physics research in Antarctica, 1991. *ANARE Research Notes Number 80*. Pp. 283 – 300.

Cole, K.D. (1962). Interaction of trapped radiation and the DS current system. *Journal of the Physical Society of Japan. 17(Supplement A1)*:296 – 300.

Davidson, G.T. (1986a). Pitch angle diffusion in the morningside aurorae. I. The role of the loss cone in the formation of impulsive bursts of precipitation. *Journal of Geophysical Research 91*:4413 – 4427.

Davidson, G.T. (1986b). Pitch angle diffusion in the morningside aurorae 2. The formation of repetitive auroral pulsations. *Journal of Geophysical Research 91*:4429 – 4436.

Johnstone, A.D. (1978). Pulsating aurora. *Nature 274*:119 – 126.

Johnstone, A.D. (1983). The mechanism of pulsating aurora. *Annales Geophysicae 1*:397 – 410.

Rees, M.H. *and* Lucky, D. (1974). Auroral electron energy derived from the ratio of spectroscopic emissions. I. Model calculations. *Journal of Geophysical Research 82*:5181 – 5186.

Smith M.J., Bryant, D.A. *and* Edwards, T. (1980). Pulsations in auroral electrons and positive ions. *Journal of atmospheric and terrestrial Physics 42*:167 – 178.

Steele, D.P. *and* McEwen, D.J. (1990). Electron auroral excitation efficiencies and intensity ratios. *Journal of Geophysical Research 95*:10321 – 10336.

Tanskanen, P.J. (1991). The pulsating aurora and its relationship to fields and charged-particle precipitation. In: Meng, C.-I, Rycroft, M.J. and Frank, L.A. (Eds). *Auroral physics*. Cambridge University Press. Pp. 351 – 360.

Thomas, R.W. *and* Rothwell, P. (1979). A latitude effect in the periodicity of auroral pulsating patches. *Journal of atmospheric and terrestrial Physics 41*:1179 – 1184.

Tsyganenko, N.A. (1987). Global quantitative models of the geomagnetic field in the cislunar magnetosphere for different disturbance levels. *Planetary and Space Science 35*:1347 – 1358.

9. DEPLOYMENT OF A DIGISONDE PORTABLE SOUNDER-4 AT CASEY STATION, ANTARCTICA

D.P. Monselesan[1], P.R. Smith[2], R.J. Morris[1] and P.L. Dyson[3]

[1] Auroral and Space Physics
Antarctic Division
Kingston Tasmania 7050
Australia

[2] Departments of Physics and of Electronic Engineering
La Trobe University
Bundoora Victoria 3083
Australia

[3] Department of Physics
La Trobe University
Bundoora Victoria 3083
Australia

ABSTRACT

The austral Summer 1992/1993 saw the installation of a Digisonde Portable Sounder-4 (DPS-4) purchased by the Australian Antarctic Division at Casey station, Antarctica. The DPS-4, developed by the University of Lowell Centre for Atmospheric Physics (ULCAR), is a pulse Doppler HF sounder, which measures amplitude, phase, range, frequency, Doppler shift, angle of arrival and wave polarisation from ionospheric echoes. The instrument, deployed by the 46th Australian National Antarctic Research Expedition (ANARE), has been in operation since the 7th of February 1993.

This paper intends to introduce Casey's new facility to the ionospheric research community. The enhanced capabilities of the DPS-4 over conventional ionosondes will contribute to a better understanding of the ionospheric structures and dynamics prevailing over Casey, a polar cap station. Preliminary results already show the emergence diurnal and seasonal patterns in both ionograms and plasma drift measurements.

9.1 INTRODUCTION

Casey, Antarctica is a polar cap station, although it changes from polar cap conditions to polar cleft and auroral oval conditions during the diurnal cycle as a function of magnetic activity and seasonal variability. Table 1 summarises Casey's geographic and geomagnetic parameters.

During the 1992/1993 austral Summer a Lowell Digisonde Portable Sounder 4 was installed at Casey, see Figure 1. In its first year of operation, the instrument has been used mainly to study the behaviour of the ionosphere from routine measurements of the electron density profile and large-scale convection of F-region plasma.

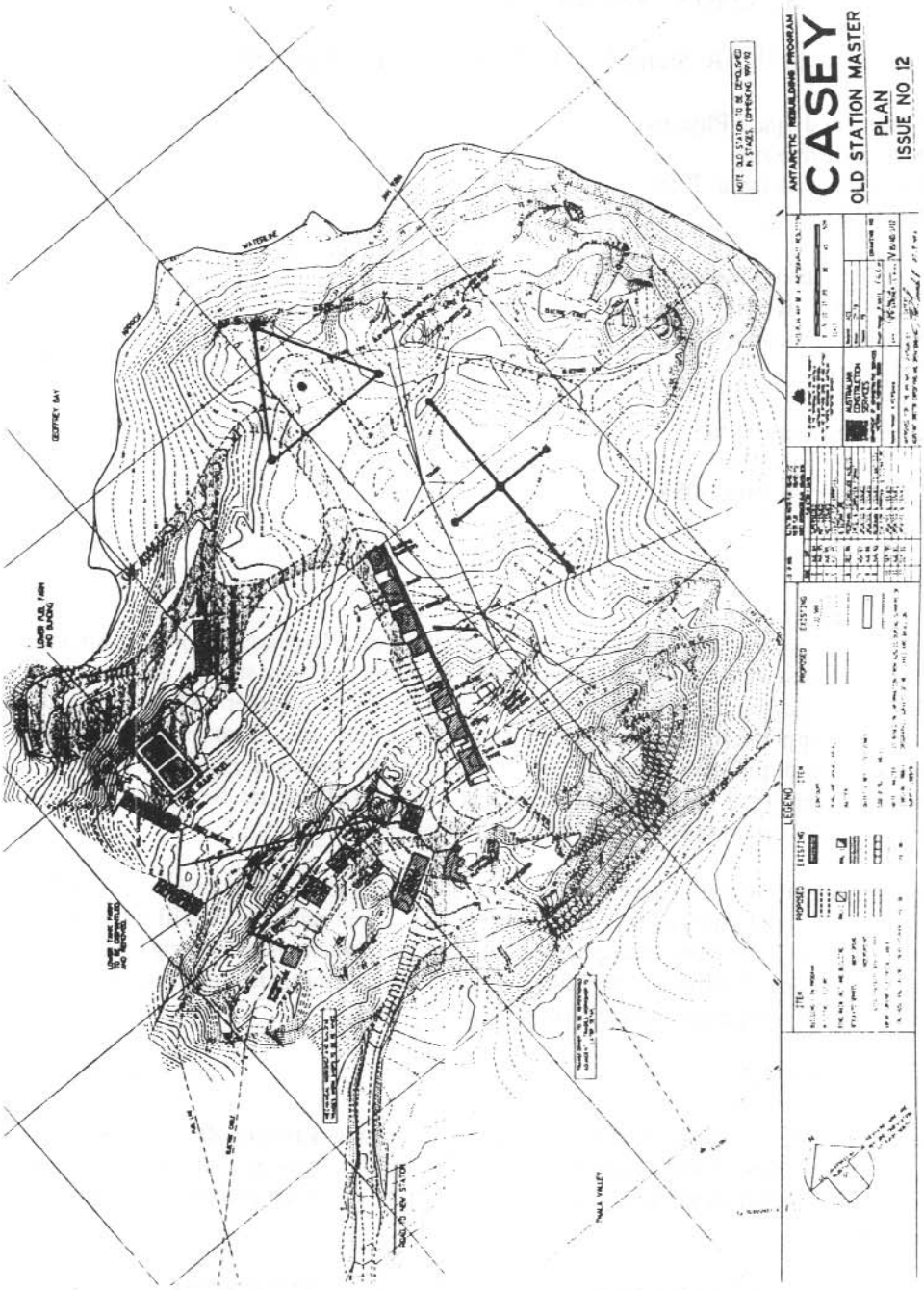

Figure 1. Topographic map of Casey Old Station showing the transmit (cross) and receive (triangle) antenna sites on the peninsula overlooking Newcomb Bay.

Table 1. Geophysical parameters for Casey, derived from the PGM magnetic coordinate system for epoch 1988. Magnetic noon and midnight times correspond to annual averages of magnetic local versus UT times.

Geographic latitude and longitude	66.3 S	110.5 E
Geomagnetic latitude and longitude	80.4 S	156.1 E
Magnetic noon and midnight	0615 UT	1816 UT

Special campaigns are currently underway to study rapidly varying phenomena such as the effects of magnetic micropulsations on the ionosphere and micro-convection regimes occurring around magnetic local noon.

In Sections 9.2 and 9.3, we will describe the DPS-4 system and measurement capabilities. Preliminary results will be discussed in Section 9.4 and Section 9.5 will summarise the different applications in which the DPS-4 may be useful.

9.2 THE DIGISONDE PORTABLE SOUNDER-4

The Digisonde Portable Sounder-4 (DPS-4) is the latest development in the series of ULCAR digital ionosondes (Bibl et al. 1975, Bibl and Reinisch 1978, Reinisch 1986, Haines and Reinisch 1992). The DPS-4 is a computer controlled pulse Doppler radar. It utilises coherent transmission and reception; that is, each transmitted pulse and the receiver local oscillator are synchronised to a free running, highly stable 16 MHz oscillator (frequency stability: 5×10^{-7}). The coherent transmission of long coded pulses – 533 μs long 8-bit complementary phase-coded pulses – and the subsequent coherent processing of the received echoes to obtain narrow pulses – nominally 66 μs after compression – enhance the detection capability of the instrument, while retaining the range resolution of a narrow-pulse system (Skolnik 1990).

The sounder has been especially designed to measure the range, the location and the velocity of multiple ionospheric reflection points, using a Doppler filtering technique to separate in the frequency domain the echoes overlapping in the time domain. Pulse compression combined with a fast Fourier analysis of the signals received on a four-antenna array is performed on a built-in Digital Signal Processing unit (DSP). This technique has several advantages; it increases the range and Doppler resolutions and improves the signal-to-noise ratio, allowing to operate the transmitter at a lower peak power, reducing therefore the size of power-amplifier stage, the cost of operation and, finally, the level of HF interference generated by the instrument.

The DPS-4 operates at the following Pulse Repetition Frequencies (PRF's) 50, 100 and 200 Hz, effectively halved by the implemented pulse compression. Therefore, the corresponding maximum available Doppler ranges are 12.5, 25 and 50 Hz. The Doppler

Coherent Integrations Times (CIT's) stretch over 2 x 2^N transmit pulses (N = 3 ... 7) resulting after DSP processing in a complex 2^N lines Doppler spectrum per receive antenna, frequency, height and polarisation. The Doppler resolution of the instrument is simply equal to the Doppler range divided by the number of Doppler lines, 2^N in each spectrum.

The instrument Doppler resolution may be further improved by multiplexing or interlacing CITs for as many as 16 frequencies and 2 polarisations. The resulting sampled data for each receiver are stored and processed in separate data buffers on the DSP board such that a unique Doppler spectrum may be calculated for each combination of frequency and polarisation, increasing the Doppler resolution by a factor 32 at maximum.

9.2.1 *System Overview*

The real-time control of the hardware is performed on a 386 PC clone main logic board expanded with a digitiser and a signal processing unit as well as interfaced to Lowell's custom hardware comprising a timing, an oscillator, a synthetiser, a transmitter-exciter and four receiver boards.

High level C and low-level assembly routines control the user interface, the communication protocol with remote sites, the precision timing, the frequency sequencing, the transmitter waveform selection, the receive antenna configuration, the receiver gain selection and, ultimately, the data acquisition, processing and transfer, from the digital signal processing unit to the main logic board.

The menu driven user interface allows the operator to modify interactively operational parameters between measurements. For unattended operation, the DPS-4 main system and a remote PC clone communicate via modems by a dedicated land line. Two 12 Volt batteries are used as a backup power supply, an other advantage of the low power consumption of the DPS-4 HF amplifier stage.

Precision timing is currently ensured by synchronising the instrument to a one Pulse-Per-Second (PPS) external reference signal. At Casey station, this one PPS signal is provided by a low drift Austron clock manually synchronised to the Casey, Auroral and Space Physics laboratory satellite clock to the nearest second, although an automatic time synchronisation routine that interrogates directly a satellite clock has been implemented on the DPS-4 by Lowell.

9.2.2 *Transmit Antenna*

The transmit antenna is a cross rhombic, see Figure 2. The main central tower is 45 m high, the satellite masts, 25 m. The compass oriented North/South and East/West arms, have different dimensions – 60 and 90 m long respectively – to compensate for nulls in the antenna frequency response inherent to the geometry of the cross rhombic elements. The Casey transmit antenna has a reasonably good frequency response up to 18 MHz (Dyson 1993).

Two 250 Watts peak solid-state power-amplifier channels feed the cross rhombic North/South and East/West elements via a pair of 60 m coaxial cables electrically matched in length according to Lowell specifications (ULCAR 1990, 1993).

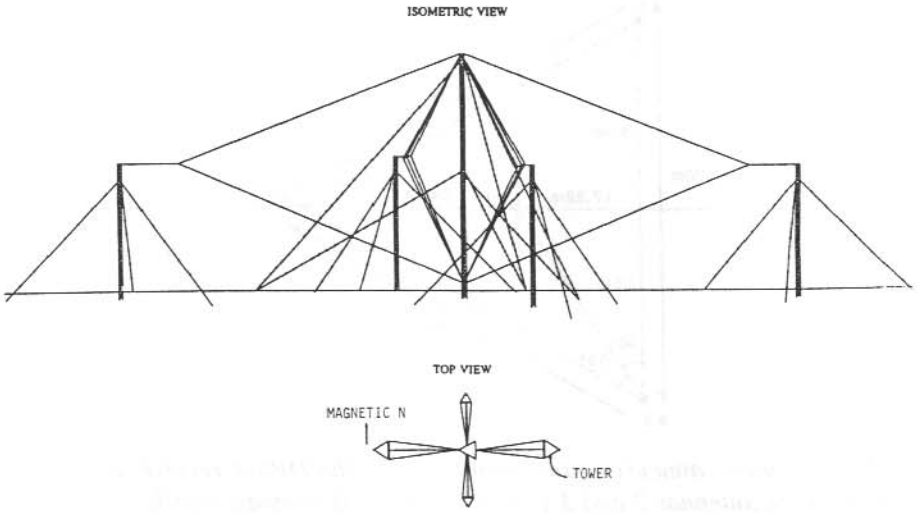

Figure 2. Isometric view, dimension and orientation of the DPS-4 cross-rhombic transmit antenna. The short and long axes are oriented along compass East/West and North/South respectively.

9.2.3 *Receive Antenna Array*

The DPS-4 receiving antenna array consists of four crossed loop antennas located at the vertices and the centre of an equilateral triangle, see Figure 3. Antennas 2, 3 and 4 are arranged anti-clockwise, with the line between antennas 2 and 3 pointing towards compass North. The separation between the outer antennas is 60 m.

Each single receive antenna consists of two crossed loops of 1.51 m diameter, perpendicular to each other, the antenna loop elements run inside a PCV pipe skeleton for support, see Figure 4. The right angle cross, viewed from the top on Figure 5, is oriented along compass North/East and South/East directions. Both loops are connected to a broad-band preamplifier, combined with a polarisation switch, which segregates ordinary and extraordinary echoes upon reception.

The four receive signals are fed to the DPS main system through four 150 m long, electrically matched coaxial cables. Each individual receive antenna has its own receiver. A simultaneous sampling of the four receive signals is therefore possible, increasing the

overall Doppler range of the instrument for a given pulse repetition frequency: the main feature of the DPS-4 model.

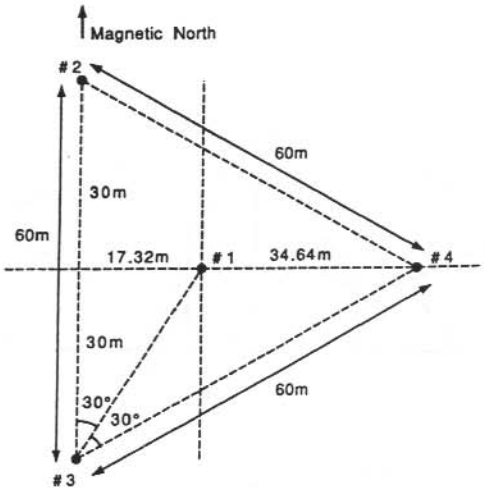

Figure 3. Top view, dimension and orientation of the DPS-4 receive antenna array. The line between antennas 2 and 3 is pointing towards compass North.

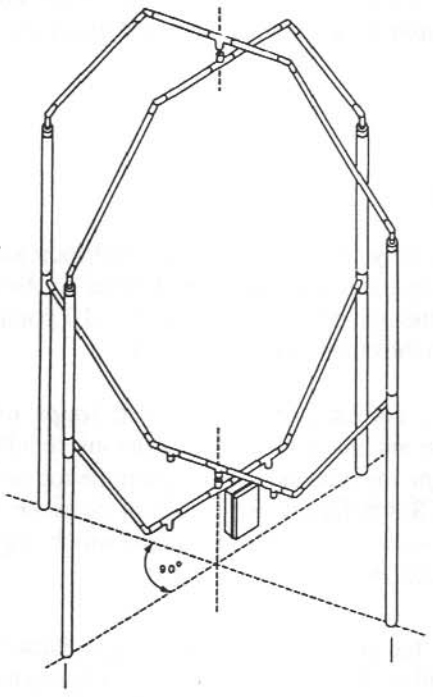

Figure 4. High gauge PVC pipe skeleton housing the cross-loop antenna elements.

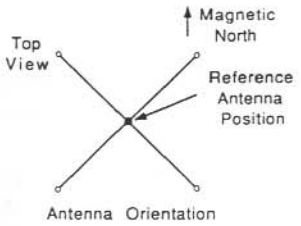

Figure 5. Receive antenna top view showing the loop orientation with respect to compass bearings.

9.3 OPERATION MODES

Standard modes of operation produce ionograms, but unlike conventional ionosondes, the DPS-4 has the capacity to:

a. differentiate between ordinary and extraordinary wave polarisations,

b. determine the Doppler shifts (Doppler sensitive scanning) or the angles of arrival (direction sensitive scanning) of the incoming waves,

c. measure accurate reflection heights (precision group height scanning) of the returned echoes by comparing the phase of two closely spaced frequencies using a differential phase technique,

$$\frac{\phi_2 - \phi_1}{f_2 - f_1}$$

It is also possible to operate the DPS in a radio silent mode for bistatic experiments using extra-long pulses to improve detection. Ionograms may be scaled automatically by the Stand-alone Automatic Real-Time Ionogram Scaler with True-height software package (SARTIST) which then calculates the true height electron density profile in real-time (Reinisch and Huang 1982, Reinisch et al. 1982). The results may be displayed, edited and printed out by the ARTIST Data Editing and Processing (ADEP) software developed by Lowell (ULCAR 1992), see Figures 6 and 7.

Fixed frequency measurements, combined with long CITs, provide a second category of operation modes. While operating at selected frequencies, the DPS-4 can coherently integrate in time the returned echoes sampled at specific heights on each individual receiving antenna. The data, buffered on the DSP unit, are then processed between CITs. The result, a Doppler spectra for each frequency, height, polarisation and antenna, are ultimately stored as raw data on the system backup facility.

The main purpose of drift measurements is to determine accurately the location and the velocity of ionospheric reflection points. The determination of these observables is not performed in real-time. The Drift Data Analysis (DDA) software package provided by

ULCAR (Scali and Reinisch 1992) may be used to convert the raw Doppler spectra into skymaps and velocity graphs, see Figures 8 and 9.

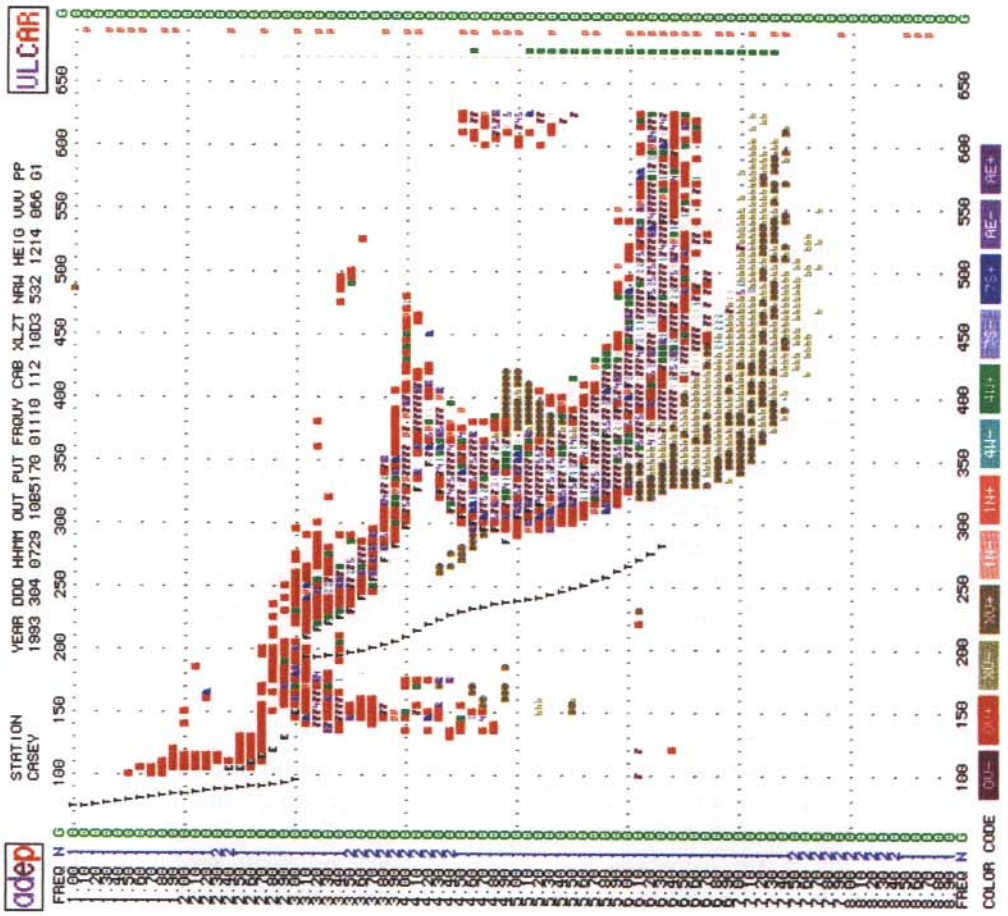

Figure 6. SARTIST scaled direction sensitive scanning ionogram recorded at 0729 UT on 31 October 1993. The ionogram shows four distinct layers: a normal E-layer (E) from 1.5 to 3.0 MHz, a sporadic E-layer extending from 2.7 to 5.0 MHz and the F-layer (F), subdivided into F1 and F2 layers. Autoscaled traces h'(f) and electron density true-height profile (T) are superimposed on the raw ionogram. Colour coded optifonts provide coarse Doppler (1 bit for ± Doppler) and angle of arrival (3 bits for vertical, oblique, North, West, South and East) information as well as differentiate between Ordinary (O) and Extraordinary (X) wave polarisation's.

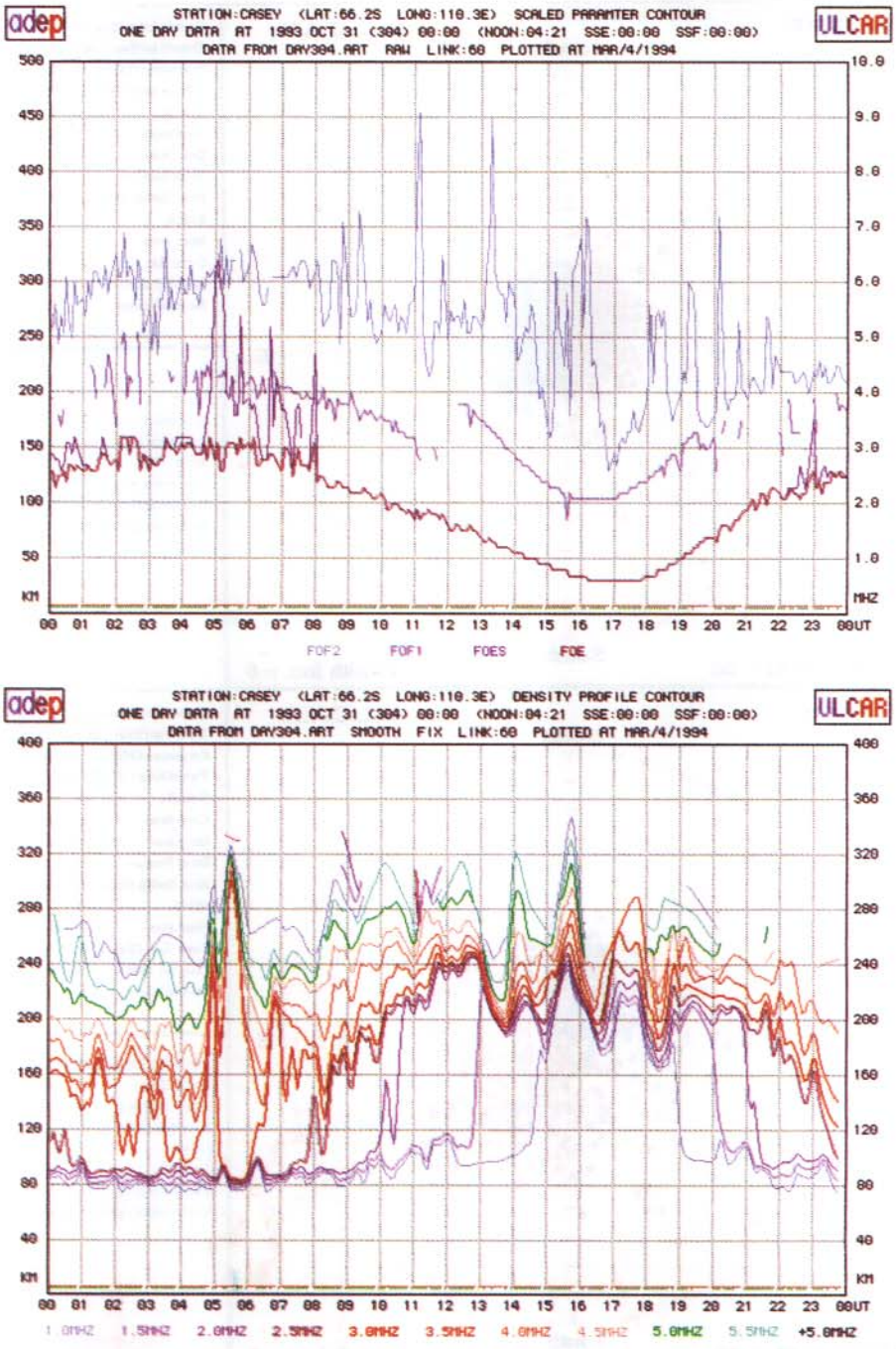

Figure 7. FoF2, foF1, foEs, foE and electron density profile variation over 24 hours UT for 31 October 1993. Sporadic E activity mainly occurs in a four hour period centred around 0600 UT on that day. SARTIST managed to scale raw ionograms despite the presence of a strong sporadic E-layer.

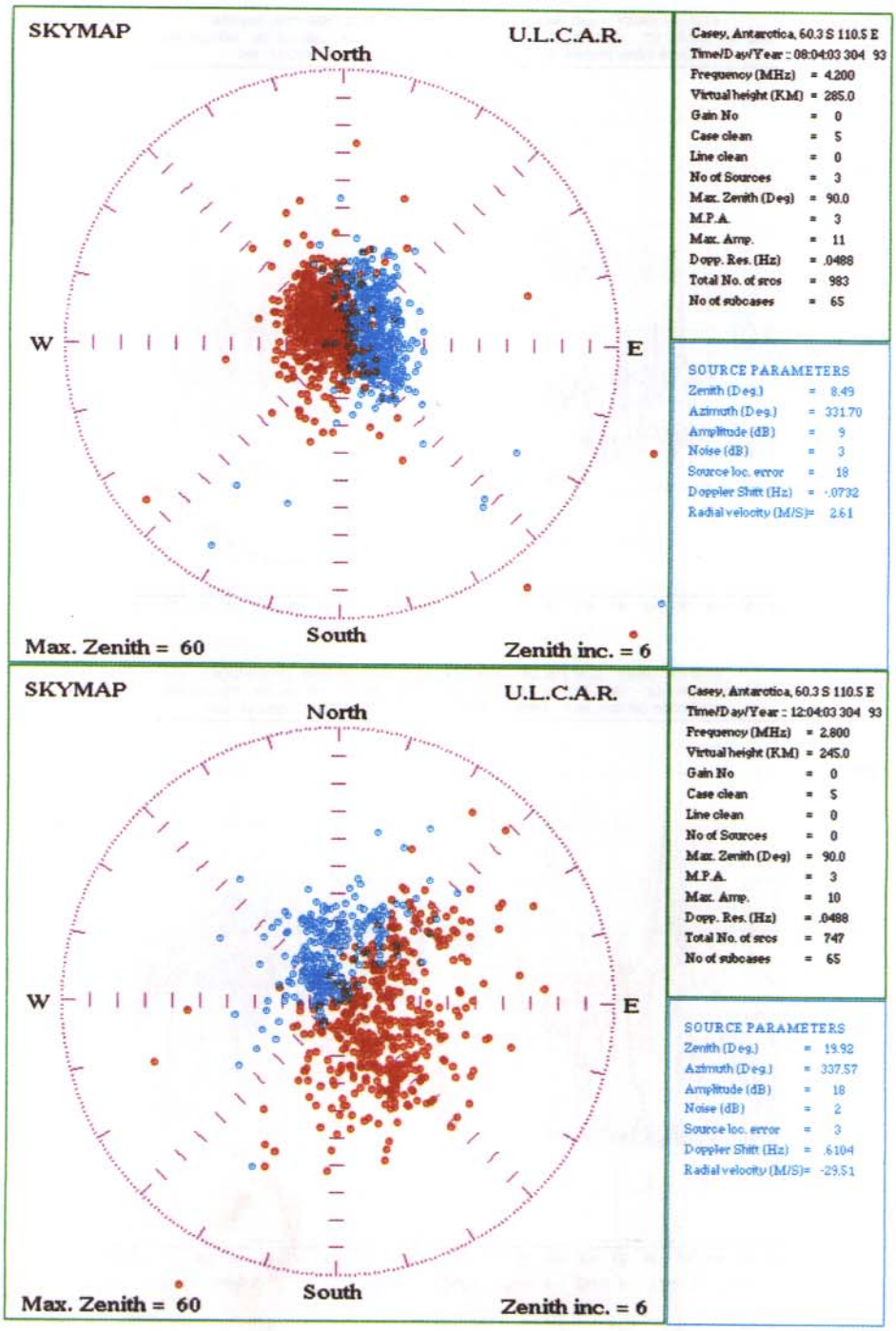

Figure 8. Skymap showing the distribution of ionospheric echoes over Casey in a geomagnetic reference system (compass) at 0804 and 1204 UT on 31 October 1993. The echoes are colour coded: red for negative Doppler and blue for positive Doppler.

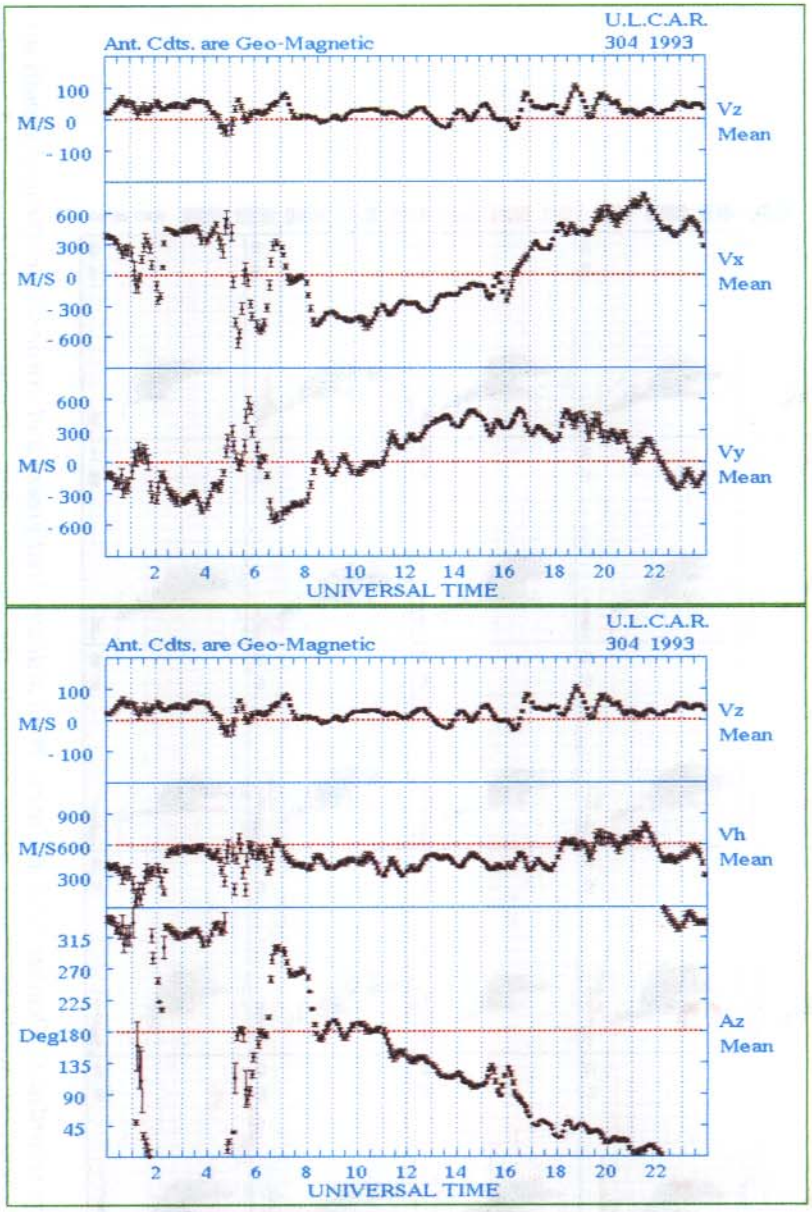

Figure 9. Velocity charts showing the electron drift over a 24 hour period on 31 October 1993. The velocity components Vx and Vy are pointing towards compass North and East respectively. The drift as a function of magnetic local time is consistent with a two-cell convection, in which the throat of the convection has been moved 2 to 3 hours in the afternoon sector. Sharp deviations from two-cell convection are clearly noticeable around 0130 and 0600 UT on the Vx and Vy velocity components. During both periods, the azimuth angle Az runs through 360° before following the usual drift pattern again.

Figure 10. Ionogram survey recorded 31 October 1993 at Casey. Both ordinary (red/green) and extraordinary (brown) signals are displayed. Red optifonts represent overhead echoes, green optifonts, the oblique ones. Ionograms are shown at 5 minute intervals over 2 hours from 0434 to 0644 UT. The frequency axis (horizontal) runs from 1 to 16 MHz, the height axis (vertical), from 50 to 750 km.

The technique, based on interferometry, deduces the angle of arrival of the incoming echoes – already separated in the Doppler domain – from the phase differences made on the four spaced receive antennas for all relevant Doppler lines in the raw spectra. Once the distribution of the reflection points has been deduced by interferometry, the plasma bulk velocity may be derived by a least-square fit, assuming for example an uniform velocity over the field of view of the instrument. By relaxing the former condition of uniformity, it may even be possible to probe the ionosphere for more detailed convection features within the field of view, provided the number of returned echoes is high enough to be statistically representative.

9.4 OBSERVATIONS

The DPS-4 has been in operation since the 7th of February 1993. Initial observations have been made using a routine setup, in which an ionogram followed by a sequence of drift measurements were obtained every 15 minutes. Since the end of August 1993, the sounding rate has been increased to 5 minutes.

The ionograms are scaled automatically by the SARTIST software, which then calculates the true height electron profile in real-time. The DPS-4 automatically selects a frequency for drift measurements, the drift frequency selection being derived from the scaling results and set to fmin + (foF2-fminF)/3, such that echoes will be reflected by the F-layer from a region with approximately minimum retardation.

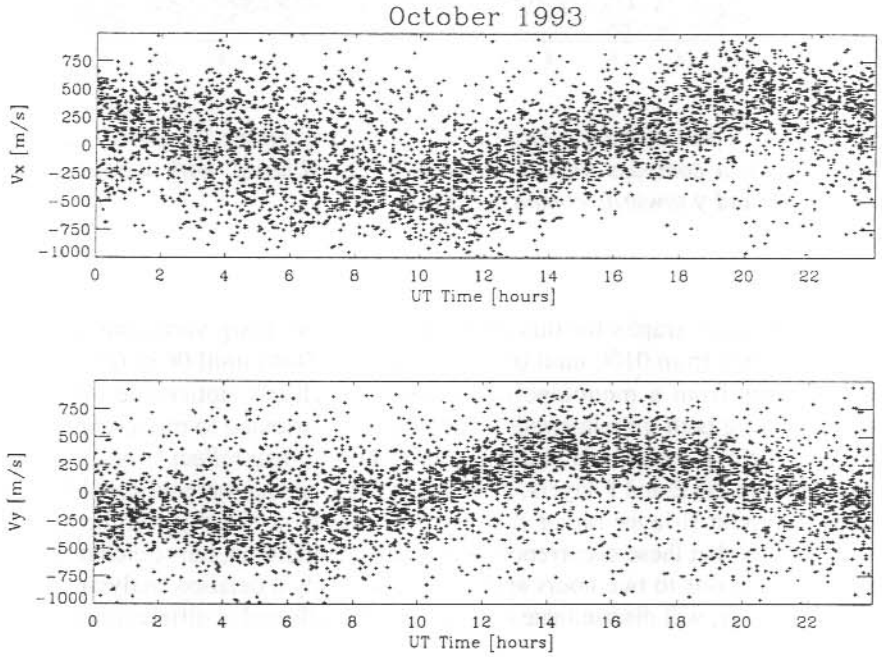

Figure 11. Mass plot of the cartesian drift velocity components Vx and Vy at Casey for October 1993 in a compass oriented system of coordinates, with x pointing towards compass North and y towards compass East.

Figure 10 shows a sequence of ionograms recorded at 5 minute intervals on the 31st of October 1993 from 0434 to 0644 UT. On several occasions, a strong sporadic E-layer may have prevented SARTIST from successfully scaling ionograms, and may also have affected subsequent automatic drift measurements, see Figure 7.

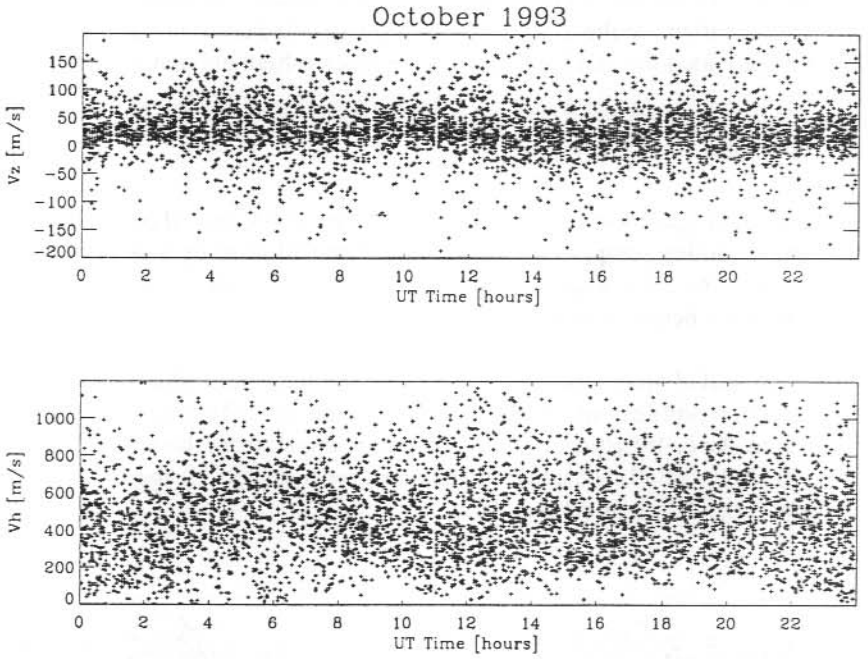

Figure 12. Mass plot of the polar drift velocity components Vz and Vh at Casey for October 1993 in a compass oriented system of coordinates, with x pointing towards compass North and y towards compass East.

Plasma drift velocity graphs for this particular day show sharp variations in the plasma convection patterns from 0100 until 0230 UT and from 0440 until 0630 UT, see Figure 9. These deviations from a monotone daily curve are clearly noticeable on all velocity components during both time intervals. They may be attributed to micro-convection cells occurring just before and around local magnetic noon or may reflect strong differences in dynamics between the E and F-layers, if the ionospheric echoes were reflected by the strong blanketing sporadic E-layer rather than by the F-layer at these particular times. It is interesting to note that these occurrences are not isolated in time, but stretch over relatively long periods, from one to two hours approximately. Only a detailed analysis of drift data, currently under way, will discriminate between echoes reflected at different heights.

The diurnal behaviour of plasma drift presented in Figure 9 for 31 October 1993 is not unique. The mass plots, Figures 11 and 12, summarise one month of drift data recorded during October 1993 and shows a well defined trend in plasma convection patterns over Casey for this period. Vertical drift velocities vary up to 200 m/s, while horizontal

velocities are as much as 1200 m/s, similar to what has been observed in the northern polar cap (Buchau et al. 1988). The measurements of the azimuth of the velocity vector (Az = arctan (Vy, Vx)) in Figure 13 show a variation from compass North-North/West at 0000 UT through 360° over the duration of the UT day. From approximately 0700 UT until 1100 UT the azimuth moves from compass West to South and then towards East. The crossing through compass South occurs generally in a four hour period centred around 0900 UT, approximately three hours after magnetic local noon, 0615 UT at Casey (PGM annual mean). Similarly, the drift velocity swings from compass East-North/East to West-North/West between 1900 and 2300 UT, after magnetic local midnight.

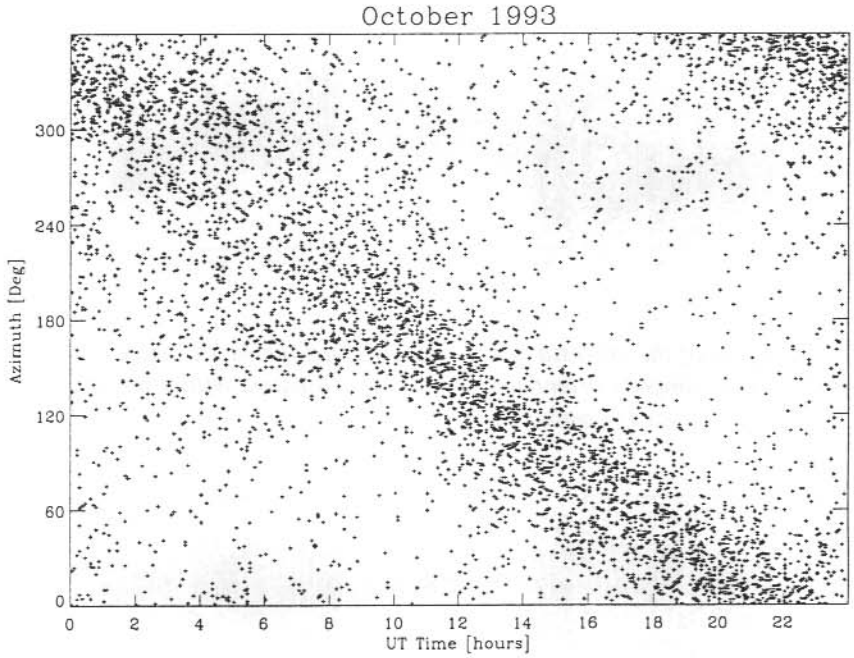

Figure 13. Mass plot of the drift velocity azimuth Az at Casey for October 1993 in a compass oriented system of coordinates, with x pointing towards compass North and y towards compass East.

The horizontal plasma drift velocity exhibits a rather puzzling behaviour around magnetic local noon. An increase in the magnitude of the horizontal velocity Vh is clearly noticeable in a four hour time interval centred around magnetic local noon and coincides with the apparent discontinuity displayed by the x component of the drift velocity around the same time. Both October 1993 data, Figures 11 and 12, and November 1993 data, Figures 14 and 15, show a similar behaviour, which is also present on the corresponding azimuth plots, Figures 13 and 16, where the azimuth angle Az changes abruptly around 0600 UT from approximately 300 to 180 degrees.

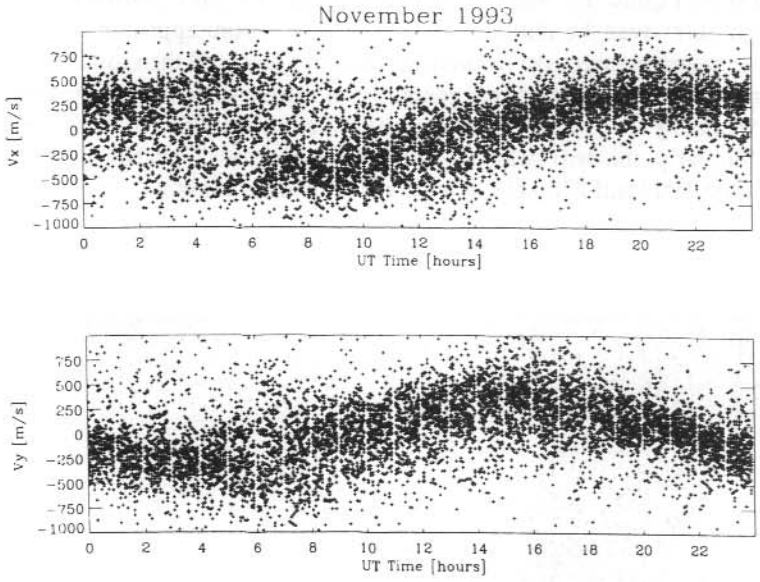

Figure 14. Mass plot of the cartesian drift velocity components Vx and Vy at Casey for November 1993 in a compass oriented system of coordinates, with x pointing towards compass North and y towards compass East.

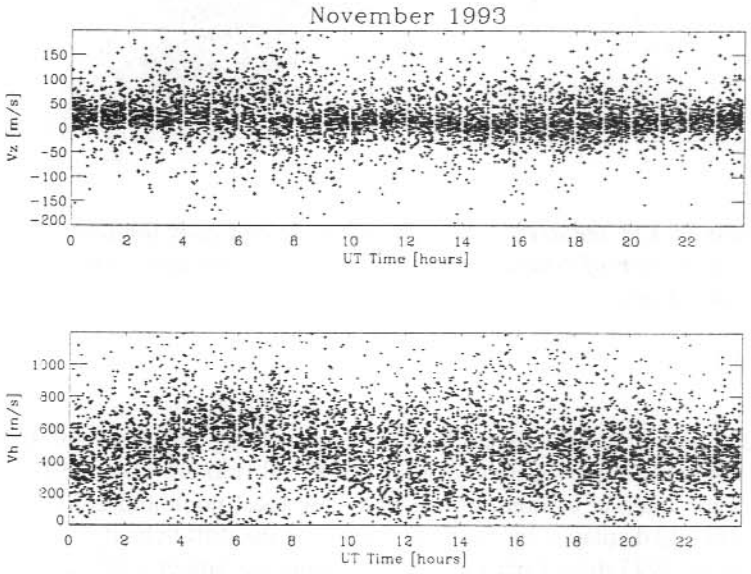

Figure 15. Mass plot of the polar drift velocity components Vz and Vh at Casey for November 1993 in a compass oriented system of coordinates, with x pointing towards compass North and y towards compass East.

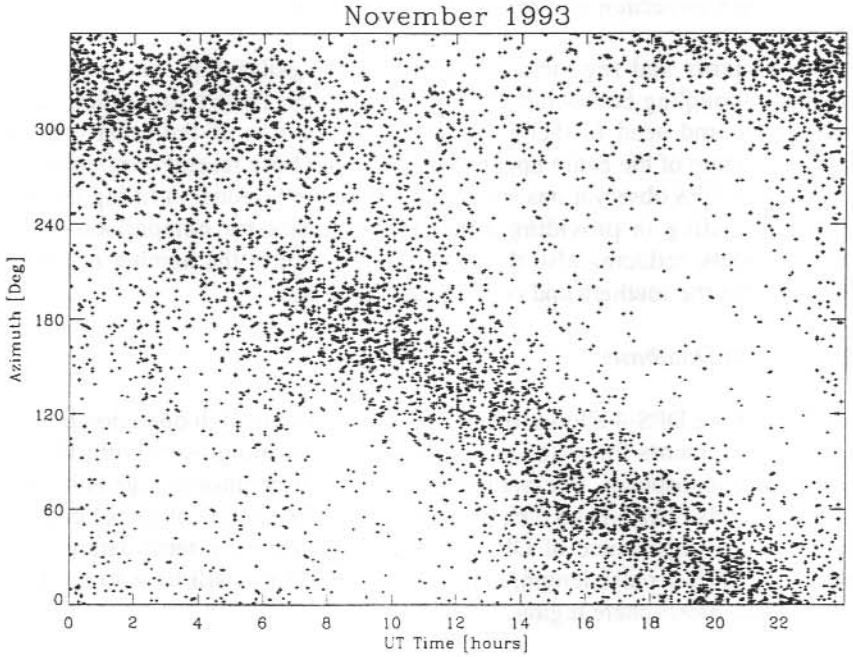

Figure 16. Mass plot of the drift velocity azimuth Az at Casey for November 1993 in a compass oriented system of coordinates, with x pointing towards compass North and y towards compass East.

Access to satellite data will allow us to correlate 1993 plasma drift measurements with the Interplanetary Magnetic Field (IMF). Satellite data may be needed to explain the detailed behaviour of global convection patterns in the polar cap. Nevertheless, the results presented in this section tend to indicate that the IMF has only a minor effect on large-scale F-region plasma convection at the invariant latitude of Casey

9.5 NEW PERSPECTIVES

Some of the results presented in the previous section underline the potential of the DPS-4 in the understanding of polar cap structures and dynamics. The combined analysis of ionogram and drift may allow us to investigate a wide range of phenomena occurring in the polar cap region. Studies conducted by Bibl et al. (1975) in the northern hemisphere already showed that it was possible to measure velocities of small and medium scale ionospheric irregularities. Buchau et al. (1988), Crowley et al. (1992) and Cannon et al. (1992) used digital ionosonde drift versus satellite data, to monitor large-scale polar convection as a function of the Interplanetary Magnetic Field and demonstrated the relevance of these observations to the modelling of high-latitude ionospheric global dynamics. Rapidly varying phenomena, such as the effects of magnetic micropulsations on the ionosphere (Tedd et al. 1989) and F-region irregularities (Scali 1989) are further domains for the application of the DSP-4 facility at Casey.

9.5.1 *Polar Cap Convection and Ionospheric Modelling*

Convection patterns and regimes, prevailing in the polar caps as a response to the electrodynamic coupling between the solar wind and the Earth's ionosphere, are still not fully understood and need further investigation. The role of the polar cap regions in defining the structure of the entire upper atmosphere has been recently recognised (CEDAR 1990). Polar cap DPS observations at Casey are therefore critical in filling the gaps in our present understanding in providing a valuable database for comparison with various ionospheric models, reducing also the current imbalance in the number of observational platforms between the southern and northern hemispheres.

9.5.2 *Long Term Database*

The flexibility of the DPS-4 allows to blend routine and campaign operation modes, so that campaign measurements for case studies may be run without sacrifying the long term monitoring of the ionosphere. For example, the recent observation at high latitudes of Polar Mesospheric Clouds (PMCs) and their possible role in the context of global climate change also underline the importance of DPS measurements for long term database. For this application, the DPS-4 pulse length, currently set to 533 μs, will have to be shortened in order to cover the mesosphere region.

9.5.3 *Correlation with Co-located Ground-based Experiments*

The Auroral and Space Physics group of the Australian Antarctic Division is currently running a series of ground-based experiments at Casey station, such as an Auroral Video Imager (AVI), a two channel Wide Angle Photometer (WAP), a Total Electron Content experiment (TEC), a fluxgate magnetometer and an induction magnetometer. Optical observations from the AVI and the WAP as well as ground-based magnetic observations, when correlated to DPS-4 data, will provide useful information to the study of auroral associated phenomena, ionospheric irregularities and the magneto-hydrodynamics wave influence on the ionosphere. TEC data, used to investigate long-lived ionisation enhancements over a wide range of invariant latitudes (Beggs et al. 1994) – typically from -70° to -90°Λ at Casey– will complement DPS-4 drift data by extending the observations of plasma patches and their dynamics far beyond the field of view the DPS-4.

9.6 ACKNOWLEDGMENTS

The deployment of the Digisonde Portable Sounder 4 was carried out by the 46th Australian National Antarctic Research Expedition (ANARE) at Casey Station. The authors thank the Antarctic Division, Department of the Arts, Sport, the Environment, Tourism and Territories for logistic support, the Australian Antarctic Maintenance Program, the Australian Construction Service and a detachment of army riggers, for the site preparation and the erection of the transmit and receive antennas. We would like to particularly thank Lloyd Symons, 1993 wintering Auroral and Space Physics engineer at Casey, for his constant technical support of the project.

REFERENCES

Baker, K.B. *and* Wing, S. (1989). A new magnetic coordinate system for conjugate studies at high latitudes. *Journal of Geophysical Research 94*:9139 – 9143.

Beggs, H. M., Essex, E.A. *and* Rasch D. (1994). Antarctic polar cap total electron content observations from Casey Station. *Journal of Atmospheric and Terrestrial Physics 56*:659 – 666.

Bibl, K., Pfister, W., Reinisch, B.W. *and* Sales G.S. (1975). Velocities of small and medium scale irregularities deduced from Doppler and arrival angle measurements. *Space Research 15*:405 – 411.

Bibl, K. *and* Reinisch, B.W. (1978). The universal digital ionosonde. *Radio Science 13*:519 – 530.

Buchau, J., Reinisch, B.W., Anderson, D.N., Weber, E. J. *and* Dozois C. (1988). Polar cap plasma convection measurements and their relevance to the modelling of the high-latitude ionosphere. *Radio Science 23*:512 – 536.

Cannon, P. S., Crowley, G., Reinisch, B. W. *and* Buchau, J. (1992). Digisonde measurements of polar cap convection for northward interplanetary magnetic field. *Journal of Geophysical Research 97*:16877 – 16885.

CEDAR Science Steering Committee Report on a Polar Cap Observatory - The next step in upper atmospheric science, 1990.

Crowley G., Cannon P.S., Dozois C.G., Reinisch B. W. *and* Buchau J. (1992). Polar cap convection for B_Z northward. *Geophysical Research Letters 19*:657 – 600.

Reinisch, B.W. *and* Huang, X. (1982). Automatic calculation of electron density profiles from digital ionograms. *Radio Science 17*:421 – 434.

Reinisch, B.W. (1986). New Techniques in Ground-Based Ionospheric Sounding. *Radio Science 21*:331 – 341.

Scali, J.L. (1989). A Study of Spread-F Irregularities at Mid-Latitudes. PhD Thesis, La Trobe University, Australia.

Skolnik, M. (1990). RADAR Hand-Book, 2nd edition, McGraw-Hill.

ULCAR 1990. University of Massachusetts Lowell, Centre for Atmospheric Research, General Specifications for the Digisonde Portable Sounder (DPS), November 1990.

ULCAR 1992. University of Massachusetts Lowell, Centre for Atmospheric Research, Artist Data Editing and Printing System User's Manual, Version 2.01, February 1992.

ULCAR 1993. University of Massachusetts Lowell, Centre for Atmospheric Research, Digisonde Portable Sounder (DPS) Series System Technical Manual, Operation and Maintenance, Version 3.0, May 1993.

Tedd, B.L., Cole, K.D. *and* Dyson, P.L. (1989). The association between ionospheric and geomagnetic pulsations in the Pc3-4 range at mid-latitudes. *Planetary and Space Science 37*:1079 – 1094.

10. DEPLOYMENT OF A MULTI-STATION MAGNETOMETER ARRAY TO EXAMINE SOURCE REGIONS OF ULF WAVES AT SOUTHERN CUSP/CLEFT LATITUDES

D.A. Neudegg[1, 2], M.J. Underwood[1], G.B. Burns[1], B.J. Fraser[2], F.W. Menk[2], H.J. Hansen[2] and R.J. Morris[1]

[1] Auroral and Space Physics
Antarctic Division
Kingston Tasmania 7050
Australia

[2] Department of Physics
University of Newcastle
Newcastle NSW 2308
Australia

ABSTRACT

Data has been taken at four Antarctic induction magnetometer sites; Davis (D) (74.60° S PGM – 88), a site on the polar plateau (130 km from D, 75.64° S PGM – 88), Law Base (115 km from D, 74.70° S PGM – 88) and Mawson (630 km from D, 70.52° S PGM – 8 8) (Baker and Wing 1989). A recording campaign was conducted from 27 July 1992 to 8 August 1992 logging H (magnetic north-south) and D (magnetic east-west) channels at 10 Hz for each site. It is expected that examination of propagating Pc1-2 (0.1 – 5 Hz) ULF waves will lead to development of a method for monitoring high latitude magnetospheric features from ground based data.

10.1 INTRODUCTION

During the southern hemisphere winter of 1992 a traverse onto the Antarctic plateau deployed induction magnetometers at two field sites to supplement the existing facility in the Auroral and Space Physics laboratory, at Davis station, in Princess Elizabeth Land. The three sites formed a triangular array that lay beneath the average position of the dayside cusp/cleft magnetospheric projection as schematically shown in Figure 1(a). Figure 1(b) shows the geographic layout of the induction magnetometer array.

Previous studies at Davis have linked Pc1-2 (0.1 – 10 Hz) magnetic pulsations with a source that can be associated with the cusp/cleft magnetospheric projections (Morris and Cole 1991). There is also ongoing work identifying a plausible set of ground diagnostics for identifying the projections of magnetospheric regions, particularly using spectral properties of magnetic pulsations (Menk et al. 1992). At present the accepted criteria for the mapping of the various magnetospheric projections is from space based particle studies using the DMSP series of satellites (Newell and Meng 1988). Previous studies examining events across the array of Australian Antarctic stations have met with mixed success due to the large distances separating the sites and the fact that they lie under differing magnetospheric projections (Francke et al. 1992).

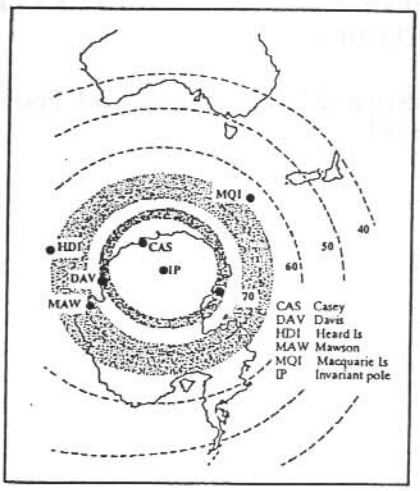

Figure 1(a). Australian Antarctic stations showing the dayside cusp projection (inner circle) and auroral zone (outer circle).

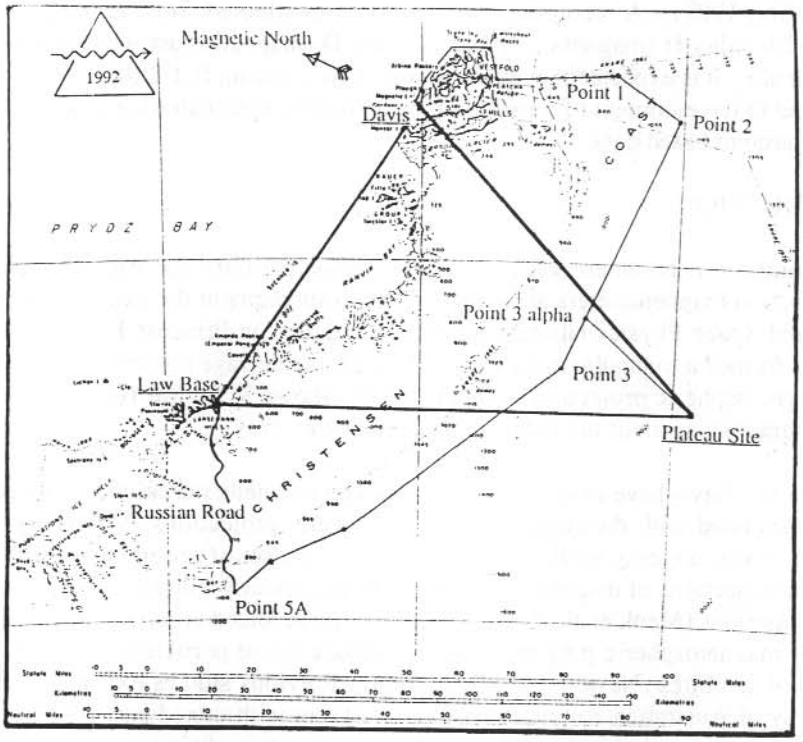

Figure 1(b). Magnetometer array and traverse route.

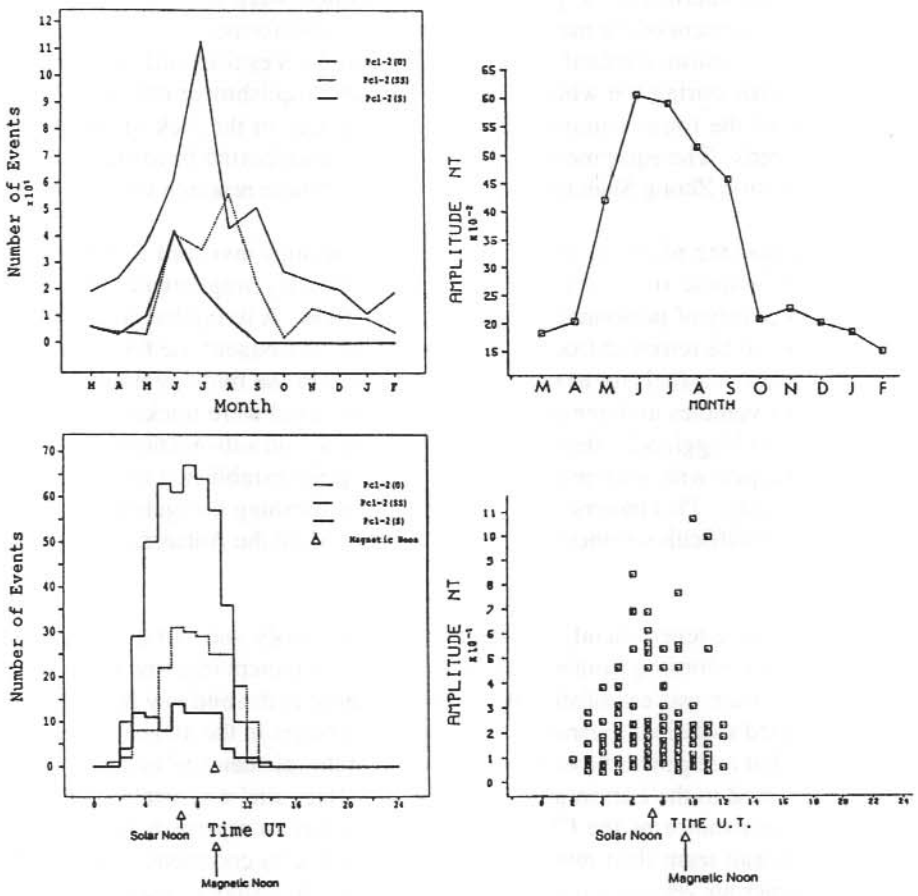

Figure 2. Results of a 1981 study of Pc1-2 pulsations at Davis (Morris and Cole 1991).

Hence, it was decided to deploy a more closely spaced magnetometer array at cusp/cleft latitudes to examine propagation speeds, directions, wave attenuation and possible source locations of Pc1-2 travelling wave phenomena. The winter period was chosen to deploy the array given the obvious peak in the event occurrence and amplitude during the winter months, as shown in Figure 2 (Morris and Cole 1991). Also shown in Figure 2 are the variations in event occurrences and amplitudes with time of day showing clear maxima near solar noon, strongly indicating that sources of the Pc1-2 waves can be associated with the cusp/cleft projection. This paper outlines the logistics involved in the array deployment, the equipment used to collect the data, the levels of geophysical activity during the recording campaign and the proposed method of analysis. Details of the analysis will be described in a companion paper.

10.2 ARRAY DEPLOYMENT AND LOGISTICS

For this particular experiment the planning and execution were closely linked with the logistics. The deployment of the magnetometer array was performed in conjunction with a need to travel the established inland route from Davis in the Vestfold Hills to Law Base in the Larsemann Hills during the winter season. This accomplishment established a three season viability of the route, summer being impossible due to the lack of sea ice in the Vestfold Hills fjords. The equipment for Law Base was transported from Davis station to the CHINARE station Zhong Shan in early 1992 by the Chinese research vessel JIDI.

The next phase was the planning of the complicated logistics involved in deploying the array as several vehicle movements were required to fully implement the recording campaign and recovery of personnel and data from the field. A living hut was constructed at Davis designed to be removed from a sled to enable its subsequent use for depoting fuel. The first traverse was a fuel run to reconnoitre the route to the midway point where fuel was deployed for vehicles and generators. The vehicles used were tracked light military personnel carriers ('Hagglunds') designed for use in Arctic and sub-Arctic regions. These vehicles are equipped with marine radars for following the established route of bamboo canes in any visibility. This traverse was important in establishing navigational methods to be employed in the difficult weather conditions experienced on the Antarctic plateau during the winter.

The scientific traverse relied mainly on fuel depoted previously and carried the personnel involved in the data recording campaign, along with the equipment required for the plateau site. A new cane route was established from the fuel depot at the midway point, to a point inland that provided sufficient separation of the magnetometers in the magnetic north-south axis. The living hut and generator van were deployed at the 'plateau site' and the remainder of the route traversed to the Larseman Hills. The 'Law Base site' was established and fuel loaded with the assistance of the CHINARE expeditioners to replenish supplies on the plateau. The plateau team then returned to the plateau site to commence the campaign, encountering numerous vehicle problems and being forced to abandon one vehicle close to the fuel depot. The thirteen day recording campaign commenced on the 27th of July and finished on the 8th of August.

The plateau team returned to Davis to perform vehicle repairs and then returned to Law Base to recover the team, equipment and data. The return journey to Davis was via the plateau site to recover equipment and was achieved in continuous blizzard conditions which tested the navigational skills developed by the traverse crew. The digital data base was corrected and collated during the remainder of the winter and telemetered back to the head office computer in Kingston via the ANARESAT link.

10.3 RECORDING EQUIPMENT AND ANALYSIS SOFTWARE

The induction magnetometer equipment at each of the three sites were identical in most respects and consisted of the following. Two orthogonal (H and D) induction magnetometer coils, aligned magnetic north-south and east-west respectively, with built in preamplifiers with a system peak response at 1 Hz from which the analogue output signal was digitally sampled at 10 Hz. The digital data were stored on a DEC RL02 drive by

Antarctic Division software running on a DEC PDP-11 computing platform. Unfiltered analogue data was recorded directly on chart paper along with H channel filtered with a Pc1-2 (0.1 – 10 Hz) filter. This filtered channel made subsequent identification of Pc1-2 'events' from the chart records considerably easier as a first reference rather than scanning the digital data. Timing accuracy better than 50 ms (usually < 10 ms) was maintained between the sites by an Austron chronometer aligned with VNG HF radio time signals from Australia. This timing was appended to the digital data files to enable computer analysis of the data on the basis of timing differences between the recording sites.

A calibration of all three sites was performed to determine response characteristics of the equipment to incident magnetic pulsations. This involved four sets of measurements.

1. Frequency response at a fixed incident magnetic field of 0.7 nT measuring peak to peak voltage output at the chart recorder across the Pc3 (0.02 Hz) to Pcl (10 Hz) frequency range.

2. Amplitude response at a fixed frequency of 1 Hz measuring output peak to peak voltage across a range of incident field values of 0 to 2 nT.

3. Absolute phase response at a fixed incident field value. The amount of phase (-180° to +180°) by which the output from the system lags the input field across the frequency range from Pc3 (0.02 Hz) to Pcl (10 Hz).

4. Relative phase response at a fixed incident field value. The amount of phase (-180° to +180°) by which the D channel leads the H channel across the frequency range from Pc3 (0.02 Hz) to Pcl (10 Hz).

All three sites exhibited normal and similar responses. Walkpasts with a bar magnet confirmed correct phase sense of the equipment from the coils to the digital and chart recording stage. The absolute phase response has subsequently been used to confirm that time delays observed for Pc1-2 events between stations are not due to differing phase responses of the three recording sites. This result will be presented in detail later. The amplitude and frequency responses enable events to be represented in terms of their incident field strengths allowing interstation comparison of amplitudes. This has implications for allowing the study of attenuation of waves across the array, which may be useful as a method for determining source directions, as well as properties of the transmitting medium.

The database was transferred via satellite from the computer system at Davis to the head office VAX computer system for more detailed analysis. Existing Australian Antarctic Division, Auroral and Space Physics group analysis software comprises waveform display, cross correlation and polarisation examination with the capability of filtering the data in any frequency band with a variety of filters. The Newcastle University, Space Plasma Waves group software housed on a PC microcomputer network focuses on spectral analysis techniques and allows production of static and dynamic spectra to examine the frequency - time structure of the event. Considerable effort has been spent converting portions of the database to a format compatible with the PC customised Data Base Management System to enable the spectral processing capability to be utilised. The two software suites complement each other in enabling full characterisation of a Pc1-2 'event'.

10.4 MAGNETIC ACTIVITY

Figure 3 shows the levels of magnetic activity during the campaign as indicated by the sum of the planetary index K_p for the day and by the local index K_{mawson} sum, compiled by the Australian Geological Survey Organisation from readings at Mawson station. The K_p index as a measure of planetary activity may be expected to predict the position of the dayside cusp insofar as whether it is polewards (low K_p) or equatorwards (high K_p) of Davis, which is believed to lie under the average position of the cusp projection in winter. This must be stated with the caveat that the sites taking the measurements upon which the K_p three hour averages and hence K_p sum are based, are mainly northern hemisphere sub-auroral sites located in Europe. Thus the index may not accurately reflect magnetic activity in the southern hemisphere on short time scales. Hence the need to examine K_{mawson} for local activity which may have a more direct influence on pulsations observed at Davis.

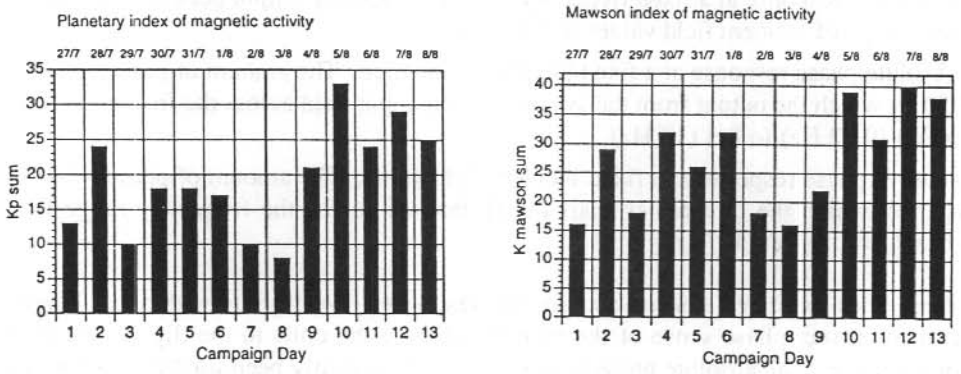

Figure 3. Planetary and local magnetic activity during the campaign.

At present there are indications that magnetic activity affects the average position of the cusp projection in a fashion analogous to the motion of the auroral oval but this is not widely verified. Figure 3 shows, that in general, the Mawson K index follows the planetary index quite closely in daily variation, as represented by the index sums with perhaps exceptions on campaign days four (30 July 1992) and six (1 August 1992), where the relative local activity appears to exceed the planetary activity compared to nearby days. These days may be of special interest in studying local effects. In general trends in the three hour values of K_p and K_{mawson} are similar indicating similar planetary and local responses to geomagnetic variations on the time scale of less than a day. The wide range of activity during the campaign will allow studies of propagation of Pc1-2 under varying conditions and studies of source location variation with both local and planetary activity.

10.5 VARIATION OF Pc1-2 ACTIVITY WITH TIME

Figure 4 displays the variation with time of day of Pc1-2 event occurrence taken as a sum across all three sites in the triangle array, as their small separation implies that they lie under

the same magnetospheric projection. This is similar in shape to the previous year long study conducted at Davis verifying that the campaign data follows a similar pattern. There is the familiar daytime activity peak with the maxima occurring closer to solar noon than magnetic noon. Unlike the previous study there is a night time peak assumed to correspond to magnetic tail activity as it occurs around the magnetic midnight period.

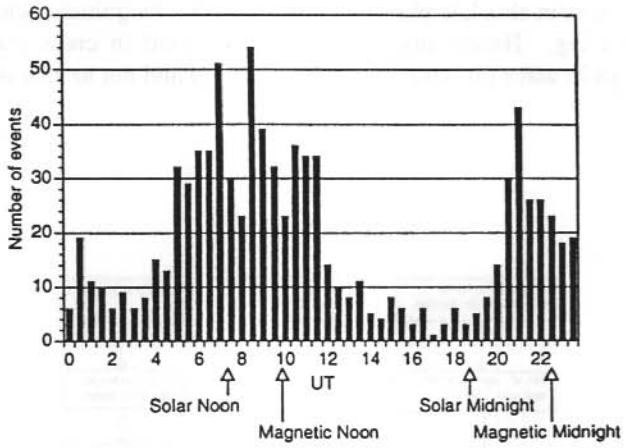

Figure 4. Number of Pc1-2 events against UT for all three sites across all 13 campaign days.

10.6 ANALYSIS

The overall analysis plan consists of several parts as displayed in Figure 5. It is intended to find a locii of sources for the Pc1-2 events by two independent methods; propagation delay via cross correlation and amplitude comparisons of waveforms. Spectral analysis of the event reveals the distribution of power and its form can be compared to those which are suggested to be associated with particular magnetospheric projections. The spectra also provide a method of selecting events from the background noise that cannot be achieved using the chart records. The accepted set of projection criteria from DMSP particle spectra can be compared with the two sets of source locii to find comparisons leading to a set of ground diagnostics which can track cusp/cleft projection location with time and varying magnetic activity if sources of Pc1-2 pulsations can be associated with those projections.

10.7 DETERMINATION OF INSTRUMENT INDUCED LAG

If the absolute phase responses of the sites differ by an appreciable amount then there will be an instrument induced lag that will vary with frequency of the incident magnetic pulsation and contaminate any attempt to measure consistent phase delays between waveforms across the sites. The smallest lag that can be measured is one digital sample point of 0.1 s. So if the differing absolute phase responses are less than this then the measured lags of waveforms between stations can be assumed not to be instrument related.

Figure 6 shows the measured differences in absolute phase response between the sites on each leg of the triangle array for both H and D channels (e.g. D-L/D denotes Davis – Law Base leg on the D channel). This is compiled with the phase difference required for a ± 0.1 s lag at various frequencies by comparing the fraction of the wave period that 0.1 s represents and converting that to degrees of phase. The phase lag on the plots actually represents the difference in the amount between the two stations by which the output lags the input. It can be seen that for all three legs of the array on both H and D channels the calculated differences in absolute phase responses are of a magnitude below that required to produce a ± 0.1 s lag. Hence any phase lags measured in cross correlations can be attributed to delays in wave propagation across the array and not to instrument artifacts.

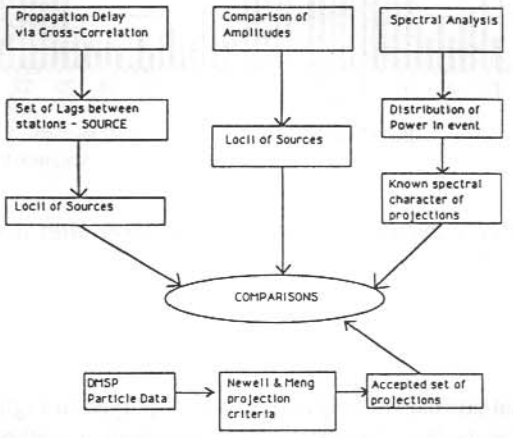

Figure 5. Analysis plan.

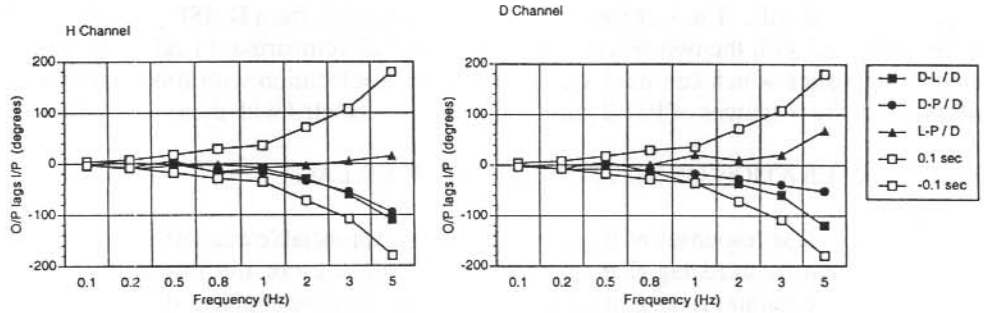

Figure 6. Comparison of absolute phase response differences between stations compared to those required for ± 0.1 s instrument lag for a simultaneous signal.

10.8 CONCLUSIONS

A temporary array of induction magnetometers has been deployed at southern cusp/cleft latitudes in the Austral winter involving a complex and intensive logistics campaign. A successful two week recording campaign was conducted and the database collated and documented. All sites were calibrated and synchronised timing to better than 50 ms allows direct comparisons of data between sites. It has been shown that the difference in the absolute phase responses of the three primary sites is insufficient to produce an instrument induced lag, hence all measured phase lags should be due to wave propagation between the sites. The background magnetic activity on a local and global scale have been catalogued and will be used to examine the variation of source location and thus magnetospheric projections with geophysical activity.

10.9 ACKNOWLEDGMENTS

The author would like to thank members of the Australian National Antarctic Research Expedition (ANARE) at Davis station and the Chinese National Antarctic Research Expedition (CHINARE) at Zhong Shan station 1992, who assisted with the large logistical program involved in this experiment.

REFERENCES

Baker, K.B. *and* Wing, S. (1989). A new magnetic coordinate system for conjugate studies at high latitudes. *Journal of Geophysical Research 94*:9139–9143.

Francke, M.H., Hansen, H.J., Menk, F.W., Fraser, B.J. *and* Morris, R.J. (1992). The propagation of Pc 1 magnetic bursts across the polar cap region. In: Burns, G. *and* Duldig, M. (Eds.). *ANARE Research Notes 88*:82–88.

Menk, F.W., Fraser, B.J., Hansen, H.J., Newell, P.T., Meng C.-I. *and* Morris, R.J. (1992). Identification of the magnetospheric cusp and cleft using Pc 1–2 pulsations. *Journal of Atmospheric and Terrestrial Physics 54*:1021–1042.

Morris, R.J. *and* Cole, K.D. (1991). High latitude day-time Pc 1–2 continuous magnetic pulsations: a ground signature of the polar cusp and cleft projection. *Planetary and Space Science 39*:1473–1491.

Neudegg, D.A. (1992). 1992 Space Science Traverse. *Australian Antarctic Division Internal Report, November 1992.*

Newell, P.T. *and* Meng, C.-I. (1988). The cusp and cleft/boundary layer: low altitude identification and statistical local time variation. *Journal of Geophysical Research 93*:14549–14556.

11. MONITORING PROPAGATION OF Pc 1–2 ULF WAVES AT SOUTHERN CUSP/CLEFT LATITUDES

D.A. Neudegg[1, 2], G.B. Burns[1], B.J. Fraser[2], F.W. Menk[2], H.J. Hansen[2], R.J. Morris[1] and M.J. Underwood[1]

[1] Auroral and Space Physics
Antarctic Division
Kingston Tasmania 7050
Australia

[2] Department of Physics
University of Newcastle
Newcastle NSW 2308
Australia

ABSTRACT

Data has been collected at four Antarctic induction magnetometer sites; Davis (D) (74.60°S PGM–88), a plateau site (130 km from D, 75.64°S PGM–88), Law Base (115 km from D, 74.70°S PGM–88) and Mawson (630 km from D, 70.52°S PGM–88) (Baker and Wing 1989). A campaign was conducted from 27 July 1992 to 8 August 1992 logging H and D channels at 10 Hz for each site. This paper describes how the analysis technique provides a method for predicting propagation speeds and directions for hydromagnetic waves. The possibility of relating the wave source to a magnetospheric projection is discussed together with the postulated mode of propagation. The use of the wave source analysis for monitoring evolution of magnetospheric projections with time and geophysical activity is also considered.

11.1 INTRODUCTION

This paper outlines progress in analysis of magnetic pulsation data from a multi-station array deployed beneath the average winter position of the dayside cusp/cleft magnetospheric projection. The overall aim of the analysis is to achieve a set of ground based criteria for mapping the projections of high latitude magnetospheric features onto the ionosphere. If the source direction of propagating ULF waves can be ascertained and tied to an accepted magnetospheric projection then the possibility of monitoring that projection through the passage of time and under varying levels of geomagnetic activity can be considered. The accepted set of criteria for the location of magnetospheric projections is from the particle signatures monitored by the DMSP series of spacecraft (Newell and Meng 1988, 1992). The first step is to determine actual wave directions and velocities across the array. The initial method chosen for this is via cross-correlation of waveforms from the three main stations in the array. The development of this method and the initial results are described herein.

11.2 PRELIMINARY ANALYSIS FOR THE CROSS-CORRELATION TECHNIQUE.

Pc1-2 events were initially chosen from a 0.1 – 10 Hz filtered channel on the chart records. Periods were chosen which appear to contain a waveform envelope of similarly related activity. Thus selection of what constitutes an 'event' is somewhat subjective and as the filtered channel covers the entire 0.1 – 10 Hz range there is no information concerning the power distribution with frequency within the selected time span. This can be established later however with a dynamic spectra and selection of events from chart records is a good starting point. The digital data is then used for a detailed examination of the event.

An initial problem is how to account for the 'field of view' overlap of the instruments. Each magnetometer has an effective field of view of 100 km radius. This can be understood by observing that the bottom of the ionosphere lies at approximately 100 km above the Earths surface. Therefore any magnetic disturbance originating above this height will propagate freely through the uncharged atmosphere below 100 km altitude to the ground. Thus a 100 km diameter 'footprint' from a point magnetic disturbance at 100 km altitude can be thought of as the same diameter field of view at the altitude for a point receiver on the ground. As the lengths of the legs in the triangular array vary between 114 km (Davis-Law Base) and 148 km (Law Base-Plateau Site) it is expected that the phenomenon may occur. High coherency (correlation number) in cross-correlations of event waveforms may be due to the phenomena rather than a magneto-hydrodynamic wave passing across the array. In essence, all sites may 'see' the same wave at the same time rather than measuring its propagation across the array. This will obscure the measurement of the propagating waves which are the main object of interest.

To resolve the 'field of view' overlap problem and also work towards a method of analysing an event to establish propagation speed and direction the following procedures were used.

a. A quiet period, a period with low activity in the Pc1-2 band, was examined to determine the amount of correlation between stations on both channels in various frequency bands. This was performed to establish the 'background' correlation could be expected beneath a Pc1-2 'event'.

b. A chart selected event was processed for the same day with the aim of examining sub-structure in time and frequency. This was done by dividing the event into 'sub-events' or smaller time intervals and comparing the correlation characteristics between stations with the 'parent' event.

It was found that for the test event selected that most time segments selected correlated with the same values of lag as the entire parent event. This gave confidence in the method of selecting an event from the chart filtered Pc1-2 channel insofar as homogeneity of its composition.

These procedures evolved into a method whereby an event is divided into one minute segments and cross-correlations performed on each segment for both H and D channels in various frequency bands for each of the three legs of the triangle array. The correlations and lags can be examined for variation with time for the duration of the event. Examining

the lag in seconds of the waveforms between the sites as a function of the correlation between the waveforms is a more useful tool. For an example refer to Figure 1. These plots can allow a determination of the time lag for the waveform across each leg of the array which can later lead to a value for propagation speed and direction for the event.

It is common to find a cluster of points with positive correlations, as selected by the routine choosing the peak in the correlation function, and a grouping of lags between -1 and +1 s. It was decided to limit the plot to this area as negative correlations are not of interest. The 'outliers' on the plot usually have lags significantly different to those in the cluster, for example 3–4 s and so can be discarded as physically meaningless. Both waves propagating along field lines and in the ionospheric duct will have velocities giving lags less than one second for this array. This is due to duct propagation velocities being measured in the hundreds of kilometres per second parallel to the ground. Field line phase velocities are predicted to be of the order of thousands of kilometres per second but the projection onto the ground at high dip angles will also be in the order of hundreds of kilometres per second.

The better the overall level of correlation the less the number of outliers. In a ten minute segment nearly all twenty (two channels with one minute segments) points will appear. When the overall level of correlation is low, inspection of the correlation function has shown that the peak in magnitude may occur at an 'unreasonable' lag or a negative correlation peak may be the greatest in magnitude, so these will be selected by the automatic peak selection software as the lag and correlation values. A secondary peak with a 'reasonable' lag and positive correlation may also exist in the correlation function, but it is only recognised by visual inspection. As the cluster of points with positive correlations and lags between -1 and +1 s reveals the information required, particularly when correlation levels are high, it is not necessary to visually inspect each of the correlation functions for the outliers to see if some can be relocated onto the plot.

11.3 QUIET PERIOD - BACKGROUND ACTIVITY

The quiet period chosen was from the chart records showing very low activity in the filtered Pc1-2 channel. A ten minute segment 1610–1620 UT was passed through the standard analysis method and the results are discussed below. This time interval is usually quiet regardless of the level of planetary magnetic activity which is the reason it was chosen rather than a quiet period during the day which may be due to low K_p. The day chosen, campaign day 12 (7th July 1992), was an active day with the three hour K_p value during the chosen period being 3+ and the K_{mawson} value being 4. Obviously a more thorough study can be carried out across varying levels of magnetic activity but this single case is sufficiently illustrative.

11.3.1 *Pc1-2 (0.1–5 Hz)*

Figure 1 illustrates correlation versus lag for each of the three legs on the array with each symbol representing a one minute segment of the waveform for which a cross-correlation has been performed between the two stations. The full Pc1-2 bandwidth (0.1–5 Hz) available to the system was examined first to look at the overall level of coherence between the stations in a period when activity in the Pc1-2 band is supposed to be negligible. The

Pc1-2 band was selected using a 6th order Butterworth filter with 3 dB cut off points at 0.1 and 5 Hz. This type of filter with varying cutoff points was used to window other frequency bands in subsequent analysis. There is quite a reasonable level of correlation on all three legs of the array indicating some level of common signal at the three sites. There is however a wide spread of lags which is not consistent with wave propagating across the sites. It is of interest to examine if any particular frequency band within the traditional Pc1-2 band is a major contributor to the level of coherency between the sites. As the lower cutoff frequency for ionospheric duct propagation lies at around 0.3 – 0.4 Hz the first band to be examined is Pc1 (0.5 – 2 Hz) representing typical ducted frequencies. The second is Pc2 (0.1 – 0.2 Hz) which should not be ducted.

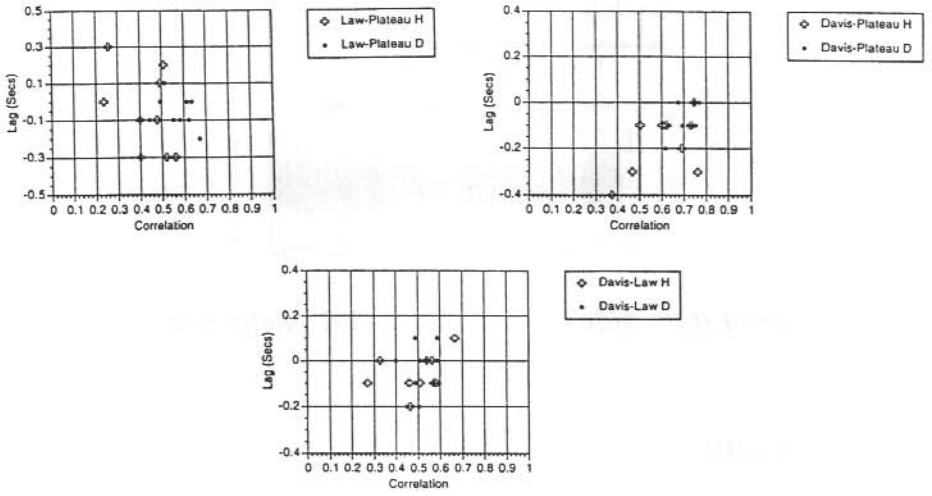

Figure 1. Quiet period 1610 – 1620 UT on 7 August 1992. Pc1-2 (0.1 – 5 Hz), $K_p = 3^+$, $K_{mawson} = 4$.

11.3.2 *Pc1 (0.5 – 2 Hz)*

Figure 2 shows the results in the Pc1 (0.5 – 2 Hz) band indicating a substantially reduced level of correlation. Several points have been removed due to negative correlations or lags beyond reasonable limits. Hence it appears that this particular band is not contributing significantly to the level of correlation observed in the Pc 1-2 band. It also seems to indicate a low level of wave propagation in the ionospheric duct if it is assumed that this phenomenon is observed in this band. This is consistent with the supposedly 'quiet' nature of this period. There is a suggestion of consistent lag on the Davis – Plateau Site leg of somewhere between zero and - 0.1 s, i.e. from Davis towards Plateau Site (polewards) consistent with a cusp/cleft projection source lying equatorwards during high magnetic activity. This may indicate a 'trickle' of duct propagating waves and is interesting to compare with the results shown later for a high magnetic activity event.

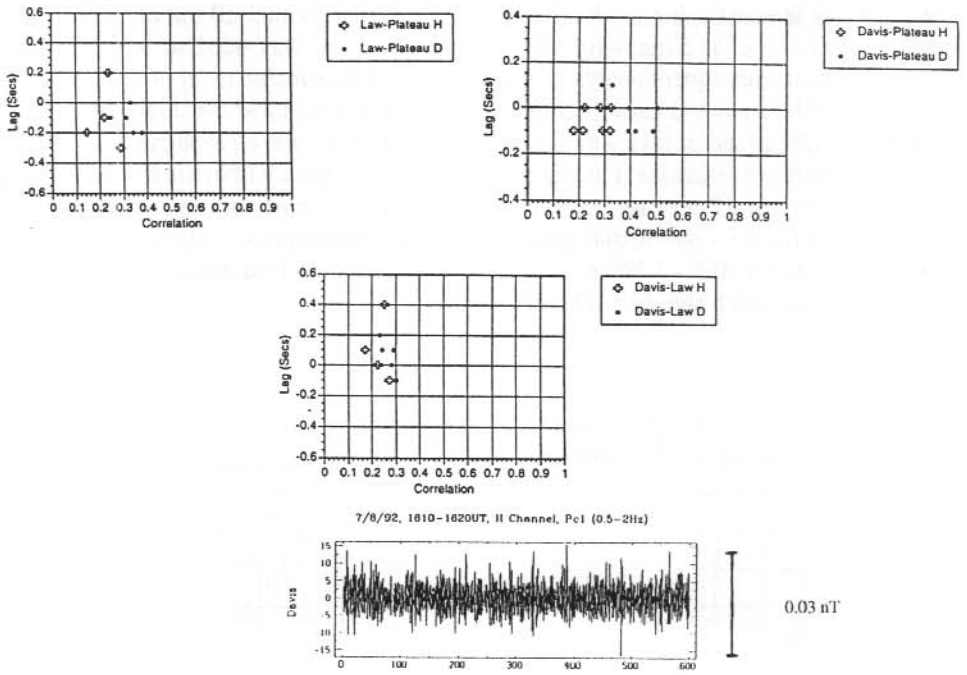

Figure 2. Quiet period 1610–1620 UT on 7 August 1992. Pc1(0.5–2 Hz), $K_p = 3^+$, $K_{mawson} = 4$.

11.3.3 *Pc2 (0.1–0.2 Hz)*

Figure 3 shows the results of the correlations in the Pc2 (0.1–0.2 Hz) band. A much higher degree of correlation is apparent than in the Pc1(0.5–2 Hz) band with most correlations exceeding 0.7. There is however a lack of consistency in the values of the lag observed suggesting that this is not a propagating wave phenomena. This would seem to indicate that what is being observed is field of view overlap between the sites and the values of the lags themselves perhaps have no physical meaning beyond that indicated by their spread in values as a group.

11.3.4 *Polarisation*

Figure 4 shows some example polarisation hodograms at the Davis site in both Pc2 (0.1–0.2 Hz) and Pc1(0.5–2 Hz) bands. The Pc1 band has a random appearance with no apparent dominant polarisation direction. The Pc2 band displays a much smoother variation with evidence of a predominance of left-hand polarisation relative to the field lines oriented upwards. Although not shown, each of the triangle sites has a very similar set of hodograms in the Pc2 band which reinforces the field of view overlap idea seen in the wave form correlations. It is expected that waves generated in the equatorial low latitude boundary layer which propagate down to the cleft projection are left-hand polarised ion cyclotron waves. Left-hand polarisation is consistent with these observations.

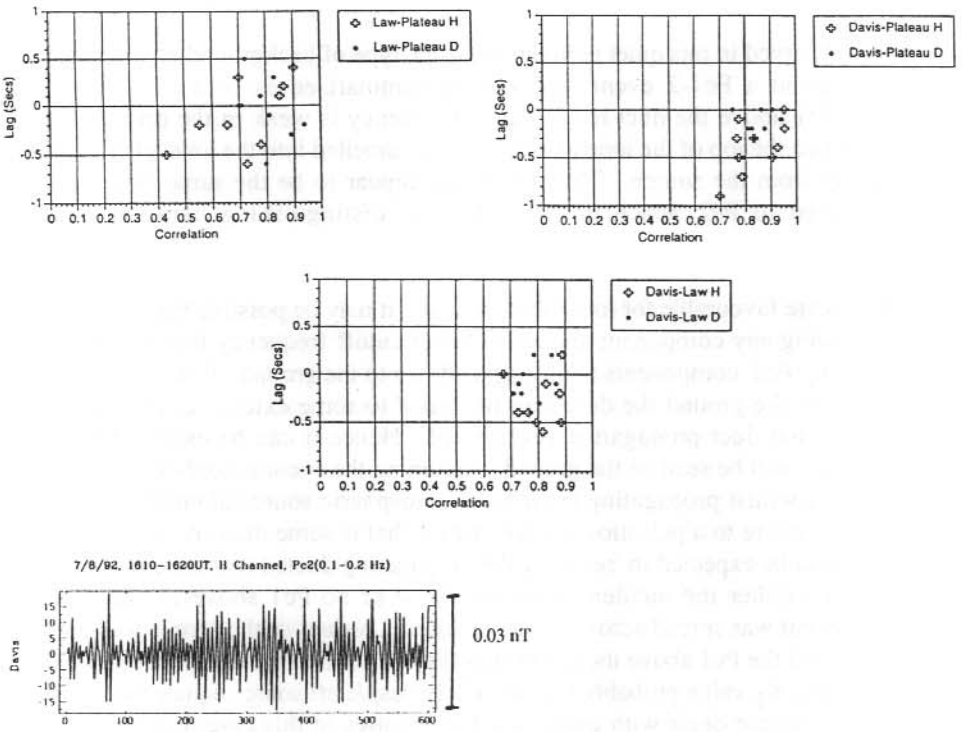

Figure 3. Quiet period 1610 – 1620 UT on 7 August 1992. Pc2 (0.1 – 0.2 Hz), $K_p = 3^+$, $K_{mawson} = 4$.

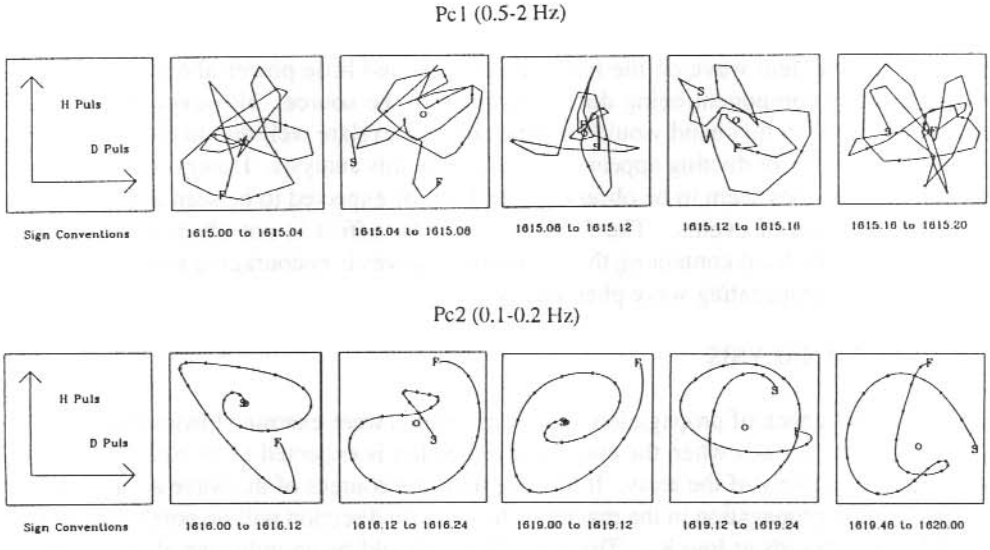

Figure 4. Quiet period 1610 – 1620 UT on 7 August 1992. Polarisation hodograms, $K_p = 3^+$, $K_{mawson} = 4$.

11.3.5 *Discussion*

What is being observed in this quiet period may be the type of background activity that can be expected behind a Pc1-2 event, and can be summarised as follows. Either the component of Pc1 above the duct lower cutoff frequency is weak in the original Pc1-2 activity incident on the top of the ionosphere or it is channelled into the ionospheric duct to propagate away from the source. There does not appear to be the same field of view overlap compared to Pc2 which does not help in distinguishing between the two possibilities.

If the conditions are favourable for ionospheric ducting it may be possible that the duct acts as a filter removing any component above the lower cutoff frequency into it leaving the remaining, mainly Pc2, components to propagate down to the ground. If duct propagating waves are seen on the ground the duct may be 'leaky' to some extent. Later analysis of events indicates that duct propagation is observed. Hence it can be expected that any activity in the duct will be seen on the ground. Assuming the event is confined to a narrow range of L-values whilst propagating from a magnetospheric source along the field lines down to the ionosphere to a pulsation 'source' region that is some distance away from the array then it would be expected to 'see' only the propagating ducted component. As this is not the case then either the incident event had little or no Pc1 above the duct cutoff frequency, the event was spread across a wide range of L-values or the source was directly above the array and the Pc1 above the cutoff was filtered off into the duct. The last case is unlikely as the high K_p value probably puts the likely cusp/cleft source equatorwards of the array. The second case deals with unknowns but requires in this case that the event be spread across several magnetospheric areas, entry layer, cusp, plasma mantle and perhaps polar cap. This requires either a source spanning all these regions which seems unlikely, given the magnetospheric topology, or propagation partially across field lines which is possible.

Probably the incident wave on the ionosphere contained little power above 0.3 – 0.4 Hz rather than this component being ducted away from the source. However even a small amount of signal in this band would be expected to correlate well due to field of overlap and so the question of ducting appears unresolved by this analysis. However the Pc2 field of view overlap does seem to be observable and can be expected to be seen as background to the observation of events. The fact that the same effect is not observed in what is expected to be the band containing the propagating waves is encouraging insofar as it may not obscure the propagating wave phenomena.

11.4 EVENT ANALYSIS

As a first order check of propagation directions, events were examined from magnetically active and quiet periods when the cusp/cleft projection is expected to be equatorward and poleward respectively of the array. If these regions are sources of the wave activity then it is expected that propagation in the magnetic north-south direction will be polewards at high K_p and equatorwards at low K_p. The time of day should be an indicator of the direction expected on the Davis – Law Base leg. If the cusp/cleft projection is at Davis magnetic longitude around local solar noon then it expected it will be east of the array prior to this

and west of the array after this time. The propagation direction would therefore be expected to be west prior to noon and east afterward.

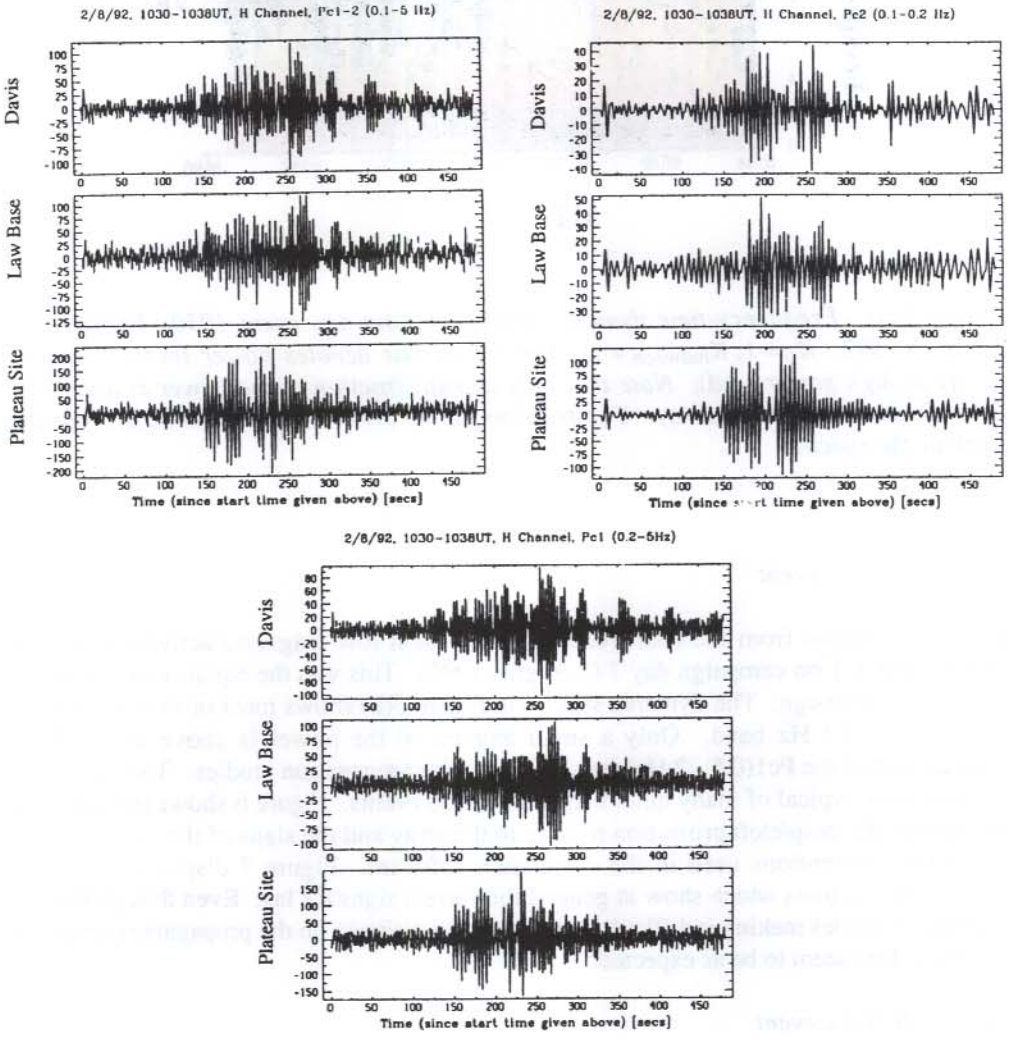

Figure 5(a). Amplitude-time records. Quiet day event 1030–1038 UT on 2 August 1992. $K_p = 1$, $K_{mawson} = 1$. 100 digital units equal 0.1 nT. The frequency bands are: (a) Pc1-2 (0.1–5 Hz), (b) Pc2 (0.1–0.2 Hz), and (c) Pc1 (0.2–5Hz).

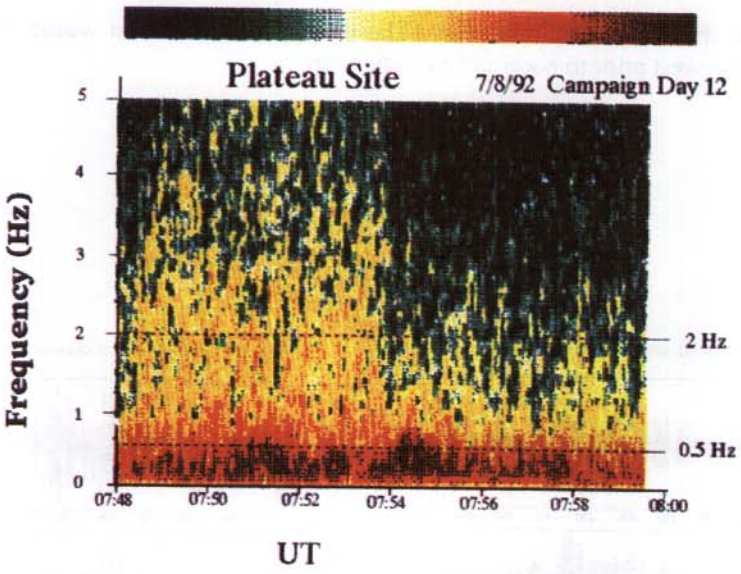

Figure 5(b). Frequency-time dynamic spectra. Quiet day event 1030–1038 UT on 2 August 1992. $K_p = 1$, $K_{mawson} = 1$. The colour bar denotes power levels from low (blue) to high power (red). Note that only a small fraction of the power is above the 0.45 Hz duct cutoff frequency. The fraction above 0.4 Hz appears to be a separate, peak in the spectra.

11.4.1 *Low K_p event*

The event chosen from the chart records to represent low magnetic activity was from 1030–1038 UT on campaign day 7 (2 August 1992). This was the equal second quietest day of the campaign. The dynamic spectra in Figure 5(b) shows most of the power to be in the 0.15–0.3 Hz band. Only a small amount of the power is above this making examination of the Pc1(0.5–2 Hz) band difficult for propagation studies. This spectrum appears to be typical of many quiet magnetic period events. Figure 6 shows the expected position of the cusp/cleft projection relative to the array and the signs of the lags expected given the conventions used in the correlation software. Figure 7 displays the actual correlation-lag plots which show in general the correct signs for lag. Even though there is a spread of values making it difficult to put a precise estimate on the propagation speed the direction does seem to be as expected.

11.4.2 *High K_p event*

The event chosen from the chart records to represent high magnetic activity was from 0744–0758 UT on campaign day 12 (7 August 1992). This was the second most active day during the campaign. The dynamic spectra in Figure 8 for the period shows a

significant amount of power in the band above 0.5 Hz although the spectrum is noisy rather than of a structured nature.

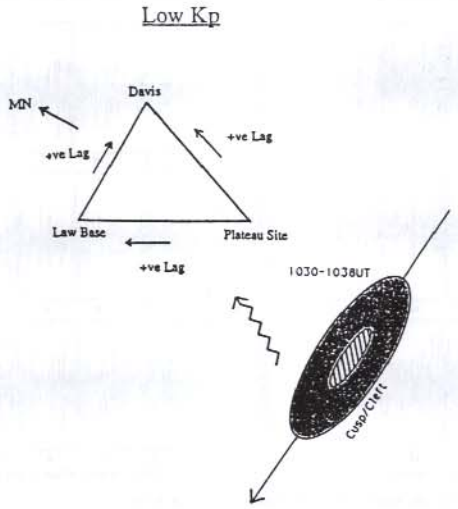

Figure 6. Quiet day event 1030 – 1038 UT on 2 August 1992. $K_p = 1$, $K_{mawson} = 1$. Expected cusp/cleft projection relative to the array and expected lag signs on each leg. MN indicates Magnetic North.

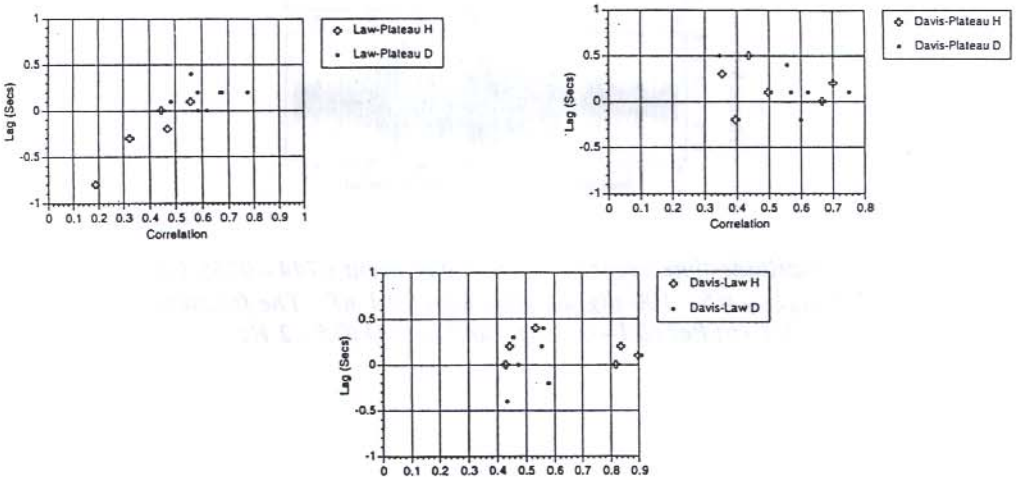

Figure 7. Quiet day event 1030 – 1038 UT on 2 August 1992. Pc1 (0.2 – 5 Hz), $K_p = 1$, $K_{mawson} = 1$.

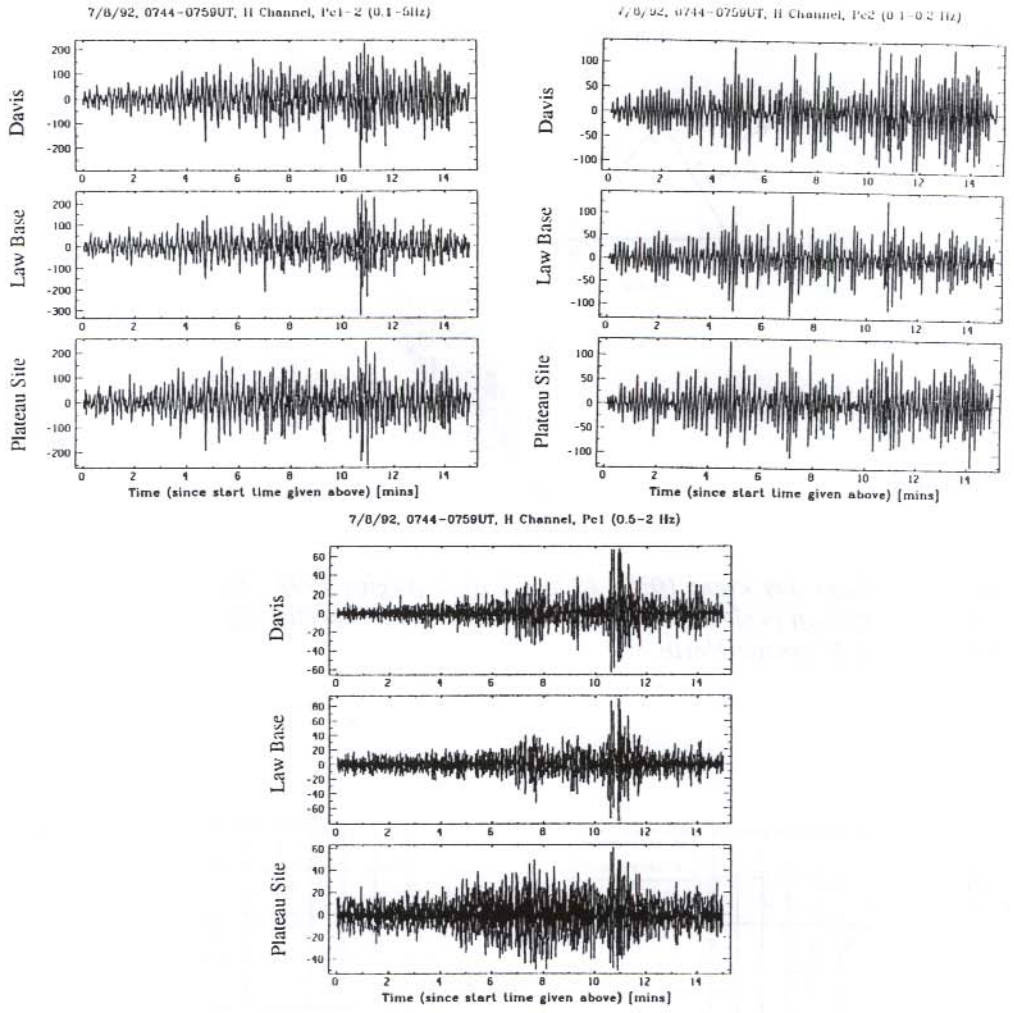

Figure 8(a). Ampiltude-time records. Active day event 0744 – 0758 UT on 7 August 1992. $K_p = 4$, $K_{mawson} = 5$. 100 digital units equal 0.1 nT. The frequency bands are: (a) Pc1-2 (0.1 – 5 Hz), (b) Pc2 (0.1 – 0 .2 Hz), and (c) Pc1 (0.5 – 2 Hz).

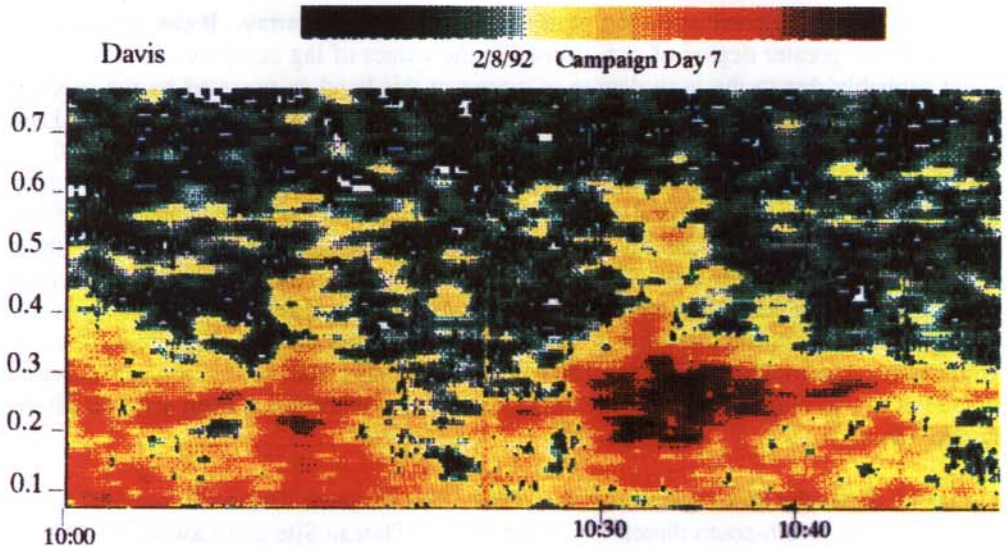

Figure 8(b). Frequency-time dynamic spectra. Active day event 0744–0758 UT on 7 August 1992. $K_p = 4$, $K_{mawson} = 5$. The colour bar denotes power levels from low (blue) to high (red). The spectra is noisy due to the high levels of magnetic activity making event selection difficult. This particular event was selected from chart records.

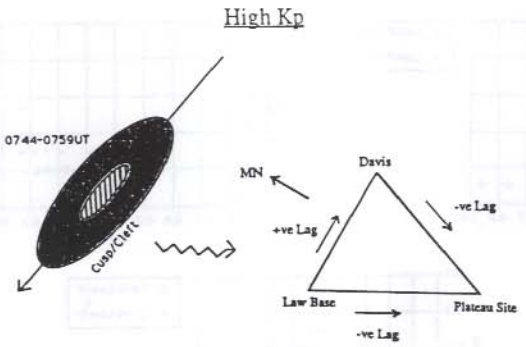

Figure 9. Active day event 0744–0758 UT on 7 August 1992. Waveforms, $K_p = 4$, $K_{mawson} = 5$. Expected cusp/cleft projection relative to the array and expected lag signs on each leg. MN indicates Magnetic North.

Figure 9 shows the expected position of the cusp/cleft projection with relation to the array and expected signs for the lags on each of the legs of the array for a poleward propagating wave in the post noon sector.

Figure 10 shows the correlation-lag plots for three legs of the array. It can be observed that there is a greater degree of consistency in the values of lag compared to the low K_p event probably due to the high degree of power in this band as revealed by the spectra. The Davis–Law Base lag appears to be +0.1 s, Davis–Plateau Site -0.3 s and Law Base–Plateau Site - 0.4 s. As the sampling rate was 10 Hz the time resolution is 0.1 s explaining the 'quantisation' effect in the plots. The true lag for Davis–Plateau Site thus lies somewhere between - 0.2 and - 0.3 s. This results in a velocity of 1150 km s^{-1} from Law Base towards Davis, 430 km s^{-1} from Davis to the Plateau Site and 370 km s^{-1} from Law Base to the Plateau Site. These velocities are typical for ionospheric F2 region waveguide propagation. It is interesting to note that both H and D channels show basically the same lags suggesting that what is observed is a wavefront propagating across the array with components in both directions. The consistency of lags from correlation values below 0.5 to 0.9 is also indicative of the amount of consistency in the event even across a fifteen minute span.

Figure 11 shows the time evolution of the event. There is some variation around 0748 UT in the magnetic north-south direction i.e. the Davis–Plateau Site and Law Base–Plateau Site legs. As the event has only been divided into one minute segments the resolution is quite crude and division into smaller segments may reveal greater structure in the time variation.

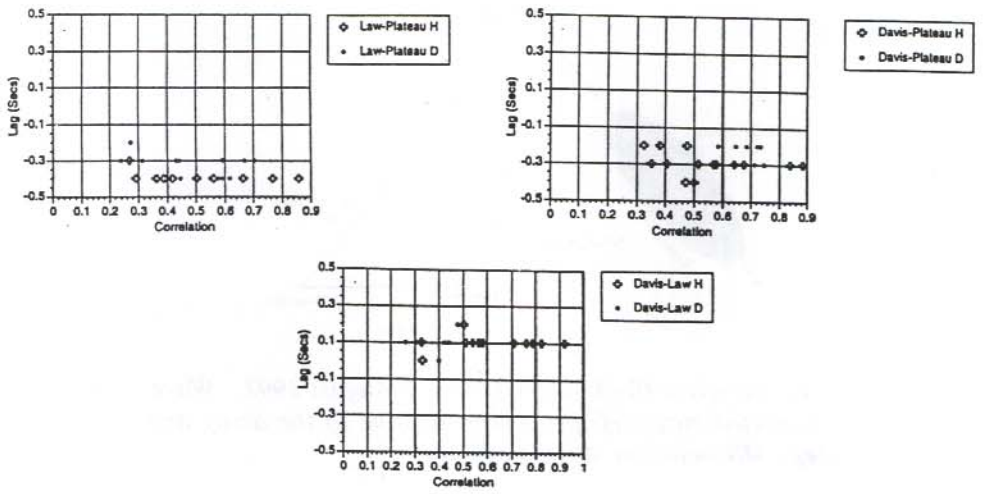

Figure 10. Active day event 0744–0758 UT on 7 August 1992. Pc1 (0.5–2 Hz), $K_p = 4$, $K_{mawson} = 5$.

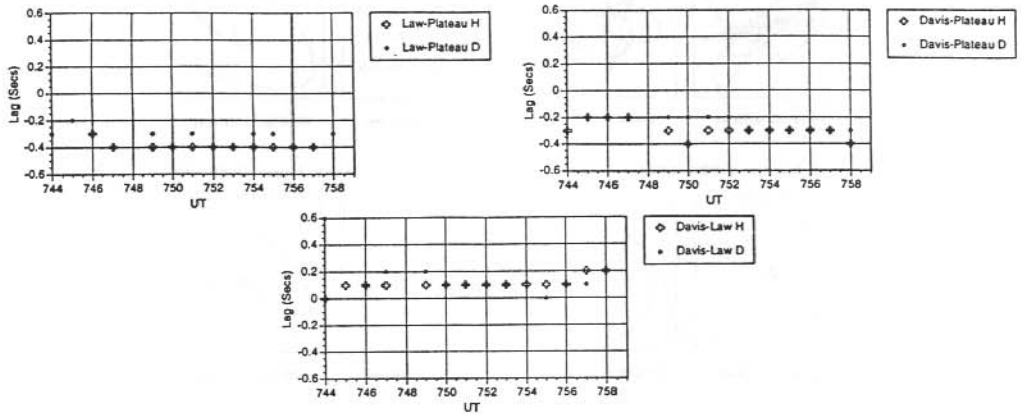

Figure 11. Active day event 0744 – 0758 UT on 7 August 1992. Pc1 (0.5 – 2 Hz). Lag against UT, $K_p = 4$, $K_{mawson} = 5$.

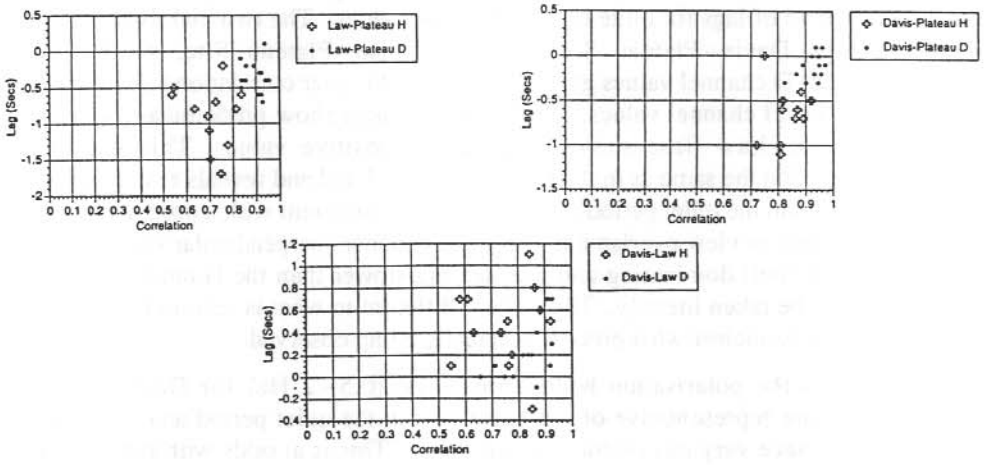

Figure 12. Active day event 0744 – 0758 UT on 7 August 1992. Pc2 (0.1 – 0.2 Hz), $K_p = 4$, $K_{mawson} = 5$.

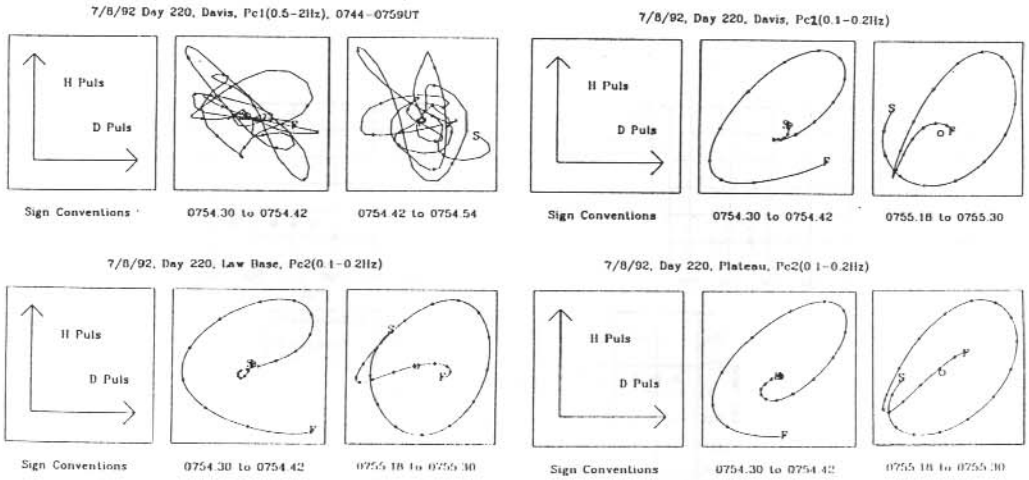

Figure 13. Polarisations. Active day event 0744 – 0758 UT on 7 August 1992. Pc2 (0.5 – 2 Hz), $K_p = 4$, $K_{mawson} = 5$.

Figure 12 shows the correlation-lag plots for the Pc2 (0.1 – 0.2 Hz) band on each of the array legs. The same field of view overlap as in the quiet period analysis seems to exist, with a wide spread of lags for quite high correlation values. The two mainly north-south (magnetic) legs, Davis – Plateau Site and Law Base – Plateau Site, show similar distributions with D channel values grouped together at higher correlation values and less negative lags than H channel values. These two legs also show predominantly negative lags whilst Davis – Law Base shows a spread of positive values. This suggests a propagation direction the same as in the Pc 1 (0.5 – 2 Hz) band and reveals a more complex physical picture than the quiet period analysis. This is consistent with a propagating wave combined with field of view overlap but with the component perpendicular to the direction of motion (D channel) dominating and propagating slower than the H channel if in this case the lags can be taken literally. This is very different to what is seen in the Pcl (0.5 – 2 Hz) band and it is unclear what process is actually being observed.

Figure 13 shows the polarisation hodograms in Pc1(0.5 – 2 Hz) for Davis over two intervals which are representative of the event. As in the quiet period analysis, the Pcl band appears to have very unstructured polarisation. This is at odds with the consistent lags which suggest structured waves in this band. This problem remains unresolved at present. The remaining three frames show Pc2 polarisations for two representative periods at all three of the array sites. They have been selected deliberately to demonstrate how closely the polarisation agrees across the array. This reinforces the 'field of view overlap' idea seen in the 'background' activity analysis.

11.5 CONCLUSIONS

Presented here are the preliminary results from the experiment which seem to indicate that it is possible to measure propagation delays of travelling waves across the array. This can lead to a determination of their direction and propagation velocity. It is assumed, and appears to be borne out by evidence, that the most likely source for the waves is the cusp/cleft projection regions indicating magnetospheric sources for the Pc1-2 pulsations in the low latitude boundary layer/entry layer, cusp/magnetosheath or plasma mantle. There appears to be different mechanisms at work within different sections of the Pc1-2 band by the time the observations are made on the ground. Interaction of the incident magnetospheric waves with the ionosphere appears to be the main reason for the differences in the observations in the various bands. The waveforms seem to show similar variations in the different bands suggesting a common generation mechanism across the Pc1-2 spectrum. It has been assumed that the waves observed propagating across the array are travelling in the ionospheric duct. This appears to be acting over a fairly short distance at these latitudes as events observed at the array are usually not observed at Mawson.

The main thrust of future analysis will be aimed at compiling a list of events with associated propagation directions, speeds and source locations and comparing this with available DMSP projection predictions. This leads to the possibility of developing the capability of tracking cusp/cleft motions, on a finer gradation of magnetic activity than the two extremes presented here. This is an important result on the way to establishing accepted ground signatures of magnetospheric projections, particularly the cusp/cleft. These results contribute significantly to the international Geospace Environment Modelling (GEM) program and Solar Terrestrial Energy Program (STEP) by providing possible cusp signatures. The direct measurement of hydromagnetic wave coupling of the magnetosphere-ionosphere system also has important implications for studies of energy transfer between the two regions.

11.6 ACKNOWLEDGMENTS

This work was conducted under the auspices of the Australian Antarctic Division, Auroral and Space Physics program. A large part of the analysis software was written by Michael Hesse. Additional scientific direction and the spectral analysis software was provided by the University of Newcastle, Space Plasma Waves Group.

REFERENCES

Bolshakova, O.V., Troitskaya, V.A. *and* Ivanov, K.G. (1980). High latitude Pc1-2 geomagnetic pulsations and their connection with location of the dayside polar cusp. *Planetary and Space Science 28*:1–7.

Francke, M.H., Hansen, H.J., Menk, F.W., Fraser, B.J. *and* Morris, R. J. (1992) The propagation of Pcl magnetic bursts across the polar cap region. In: Burns, G. *and* Duldig, M. (Eds). *ANARE Research Notes 88*:82–88.

Hayashi, K., Kokubun, S., Oguti, T., Tsuruda, K., Machida, S., Kitamura, T., Saka, O. *and* Watanabe, T. (1981). The extent of Pcl source region in high latitudes. *Canadian Journal of Physics 59:*1097 – 1105.

Manchester, R.N. (1968). Correlation of Pcl micropulsations at spaced stations. *Journal of Geophysical Research 73*:3549 – 3556.

Menk, F.W., Fraser, B.J., Hansen, H.J., Newell, P.T., Meng C.-I. *and* Morris, R.J. (1992). Identification of the magnetospheric cusp and cleft using Pc 1-2 pulsations. *Journal of Atmospheric and Terrestrial Physics 54:*1021 – 1042.

Morris, R.J. *and* Cole, K.D. (1991). High latitude day-time Pc1-2 continuous magnetic pulsations: a ground signature of the polar cusp and cleft projection. *Planetary and Space Science 33*:1473 – 1491.

Morris, R.J., Cole, K.D., Troitskaya, V.A., Fraser, B.J. *and* Menk, F.W. (1992). Multi-site high latitude ULF magnetic pulsation studies. In: Burns, G.B. *and* Duldig, M.L. (Eds). *ANARE Research Notes 88*:13 – 18.

Neudegg, D.A., Underwood, M.J., Burns, G.B., Fraser, B.J., Menk, F.W., Hansen, H.J. *and* Morris, R.J. (1994). Deployment of a multi-station magnetometer array to examine source regions of ULF waves at southern cusp/cleft latitudes. In: Morris, R.J. (Ed). *ANARE Research Notes 92*:135-143.

Newell, P. T. *and* Meng C.-I. (1988). The cusp and the cleft/boundary layer: low-altitude identification and statistical local time variation. *Journal of Geophysical Research 93:*14549 – 14556.

Newell, P.T. *and* Meng C.-I. (1992). Mapping the dayside ionosphere to the magnetosphere according to particle precipitation characteristics. *Geophysical Research Letters 19:*609 – 612.

Olson, J.V. (1990). ULF pulsations associated with the magnetospheric cusps. *Preprint: Geophys. Inst. Dept. Phys., University of Alaska, Fairbanks.*

12. INTERSTATION ANALYSIS OF DAYSIDE 30–60 mHz Pc3 GEOMAGNETIC PULSATIONS

H.J. Hansen[1], B.J. Fraser[1], F.W. Menk[1], P.T. Newell[2], C.-I. Meng[2] and R.J. Morris[3]

[1] Department of Physics
University of Newcastle
Newcastle NSW 2308
Australia

[2] Applied Physics Laboratory
Johns Hopkins University
Laurel MD 20707
U S A

[3] Auroral and Space Physics
Antarctic Division
Kingston Tasmania 7050
Australia

ABSTRACT

The origin of dayside mid-period Pc3 (30–60 mHz) magnetic pulsations has been investigated using induction magnetometer data recorded at Mawson (L = 8) and Davis (L = 10), Antarctica. These sites are located beneath the average auroral oval and magnetospheric cusp positions respectively. Interstation comparison and cross-spectral analysis of common signals, recorded during different locations of the DMSP-F9 satellite BPS low altitude signature, demonstrate the common activity peaks in amplitude in the pre-noon local time sector and exhibits larger magnitude variations at the site closest to the low altitude BPS signature. It appears that the waves responsible spread from the BPS field lines at ionospheric (apparent) speeds upward of 40 km s^{-1}. These speeds relate to magnetospheric speeds upward of ~1000 km s^{-1} which could suggest the fast compressional mode is the dominant means of entry of solar wind wave energy into the magnetosphere.

12.1 INTRODUCTION

The ionosphere beneath the dayside magnetospheric cusp region spans a few hundred square kilometres. Within this area flow the currents associated with waves and particles in the central cusp, the boundary layers and the closed field lines just within the magnetopause, as virtually the entire dayside magnetopause is imaged to this region. Since ground based magnetometers respond to currents flowing within a hundred or so kilometres of the zenith, magnetometer data will contain a complex superposition of pulsations arising from waves propagating from the many source regions (Glassmeier 1989).

The cusp-associated pulsations are generally a consequence of the solar wind – geomagnetic field interaction at the magnetopause. Processes such as Kelvin-Helmholtz surface wave generation make a dominant contribution to the pulsation signals recorded by magnetometers beneath boundary layer field lines (Takahashi et al. 1991, Samson et al. 1971, Chen and Hasegawa 1974, Olso and Rostoker 1978). The solar wind region upstream of the magnetopause also provides a substantial amount of wave energy which enters the magnetosphere and contributes to the mid-period 30 – 60 mHz ULF magnetic spectrum recorded at cusp locations (Fairfield and Ness 1967, Wolfe and Kaufman 1975, Russel et al. 1983, Greenstadt et al. 1972, 1979,1980, Odera 1986).

The means of entry of this upstream solar wind energy is debatable. It has been suggested that compressional mode waves propagate through the equatorial magnetosphere when the IMF cone angle is small (Greenstadt et al. 1979, 1980). Alternatively the wave energy appears to be able to spread onto magnetospheric field lines both equatorward and poleward of the cusp and cleft ionosphere, since the cusp and cleft field lines comprise the funnel between open and closed field lines and electron precipitation in the cusp ionosphere accompanies pulsations which have been associated with the upstream region (Engebretson et al. 1991).

This study represents the results of the analysis of pulsation observations at Davis and Mawson, Antarctica, which are important in understanding the mechanisms of external wave entry into the magnetosphere from the solar wind upstream region. Boundary layer field lines, mapping from the magnetospheric equator to the dayside auroral ionosphere, are identified as the magnetospheric source of the activity since interstation signal comparison, incorporating cross-spectral analysis, established that the waves move over ground magnetometers poleward and equatorward from the BPS signature. The interstation phase difference measurements that are presented here must be taken into account by whatever wave entry process is providing the dayside magnetosphere with the solar wind energy.

12.2 MULTISTATION ARRAY

The observations to be described were recorded with induction magnetometers at Davis and Mawson in the Australian Antarctic Territory. Figure 1 shows that these stations are favourably situated to record cusp and boundary layer-associated pulsations and to study the physical processes responsible for them. Davis (gm 74.5°S; 29.6°E) is located at local noon near the foot of the average position of the cusp. Here solar wind plasma funnels directly to the ionosphere. The speckled torus represents the average locus of the cusp. Mawson (gm 70°S; 19.6°E) is a typical auroral oval station above which the normally closed field lines contain precipitating plasmasheet (PS) and boundary plasmasheet particles (BPS) which cause associated optical auroral activity. This region maps to the equatorial magnetospheric boundary layer, through which wave energy must propagate to get from the upstream solar wind into the magnetosphere.

At each recording site, induction sensors in the geomagnetic North-South (H) and East-West (D) directions record magnetic variations due to ionospheric current perturbations which are related through electrodynamic coupling to magnetospehric solar wind processes. The minimum detectable magnetic field variation at each site is 0.03 nT at 1 Hz (Fraser

et al. 1991). The data were recorded digitally using PDP-11 computers sampling at 0.33 Hz.

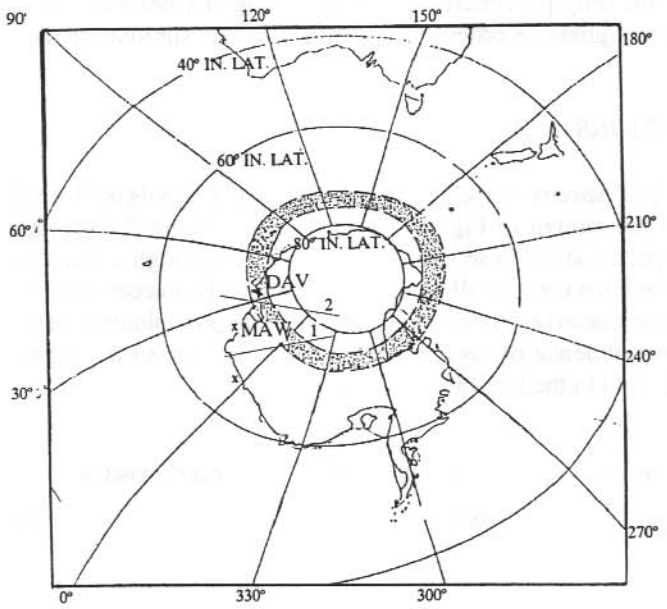

Figure 1. The locations of Davis (DAV) and Mawson (MAW) in geomagnetic coordinates. The speckled region shows those Antarctic locations that rotate beneath the dayside cusp. Traces 1 and 2 show DMSP-F9 orbits above Antarctica between 0300 and 1000 UT on 7 April 1990.

The computers were networked via a satellite link to the Antarctic Division and then the University of Newcastle. Timing accuracy at each site is within 10 ms through daily comparison with international shortwave standards. At Newcastle, the data were converted to a common format using a customised Data Based Management System and accessed through a dedicated LAN with PC 286/386/486 microcomputers. Specific intervals were analysed using multi-channel state vector time series and cross spectral analysis techniques (Samson 1983). This allowed separation of the coherent signals between Mawson and Davis from incoherent or local signals at the two stations.

Six pre-noon intervals of pulsation activity have been studied, on 7, 13 and 14 April 1990 and 20, 21 and 22 January 1991. The chosen intervals range from quiet to active magnetic periods and accordingly are associated with different locations of the DMSP spacecraft's low-altitude boundary layer signature with respect to the Davis and Mawson magnetometers. Figure 1 shows the orbital projections of DMSP-F9 above Antarctica for two successive passes above our array, at 0447 and 0615 UT on 7 April 1990. This spacecraft is in a low altitude sun synchronous orbit and monitors down to < 100 eV

magnetospheric particle signatures (Newell and Meng 1988). Consequently, this demonstrates that during the intervals between 0300 and 1000 UT, the particle topology of the magnetosphere above the induction magnetometer array is known.

Detailed analysis is only presented for the quiet 7 April 1990 and active 13 April 1990 intervals since the signals recorded during these periods summarise the features of this study.

12.3 OBSERVATIONS

The 1 – 70 mHz ULF spectra of the Davis and Mawson H signals on 7 April for the 0412 – 1030 UT period are shown in Figure 2 (left panel). Figure 2 (right panel) shows the corresponding spectra after these signals were passed through a pure-state filter which reduces the uncorrelated noise in all records. Consequently, uncorrelated variations to field lines, such as those caused by localised auroral particle precipitation, have been removed. The spectra show evidence of correlated wave activity due to the strong signals in the Pc5 (1 – 20 mHz) and in the Pc3 (30 – 60 mHz) bands.

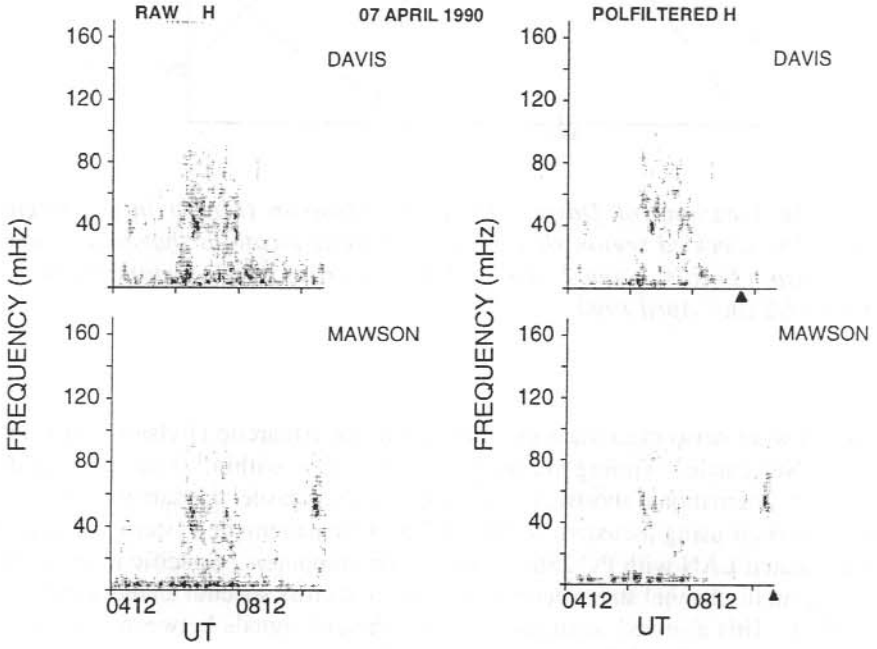

Figure 2. Frequency-time spectra of concurrent magnetic pulsation activity (0 – 70 mHz) recorded on the H component at Davis (top) and Mawson (bottom) on 7 April 1990 from 0412 to 1030 UT. The FFT was evaluated over 256 points in steps of 100 points (33 s). Those spectra were evaluated using the raw signals whereas those on the right show common signals. Local noon at each station is shown by the dark triangles.

The Pc3 30 – 60 mHz activity is bursty within the band and exhibits peak power at 40 mHz. Local noon at each site is indicated by the triangles and clearly these emissions are prevalent in the pre-noon local time sector, 1 – 3 hours before local noon.

The spectrograms also show ~70 mHz bursts just before 1030 UT with amplitudes greater at Mawson than at Davis, although Mawson was further from the BPS in MLAT than Davis.

Figure 3 depicts the amplitude-time series of the ~ 40 mHz emissions recorded from 0745 – 0842 UT at Davis and Mawson. The signals shown have been band-passed filtered between 30 and 60 mHz. The peak amplitude is 8nT at Davis and 4 nT at Mawson.

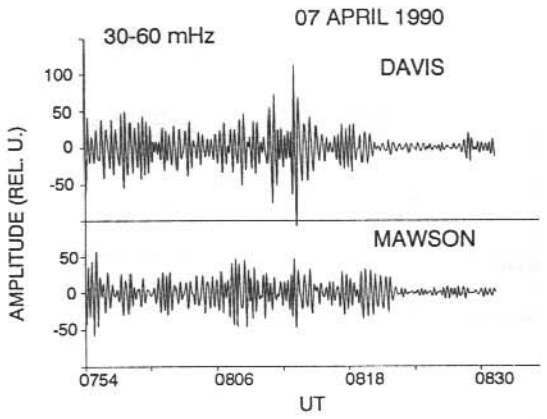

Figure 3. 30–60 mHz amplitude-time variations of H component at Davis and Mawson commencing at 0754 UT on 7 April 1990 (100 Relative Units = 8 nT).

The ULF spectrum from 7 April is typical of dayside activity observed when Davis and Mawson are equatorward of the low altitude BPS. Figure 4 depicts successive locations of the poleward and equatorward edge of the boundary layer-polar mantle field lines throughout the pre-noon local time sector as measured by DMSP-F9. The UT shown corresponds to the time that the spacecraft passed through the BPS signature. For our purposes, we regard the transition between BPS and mantle signatures as the boundary between open and closed field lines. The BPS signature equatorward of this thus embraces the field lines which map to the equatorial low latitude boundary layer, and the cleft field lines which map to the equatorial nose of the magnetopause, whilst the mantle signatures are on those field lines dragged tailward of the cusp. During 7 April, a magnetically quiet day (Kp ~ 2; ΣKp = 17), the poleward edge of the BPS was poleward of both Davis and Mawson with the latter at least 7° equatorward of the boundary layer.

The phase differences between common 40 mHz activity at Davis and Mawson as a function of UT are shown in the top panel of Figure 5. The phase differences were

evaluated between both sets of North–South (H) and East–West (D) signals. Positive phase values indicate Davis leading. Each data point shown is the phase difference associated with the frequency of peak power and was evaluated over 256 points (75 s) in steps of 100 points (33 s). The phase differences were calculated from the ellipticity and azimuth parameters at the common frequencies, in a narrow band centred on 40 mHz where most power was present in the co-spectrum. Values where the degree of coherency (or % polarisation) was less than or equal to 70 % were discarded. This accounts for the irregular spacing of the phase difference values with time. The most notable feature of the top panel in Figure 5 is that the initially positive phase differences, changed to negative values as the sites rotated towards local noon. Initially, before 0600 UT, values are typically positive around 100°. After 0700 UT, negative phase differences of up to 100–150° are shown. Phase differences of about 150° relate to time delays of 10 s at a frequency of 40 mHz.

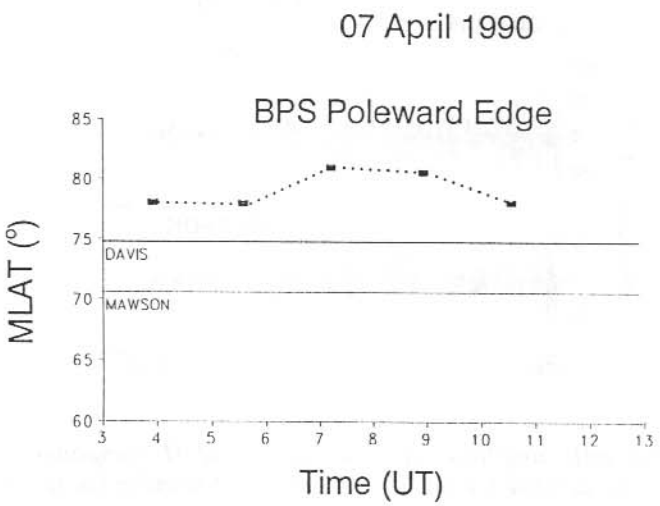

Figure 4. DMSP-F9 location of the low altitude transition between the boundary layer region and the polar mantle on 7 April 1990. Both Davis and Mawson geomagnetic latitudes are indicated.

Direct comparison of the signals is valid because both sets of instrumentation exhibit similar responses. Consequently, the relative power of the variations should be smaller at the site further away from the source. The middle panel of Figure 5 displays the relative power between 40 (±5) mHz signals at Davis (crosses) and Mawson (squares) and clearly the power was greater at Davis than at Mawson. It should be noted that signal power at both sites peaked between 0600–0800 UT, coincident with the change in phase from Davis leading to Mawson leading. During this period, peak-to-peak amplitudes of correlated bursts at Davis were about 6 nT in both components compared to 3 nT at Mawson.

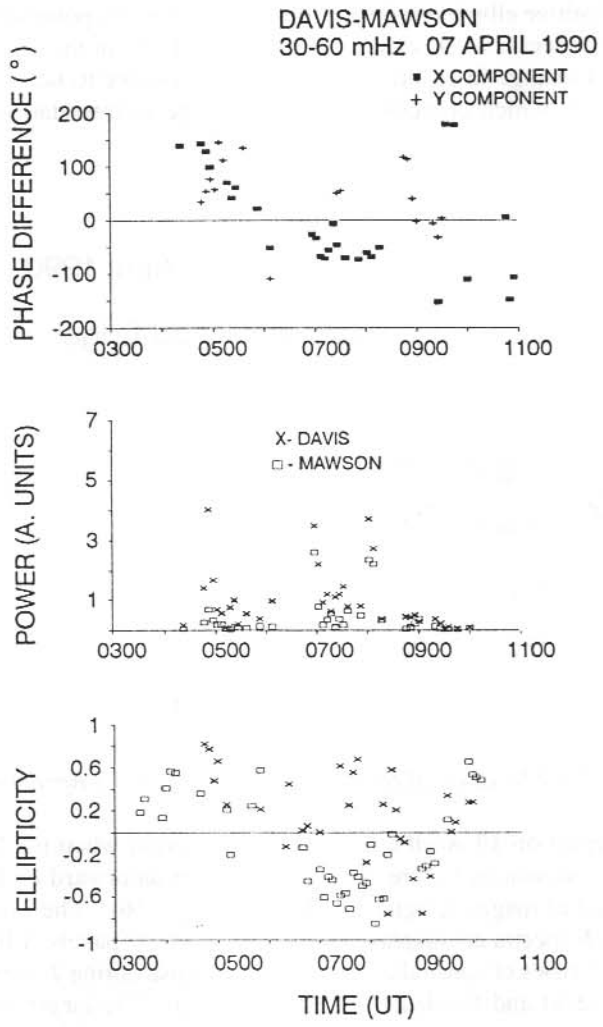

Figure 5. Phase differences of the 40 mHz activity propagating between Davis and Mawson. Positive phase differences means Davis leading. The x/y component refers to the phase differences between signals recorded on the North-South/East-West sensors (top). Relative power versus UT for concurrent Davis and Mawson 40 mHz activity. Relative signal strength is indicted by comparing coincident Davis (X) and Mawson (□) pairs (middle). Ellipticities exhibited by the Davis and Mawson ~40 mHz activity (bottom).

The sense of polarisation and the orientation of the major axis of the polarisation ellipse (the azimuth angle) between these signals are important parameters relating to the waves responsible. The bottom panel of Figure 5 displays the polarisation ellipticity over the interval examined with Davis values indicated by the crosses and the Mawson values by the

open squares. Positive ellipticities imply right-hand circularly polarised waves and negative implies left-handedness, when viewed along the field line in the direction of the ambient field. A distinct change in ellipticity is seen from positive to negative values at around 0700 UT, the time which coincided with the change in interstation phase and peak in power.

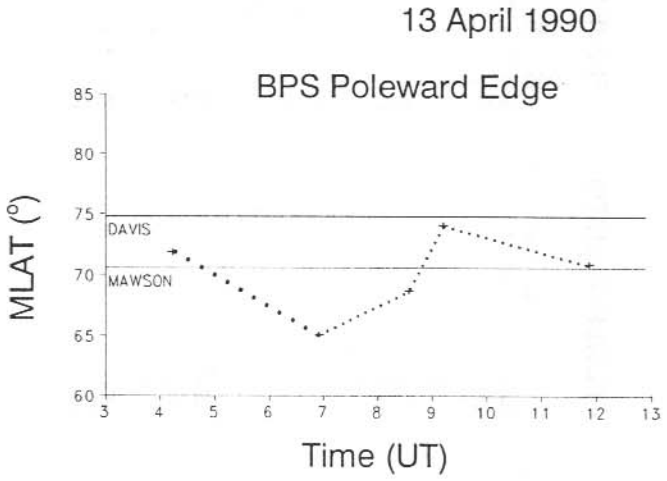

Figure 6. DMSP-F9 location of the low altitude BPS on 13 April 1990.

The second interval on 13 April corresponds to a period when the DMSP-F9 boundary layer signatures, shown in Figure 6, were located equatorward of Davis and Mawson. This was a period of magnetic agitation (Kp ~ 5; ΣKp = 36). The raw and filtered Davis and Mawson ULF spectra are displayed in the left and right panels of Figure 7 respectively. Generally similar types of spectral characteristics to those during 7 April are exhibited, viz., the Pc5 (< 20 mHz) and banded Pc3 (30 – 60 mHz). The larger power at Mawson is evidence that this site was closer to the ionospheric footprint of the field lines on which the wave energy entered the magnetosphere. This is significant since the relative signal strength was reversed during 7 April when the BPS signature was poleward of the array. It is important to note that the concurrent mid-period Pc3 band exhibited maximum power at about 49 mHz, different from the dominant 40 mHz frequencies recorded on 7 April, and these signals peaked in amplitude before 0634 UT, about 1.5 hours earlier than during 7 April. Figure 8 displays typical filtered amplitude-time records of the concurrent H activity at Davis and Mawson. At 0504 UT, the peak-to-peak amplitude of the Mawson signal was 8 nT and the Davis signal was 5 nT.

The top panel of Figure 9 depicts the phase differences for this concurrent Pc3 activity, determined in an identical fashion to Figure 5. The common 49 mHz signals exhibited phase differences which were predominantly negative indicating the waves responsible arrived at Mawson before Davis. It is also evident that the phase differences did not gradually change but were constant (~ -100°). Again this phase difference corresponds to a time delay from Mawson to Davis of ~ 10 s.

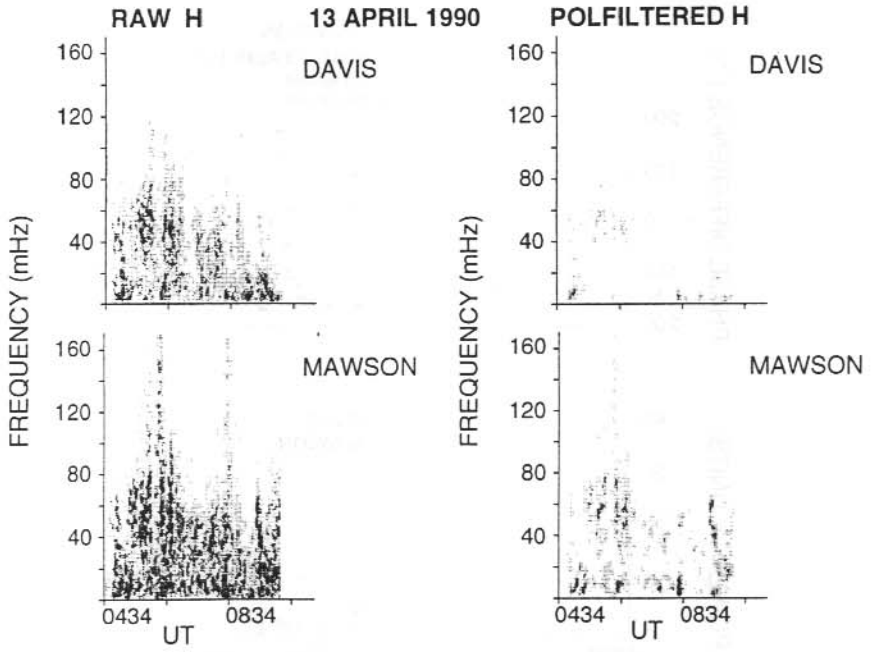

Figure 7. Frequency-time spectra of concurrent magnetic pulsation activity (0–70 mHz) at Davis and Mawson on 13 April 1990. Same format as for Figure 2.

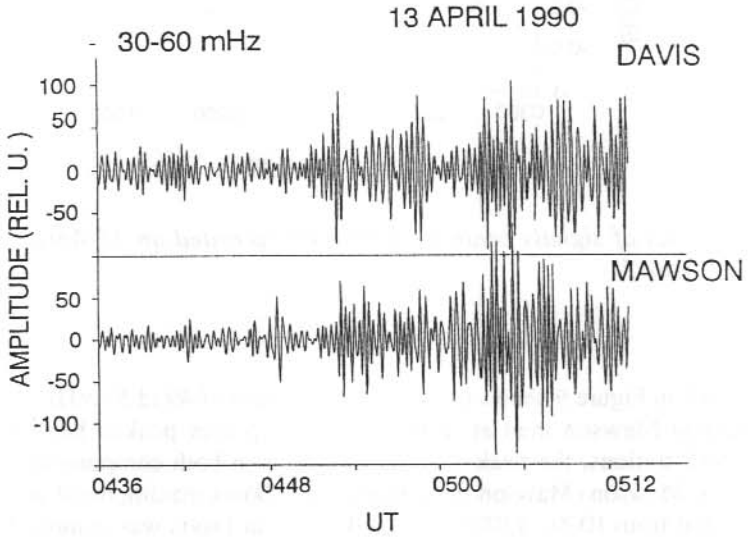

Figure 8. Amplitude-time variations (30–60 mHz) at Davis and Mawson commencing 0436 UT on 13 April 1990 (100 Relative Units = 8 nT).

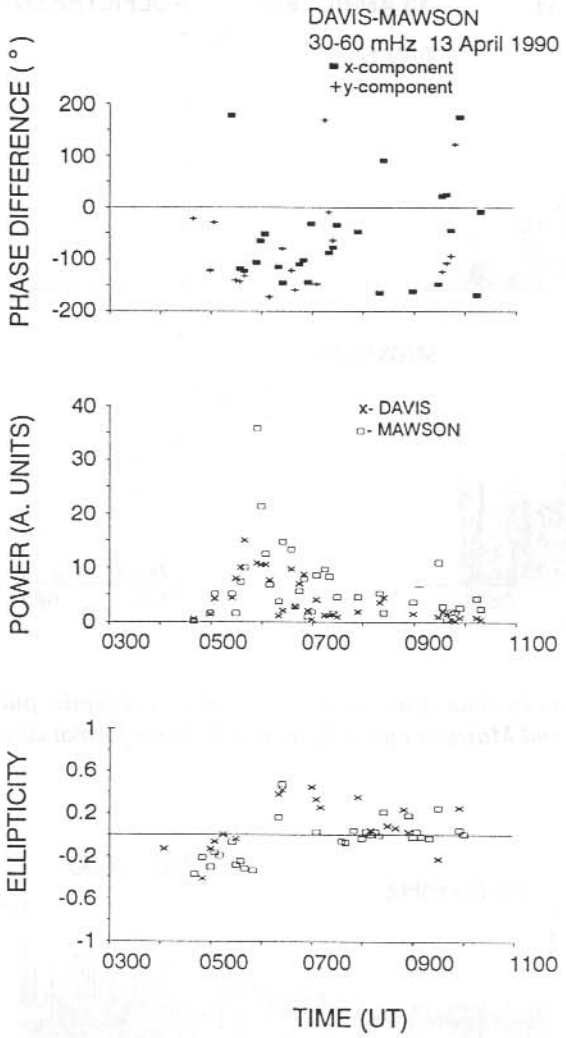

Figure 9. Analysis of signals centred on 49 mHz recorded on 13 April 1990. Same format as for Figure 5.

The middle panel in Figure 9 shows that the relative power of 49 (± 5) mHz signals at each site was larger at Mawson than at Davis. Whereas power peaked between 0500 and 0700 UT at both stations, the peak-to-peak variations in both components were at least twice as large at Mawson (Mawson maximum = 7nT; Davis maximum = 4 nT). It should also be noted that from 1000 – 1100 UT, signal power at Davis was comparable to that at Mawson and there was more power over a wider range of local times at both sites than on 7 April.

The polarisation analysis of the local activity at Davis and Mawson yielded ellipticities which contrast with those values associated with the quiet 7 April period. The bottom panel in Figure 9 shows almost linear ellipticities (± 0.2) throughout the interval, changing from just negative to just positive (left-hand to right-hand sense of rotation), an opposite sign change to that shown in Figure 5. However, as with the previous interval, the change in sign of ellipticity is coincident with the signals exhibiting maximum variations at both sites.

Table 1. Summary of the observational features of the coherent Pc3 activity during the intervals studied.

Interval	7 April 1990	13 April 1990	14 April 1990	21 January 1991	22 January 1991
frequency (mHz)	40	50	40	30	45
BPS w.r.t array	poleward of Davis	equatorward of Davis	poleward of Davis	poleward of Davis	poleward of Davis
Relative signal strength	Davis > Mawson	Davis > Mawson	Davis > Mawson	Davis > Mawson	Davis > Mawson
Propagation Direction	Changes: Davis to Mawson, then Mawson to Davis	Mawson to Davis	Davis to Mawson	Davis to Mawson	–
Ground Speeds (km s^{-1})	above 40	~40	~40	above 40	–

Table 1 summarises these observational features of the coherent pre-noon Pc3 activity, including the results of similar analyses for three further intervals. Each interval displays signals exhibiting a different centre frequency. This was most clear on 13 and 14 April and inspection of IMP-8 B_{IMF} observations for these days shows that the centre frequencies, f, vary in accordance with the empirical $f \sim B_{IMF}/160$ relation (Gul'elmi et al. 1973, Vero and Hollo 1978). B_{IMF} during 13 April ($7.4 < B_{IMF} < 8.5$ nT) was higher than that measured during 14 April ($6.7 < B_{IMF} < 7.1$ nT). We regard this as evidence that the processes responsible for the Pc3 activity originate in the region upstream of the magnetopause.

The relative amplitudes of the signals at Mawson and Davis show the signals are larger closer to the BPS. During 14 April and 21 January, the poleward edge of the BPS was observed poleward of Davis and Mawson and phase differences are consistent with propagating waves moving from Davis to Mawson away from the BPS signatures.

12.4 DISCUSSION

It is well known that both coherent and incoherent Pc3 pulsations observed with spaced stations are prominent features of the high latitude ULF spectrum (Olson 1986). The polarisation filtering (Samson 1983) that has been used here ensures that the localised uncorrelated activity has been removed. This incoherent contribution comprises the localised signals generated in the overhead ionosphere by fluctuating kilovolt electrons. Both Engebretson et al. (1986, 1987) and Olson (1986) have shown a close association between these signals and boundary layer λ 557.7 nm auroral emissions.

One of the goals of this study has been to further understand the nature and source of coherent ground magnetic signals recorded both poleward and equatorward of the low altitude BPS signature which we assume to map to the transition between open and closed field lines in the dayside magnetosphere. This study of mid-period Pc3 activity extends a previous study concerned with the nature of coherent low frequency (< 20 mHz) high latitude activity (Dunlop et al. 1993) to higher frequencies. They associated low frequency activity both with the Kelvin-Helmholtz surface-like waves generated in the equatorial magnetospheric boundary, and with solar wind pressure pulses on the magnetopause. We are now able to address the most likely propagation processes involved with getting upstream solar wind associated, mid-period 30 – 60 mHz activity into the dayside magnetosphere.

The isotropic fast compressional mode plays an important role because of the apparent phase speeds determined from the interstation phase delays. Phase differences between Davis and Mawson of 0 to 100° relate to time delays from 0 – 10 s for 40 mHz signals and to delays of 0 – 6 s for 49 mHz waves. The separation between Davis and Mawson is about 400 km in latitude and about 400 km in longitude and so observational speeds upward of 40 km s^{-1} in the ionosphere can be inferred assuming a 10 s time delay. If dipole geometry is assumed and if it can be considered that the wave information takes approximately the same time interval to get from the equator to the ground along the Davis (L = 10) and Mawson (L = 8) field lines, the 40 km s^{-1} speeds map to 800 km s^{-1} speeds in the equatorial plane. Speeds > 800 km s^{-1} are expected to be more correct because the distortion of the geomagnetic field lines at high latitudes will make the equatorial distance between Davis and Mawson field lines smaller. These values are comparable to the previous estimates of phase velocities that have been determined from ULF activity observations associated with the magnetospheric boundary layer region (Takahashi et al. 1991, Samson et al. 1971). The Alfvén velocity

$$V_a = \frac{B}{\sqrt{\mu_o 4\pi n}}$$

dependent on the local magnetic field B and the local plasma density and substituting typical values (B = 80 nT, n = 5 cm^{-3}) seen on ISEE (Russell and Elphic 1978) or other spacecraft,

e.g., SCATHA (Takahashi et al. 1991) in the boundary layer yields a v_a = 800 km s^{-1} which is consistent with the speeds determined from our observations.

The apparent phase differences between Davis and Mawson indicate that wave energy spreads throughout the magnetosphere into the equatorial region rather than at ionospheric altitudes. We view the waves spreading isotropically from magnetopause field lines into the magnetosphere. As they cross magnetospheric field lines, shear Alfvén waves will be excited, guiding wave energy to the ionosphere which then causes the magnetic variations which the magnetometers detect. Those field lines both poleward and equatorward of the BPS field lines will always be disturbed after the magnetopause BPS field line and therefore magnetometer signals located far from the BPS will be delayed. Wave energy entry via the particle cusp and ionosphere is not important here because propagation via this route should yield no phase difference between our two recording sites over the whole dayside sector and this was not evident during any interval in the analysis.

Wave entry via the isotropic compressional mode in the equatorial magnetosphere can account for the phase delay features observed during on both 7 and 13 April in the following way. These waves would enter through the boundary layer and spread into the magnetosphere in the pre-noon local time sector and it can be speculated that the local time sector extent of this entry region will be broad or narrow depending on the IMF cone angle and the level of magnetic activity. During the quiet 7 April period, signal amplitudes and power peaked over a narrow region from 0700–0800 UT as seen in Figure 5. Prior to 0600 UT, Davis and Mawson were located equatorward of boundary layer field lines but west of the longitude where the energy was entering. Consequently, isotropic compressional waves entering at this time should reach Davis before Mawson. Later, after both stations had in turn rotated past the wave source, the waves were seen at Mawson then Davis. On 13 April, the interstation phase was constant between 0500 and 0700 UT. In this instance, we speculate the wave energy entered the magnetosphere over a broader source region (suggested by the amplitudes peaking over a broad range of local times) and thus the waves will spread radially to Davis and to Mawson field-lines. This would lead to the observed constant phase differences, determined by the fixed magnetospheric radial distance ΔL between Davis and Mawson field lines. Although this does not explain the smaller Mawson signal strength after 0700 UT on 7 April than that at Davis, this inconsistency was not present during the other intervals studied. Table 1 shows that mostly observations of higher signal strengths and leading phase went together when comparing the signals at two sites.

The polarisation ellipticities, particularly the reversal in the pre-noon sector relating to this Pc3 activity, are in accordance with the property of pre-noon and postnoon waves moving anti-sunward after entry through the pre-noon boundary layer.

The identification of a region of Pc3 wave energy entry into the magnetosphere in the pre-noon local time sector points to a wave definition for the cusp, where the term cusp refers to direct energy input from solar wind into the magnetosphere. Currently, the cusp is thought of in terms of a particle definition, viz., the region within the magnetosphere where magnetosheath particles (defined by flux and energy characteristics) are found (Newell and Meng 1988). The wave cusp can be viewed as a region in the noon local time sector where energy spreads into the magnetosphere from the equatorial boundary layer and through the

ionosphere from those field lines which map to the equatorial magnetospheric boundary layer. Physically this relates to the region where bow shock turbulence maximises and the local time of occurrence will be specified by the IMF cone angle. Compressional wave energy propagates directly from this region into the magnetosphere (Takahashi et al. 1991).

Finally, a scenario is outlined which summarises the dominant source of solar wind associated Pc3 pulsations for the 7, 13 April and other intervals presented in Table 1. The association of IMF magnitude with pulsation frequency points to ion cyclotron waves in the region upstream of the bow shock as being responsible for the 30–60 mHz Pc3 activity. The wave energy most likely enters the equatorial magnetospheric boundary region from the bowshock propagating isotropically in the fast Alfvén mode (Greenstadt et al. 1980, Chen and Hasegawa 1974). As wave energy propagates across magnetospheric field lines, some of the energy is dissipated as field aligned shear Alfvén mode waves, which are guided to the ionosphere. These perturb the ionospheric current systems and cause the magnetic field variations detected by magnetometers. The observed phase delays between common magnetic signals are associated times of travel of the fast mode wave energy within the magnetosphere, however this must be verified since the shear Alfvén mode propagation times from the equator to ionosphere were not considered. Superimposed upon this spectrum are localised signals associated with auroral precipitation and correlated optical emissions which are not coherent between Davis and Mawson.

12.5 ACKNOWLEDGMENTS

Thanks are due to Antarctic Division for providing the field logistics for this research. The authors also acknowledge the Australian Research Council (ARC) and the Antarctic Science Advisory Committee (ASAC) for financial support.

REFERENCES

Chen, L. *and* Hasegawa, A. (1974). A theory of long-period magnetic pulsations 1, Steady state excitation of field line resonance. *Journal of Geophys. Research 79*:1024–1032.

Dunlop, I.S., Menk, F.W., Hansen, H.J., Fraser, B.J. *and* Morris, R.J. (1993). A multistation study of long period geomagnetic pulsations at cusp and boundary layer latitudes. *Journal of Atmospheric and Terrestrial Physics 56*:667–679.

Engebretson, M.J., Meng, C.-I., Arnoldy, R.L. *and* Cahill, L.J. (1986). Pc3 pulsations observed near the south polar cusp. *Journal of Geophysics Research 91*:8909–8918.

Engebretson, M.J., Zanetti, L.J., Potemra, T. A ., Baumjohann, W., Luhr, H. *and* Acuna, M.H. (1987). Simultaneous observation of Pc3-4 pulsations in the solar wind and in the Earth's magnetosphere. *Journal of Geophysics Research 92*:10053–10062.

Engebretson, M.J., Cahill, L.J.(Jnr), Arnoldy, R.L., Anderson, B.J., Rosenberg, T.J., Carpenter, D.L., Inan, U.S. *and* Eather, R.H. (1991). The role of the ionosphere in coupling upstream ULF wave power into the dayside magnetosphere. *Journal of Geophysics Research 96*:1527 – 1542.

Fairfield, D.H. *and* Ness, N. F. (1967). Magnetic field measurements with the IMP 2 satellite. *Journal of Geophysics Research 72*:2379 – 2402.

Fraser, B.J., McNabb, P.W., Menk, F.W. *and* Waters, C.L. (1991). A personal computer induction magnetometer system for recording geomagnetic pulsations. *ANARE Research Notes 80*:83 – 92.

Glassmeier, K.H. (1989). ULF pulsations in the polar cusp and cap. In: *P.* E. Sandholt and A. Egeland (Eds). *Electromagnetic Coupling in the Polar Clefts and Caps.* Kluwer, Dortrecht. Pp. 167 – 186.

Greenstadt, E.W. (1972). Field-determined oscillations in the magnetosheath as a possible source of medium period, daytime micropulsations. *Proceedings of Conference on S.T. Rel.*, University of Calgary. P. 515.

Greenstadt, E.W., McPherron, R.L. *and* Takahashi, K. (1980). Solar wind control of daytime, midperiod, geomagnetic pulsations. *Journal of Geomagnetic and Geoelectricity 32*:89 – 108.

Greenstadt, E.W., Singer, H.J., Russell, C.T. *and* Olson, J.V. (1979). IMF orientation, solar wind velocity, and Pc3-4 signals: A joint distribution. *Journal of Geophysics Research 84*:527.

Gul'elmi, A.V., Plyasova-Bakunina, T.A., Shchepetnov, R.V. *and* Troitskaya, V.A. (1973). Relation between the period of geomagnetic pulsations Pc3-4 and the parameters of the interplanetary medium at the Earth's orbit. *Geomagnetism and Aeronomy 13*:331 – 333.

Newell, P.T. *and* Meng, C.-I. (1988). The cusp and cleft/boundary layer low altitude identification and statistical local time variation. *Journal of Geophysics Research 93*:14549 – 14556.

Odera, T.J. (1986). Solar wind controlled pulsations: A review. *Review of Geophysics Research 24*:55 – 74.

Olson, J.V. (1986). ULF signatures of the polar cusp. *Journal of Geophysics Research 91*:10055 – 10062.

Olson, J.V. *and* Rostoker, G. (1978). Longitudinal phase variations of Pc4-5 micropulsations. *Journal of Geophysics Research 83*:2481 – 2488.

Russell, C.T. *and* Elphic, R.C. (1978). Initial ISEE magnetometer results: Magnetopause observations. *Space Science Reviews* 22:681 – 715.

Russell, C.T., Luhmann, J.G., Odera, T.J. *and* Stuart, W.F. (1983). The rate of occurrence of dayside Pc3-4 pulsations: The L value dependence of the IMF cone angle effect. *Geophysics Research Letters 10*:663 – 666.

Samson, J.C., Jacobs, J.A. *and* Rostoker, G. (1971). Latitude dependent characteristics of long period geomagnetic micropulsations. *Journal of Geophysics Research 76*:3675 – 3683.

Samson, J.C. (1983). The spectral matrix, eigenvalues, and principal components in the analysis of multichannel geophysical data. *Anns. Geophys 1*:115 – 119.

Takahashi, K., Sibeck, D.G., Spence, H.E. *and* Newell, P.T. (1991). ULF waves in the low latitude boundary layer and their relationship to magnetospheric pulsations: A multisatellite observation. *Journal of Geophysics Research 96*:9503 – 9520.

Vero, J. *and* Hollo, L. (1978). Connections between IMF and geomagnetic pulsations. *Journal of Atmospheric and Terrestrial Physics 40*:857 – 865.

Wolfe, A. *and* Kaufmann, R.L. (1975). MHD wave transmission and production near the magnetopause. *Journal of Geophysics Research 80*:1764 – 1775.